Application of a novel CCD technology to medical imaging

Emma Jane Harris

UNIVERSITY COLLEGE LONDON

Submitted for
The Degree of Doctor of Philosophy
The University of London

OCTOBER 2002

ABSTRACT

This thesis describes an evaluation of a novel low light level charge couple device (L3CCD) technology.

Two L3CCDs have been fully evaluated in terms of their signal and noise properties. The primary aim of this work is to identify the device characteristics that affect the overall performance. Conclusions have been made to this end and a prediction of the optimal performance in terms of the device sensitivity is made. Comparisons with other detectors suitable for use in medical imaging have shown that the L3CCD surpasses other detectors in specific performance characteristics and is comparable in others. The competitive performance of the L3CCD confirms that it may afford benefits in those areas in which the L3CCD has superior performance compared to other detectors.

Two diagnostic imaging techniques which were identified as applications of L3CCD technology have been investigated.

Linear systems analysis has been used to predict the performance of two L3CCD based imaging systems for use in fluoroscopic imaging. Comparison of the predicted performance of the two system with systems in clinical use show that an L3CCD coupled to an x-ray phosphor via a tapered fibre optic is a competitive alternative to present fluoroscopic imaging systems. Experimental validation of the model has confirmed this conclusion.

An L3 detector has been designed, built and evaluated for diffraction enhanced breast imaging. To demonstrate the use of the L3 detector for diffraction enhanced breast imaging it has been used to acquire diffraction images of human breast tissue with cancerous inclusions. Measurements of scatter contrast confirm improvements in scatter contrast compared to transmission contrast. The successful demonstration of the L3CCDs ability to collect diagnostic information has shown that the L3CCD is suitable for diffraction enhanced breast imaging.

TABLE OF CONTENTS

Page No.

Abstract 2

Contents 3

Figures 9

Tables 14

Acknowledgements 15

CHAPTER 1
Introduction

1.1. Considerations for optimal x-ray detector performance 16

1.2. Low light level charge coupled device technology 19

1.2.1 Aims and objectives of the thesis 20

1.3. An overview of CCDs in digital radiography 20

1.4. Other detectors in digital radiology 23

1.5. Description of the thesis 24

CHAPTER 2
The CCD65: background and theory

2.1. Basic Principles of CCD operation 26

2.1.1. BCCD design and operation 26

2.1.2. Charge transfer 28

2.1.3. Charge read out 29

2.1.4. CCD architecture 30

2.1.5. Optical response 32

2.1.6. CCDs for x-ray detection 33

2.1.7. Dark current 35

2.1.7.1. Inverted mode operation 37

2.2. Noise 39

2.2.1. Input noise 39

2.2.1.1. Input shot noise 40

2.2.1.2. Thermal noise 40
2.2.1.3. Fixed pattern noise 40
2.2.2. Transfer noise 40
2.2.3. CCD system noise 41
2.2.3.1. Reset noise 42
2.2.3.2. Amplifier noise 42
2.2.3.3. Digitisation noise 43
2.2.3.4. Background electronic noise 43
2.2.3.5. Total system noise 43
2.3. L3 Technology 44
2.3.1. CCD65 sensors 44
2.3.2. L3 gain 46
2.3.3. Impact ionisation 48
2.3.4. Temperature dependence of gain 49
2.3.5. Gain register design 50
2.3.6. CCD65 dark signal performance 51
2.4. Excess noise factor 53
2.4.1. Physical parameters affecting the excess noise factor 53
2.4.2. Physical properties of the L3 gain register affecting excess noise 55
2.4.3. Quantification of the excess noise factor 56

CHAPTER 3
Camera Characterisation

3.1. Description of the system 62
3.1.1. Detector design 62
3.1.2. The L3CCD camera 63
3.1.3. Image acquisition 64
3.1.4. Cooling 65
3.1.5. Full well capacity 66
3.1.6. Dark current and electrical offset 67
3.1.7. Image correction 67
3.2. Conversion gain calibration 68
3.2.1. Determination of C 69
3.2.2. Summary of the calibration results 75

3.3. Gain characterisation 76
3.3.1. Gain calibration 77
3.3.1.1. Theoretical analysis of the gain mechanism 79
3.3.2. Gain as a function of temperature 81
3.3.2.1. Theoretical analysis of the temperature dependence of gain 82
3.3.3. Gain linearity 83
3.3.4. Conclusions about the gain mechanism 85
3.4. Noise Measurements 85
3.4.1. Fixed pattern noise 86
3.4.2. CCD system noise 87
3.4.3. CCD system noise as a function of gain 88
3.4.4. Signal to noise ratio as a function of gain 90
3.4.5. Calculation of limiting SNR 92
3.4.6. Calculation of the minimum detectable signal 93
3.4.7. CCD dark noise as a function of temperature 94
3.4.8. Conclusions about CCD65 noise 95
3.5. Excess noise factor 98
3.6. Dynamic Range 101
3.7. Discussion and conclusions 105
3.7.1. Characterisation results 105
3.7.2. Comparison of L3 performance with other detctors 107
3.7.3. Possible medical applications 110
3.7.3.1. Fluoroscopy 110
3.7.3.2. Diffraction enhanced breast imaging 112

CHAPTER 4
L3 technology application to medical imaging: Fluoroscopic imaging

4.1. Fluoroscopic imaging 116
4.1.1. Fluoroscopic imaging systems 117
4.1.1.1. X-ray image intensifiers 117
4.1.1.2. Active matrix flat panel imagers 118
4.1.2. Imaging requirements 118
4.1.2.1. Input dose rate 119
4.1.2.2. Dynamic range 119
4.1.2.3. Detective quantum efficiency 119

4.1.2.4. Spatial resolution 120
4.1.2.5. Field of view 120
4.1.3. L3 fluoroscopic imaging 120
4.2. Modelling the L3 fluoroscopic imaging system 121
4.2.1. Linear systems analysis 121
4.2.1.1. Zero-frequency noise propagation 122
4.2.1.2. Zero-frequency DQE 123
4.2.2. Coupling efficiency 123
4.2.3. System description 124
4.2.4. Stages and quantities used in the model 125
4.2.5. Results of the model 128
4.2.5.1. Quantum accounting diagram 129
4.2.5.2. Coupling efficiency 130
4.2.5.3. Zero-Frequency DQE 130
4.2.5.4. Spatial resolution 132
4.2.5.5. Dynamic range 132
4.2.5.6. Conclusions about the model results 132
4.3. L3 fluoroscopic system measurements 134
4.3.1. System linearity, zero-frequency DQE and coupling efficiency 134
4.3.2. Frequency dependent detective quantum efficiency 137
4.3.2.1. Modulation transfer function 137
4.3.2.2. Noise power spectra 139
4.3.2.3. Frequency dependent DQE 140
4.4. Conclusions 142

CHAPTER 5
L3 technology application to medical imaging: Diffraction enhanced breast imaging

5.1. Diffraction enhanced breast imaging 145
5.1.1. Physics of diffraction mammography 145
5.1.2. Work to date 146
5.1.2.1. Distinction between diseased and normal tissue 146
5.1.2.2. Breast imaging 147
5.1.3. Proposed DEBI system 149
5.1.4. Aims and objectives of this work 150

5.2. Design of the L3 DEBI system 150
5.2.1. Components of the diffraction imaging system 151
5.2.1.1. The x-ray source 151
5.2.1.2. The breast phantom 152
5.2.1.3. The collimation system 152
5.2.1.4. Scatter detector 154
5.2.2. Collimation system design 154
5.2.2.1. Collimator design parameters 156
5.2.2.2. Model results 158
5.2.2.3. Collimator description 159
5.2.2.4. Momentum resolution of the L3 DEBI system and predicted contrast 160
5.2.3. Detector design 160
5.2.3.1. Model results 162
5.2.3.2. Detector Performance 163
5.3. Materials and methods 164
5.3.1. Description of the experimental set-up 165
5.3.1.1. The X-ray source 165
5.3.1.2. Primary collimators 166
5.3.1.3. Ion chamber 166
5.3.1.4. L3 Detector and collimator holder 166
5.3.1.5. Supporting framework and translational equipment 167
5.3.1.6. Primary beam shielding and multiple scatter 167
5.3.1.7. The breast tissue phantom 167
5.3.2. Data acquisition 168
5.3.2.1. System alignment 168
5.3.2.2. Integration time 170
5.3.2.3. Description of programme used for data collection 170
5.3.2.4. Data corrections 171
5.4. Diffraction Imaging 172
5.4.1. In vitro diffraction imaging using the L3 detector 172
5.4.2. Investigation of additional contrast information 175
5.5. Conclusions 178

CHAPTER 6
Conclusions and further work

6.1. Evaluation of L3 technology 180

6.2. L3 technology application to medical imaging 182

APPENDIX A 184

REFERENCES 186

FIGURES

		Page No.
CHAPTER 2		
Figure 2.1	A schematic representation of a cross section through a BCCD.	27
Figure 2.2	Potential profile through the BCCD structure shown in figure 2.1.	28
Figure 2.3	Movement of charge through the CCD by clocking electrode voltages.	29
Figure 2.4	Typical CCD output structure	29
Figure 2.5	(a) to (d) Schematic representation of a typical frame transfer CCD.	31
Figure 2.6	Quantum efficiency plotted as a function of wavelength for front and back illuminated devices.	32
Figure 2.7	Illustration of the effect of phosphor thickness on the spread of light across the CCD.	34
Figure 2.8	Schematic of the CCD65 architecture.	45
Figure 2.9	An illustration of the two-phase clocking sequence used to achieve interlacing.	46
Figure 2.10	Schematic diagram of the gain register operation.	47
Figure 2.11	Schematic diagram a gain register element.	50
Figure 2.12	Schematic diagram of the gain register element after Burt and Bell	50
Figure 2.13	A typical variation of dark signal, measured by E2V Technologies Ltd, as a function of temperature for the CCD65.	51
Figure 2.14	Predicted potential distribution during transfer of charge from $R\varnothing_1$ to $R\varnothing_2HV$.	55
Figure 2.15	The excess noise factor calculated for the L3 gain register.	58

CHAPTER 3

Figure 3.1	An illustration of the CCD65-02 x-ray sensor design which is intended for single x-ray photon detection in the 15 to 20 keV energy range	63
Figure 3.2	Cooling curve for CCD65-02.	66
Figure 3.3	Schematic representation of the gain stages involved in the photon detection process.	68
Figure 3.4	Schematic of the experimental set up for the CCD calibration measurements.	72
Figure 3.5	Detector linearity is illustrated in this plot of digital signal vs incident irradiance for CCD65-01.	73
Figure 3.6	Mean-variance plots obtained CCD65-01.	74
Figure 3.7	Gain calibration at –7 °C, 15 °C and 41 °C . (a) The total gain as a function of $R\varnothing_2HV$. (b) The gain per stage as a function of $R\varnothing_2HV$.	78
Figure 3.8	Ionisation rate plotted as a function of inverse electric field.	80
Figure 3.9	(a) Measured temperature dependence of the total gain. (b) The percentage increase in gain per stage plotted as a function of temperature.	81
Figure 3.10	Measured multiplication gain for different input signals S compared to measured multiplication gain for S = 1.4DN.	84
Figure 3.11	Measured standard deviation due to FPN as a function of the mean output signal.	87
Figure 3.12	Total CCD system noise as a function of total multiplication gain and gain per stage (a) and (b) for CCD65-01 and (c) and (d) for CCD65-02	90
Figure 3.13	Measured SNR and total noise variation with gain.	91
Figure 3.14	Theoretical plots of SNR versus gain as a function of input signal and system noise.	92
Figure 3.15	System noise plotted as a function of temperature for CCD65-02 at $R\varnothing_2HV$=53.9 V.	95

Figure 3.16	The percentage increase in gain with decreasing temperature and the percentage decrease in thermal noise with decreasing temperature.	96
Figure 3.17	Thermal noise and spurious noise as a function of temperature.	96
Figure 3.18	The excess noise factor plotted as a function of gain, (a) S_i = 50 DN (b) S_i = 16.5 DN and (c) S_i = 3.4 DN.	100
Figure 3.19	Schematic of the variation of dynamic range with gain.	102
Figure 3.20	Variation of dynamic range with gain for CCD65-01 operating at 15 ° C and the CCD65-01 operating at -7 ° C.	104

CHAPTER 4

Figure 4.1	Schematic of the L3 based fluorscopic system.	124
Figure 4.2	QADs for the three square input field sizes for the L3 fluoroscopic system with M =100 shows the number of quanta per incident x-ray in each stage.	130
Figure 4.3	Measured variation of SNR with incident dose rate.	135
Figure 4.4	Comparison of predicted and measured $DQE(0)$.	136
Figure 4.5	The *MTF* of the imaging system with different levels of gain used to compensate fall in coupling efficiency affected by the use of ND filters.	139
Figure 4.6	Noise power spectra for the L3 fluoroscopic imaging system. Data has been binned into 0.4 mm^{-1} intervals and averaged.	140
Figure 4.7.	The *DQE* as a function of spatial resolution for the L3 fluoroscopic imaging system.	141

CHAPTER 5

Figure 5.1	Comparison of the scatter signatures for the 'pure' carcinoma sample with that of both normal breast tissue (50:50 fat/fibrous mixture).	147

Figure 5.2	The proposed DEBI system that employs the L3CCD detector to acquire scatter images using a slit beam of radiation.	149
Figure 5.3	A schematic of a diffraction set-up.	151
Figure 5.4	Incident x-ray spectra from Mo anode/filter x-ray tubes at 30kVp (Birch and Marshall, 1979).	152
Figure 5.5	The scatter volume defined in terms of the spatial resolution in the x-, y- and z- directions	153
Figure 5.6	Schematic representation of the gain stages involved in the photon scatter process.	155
Figure 5.7	Range of momentum transfer values recorded as a result of the finite angular acceptance of the collimator	157
Figure 5.8	The spatial resolution in the x-direction plotted as a function of collimator length for fixed values of collimator width.	158
Figure 5.9	A schematic representation of the design of the scatter collimator to be used in the L3 DEBI system.	159
Figure 5.10	Schematic representation of the CCD65 detection process for a 17.4keV x-ray photon.	161
Figure 5.11	Images of direct and indirect x-ray photon interactions acquired with the CCD65-02. In (a) phosphor interactions and (b) silicon interactions at gain M =4096±86.	163
Figure 5.12	Schematic illustration of the experimental L3 DEBI set up at the SYRMEP beam line.	165
Figure 5.13	Photograph of the L3 detector, the collimator and the breast phantom.	167
Figure 5.14	The human breast tissue phantom, (a) schematic representation of the Perspex holder and the position of the cancerous inclusions identified by the histo-pathologist and (b) digital radiographic image of the phantom.	168
Figure 5.15	System alignment.	169
Figure 5.16	The variation in scatter intensity with variation of collimator height above the beam.	170

Figure 5.17	Images of the cancerous tissue inclusions in the breast tissue phantom (a) diffraction and (b) transmission. The highlighted area shows a region of normal breast tissue, which was used to normalise the images for comparison.	173
Figure 5.18	Profiles through scatter and transmission images (a) strip1, (b) strip2 and (c) strip3. The y-ordinate values equal the total digital signal per image pixel.	174
Figure 5.19	Momentum transfer values of interest; 1.1nm^{-1} provides the maximum contrast (51%), at 1.6 nm^{-1} the contrast is reversed (-13%) and at 1.4nm^{-1}, $\chi_{h} = \chi_{d}$ and the contrast is zero.	176
Figure 5.20	Diffraction images recorded at 3 different momentum transfer values.	177
Figure 5.21	Profiles through the centre column of pixels for diffraction image recorded using at 1.1nm^{-1} 1.4nm^{-1} and 1.6 nm^{-1}.	177

TABLES

Page No.

CHAPTER 2

Table 2.1 Main characteristics of the CCD used in this study. 44

CHAPTER 3

Table 3.1 Full well capacity data for CCD65-01 and CCD65-02 image and gain register sections. 75

Table 3.2 Comparison of L3CCD performance with other detectors that employ gain. 106

Table 3.3 Comparison of the L3CCD performance with other indirect detectors 108

Table 3.4 Comparison of the L3CCD performance with direct detectors 109

CHAPTER 4

Table 4.1 Description of the gain and Poisson excess values for each stage of the L3 imaging system. 129

Table 4.2 Zero-frequency DQE values for the modelled fluoroscopic imaging system. 131

CHAPTER 5

Table 5.1 Output parameters from the diffraction model for values of SR_x 158

Table 5.2 The average measured contrast between diseased and normal tissue for each strip. 175

Errata

P.1 Pa.1 for 'charge couple device' read 'charge coupled device'.

P.15 Pa. 6 for 'EPSERC' read 'EPSRC'.

P.17 Pa.3 for '(the x-ray phosphor,)' read '(for the x-ray phosphor),'.

P.24 Pa.2 for 'a through understanding' read 'a thorough understanding'.

P.26 Pa.1 for 'operation L3 technology' read 'operation of L3 technology'.

P.36 Pa.2 for 'the variation of n_I' read 'the variation of n_i'.

P.38 Pa.1 for "inverts" read 'inverts'.

P.44 Pa. 2 for '576 active rows' read '576 active coloumns'.

P.49 Pa.2 for 'been used to derived' read 'been used to derive'.

P.52 Pa.2 for 'interface sates' read 'interface states'.

P.53 Pa.4 for 'showed that the excess it was' read 'showed that the excess noise was'.

P.55 pa.2 for 'consider the parameters k and M will be considered' read 'the parameters k and M will be considered'

P.56 Pa.2 for 'through the gain stage' read through the gain stages'.

P.61 Pa.3 for 'been made soley' read 'been made solely'.

P.62 Pa.4. for 'diffraction enhance imaging' read 'diffraction enhanced imaging'.

P.63 Pa.1 for 'was found give' read 'was found to give'.

P.105 Pa.1 for 'gain is compare' read 'gain is compared'.

P.106 T3.2 for 'Is the max<' read Is the max gain <'.

P.108 Pa.1 for 'except for the PSPMT' read 'except for the PSPMT and the HAPD'

P.113 Pa.4 for 'primarily concerned is with' read 'primarily concerned with'.

P.116 Pa.1 for 'perhaps its most' read 'perhaps it's most'.

P.121 Pa.2 for 'the QAD will be adjusted' read 'the DQE will be adjusted'.

P.123 Pa.3 for 'Maidement' read 'Maidment'.

P.129 Pa.1 for '$\sqrt{35\times0.04}$' read '$\sqrt{27\times0.04}$'.

P.130 Pa.1 for 'efficncy' read 'efficiency'.

P.131 T4.2 for '11264' read '1126'.

P.139 Pa.3 for '(30μm)' read '(20μm)'.

P.139 Pa.3 for '(2mm)' read '(3mm)'.

P.152 Pa.1 for 'was the thickness was' read 'was the thickness'.

P.152. Pa.2 for 'only the inclusion of' read 'only the tissue of'.

P.155 Pa.1 for 'before scatter in this' read 'before being scattered in this'.

P.156 Pa.1 for 'phantom.' read 'phantom'.

P.157 Pa.2 for 'equation 5.1' read 'equation 5.5'.

P.158 Pa.1 for 'larget dimension' read largest dimension'.

P.158 Pa.1 for 'in the x-direction ≈ 1mm' read 'in the x-direction ≈ 10mm'.

P.158 Pa.2 for 'widths and height' read widths and heights'.

P.161 Pa.1 for '20 μm' read '25 μm'.

P.162 Pa.3 for 'loss even' read 'loss of even'.

P.164 Pa.2 for '530,000/4369' read '530,000/4096'.

P.166 Pa.4 for 'collimator wais' read 'collimator was'.

P.167 Pa.2 for 'Incoherent may' read 'Incoherent scatter may'.

P.181 Pa.3 for 'spurious becomes' read 'spurious noise becomes'.

P.182 Pa.2 for 'completive' read competitive'.

ACKNOWLEDGEMENTS

I would like to thank my supervisor Dr. Gary Royle for his support, advice and endless patience during this project. My gratitude also goes to Prof. Robert Speller for his guidance and constant encouragement during this project. Thanks are also due to my colleagues Jenny Griffiths for her support and attention to detail, Kenny Watson for all the coffee, and Marinos Metaxas for his energetic discussion.

The final part of this project would not have been possible without the contributions made by the mechanical workshop, for this I would like to thank Stewart Morrison, Billy Raven and Denzil Booth. Thanks also goes to the members of the biomedical optics research group that have provided me with advice and equipment on numerous occasions, in particular Dr. Dave Kirkby and Dr. Iain Tullis.

Amongst the numerous people that have participated in this project, I am particularly indebted to David Burt for his time, and for providing me with helpful advice and information throughout this project. Thanks also Simon Spencer, Ray Bell, Mark Robbins and Wolfgang Suske of E2V Technologies Ltd. I am also grateful to Prof. Andrew Hanby for his help in providing me with breast tissue samples.

My very special thanks go to my family for their encouragement throughout my university studies. I would like to thank in particular my parents for their love and support.

My deepest gratitude must go to Ben for 'being' in the world.

Finally, I would like to thank E2V Technologies Ltd and EPSERC for funding this project.

CHAPTER 1

Introduction

During the development of digital x-ray imaging systems for use in diagnostic radiography, consideration of the diagnostic value of the images and the dose delivered to the patient is needed. The performance of the detector is key in determining the efficiency with which images are produced and their intrinsic quality. An optimal system employs a detector that meets the necessary imaging requirements and makes the most efficient use of the x-radiation.

This thesis is concerned with applications in medical imaging that require low flux x-ray detection. It is therefore necessary to identify the salient features of a detector suitable for this imaging requirement. Some of the most important features of detector performance that need to be considered when assessing system efficiency are the quantum efficiency of the detector, the sensitivity, the inherent detector noise and the detective quantum efficiency. These parameters are especially important where the detector is to be optimised for the detection of low signal levels. Additionally, in considering a detector for a particular imaging task the following detector properties need to be addressed: the field coverage, geometrical considerations, the spatial resolution, the dynamic range and the uniformity (Yaffe and Rowlands, 1997).

1.1 Considerations for optimal x-ray detector performance

The quantum efficiency η, of the detector is defined as the proportion of incident x-ray quanta that are absorbed by the detector (Yaffe and Rowlands, 1997). The quantum efficiency places a fundamental limit on the signal to noise ratio (*SNR)* of the imaging system. If N_o quanta are incident upon a detector, the number of interacting quanta N_i is given by ηN_o. The fluctuation about N_i is given by $\sigma_{N_i} = \sqrt{N_i} = \sqrt{\eta N_o}$ and defines the maximum *SNR* of the imaging system. Consequently the *SNR* improves as the square

root of the number of incident x-ray quanta, N_o, and the x-ray quantum efficiency. An increase in N_o will often result in an increase in patient dose, thus it is important to optimise η. In diagnostic radiography there is often a requirement for very low levels of x-ray flux; particular cases include diagnostic techniques for which long exposure times are required or when radiosensitive organs are being imaged. Here the signal information is carried by a low number of x-ray quanta and therefore it is important that most, if not all, of the signal information is collected by the detector, i.e. that every x-ray photon is detected.

The x-ray quantum efficiency can be maximised by increasing the detector thickness or using a detector material of a high atomic number or electron density, such as an x-ray phosphor. Most currently used detectors employ an x-ray phosphor, which converts the x-ray energy to light. The optical image is then recorded using an optical sensor or photodetector. This method of x-ray imaging is referred to as indirect detection. An alternative method for increasing η is to use direct-conversion techniques (or direct detection). A photoconductor plate (typically a semiconductor) is used to convert x-rays directly to electron-hole pairs. An applied electric field attracts the electrons towards the entrance surface of the photoconductor where a latent image is formed. The latent image is then read out using a suitable detector, which can be closely coupled to the photoconductor resulting in little or no signal losses. The advantage of using a photoconductor is the high signal available from direct conversion that can overcome high levels of detector noise.

The transfer of the signal through the detector system should be such that image information is not degraded by the system itself and an adequate signal-to-noise ratio (*SNR*) is maintained. If the *SNR* of the system is governed by the *SNR* at the point of x-ray interaction, (the x-ray phosphor,) the system is deemed x-ray quantum limited. However, the *SNR* will generally become degraded due to signal losses. Signal losses often occur because of poor sensitivity. The sensitivity of the detector is determined from the product of the quantum efficiency, the conversion efficiency and the coupling efficiency. For example, most photodetectors are limited in size, therefore for large field applications image demagnification is required. Image demagnification is inherently inefficient and results in large signal losses. Noise sources, which are

inherent in the detector, will also degrade the *SNR*. The biggest source of noise in most digital detectors is most often that due to electronic output amplifier noise in the read out circuitry. These noise sources combine additively with quantum noise and noise sources associated with detector gain. Consequently the quantum efficiency is inadequate to describe the *SNR* performance of the system and a more complete description of detector performance should include the effects of the transfer of both signal and noise through the system.

The most commonly used measure of *SNR* degradation by the imaging system is the detective quantum efficiency (*DQE*). The concept of *DQE* was developed in the late 1940s in order to find a detector performance parameter that could be used to describe different imaging modalities (Jones, 1949). The noise associated with the input quanta, σ_{N_i}, provides an absolute scale with respect to which the output noise can be normalised, and it is defined as

$$DQE = \frac{(SNR_S)^2}{(SNR_i)^2} = \frac{(N_S/\sigma_{N_S})^2}{(N_i/\sigma_{N_i})^2} \tag{1.1}$$

where N = signal, σ = noise and the subscripts i and S refer to the input and output of the detector system, respectively. All input signals have noise, hence the *DQE* measures the additional noise imparted by the detection process. If $DQE = 1$ then no additional noise is added and the detector is an ideally noiseless detector (Dainty and Shaw, 1974).

Thus, for quantum limited imaging to be realised, an optimal detector for medical imaging will have high quantum efficiency, low noise and high sensitivity resulting in a high *DQE*. These detector characteristics are not always obtainable. One method of overcoming further degradation in *SNR* in indirect-detection devices is to provide quantum gain in the imaging chain often referred to as image intensification. The use of a phosphor screen is one method of providing quantum gain in the imaging chain, as one x-ray quanta is converted to many optical quanta. However, due to inefficient optical coupling, further intensification may be required. Image intensifiers can be used

for this purpose. The advantages and disadvantages of image intensification will be discussed later in section 1.3.

1.2 Low light level charge coupled device technology

The detection of low signals in conventional charge coupled devices (CCDs) is ultimately limited by the noise within the device. The main source of noise in a CCD is output amplifier noise. Amplifier noise is a function of pixel read out speed and consequently, noise of less than 2 electrons r.m.s. per pixel can be achieved at very low read out rates (~kHz) (Jerram *et al.*, 2001). Due to the demand for higher spatial resolution and increased imaging areas, the number of pixels in an imaging device is commonly now greater than 1,000,000. The combination of high numbers of pixels and slow readout rates lead to long integration periods, which are impractical and result in high dark current. Unfortunately, the realization of real-time CCD imaging is at the cost of higher noise levels, as read out amplifier noise rises to tens of electrons at the read out rates required (MHz). A new photodetector, the low light level charge coupled device (L3 Vision CCD) technology has been developed by E2V Technologies Ltd, Chelmsford, U.K. (formerly Marconi Applied Technologies Ltd). The L3 Vision CCD technology, herein known as the L3CCD or L3 technology, has been developed with the intention of displacing image intensifier technology (Jerram *et al.*, 2001). The target market for this new technology is military applications where it is hoped that its superior *SNR* performance will replace intensified CCD cameras. The L3CCD overcomes the problem of high noise by applying gain, using an amplification mechanism internal to the sensor, to the signal charge prior to the read out output amplifier. This reduces the magnitude of the read out noise with respect to the signal. As a result, the L3CCD is effectively noiseless making any pre-CCD intensification redundant.

In view of the above discussion of optimal detector performance (section 1.1), the benefits of a low noise detector are obvious. Coupled with an x-ray phosphor, the L3 could form the basis of a high quantum efficiency and high *SNR* x-ray imaging detector. In addition, because the L3 performance is unaffected by amplifier noise, it can be operated at read-out rates that will facilitate real-time x-ray imaging.

1.2.1 Aims and objectives of the thesis

The aim of this thesis is to make a comprehensive evaluation of the L3CCD performance in terms of its application to diagnostic radiology. An assessment of detector performance in terms of its gain, noise and imaging characteristics will be undertaken. These parameters will be quantified and the limitations of the device identified. It is the intention that this information will be used to determine the benefits such a detector would offer in terms of the development of new techniques and the improvement of existing imaging modalities. The feasibility of the application of the L3CCD to specific x-ray imaging techniques will be evaluated both theoretically and experimentally.

1.3 An overview of CCDs in digital radiography

The L3CCD has all the attributes of a conventional CCD, with the added advantage that it has low noise. Therefore, the L3 could be used to improve imaging systems that currently employ conventional CCDs. The following gives a description of the use of CCDs in medical x-ray imaging systems.

In general, digital conventional CCD-based image acquisition is widely used in medical x-ray imaging. Due to their poor x-ray quantum efficiency, CCDs are typically used in conjunction with an x-ray phosphor. The imaging area of a CCD is on the order of ~ 1 $\times$ 1cm^2; larger scientific devices provide a maximum imaging area of generally 3 $\times$ 3cm^2. Where the phosphor is viewed directly, the small size of the CCD sensor has limited its application to small-field radiography. As a result, CCDs are most commonly found in intra-oral dental radiography and breast biopsy-guidance or slot scanned mammography applications (Yaffe and Rowlands, 1997).

In order to image the larger areas required in full-field mammography and general classical radiography, the phosphor screen may be optically coupled to CCD via a lens or a de-magnifying (tapered) fibre optic. However, there is a drawback with the use of de-magnifying optics, the optical coupling efficiency is inversely proportional the square of the demagnification factor, m, where m is the ratio of the image size to the

object size. Poor coupling efficiency leads to signal losses and hence, degradation of the *SNR*. CCDs and x-ray phosphors coupled with de-magnifying fibre-optics (tapers) were employed in the first digital mammography imaging systems. These were small format devices for the guidance of biopsy procedures (Roehrig *et al.*, 1993). A full-field mammography imaging system was fabricated using a mosaic of 3 × 4 of these detectors. Using this device it was found that a demagnification factor of two can be used with acceptable efficiency for mammography. A theoretical assessment of CCD-based x-ray imaging systems for digital chest radiography has been undertaken by Hejazi and Trauenicht (1997). Both tapered fibre optic and lens systems were modelled. The fibre-optic system was found to be six times more efficient than the lens system and was found gave adequate image quality for chest radiography at demagnifications of 3 or lower. Lui *et al.* (1993) have described the problems of lens or fibre optic coupling where large signal losses.

CCD-based full-field mammography systems are currently commercially available from manufacturers such as Fischer Inc. and LoRad Corporation (Yaffe, 2001, Cowen, 1997). These systems employ a slot format and a CCD image acquisition mode called time delay and integrate (TDI). A phosphor is coupled through a 1:1 fibre optic faceplate to a linear array of CCDs. The image is acquired by scanning the detector array and the x-ray tube along an arc beneath the breast. Typically slot scanned systems achieve spatial resolutions of 50 μm. The advantages of slot scanning systems are a reduction in breast dose due to high scatter rejection and variations in the x-ray flux due to the heel effect are avoided. The primary drawback of such line scanning techniques in clinical applications is the demand for a very high x-ray tube output in order to acquire enough x-ray photons during the short exposure times required. Direct deposition of the x-ray phosphor on to the CCD offers higher resolution and greater efficiency (Taibi *et al.*, 1997). However, due to the loss of image quality through direct interactions in the CCD, fibre optic coupling is preferred.

Another important area of radiography that uses CCDs is digital fluoroscopy. Fluoroscopy is the most dose-efficient x-ray procedure that allows real-time visualisation. Real-time x-ray images are acquired using an x-ray image intensifier (XRII). X-rays are converted to light by a phosphor screen that is coupled to a photo-

cathode. Electrons liberated by the phosphor emission are accelerated across a vacuum under a high potential into a phosphor output screen. The intensified image from the XRII is usually imaged using a CCD coupled either by a lens or fibre optic to the output phosphor. The majority of the image de-magnification takes place in the XRII where the electrons are electro-statically focused resulting in a much greater coupling efficiency (Yaffe and Rowlands, 1997).

A fluoroscopic imaging system in which a phosphor screen is imaged by a CCD via a lens has been developed by Drake *et al.* (2000). The system has been implemented on a medical linear accelerator system using kilovoltage radiation to verify radiotherapy field location. Measurements have shown that it was sub-optimal for diagnostic imaging due to its poor light collection efficiency. However the system was found to be a significant improvement on similar electronic portal imaging detectors which operate using megavoltage radiation.

The advantages and disadvantages of the use of image intensifiers in x-ray detectors based on CCDs have been explored by Tate *et al.* (1997). Assessment of several imaging systems has shown that the removal of the image intensifier stage from the detector chain offers several improvements in detector performance. Electro-statically focussed and micro-channel plate (MCP) image intensifiers were found to plague an imaging system with various additional noise sources, reduced contrast due to veiling glare and scattering in the x-ray tube arising from the conversion stages. The absence of an image intensifier stage will lead to a more compact system that does not employ high voltages. The use of an array of CCDs coupled with tapered fibre optics will give better image quality overall, however it will ultimately be less sensitive. The disadvantages of image intensifiers indicate that the use of a CCD based imaging system that does not require one offers certain advantages. Use of the L3CCD would mean there are no extra conversion stages that cause scattering and veiling glare. The L3CCD is compact, improving the versatility of an x-ray imaging system in terms of better patient views and mobility. Moreover, the L3 has very low noise in comparison with conventional CCDs and therefore will have a higher sensitivity in a phosphor/taper/CCD system.

1.4 Other detectors in digital radiology

To ensure that the optimal detector is employed for a specific imaging technique, it is important to compare and contrast the performance of all suitable detectors. There are a number of x-ray detectors currently used in medical x-ray imaging and many more are being investigated by various workers for the application to different radiographic techniques.

Most of the digital detectors currently used in diagnostic radiology employ indirect detections methods, these include: x-ray image intensifiers for fluoroscopy; active matrix flat panel imagers (AMFPIs) for cardiac fluorography, portal imaging and general radiography (Yaffe and Rowlands, 1997); and, CCDs for dental radiography and mammography (Yaffe, 2001). Other indirect detectors that have potential for the application to diagnostic radiology include: electron bombarded charge coupled devices (EBCCDs) (Rossi *et al.*, 2000); avalanche photodiodes (APDs)(Kobayahi *et al.*, 1995); hybrid avalanche photodiodes (HAPDs) (Arisaka *et al.*, 2000); hybrid photodiodes (HPDs) (Calvi *et al.*, 2002); and, position sensitive photo multiplier tubes (PSPMTs) (Arisaka *et al.*, 2000).

The most commonly employed direct detection detectors in medical radiography are amorphous silicon (*a*-Si:H) or amorphous selenium (*a*-Se) AMFPIs. Both have found extensive application in radiotherapy portal imaging (Yaffe and Rowlands, 1997). Other direct detection devices include pixel array detectors (PADs) (Mainprize *et al.*, 2002, Renzi *et al.*, 2002) and silicon microstrip detectors (Speller *et al.*, 2001).

The detectors listed here have been identified as those that represent competing technologies for the L3CCD. Digital x-ray detectors can be divided into two broad categories; those that employ indirect detection and those that employ direct detection. A full discussion of the advantages and disadvantages of each detector technology in terms of their application to digital radiology will be given later in this thesis. In addition, the performance of the L3CCD will be compared to that of the above detectors to identify the possible benefits of L3 technology for specific imaging techniques.

1.5 Description of the thesis

The work described in this thesis has been undertaken in order to assess a new technology still in the early stages of development, with a view to its application in medical imaging. Chapter one has introduced L3CCD technology and described some of the important parameters that need to be considered when evaluating a new detector for application to diagnostic radiology. The remaining chapters are organised as follows:

Chapter 2: In order to predict its full potential, a through understanding of L3 technology is required. The design and operation of the L3CCD is explained in terms of the physical processes that govern both L3CCD noise and the gain mechanism. The various sources of noise within the L3CCD are described. Due to the random nature of the gain mechanism it is expected that the gain will give rise to excess noise. An analysis of the physical parameters which give rise to excess noise has been made. A full discussion of these parameters with respect to the physical characteristics of the CCD is given and conclusions are made about a suitable model for the prediction of excess noise.

Chapter 3: Before any potential benefits are realised, the performance parameters need to be evaluated. Accordingly, measurements have been made in order to characterise the device in terms of its imaging characteristics. Measured results are compared to results predicted from analyses of the physical processes influencing gain and noise. The primary aim of this work is to identify the device characteristics that affect the overall performance. Conclusions have been made to this end and a prediction of the optimal performance in terms of the device sensitivity is made. In addition comparisons of the L3 performance parameters with those of other detectors that are used or have potential for use in digital radiology are made.

Chapters four and five consider the application of the L3CCD in two specific imaging areas.

Chapter 4: This work builds on the findings from the characterisation work in chapter three. It assesses the performance of the L3CCD in an x-ray imaging system. An evaluation of the use of a L3CCD as a replacement for the image intensfier in optically coupled systems is made. An imaging system has been modelled in terms of its signal and noise transfer properties through the imaging chain. Its performance is measured using the detective quantum efficiency. Conclusions are made regarding the use of L3 technology in phosphor/lens/CCD and phosphor/fibre optic/CCD x-ray imaging systems.

Chapter 5: Based upon the results described in chapter three an L3CCD has been identified as a suitable detector for clinical diffraction enhanced breast imaging (DEBI). DEBI requires a low x-ray flux-imaging detector. It is a relatively new imaging technique and the L3CCD is expected to advance its development toward a feasible clinical system. The diffraction imaging system has been modelled in order to design an optimal detector for single low energy (17.4 keV) x-ray quanta. An L3 detector has been built, its performance evaluated and it has been used to collect diffraction data from human breast tissue phantoms. The results validate the feasibility of an L3 DEBI system and show that scatter contrast can be further improved using pre-defined regions of momentum transfer.

CHAPTER 2

The CCD65: background and theory

2.1 Basic Principles of CCD operation

Boyle and Smith developed the charge coupled device (CCD) in 1969 (Boyle and Smith, 1970). Due to its high dynamic range, intrinsic position sensitivity, good response in the visible region of the spectrum and compactness, the CCD has found many applications, and most recently in digital imaging. The work in this thesis is concerned with the structure and operation L3 technology, which has been developed from conventional buried channel charge coupled device technology. The fabrication of the CCD and the physical processes involved in its the operation are well understood. This section is intended to provide the reader with a brief description of the more salient aspects of the CCD that will be important for later discussion of the characteristics of L3 technology. For a more complete discussion of the CCD the reader is referred to Beynon and Lamb (1980), who have elucidated the principles behind CCD operation and design.

2.1.1 BCCD design and operation

The CCD is a silicon integrated circuit based on a metal-oxide-semiconductor (MOS) structure. By depositing a series of metal or polycrystalline silicon (polysilicon) overlapping electrodes called gates on an oxide-covered semiconductor substrate an array of MOS capacitors, which is the basis of a CCD, can be formed. The first CCDs were so-called surface channel devices (SCCDs). SCCDs suffered from high charge transfer noise owing to large densities of fast interface states that trap charge at the surface. As a result they were quickly succeeded by bulk or buried channel devices. In buried channel CCDs (BCCDs), charge is transferred at some distance below the surface and consequently not subject to trapping in surface states. Figure 2.1 is a schematic diagram of the cross-section through a BCCD. The substrate of the BCCD is

fabricated from two layers of silicon; a thin n-type layer is placed on top of a thicker, more lightly doped p-type layer to form a reverse biased p-n junction. A dioxide layer (SiO_2) is formed on top of the silicon, upon which the electrode is deposited.

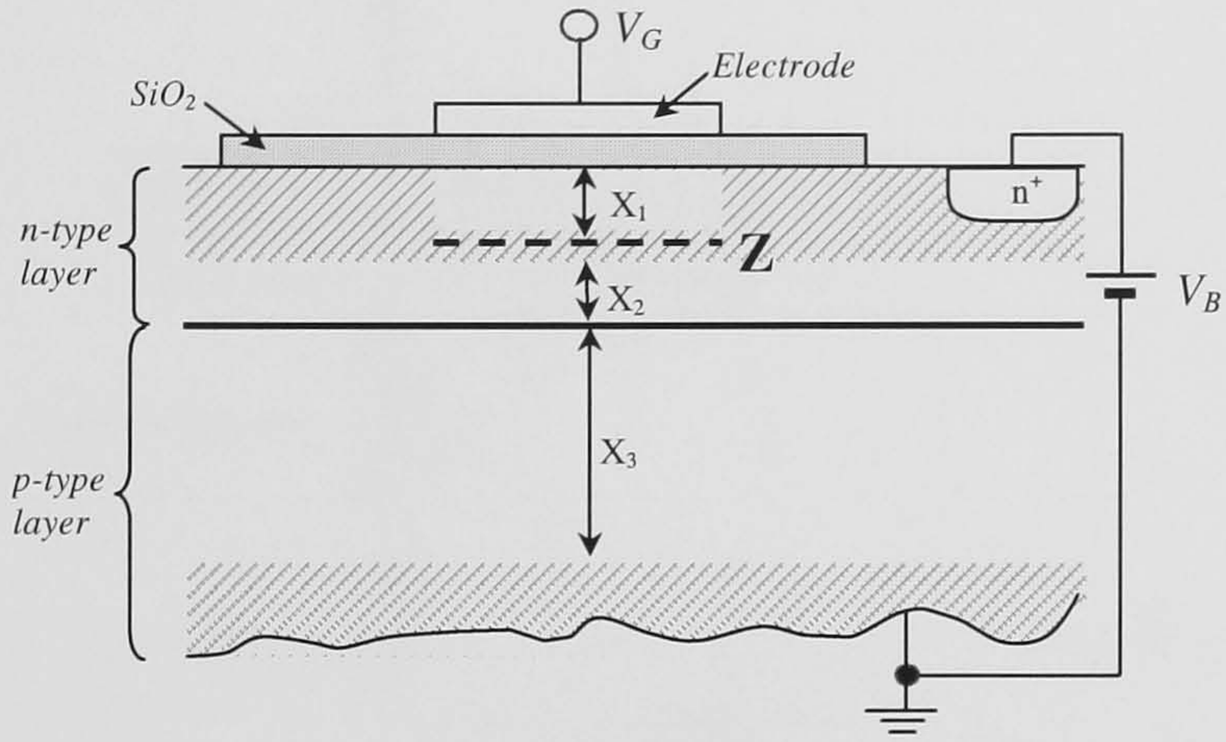

Figure 2.1. *Schematic representation of a cross section through a BCCD. This shows the formation of field induced (X_1) and p-n junction (X_2 and X_3) depletion regions (Beynon and Lamb, 1980).*

If we consider that the gate voltage V_G and the substrate are set at zero potential, the potential of the n-type layer can be increased by increasing the bias voltage V_B. This results in a depletion layer, X_1, being formed in the n-type layer directly beneath the gate and a depletion layer of thickness $X_2 + X_3$ at the reverse p-n junction. If V_B is further increased, eventually it will reach a potential that causes the two depletion layers to meet at the plane Z. This is known as bias 'pinch-off', prior to which, $V_Z = V_B$. At pinch off, V_Z remains constant and any further increase in V_B does not affect it.

A typical potential profile is shown in figure 2.2. For any bias voltage the potential at Z is the most positive in the semiconductor below the electrode. As a result, electrons generated due to photon interactions in the silicon will be attracted to Z. In this way the BCCD can store negative charge at this point beneath the gate electrode. As the negative charge collects at Z, the positive potential reduces and the depletion layer shrinks. This mechanism is normally analogised to the formation of a potential well with a depth proportional to the gate voltage applied. For a given gate voltage, the depth of the well will decrease linearly with the amount of negative charge present at Z. Any positive charges, or holes, which are also generated by photon interactions are repelled away from Z. Holes which are generated outside of the depletion region flow into the p-type substrate. Those that are generated within the depletion region flow to

the surface and from there flow into the p-type substrate via the channel stop diffusions. These p-type diffusions are provided for isolation purposes and define the lateral extent of each transfer channel, as shown later in figure 2.5.

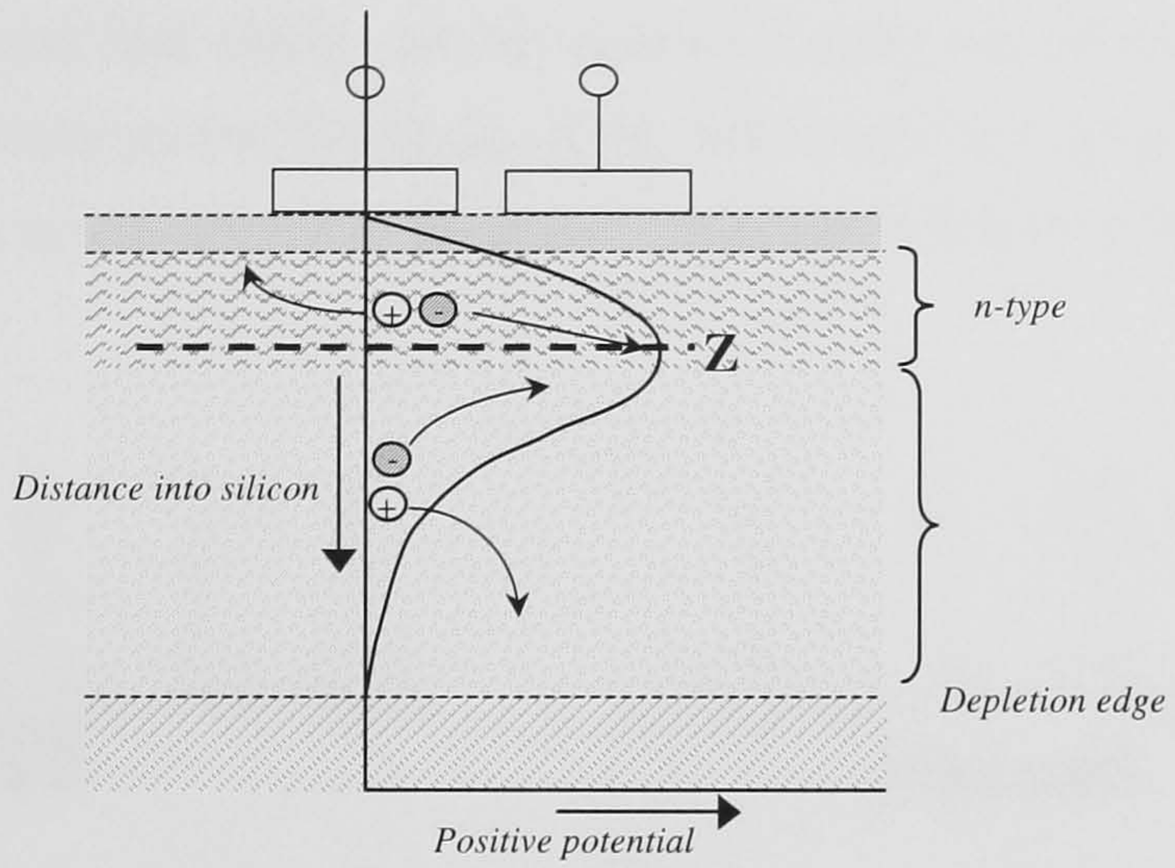

Figure 2.2. *Potential profile through the BCCD structure shown in figure 2.1. The region of maximum potential is at point Z. Electrons are attracted to Z and stored. Holes are repelled away from Z (Beynon and Lamb, 1980).*

The amount of charge that can be stored in a potential well is dependent upon device geometry and the bias voltages. Also for a buried channel device, the charge capacity is a complex function of the width of the depletion region and the n-type channel doping concentration. If the amount of charge generated in the device exceeds the full well capacity 'blooming' occurs. This may happen in the case of a region of intense illumination in the image. When such an overload of an element occurs, the excess electrons spread side-ways into adjacent potential wells to an extent that is proportional to the size of the overload. In some devices a special structure called an anti-blooming drain is incorporated within the image section in order to remove the excess charge.

2.1.2 Charge transfer

Charge coupling is the technique used to transfer signal charge from under one electrode to the next one in order to move the charge to the read out node. Charge coupling in a three-phase device is illustrated in figure 2.3. Initially it is assumed that charge is stored under the second electrode $\varnothing_2$, which is biased at 10V. When positive bias is applied to $\varnothing_3$, because the associated potential well is initially empty, its

potential will be much higher than at $\varnothing_2$. Thus electrons will tend to move from $\varnothing_2$ to $\varnothing_3$, until eventually the charge is shared equally between them. If the bias on $\varnothing_2$ is then reduced to 0V the remaining charge will be transferred to $\varnothing_3$. The whole process can then be repeated and thus charge can be transferred along the columns of electrodes using suitable clocking pulses. Electrodes of the same phase have common connections, i.e. $\varnothing_1$, $\varnothing_2$ and $\varnothing_3$, as will be seen in the frame transfer array shown in figure 2.5.

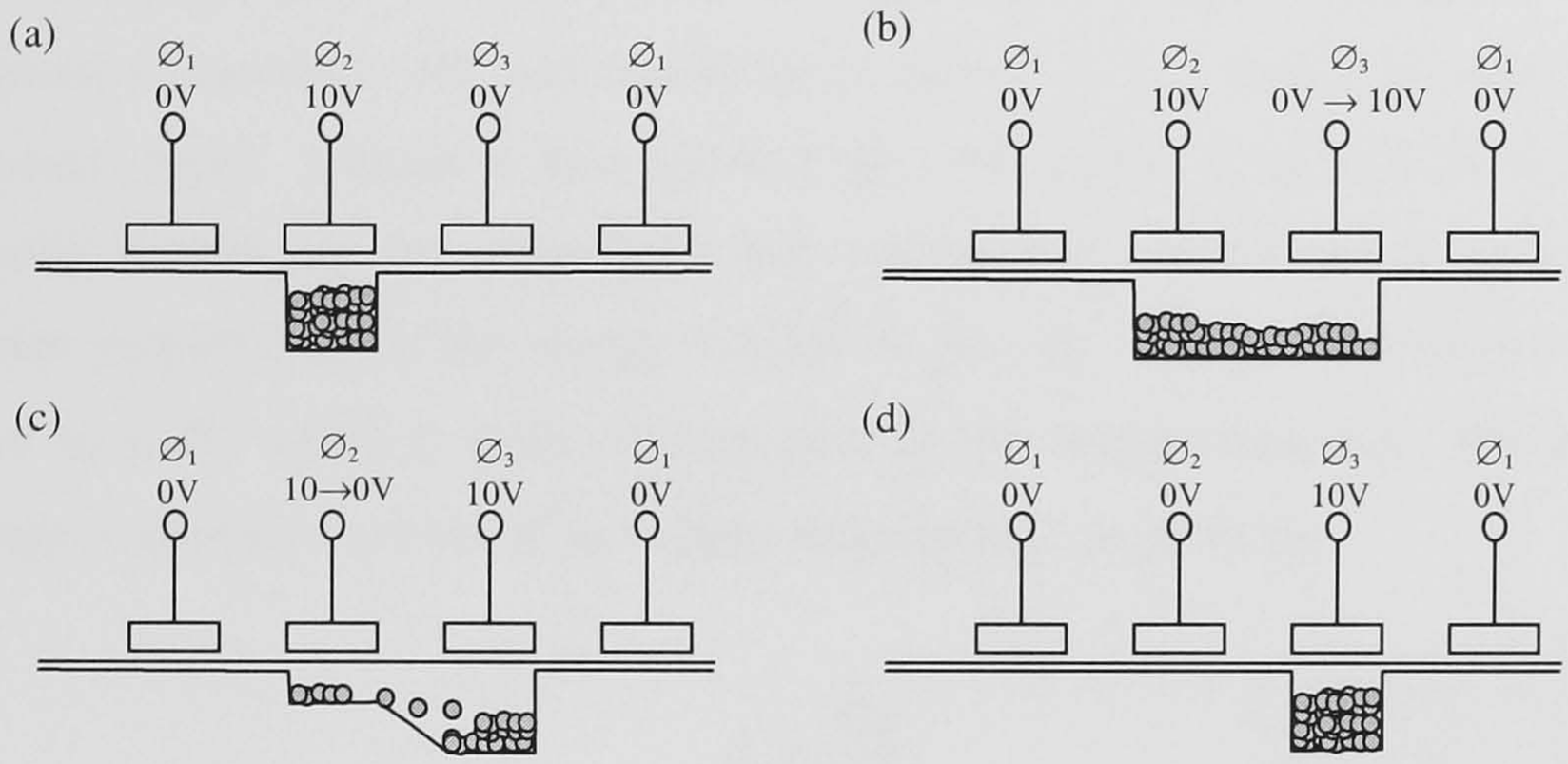

Figure 2.3. *(a) to (d) Movement of charge through the CCD by clocking electrode voltages.*

2.1.3 Charge read out

Once the charge has been transferred through the register it is converted into a voltage signal at the output.

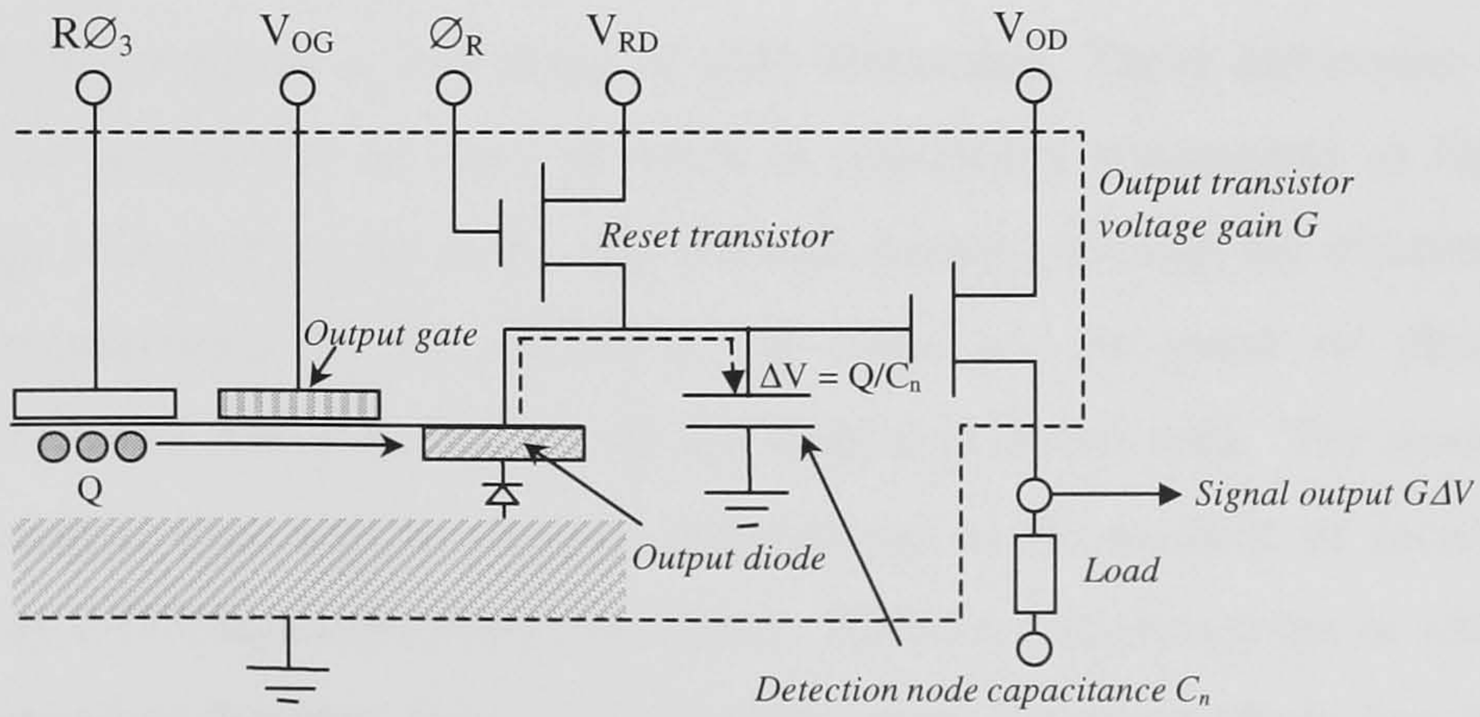

Figure 2.4. *Typical CCD output structure*

A typical CCD output circuit called a 'floating diffusion' type circuit is illustrated in figure 2.4. Although shown as separate components, the individual circuit elements are integrated within the silicon of the CCD. Transfer of charge Q between the last CCD electrode and the output circuit is via an n-type diffusion or 'output diode'. The diffusion is connected to the gate of the output transistor. The capacitance at this point, the sum of many parasitic components, is called the 'detection node capacitance' and designated C_n. To read out charge, first the reset transistor is switched 'on' to charge the capacitance (C_n) to the potential of V_{RD} (the reset drain voltage). The reset transistor is switched 'off' and the diffusion 'floats' at V_{RD} (hence the name 'floating diffusion' type). Charge is then clocked onto the output diode and flows as shown partially discharging the capacitance and causing the potential on it to drop by an amount proportional to the charge transferred, i.e. $\Delta V = Q/C_n$. The signal output is given by $G\Delta V$, where G is the voltage gain on the output transistor. The charge-to-voltage conversion in terms of an "output responsivity" as given by:

$$R_o = \frac{Gq}{C_n} \tag{2.1}$$

where q is the charge on the electron. Values for R_o are often quoted in units of microvolts per electron.

2.1.4 CCD architecture

Typically the BCCD comprises a 2-D array of gate electrodes. These electrodes are most often made of polysilicon as such material is reasonably transparent to light. When a light image focussed on the array, any photons passing through the electrodes may generate photoelectrons in the silicon at, or close to, the point of photon interaction. The photoelectrons are collected by the nearest potential well. The amount of charge in a potential well will be directly proportional to the number of incident photons; in this way 2-D image information is stored. There are various ways in which CCDs can be organised so that they form a 2-D imaging array. In this work devices that have frame transfer CCD architecture have been used. A schematic representation of a three-phase frame transfer CCD is shown in figure 2.5. The electrodes in frame transfer

CCDs are divided into three sections: the image section, the store section and the read out register. The arrangement of electrodes and channel stop isolation diffusions gives an array of 3 × 7 independent charge storage elements in both image and store sections, each element comprising a triplet of electrodes. The elements in the image section are often called pixels. The register has 7 elements.

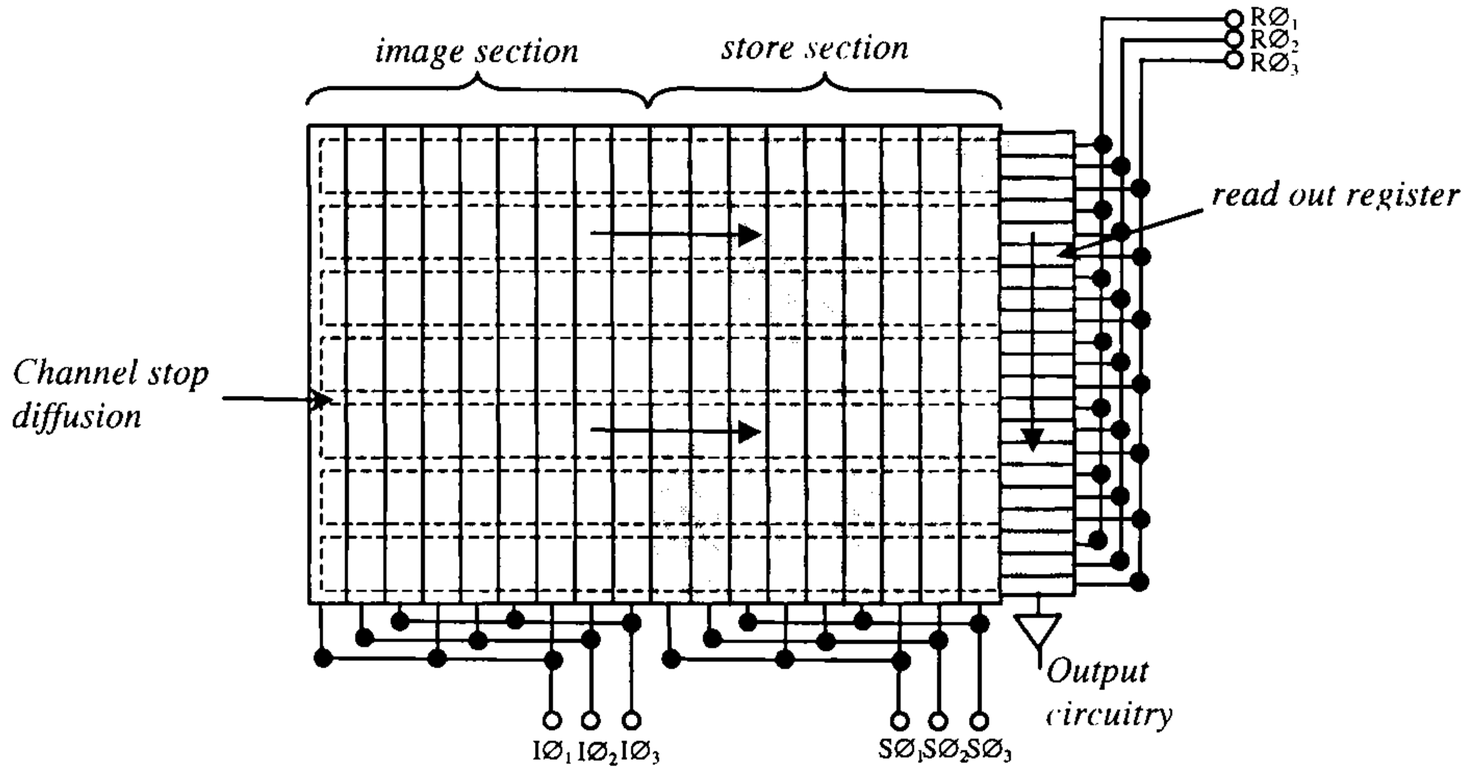

Figure 2.5. *Schematic representation of a typical frame transfer CCD. Phases IØ, SØ and RØ represent the clock pulses of the image, store and readout sections respectively.*

A frame of charge is collected in the image section by applying a positive bias to the middle electrodes during the integration period, i.e. those connected to $I\varnothing_2$. The electrodes on either side, which are connected to $I\varnothing_1$ and $I\varnothing_3$ are held at a low bias, in combination with the channel stop diffusion regions contain the charge within the sensing element. Once the integration period finishes, the frame of charges is transferred very rapidly into store section that is shielded from incident illumination. This is done by applying appropriately timed clock pulses to $I\varnothing_1$, $I\varnothing_2$, $I\varnothing_3$, $S\varnothing_1$, $S\varnothing_2$ and $S\varnothing_3$. The frame of charges is then moved line-by-line down the store section for sequential read out by applying appropriate clock pulses to the store and read out register, i.e. $S\varnothing_1$, $S\varnothing_2$, $S\varnothing_3$, $R\varnothing_1$, $R\varnothing_2$ and $R\varnothing_3$. In each cycle of the operation the last line of charges transfers to the storage elements of the register. These charges are then transferred to the final output circuit by applying clock pulses to only the register, i.e. $R\varnothing_1$, $R\varnothing_2$ and $R\varnothing_3$, such that the charge signals appear in the output circuit in time-staggered sequence. Once a whole line has been read out, the next line is transferred from the store section, and so on through all lines comprising the frame. The next

frame of image charges is being collected whilst this first frame is being read out, and so on through successive frames.

2.1.5 Optical response

The response of a CCD sensor to incident irradiation is determined by its quantum efficiency (*QE*), signal handling capability and noise performance. Quantification of these parameters depends on the CCD architecture, the wavelength of the incident illumination and the illumination method (back side or front side illumination). The QE is the fraction of the incident photons giving useful signal. Figure 2.6 shows the *QE* plotted as a function of wavelength for a typical front and back illuminated CCD.

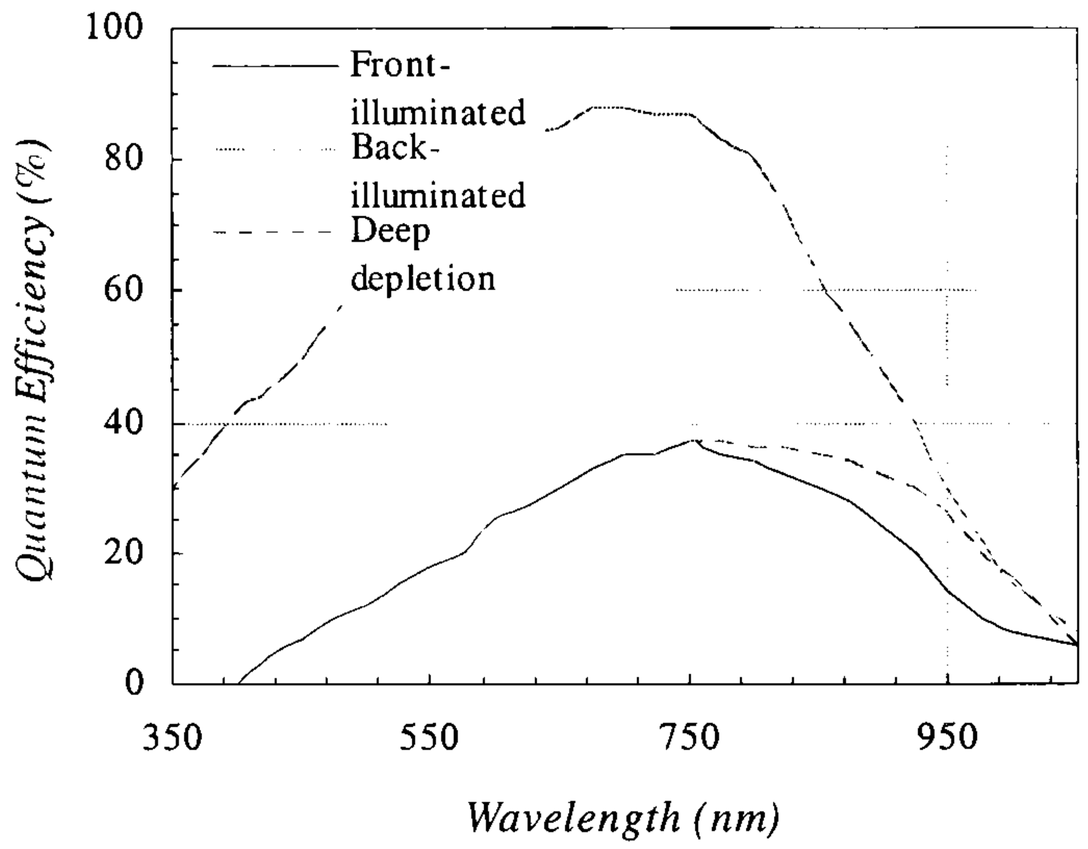

Figure 2.6. *Quantum efficiency plotted as a function of wavelength for front and back illuminated devices. Data provided by E2V Technologies Ltd.*

In order to increase the sensitivity of the CCD the *QE* should be maximised. At shorter wavelengths the *QE* is low due to interference and absorption effects caused by the polysilicon layer which reduces the number of photons reaching the underlying silicon. To obtain optimum *QE* performance for shorter wavelengths backside illumination devices have been developed. The substrate of the CCD can be thinned and devices are illuminated on the opposite side to the dielectric and gates, therefore eliminating absorption in these structures. The improvement in *QE* for backside-illuminated devices at shorter wavelengths is illustrated in figure 2.6. Note that *QE* does not reach 100%. This is due to the surface treatments and any protective coatings that are

necessary to stabilise the back surface to reduce trapping and emission of signal carriers. At longer wavelengths *QE* decreases due to low absorption, effectively the photons pass right through the active thickness of the device without an interaction giving signal charge. To improve *QE* at longer wavelengths the depth of the active thickness can be increased. The effect of increasing the depletion depth is illustrated in figure 2.6. To avoid loss of spatial resolution the depth of depletion has to be increased and this is limited by the doping concentration. Typically the depletion depth is made equal to the pixel pitch for deep depletion devices.

In general it is difficult to measure the QE directly, but values can be derived from the 'optical responsivity'. The optical responsivity is the ratio of the photo-generated current to the input illumination power at wavelength λ. It is given in units of current per unit power and is related to the quantum efficiency by the following equation:

$$R_\lambda = \frac{q\lambda}{hc} QE_\lambda \tag{2.2}$$

where q is the charge on an electron, h is Plank's constant and c is the speed of light.

Values for R_λ can be obtained from a simple two-terminal measurement by measuring the photogenerated current flowing between the reset drain and substrate whilst the device is subject to monochromatic illumination of known power. The device can be clocked as normal or held in a static mode with all electrodes at 0V (Burt and Bell, 2002).

2.1.6 CCDs for x-ray detection

In order to acquire an x-ray image, incident x-ray quanta must interact with the detector. The probability of interaction or x-ray quantum efficiency, η, for photons of energy $E=hv$ is given by

$$\eta = e^{-\mu(E)w} \tag{2.3}$$

where μ is the linear attenuation coefficient of the detector material and is a function of atomic number and material density, and w is the active thickness of the detector. In general, CCD detectors that are employed in medical x-ray imaging do not detect x-rays directly. Due to the low atomic number of silicon (Z = 14) combined with their small active thickness, CCDs have poor x-ray quantum efficiency at typical diagnostic photon energies (15 – 90 keV). Therefore an x-ray phosphor is used to convert the x-rays into visible light. The ideal x-ray phosphor will have a high linear attenuation coefficient, a high light yield and its emission will closely match the spectral response of the CCD.

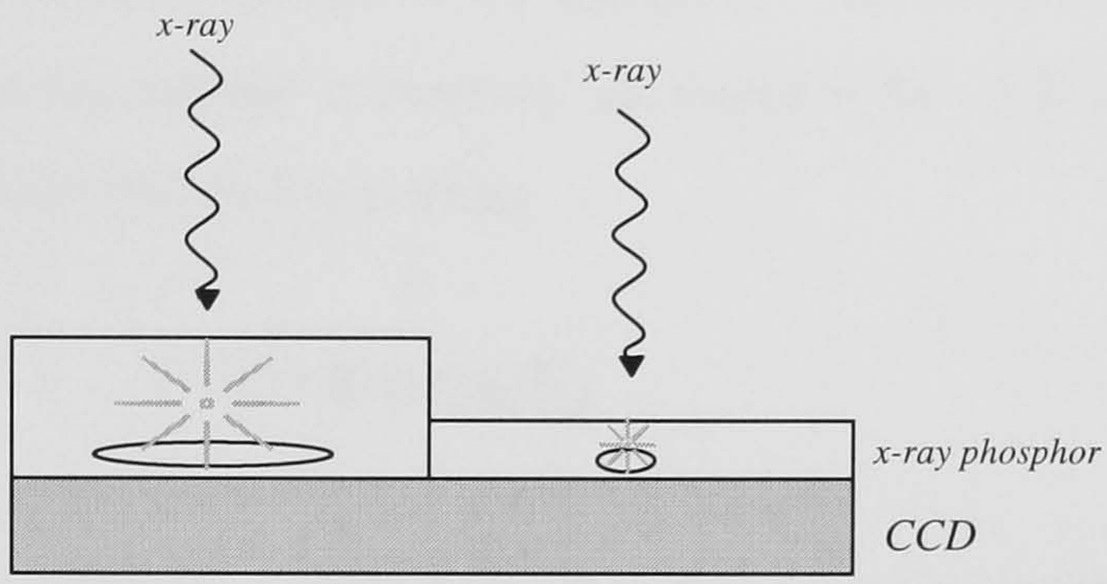

Figure 2.7. *Illustration of the effect of phosphor thickness on the spread of light across the CCD.*

A high linear attenuation coefficient implies that a thin layer of phosphor will be sufficient to stop all a significant number of the incident x-ray photons. This is important because the light emitted from an x-ray interaction is emitted isotropically. When x-ray interactions occur at the top of a layer of phosphor the light spreads out until it reaches the CCD (Yaffe and Rowlands, 1997). Thus for a thicker phosphor the signal is shared between a larger number of pixels and acts to reduce the spatial resolution of the detector. This effect is illustrated in figure 2.7. In a thinner layer of phosphor, interactions can only occur at smaller distances from the CCD and the light does not spread as much before reaching the CCD and the signal is contained within a smaller number of pixels. Consequently the spatial resolution of the system will increase. Clearly the choice of x-ray phosphor thickness is a compromise between spatial resolution and η.

The choice of phosphor is also dependent on the spectral response of the CCD. As observed in figure 2.6, the CCD optical quantum efficiency is a function of the

wavelength of the incident radiation. It is therefore necessary to match the spectral emission of the x-ray phosphor with the response of the CCD. An effective quantum efficiency can be calculated using:

$$QE_{eff} = \frac{\int_{\lambda=\min}^{\lambda=\max} N_\lambda(\lambda) QE_{CCD}(\lambda) d\lambda}{\int_{\lambda=\min}^{\lambda=\max} N_\lambda(\lambda) d\lambda} \tag{2.4}$$

where N_λ is the output emission spectra of the phosphor. The overall CCD/phosphor sensitivity Γ, in terms of the number of electrons generated in the CCD per incident x-ray photon of energy E may then be found using

$$\Gamma = \xi \times E \times \eta \times QE_{eff} \tag{2.5}$$

where η is the x-ray quantum efficiency of the phosphor for x-ray quanta of energy E and ξ is the x-ray phosphor light yield (equal to the number of light photons emitted per unit x-ray energy deposited). Γ can be used as a figure of merit to help choose the most appropriate x-ray phosphor for the imaging task.

2.1.7 Dark current

The thermal contribution to the output signal, which is present even in the absence of an input signal, is widely referred to as dark current. Charge is continuously produced in all semiconductors due to the thermal generation of electron-hole pairs. Electrons, which are generated in this way, within or close to the depletion layer, are collected in the potential wells. The major source of thermally generated dark current is from 'dangling bonds' that are present at the Si-SiO_2 interface. These bonds are a result of the formation of the SiO_2 layer on the surface of the crystalline silicon that produces energy states or 'traps' within the silicon band gap. These states provide 'stepping stones' for electrons to be elevated into the conduction band more easily.

The rate of carrier generation per unit volume per second, U, is given by the classic 'Shockley-Read-Hall' theory as (Grove, 1967):

$$U = \sigma_s v_{th} N_t \frac{(n_i^2 - pn)}{n + p + 2n_i \cosh \frac{(E_t - E_i)}{kT}} \tag{2.6}$$

where σ_s is the cross section of the trap (assumed the same for electrons and holes), v_{th} is the thermal velocity of carriers, N_t is the density of traps per unit volume, p is the hole concentration per unit volume, n is the electron concentration per unit volume, n_i is the intrinsic carrier concentration per unit volume, E_t is the trap energy, E_i is the mid-band energy, k is Boltzmann's constant and T is absolute temperature. The resulting current is qU, where q is the charge on the electron. Hence, in the case of a depleted surface, both n and p are effectively zero and equation 2.6 reduces to (Sze, 1981, Grove, 1967):

$$I_{ds} = q\sigma_s v_{th} N_s \frac{n_i}{2} \tag{2.7}$$

where I_{ds} is the dark current per unit area arising from N_s surface states per unit area, with these states having an energy level in the vicinity of mid-band, i.e. $(E_t - E_i)$ tends to zero (Sze, 1981). Typical room temperature values are $\sigma_s \sim 10^{-15}$, $v_{th} \sim 10^7$ cms^{-1} and $N_s \sim 10^8$ cm^{-2}. Hence, with $q = 1.6 \times 10^{-19}$C and $n_i = 1.2 \times 10^{10}$cm^{-3}, a typical dark current is in the region of 1nAcm^{-2} at about 20°C. Note, however, that the value of N_s tends to vary with wafer processing conditions, thus dark current values can show considerable variation between different devices, process batches and manufacturers (Burt and Bell, 2002).

This dark current is strongly temperature dependent, largely through the variation of n_I, which may be expressed:

$$n_i \propto e^{(-E_g/2kT)} \tag{2.8}$$

where E_g is the band-gap for silicon. The other terms have some temperature dependence, but this is generally small in comparison with that due to n_i (Sze, 1981).

The dark signal collected in the CCD in terms of electrons per pixel is therefore given by:

$$N_d = I_{ds} A_{pix} \frac{t_i}{q} \tag{2.9}$$

where A_{pix} is the pixel area and t_i is the integration period. Equations 2.8 and 2.9 are often used to normalise a dark signal measured for a given size of pixel, integration time and temperature to a dark current at a specified temperature, often 20°C. In this way it is possible to compare the performance of sensors having very different sizes of pixels and operating conditions.

The dark signal given by equation 2.9 is a mean value. There is generally a pixel-to-pixel variation of a few percent arising from local fluctuations in the value of N_s, which is generally termed dark signal non-uniformity (DSNU), and temporal variations (or thermal noise), as described later in section 2.2.1. Some pixels can have a very large dark signal through the presence of localised crystal damage, e.g. stacking faults, and/or metallic contamination. Such outputs are often described as 'spikes' from their appearance in a video line display and the pixel is said to have a defect (Howes and Morgan, 1979).

As well as introducing noise, as described later, dark current introduces a dark signal offset, thereby reducing dynamic range, and limits the integration period. Consequently, CCDs are often cooled to below room temperature, and where long integration times are required, they are kept at cryogenic temperatures.

2.1.7.1 Inverted mode operation

In order to reduce the level of dark current, most CCDs are operated in the 'inverted mode', also described as 'multi-phase pinned' (MPP). In inverted mode operation (IMO), the electrode voltages are taken to negative values such that holes flow to the surface from the substrate. It may be seen from figure 2.2 that whereas Z is a potential

maximum for electrons, the surface is a potential maximum for holes (i.e. opposite polarity). The presence of the holes effectively "inverts" the surface from n-type to p-type and causes the potential to become always equal to that of the underlying p-type substrate material, i.e. 'pinned' to it.

Under conditions of surface inversion equation 2.6 now requires that $p = p_s$, where p_s is the hole concentration in the surface region, and equation 2.7 becomes:

$$I_{ds} = q\sigma_s v_{th} N_s \frac{n_i^2}{p_s} \tag{2.10}$$

The surface dark current is therefore reduced by a factor $p_s/2n_i$, easily many orders of magnitude, and is therefore effectively suppressed (Grove, 1967). The major source of dark current is now that generated in the underlying bulk silicon. Bulk states commonly present in relatively high concentrations are shallow levels (i.e. near conduction band) arising from the presence of oxygen atoms and lattice vacancies. If the density of such states per unit volume is N_b and their capture cross section (again assumed equal for electrons and holes) is σ_b, then for the depleted silicon below the electrode equation 2.6 still has $n = 0$ and $p = 0$ and the bulk equivalent to equation 2.7 becomes:

$$I_{bds} = q\sigma_s v_{th} w_d N_b \frac{n_i}{2\cosh\dfrac{(E_t - E_i)}{kT}} \tag{2.11}$$

where w_d is the thickness of the depleted silicon. There is also a contribution from the underlying non-depleted 'neutral' silicon. In this case n is still zero because any free electrons are attracted to the depleted silicon for collection in the potential well, but p is equal to the p-type doping concentration N_A. The additional contribution is therefore given by:

$$I_{bds} = q\sigma_s v_{th} (w - w_d) N_b \frac{n_i^2}{N_A + 2n_i \cosh\dfrac{(E_t - E_i)}{kT}} \tag{2.12}$$

where w is the total active thickness of the silicon. Of these two equations, since w is generally much larger than w_d (Burt and Bell, 2002), 2.12 tends to be the larger and to a reasonably good approximation the bulk dark current can be represented as:

$$I_{bds} = q\sigma_s v_{th} w N_b \frac{n_i^2}{N_A} \tag{2.13}$$

Typical room temperature values are $\sigma_b \sim 10^{-14}\text{cm}^{-2}$ and $N_b \sim 10^{-11}\text{cm}^{-3}$. Devices are typically fabricated with $N_A \sim 10^{14}\text{cm}^{-3}$ and $w \sim 25\mu\text{m}$. Hence, a typical bulk dark current is in the region of 5pAcm^{-2} at about 20°C, which is over two orders of magnitude lower than the surface component. The dark current now varies with n_i^2 rather than n_i, meaning that there is a faster reduction with temperature. The dark signal per pixel is given by equation 2.9, as before. The same comments regarding spatial and temporal variations also apply.

2.2 Noise

Noise is introduced into the output signal of a CCD from various sources. It is convenient to divide these into three categories:

(i) Noise arising from the temporal and spatial variations of the injection of charge into the device (input noise);
(ii) Noise attributed to fluctuations in the charge transferred from one electrode to the next (transfer noise);
(iii) Noise introduced in the read out circuitry (system noise).

The following is a description of the important noise sources that fall into these three categories.

2.2.1 Input noise

Input noise can be sub-divided into three separate sources.

2.1.7.2 Input signal shot noise

A Poisson-distributed photon stream incident on a detector will produce a Poisson-distributed photoelectron stream (see Appendix A) (Barrett and Swindell, 1981). Consequently the number of photoelectrons generated in a CCD potential well in a time t, N_S, is a random variable and the standard deviation of the number of electrons collected σ_S equals the square root of the mean, i.e. $\sigma_S = \sqrt{\overline{N_S}}$.

2.1.7.3 Thermal noise

Like photon emission, dark current generation is a random process governed by Poisson statistics. Thus thermal noise is the shot noise associated with dark current, giving rise to a standard deviation equal to the square root of the mean signal generated.

2.1.7.4 Fixed pattern noise

At high signal levels the total noise is dominated by pixel-to-pixel sensitivity variations within the device. This is often referred to as fixed pattern noise (FPN) or photo-response non-uniformity. Pixel-to-pixel non-uniformities arise during the manufacturing process. As a consequence each element has its own collection volume and its own characteristic quantum efficiency. Another source of fixed pattern noise is dark signal non-uniformity (DSNU), as described in section 2.17.

2.2.2 Transfer noise

There are two basic origins of transfer noise: that due to imperfect charge transfer efficiency and that due to the trapping of charge in surface states. The charge in a BCCD is transferred at a distance below the surface in the buried channel and such surface state trapping does not occur. However there is an equivalent trapping by bulk states, but due to the low densities of such states the noise arising from these is negligible in comparison to the noise due to imperfect charge transfer (Howes and Morgan, 1979). This is only in relation to charge transfer, the density is high enough to give the bulk dark current described earlier in section 2.1.7.1.

Imperfect charge transfer noise arises from the fact that there are random fluctuations in the amount of charge transferred between potential wells. Theoretically, three

mechanisms are most important for efficient charge transfer in a CCD: thermal diffusion, self-induced drift and the fringing field effect. The relative importance of each of these depends primarily on the charge packet size. Self-induced drift is caused by the mutual electrostatic repulsion of the carriers within a packet and dominates for larger charge packets. Thermal diffusion and the fringing field effect are important when transferring small amounts of charge. However, it has been found by Janesick *et al.* (1987) that all of the above effects are only of secondary importance and the charge transfer efficiency (CTE) is generally influenced by another factor called 'spurious pocket potential' (SPP). SPP represents the loss of charge during transfer due to improper potential well shape and/-or depth beneath the pixel.

If a potential well contains N_S signal electrons then on average εN_S will be left behind at each transfer, where ε is the charge transfer inefficiency. The noise associated with this charge is $\sqrt{\varepsilon N_S}$. This noise is introduced as charge enters and leaves a potential well, therefore the total noise is $\sqrt{2\varepsilon N_S}$. If N_T is the number of transfers, the transfer noise is given by (Beynon and Lamb, 1980)

$$\sigma_{trans} = \sqrt{2\varepsilon N_T N_S} \tag{2.14}$$

Since ε is generally small, ~ 10^{-5} or less, for devices with no more than a few thousand transfers (e.g. 3589 for the CCD65 described later) the factor $2\varepsilon N_T$ is less than unity and σ_{trans} is less than the inherent shot noise (i.e. $\sqrt{N_s}$) and therefore negligible.

2.2.3 CCD system noise

System noise is introduced after the detection process and is generally present as a fluctuating zero level or an interfering voltage. It is conventional to relate this noise back to an equivalent number of signal electrons that would produce the same voltage noise, i.e. the noise equivalent signal in electrons, usually specified as an r.m.s. value.

As with input noise, system noise can be sub-divided into separate sources.

2.2.3.1 *Reset noise*

Charge is clocked from the CCD registers and then 'detected' at the output node as a change in voltage on the output node capacitance (see section 2.5). Once the charge in a pixel has been detected the node is reset. As a result of Johnson noise, that is due to the thermal motion of electrons, associated with the channel resistance of the switch transistor, there is always an uncertainty in the voltage to which the node is reset. This uncertainty leads to an effective variation in the zero signal level from output to output termed 'reset noise', the magnitude of which is given (Howes and Morgan, 1979)

$$\sigma_{reset} = (kTC_n)^{1/2}(1/q) \tag{2.15}$$

At room temperature this noise is approximately $400\sqrt{C_n}$ electrons r.m.s., when C_n is expressed in units of pFs. This source of noise can be eliminated from the signal using a technique known as 'correlated double sampling' (CDS), in which the reset level and the level after charge transfer to the output node are both sampled. The results are subtracted leaving only the component due to the signal.

2.2.3.2 *Amplifier noise*

The post detection-node amplification stages both integrated with the device (e.g. the output transistor shown in figure 2.5) and in the external electronics contribute noise, and this can be the most significant of the system noise components. The noise generally consists of two noise components: white noise and $1/f$ noise. The white noise component arises from Johnson noise. This noise increases as the bandwidth of the device increases, and thus operating the device at a lower frequency can reduce it. The latter is occasionally called 'flicker noise' and is thought to arise from the trapping and re-emission of charge carriers in bulk or surface states. It is a type of noise whose power spectra $P(f)$, as a function of the frequency, behaves as $P(f) = 1/f^{n}$ where n is very close to unity. Note that the use of correlated double sampling actually increases the magnitude of the amplifier noise, firstly because two samples are differenced (i.e. increase by $\sqrt{2}$), secondly because the taking of two samples within a single read-out period requires the bandwidth to be doubled (which therefore increases the white noise by $\sqrt{2}$). However the $1/f$ noise spectrum is flattened by CDS and it acts to suppress

subjectively annoying image 'streakiness' caused by low-frequency components in a display.

2.2.3.3 *Digitisation noise*

Noise is introduced by the scalar quantization of the analogue-to-digital converter (ADC). For a linear ADC with a quantization level Q_f, which is the number of electrons represented by one digital number, the quantization error is given by (Holdsworth *et al.*, 1990)

$$\sigma_{dig} = Q_f (N_{bits})^{-1/2} \tag{2.16}$$

where $2^{N_{bits}}$ is the dynamic range of the ADC in bits.

2.2.3.4 *Background electronic noise*

CCD amplifiers can be very susceptible to external electromagnetic interference (EMI) and care is needed to screen all signal cables and the CCD. Background electronic noise can often be the most significant source of noise after input quantum noise (Holdsworth *et al.*, 1990). Note, however, that this is *extraneous* noise, whereas all the other noise sources are *intrinsic* to the basic operation of the device, many of which are of a *fundamental* nature, e.g. shot noise, and therefore irreducible.

2.2.3.5 *Total system noise*

All of the above noise sources are so-called additive noise sources and can be combined to give a total system noise using

$$\sigma_{sys} = \sqrt{\sigma_{therm}^2 + \sigma_{reset}^2 + \sigma_{amp}^2 + \sigma_{dig}^2 + \sigma_{trans}^2 + \sigma_{EMI}^2} \tag{2.17}$$

2.3 L3 Technology

L3 technology uses an internal gain mechanism to amplify the signal prior to the CCD read out electronics, thereby increasing *SNR* performance and facilitating real-time imaging at low light levels. This section includes a description of the L3 sensor design and the gain mechanism. The physical properties affecting gain and the variation of gain are discussed.

2.3.1 CCD65 sensors

The two image sensors that were used in this work were manufactured by E2V Technologies Ltd, Chelmsford, U.K. The sensors are TV- 625 line format. The main characteristics of the CCD65 are listed in table 2.1.

Table.2.1. *Main characteristics of the CCD used in this study*

	CCD65
Format	1”
Active image area (mm)	11.52 × 8.64
Active pixels (image section)	576(H) × 288(V)
Pixel size (μm)	20 × 30
Fill factor (non-antibloom operation)	100%
Dark reference columns	15
Overscan rows	8
Spectral range (nm)	400 - 1060
Responsivity @ λ = 633nm (mAW^{-1})	230

The sensors are front-illuminated and have no antiblooming drains. The CCD65 architecture is shown in figure 2.8. The device has conventional frame transfer architecture, comprising of image and store sections and a read out register. The image section has 576 active rows and 15 ‘dark reference’ columns, i.e. optically shielded to provide a zero signal reference. Eight rows are similarly shielded. The read out register spans the width of the device and therefore comprises 591 elements. In addition, the CCD65 has an extended section of register situated below the read out register, known as the ‘gain register’. The gain register has the same number of elements as the normal read out register and therefore the read out is only delayed by one line. Charge is clocked along the read out register in an identical manner to a conventional frame

transfer device. It then travels through 16 corner elements and through the gain register (where it is multiplied) to the output circuitry.

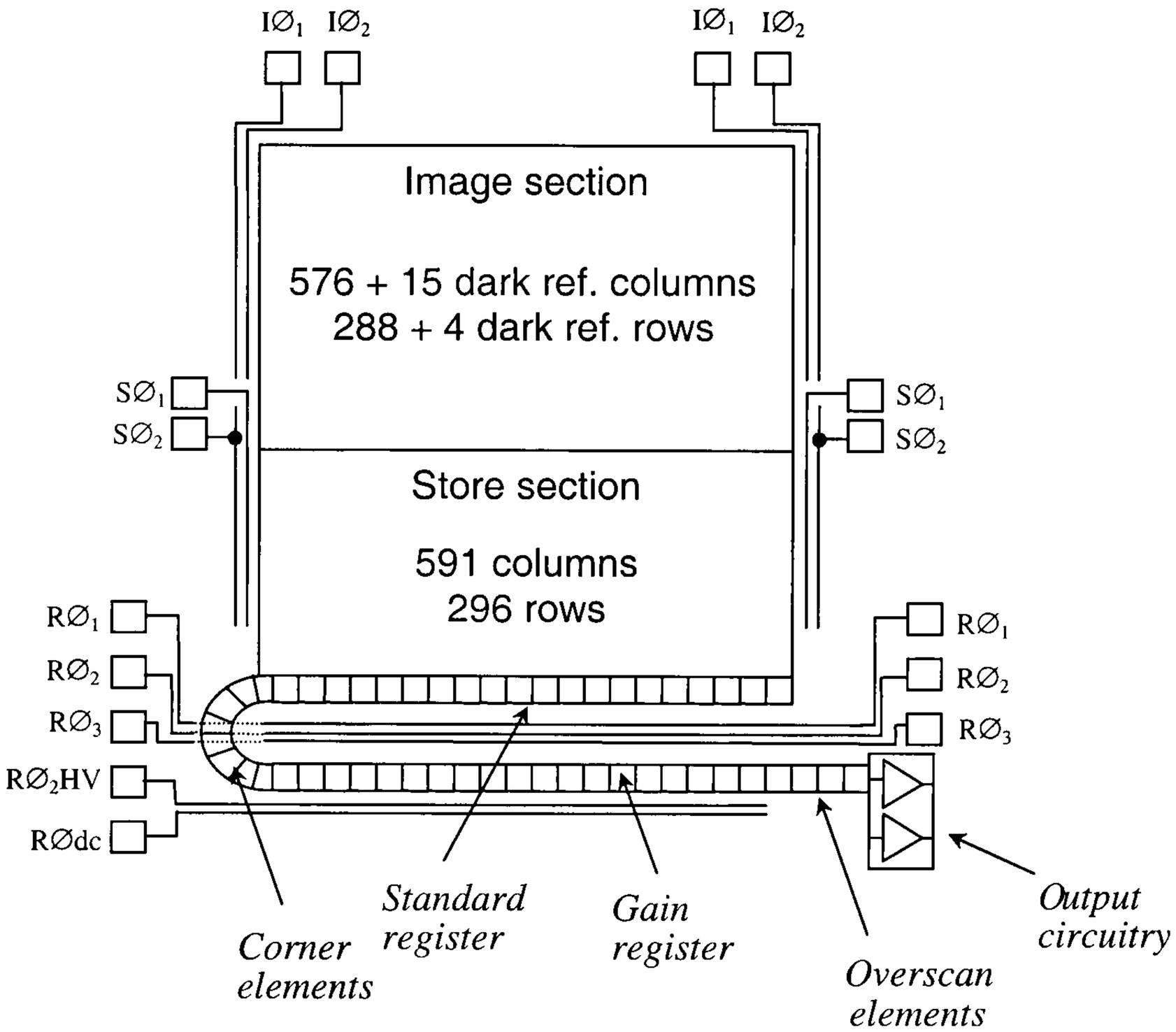

Figure 2.8. *Schematic of the CCD65 architecture. The device comprises of image section, store section, read out register and an extended section of the read out register known as the 'gain register' (Marconi Applied Technologies, 2002(a)).*

To achieve TV interlacing operation, the image and store sections are clocked using a two-phase clocking sequence. Unlike the three-phase arrangement described in section 2.1.2, each phase electrode comprises a pair of joined electrodes with one of them having additional p-type dopant in the underlying silicon (formed as a boron implant) to give a defined voltage step. This clocking sequence is shown in figure 2.9. During integration all electrodes are held high. The first field (odd) is read out by sharing the charge underneath both phases. The combined charge constitutes the charge collected in one pixel. In figure 2.9 electrode pairs 1 and 2 are joined, 3 and 1 are joined, and so on. After the next integration period the second field (even) is read out by again combining the charge between two electrode pairs, however this time the charge is combined between pixels 2 and 3, 1 and 2.

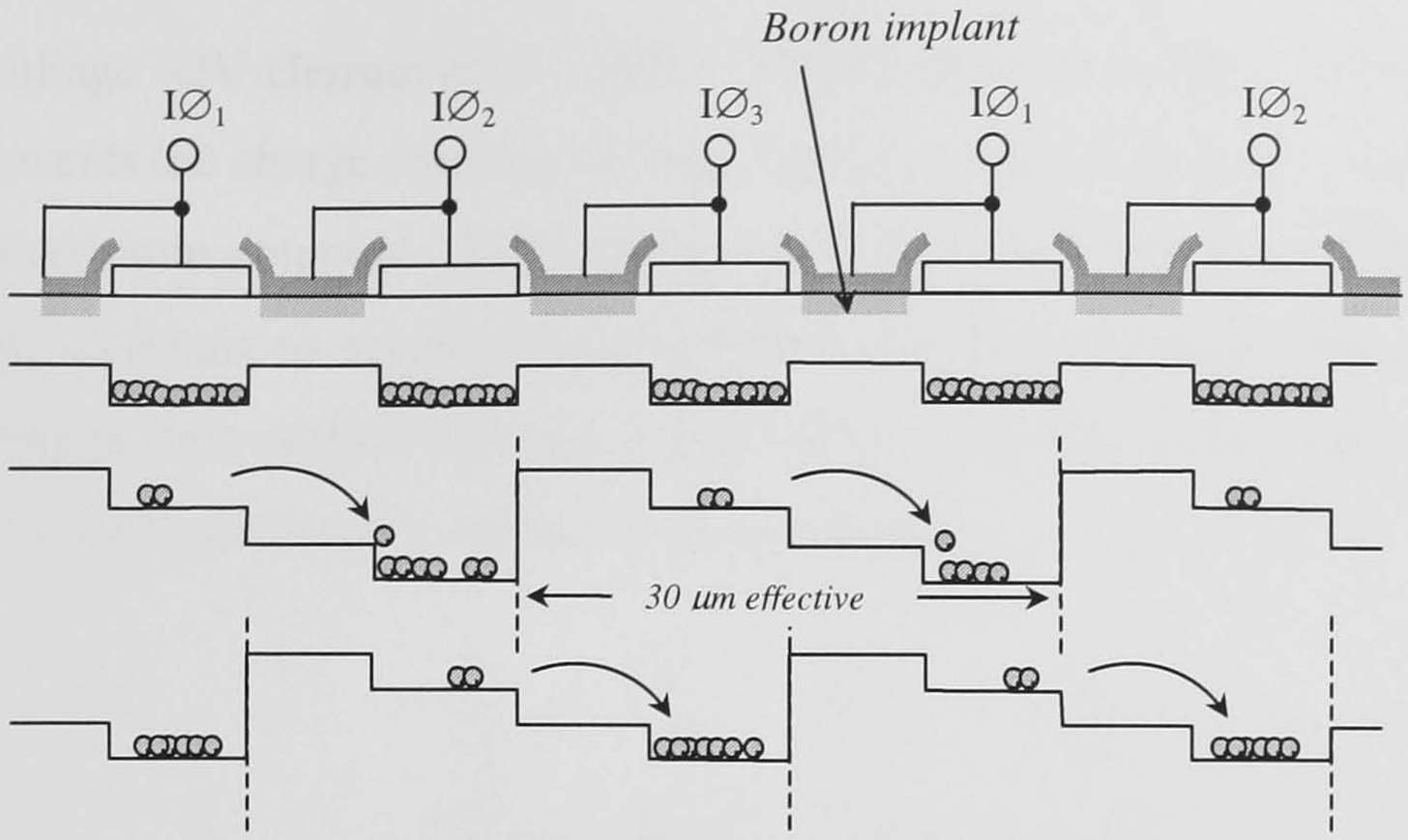

Figure 2.9. *An illustration of the two-phase clocking sequence used to achieve interlacing. Boron implants are used to create potential barriers that separate adjacent wells.*

The phases are shown in figure 2.8, $I\varnothing_1$ and $I\varnothing_2$ in the image section and $S\varnothing_1$ and $S\varnothing_2$ in the store section. The read out register is clocked using a three-phase clock sequence, $R\varnothing_1$, $R\varnothing_2$ and $R\varnothing_3$. The gain register requires four phases: $R\varnothing_1$, $R\varnothing_3$, a high voltage phase, $R\varnothing_2HV$ and a non-clocked phase $\varnothing_{dc}$. Two phases, $R\varnothing_1$ and $R\varnothing_3$, are clocked with normal amplitude drive pulses ~10 volts. The drive pulses of the second phase, $R\varnothing_2HV$, are much higher in amplitude ~ 40-50 volts. The d.c. electrode is held at ~ 2 volts. The image and store sections are operated in IMO to reduce the rate of dark current generation. The gain register is not operated in IMO. This reduces the probability of spurious charge generation, as described later.

2.3.2 L3 gain

The amplification of signal takes place in the CCD65 gain register. To illustrate how charge amplification is achieved a schematic of the potential profile within one element of the gain register is given in figure 2.10. Charge is transferred along the gain register using normal clocking pulses in a manner similar to normal operation. Two phases, $R\varnothing_1$ and $R\varnothing_3$, are clocked with normal amplitude, typically 10V. Charge multiplication does not occur in conventional CCDs during this process. To instigate charge amplification the second phase ($R\varnothing_2HV$) is clocked with a much higher amplitude, typically 40-50V, and an additional phase is added ($R\varnothing_{dc}$) which is held at a

low dc voltage ~2V (Jerram *et al.*, 2001). The dc phase provides a momentary barrier which prevents the charge entering the high field region until the high voltage phase had reached maximum potential. The large potential difference between $R\varnothing_2HV$ and $R\varnothing_{dc}$ causes the electrons to accelerate and acquire considerable kinetic energy. Some of these electrons then collide with the silicon lattice with such force that more charge is created. This phenomenon is called 'impact ionisation'.

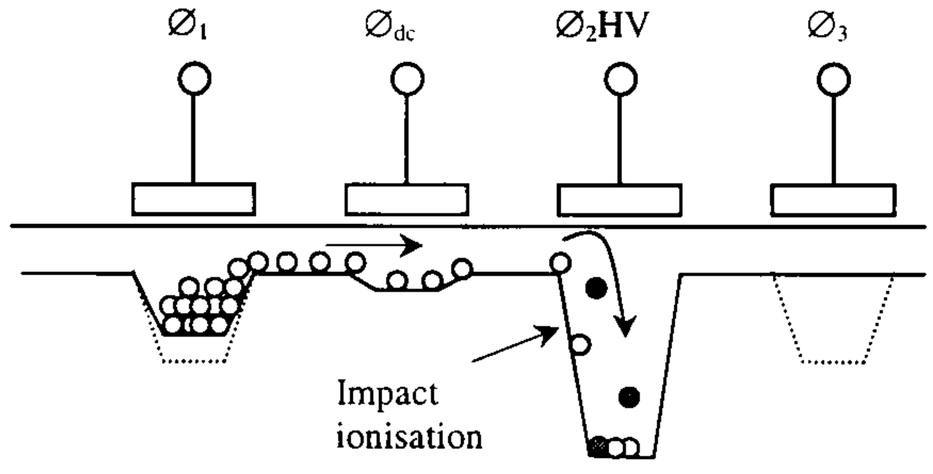

Figure 2.10. *Schematic of the gain register operation. Similar to a conventional CCD, charge is moved along the register using clocked voltage phases. The gain register employs an additional high voltage phase. The potential difference between the dc phase ($\varnothing_{dc}$) and the high voltage phase ($\varnothing_2HV$) causes the electrons to accelerate and impact ionise.*

Figure 2.10 shows one element or gain stage of the gain register. The gain per stage is proportional to the magnitude of $R\varnothing_2HV$ but is generally small, typically of the order of 1.01. However, with the very large number of gain stages through which the electrons are transferred (591 for the CCD65) means the total gain achievable is high. The mean total multiplication gain is given by:

$$\overline{M} = \overline{g}^{n} \tag{2.18}$$

where $\overline{g}$ is the mean gain per stage and n is the number of stages. Using equation 2.18, for a gain register of 591 elements and $g = 1.01$, $M = 358$. For $g = 1.015$, $M = 6629$.

2.3.3. Impact ionisation

The following gives more detail of the L3 gain mechanism.

The gain characteristics are a result of the transport properties of electrons in silicon. In normal mode operation electrons are transferred through the buried channel under low electric field conditions. The charge is transferred under the influence of two components: a drift component caused by the lateral electric field and a diffusion component caused by the electron concentration gradient. The diffusion component is normally rendered negligible by the fringing field between the electrodes. With no electric field electrons undergo only chaotic thermal motion in which they collide with lattice vibrations. As a result electrons continuously emit and absorb phonons; at thermal equilibrium the net rate of exchange is zero. Under the influence of a low electric field, the electrons continue to undergo thermal motion but begin to drift in the direction of the electric field. The net drift velocity of an electron is proportional to the electric field and is given by

$$v_e = \mu_e \mathrm{E} \tag{2.19}$$

where μ_e is the electron mobility and E is the electric field magnitude. At high fields the electrons acquire energy from the field and lose it by emitting phonons during lattice collisions. As the electric field increases, electrons, on average, acquire more energy than they had at thermal equilibrium and therefore have an effective temperature higher than the lattice temperature. When fields are sufficiently high (~ $5\mathrm{V\mu m^{-1}}$ for silicon at room temperature) non-linearities in the mobility and saturation of the drift velocity occurs. At still larger fields impact ionisation occurs. When the electric field is increased above a certain value, the electrons gain enough energy so that they can excite electron-hole pairs (Sze, 1982). The ionisation rate α is defined as the number of electron-hole pairs generated by a carrier per unit distance travelled. In this discussion we will only consider the electron ionisation rate, as we assume that any holes that are generated in the process of impact ionisation are repelled toward the surface and drained away by the CCD channel stops and so do not participate in the multiplication process any further.

Impact ionisation only occurs when the electron gains at least the threshold energy for ionisation E_I from the electric field. It is generally accepted that impact ionisation occurs at electric fields of the order of $10 V\mu m^{-1}$ for silicon at room temperature (Hess, 1988). An approximation of the electric field in a single L3 gain element can be made using the potential difference between $R\varnothing_{dc}$ and $R\varnothing_2HV$ and the distance between them. The potential difference between $R\varnothing_{dc}$ and $R\varnothing_2HV$ is of the order of 50V and the distance between them is ~ 4μm. Thus electric fields of ~ 10 $V\mu m^{-1}$ are achieved in the gain register. A number of studies, both experimental and theoretical, demonstrate that the temperature and field dependence of impact ionisation is well described by the empirical expression of Chynoweth (1958)

$$\alpha = a\exp(-b/\mathrm{E}) \tag{2.20}$$

There is a large spread in the experimental data that have been used to derived parameters a and b. Maes *et al.* (1990) have compared their own experimental data with the ionisation rates derived from the 'Chynoweth expressions' of a number of workers. Results show that the parameters derived by Van Overstraeten and De Man (1969) are the most suitable for the prediction of ionisation rates, due to the fact that these results have been obtained from data measured over a large range of electric field strengths.

2.3.4 Temperature dependence of gain

As temperature decreases, lattice vibrations decrease and the electrons are subject to less collisions. As a result, the mean free path of an electron increases and the electrons are able to acquire greater energy from the electric field. Thus the electrons are more energetic and more likely to cause impact ionisation (Crowell and Sze, 1966). Consequently, as the temperature decreases, the L3 gain register requires a lower potential to be applied to the $R\varnothing_2HV$ gate electrodes to achieve the same gain.

2.3.5 Gain register design

The first CCDs to incorporate a charge amplification stage were unsuccessful due to excess levels of dark current. Gajar and Burke (1998) report enhanced dark current levels in a conventional BCCD in which they applied high voltages between gate electrodes to induce impact ionisation. They observed that electrons (other than from impact ionisation) were being added to the packet during the gain procedure. Hyneček (1992) also reported problems with high levels of background charge at increased volatges.

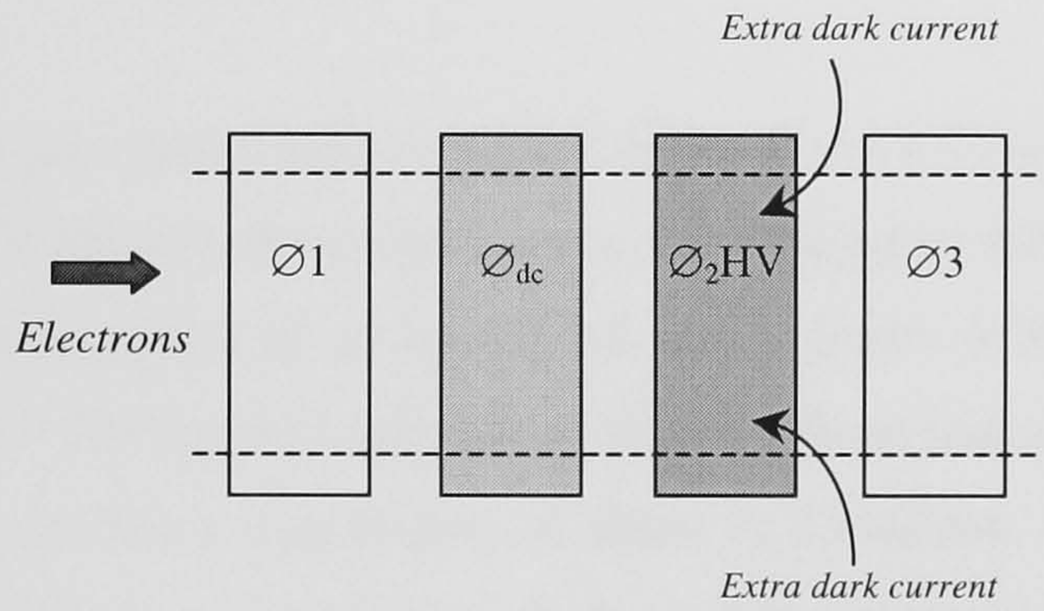

Figure 2.11. *Schematic of a gain register element. Due to high density of surface states at the edge of the electrodes thermal current is generated more easily. Thermal electrons are accelerated towards the high voltage electrode creating unwanted dark current (Burt and Bell, 2001).*

Burt and Bell (2002) identified the cause of the high thermal current levels to be due to the interface trapping states, i.e. N_s in section 2.1.7. At the edge of the register electrodes there is an increased density of surface states, which arises during CCD fabrication (see figure 2.11). The resulting thermal electrons are accelerated by the high electric field between R$\varnothing_{dc}$ and R$\varnothing_2$HV electrodes running parallel to the electrode edges. This gives rise to spurious charge which increases the noise and adds uncertainty to the gain mechanism.

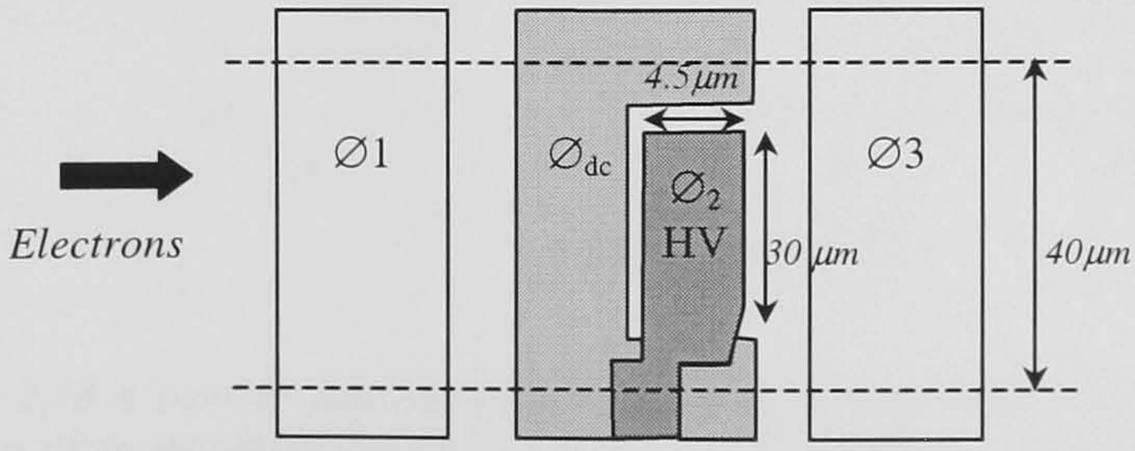

Figure 2.12. *Schematic diagram of the gain register element after Burt and Bell (2001).*

Density of surface states depends on the orientation of the silicon substrate and, very critically, on fabrication. To overcome the excess dark current a new gain register structure was designed. The new gain register element is illustrated in figure 2.12. This structure uses the dc electrode for shielding purposes such that the high field does not run along the edge of the electrodes. Only after this structure was implemented was a CCD with an internal amplification stage realised.

2.3.6 CCD65 dark signal characteristics

The basic pre-gain performance characteristics of the CCD65 are very similar to other comparable TV-based frame transfer sensors produced by E2V (E2V Technologies Ltd, 2002). The peak signal, as set by the full-well capacity of the pixel, is of the order of 100k electrons. The spectral response is that of a front-face device shown in figure 2.6. The output circuit has a responsivity of about 1μV/electron. Without CDS the noise is dominated by the reset contribution of about 100 electrons r.m.s. Multiplication gains of at least 1000 can be achieved with an RØ2HV clock of about 45-50 volts amplitude. A maximum multiplied signal of about 1M electrons can be accommodated before charge spill-back occurs. A typical variation of dark signal with temperature for the CCD65 has been measured by E2V Technologies and is shown in figure 2.13.

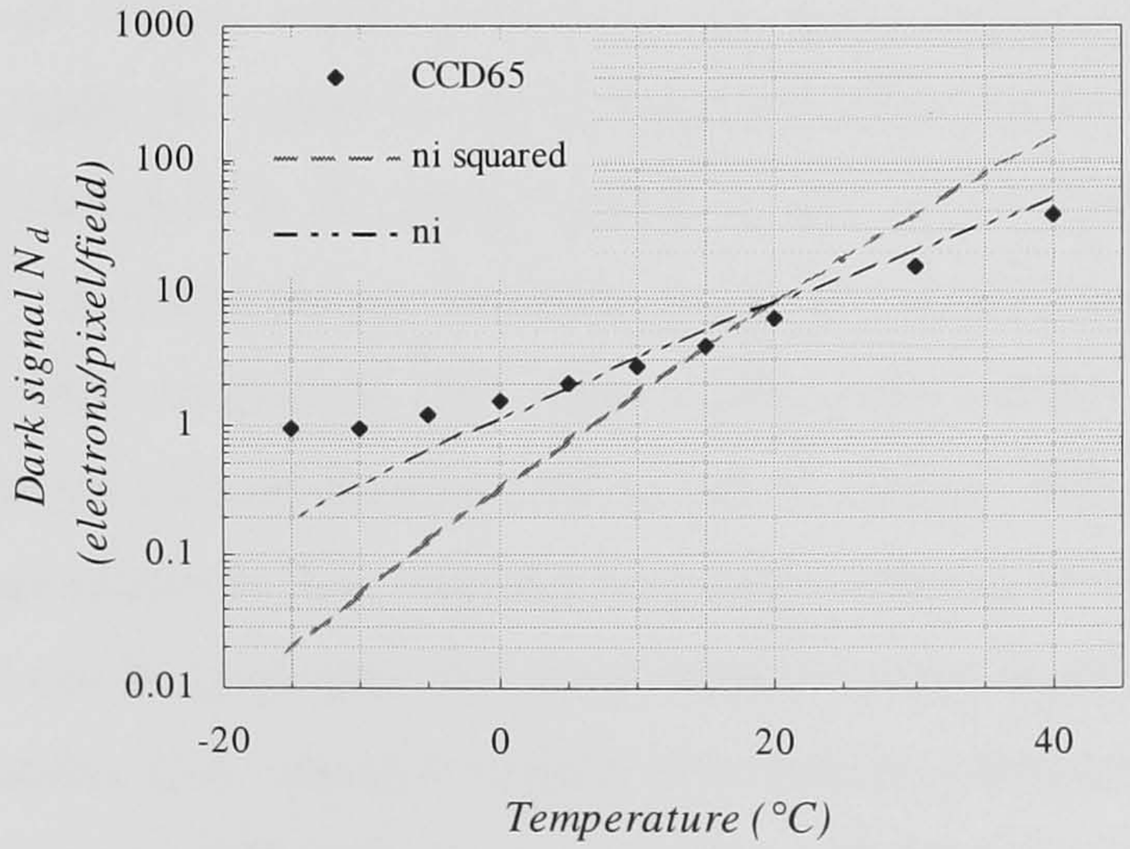

Figure 2.13 *A typical variation of dark signal, measured byE2V Technologies, as a function of temperature for the CCD65 (E2V Technologies Ltd, 2001). Predicted dark signal values have been calculated using equations 2.7, 2.8, 2.9 and 2.13 for* n_i *and* n_i^2 *dependencies.*

The image and store sections are operated in the inverted mode with the mean collection time of 20 ms. Hence, using equation 2.9, with a pixel size of 20μm × 30μm and a dark current of 5pAcm^{-2}, a dark signal of about 3.7 electrons can be expected from these sections. The register elements are of similar area but operated non-inverted with a dark current of 1nAcm^{-2} at 20°C. The charge collection time (i.e. the time a potential well spends on transit through the registers) is however only 128μs, so an additional dark signal of about 4.8 electrons can be expected. A predicted total dark signal in the region of 8.5 electrons per pixel at 20°C can thus be expected, much as is found in practice (see figure 2.13). The measured data is compared with predicted values calculated using the total predicted dark signal at 20°C of 8.5 electrons and the relationship between n_i and temperature given in equation 2.8 for n_i and n_i^2. The temperature variation is nearer to n_i than n_i^2. However, contrary to theory (described earlier in section 2.17), values below about 0°C appear to flatten off. It is believed that this is due to another charge-generating mechanism, as now described.

An additional source of dark current, spurious 'transfer induced' charge, is now known to be generated in Inverted Mode Operation (IMO) devices (Janesick *et al.*, 2002). In IMO, as described earlier, the surface potential is pinned to the substrate potential by the migration of holes from the channel stops to beneath the electrodes. Some holes become trapped in interface sates. When the gate is clocked out of inversion, the holes are accelerated away from the interface states. A fraction of the holes will have gained sufficient energy to impact ionise and create electron-hole pairs (exactly the same mechanism gives gain for electrons in the multiplication register). The 'spurious' electrons are then collected in the nearest potential well in the same way as thermally generated charge. Spurious charge has been found to be an exponential function of clock pulse rise time, magnitude and pulse width, but models for predicting the magnitude have not yet been developed (Janesick *et al.*, 2002). Although the fields with normal clocking are relatively low, with the very large numbers of holes involved a few spurious electrons can be generated, the actual number being dependent on the number of cycles. The number also increases slightly with reducing temperature on account of the increasing ionisation coefficient. In the case of the CCD65 this number is obviously very small (see figure 2.13), on average a total of less than one electron per pixel, but it does set a performance 'floor'. Some slight improvement may be possible by slowing the leading edges of the clock pulses (Burt and Bell, 2002).

2.4 Excess noise factor

Due to the random nature of the impact ionisation mechanism we expect the gain to have variance. If we consider a single gain stage with exactly N_i electrons entering the gain element the average number of electrons to leave will be $\overline{N}_1 = \overline{g}\, N_i$, where $\overline{N}_1$ will have an associated variance due to the gain. Consequently this variance will introduce an excess noise into the output signal.

The excess noise is commonly described using the excess noise factor F, which is defined as the variance of the multiplication for a single event at the input normalized by the square of the mean gain and given by:

$$F = \frac{\overline{M^2}}{\left(\overline{M}\right)^2} \tag{2.21}$$

where M is the multiplication gain in an avalanche multiplication process (Matsuo *et al.*, 1985). The term avalanche multiplication describes a cascaded impact ionisation event in which a single electron impact ionises and creates a secondary electron; the secondary and the primary then go on to impact ionise further, creating a cascade of impact ionisations.

2.4.1 Physical parameters affecting the excess noise factor

The excess noise factor for the avalanche multiplication process has been shown to be primarily dependent upon the multiplication gain $\overline{M}$ and two physical parameters: the ratio k of the ionisation coefficients for holes (β) and electrons (α) and the relative dead space (d/w), which is the ratio of the dead space to the multiplication region.

The excess noise factor was first quantified by McIntyre (1966) who showed that the excess it was dependent on the mean gain $\overline{M}$ and on k. This result relies on two assumptions. Firstly, the multiplication process is Marokavian, that is, the time necessary for carriers to acquire enough kinetic energy for the next impact ionisation is short and the electron-hole pair generation process is independent of the history of the

primary carrier. Secondly, it was assumed that the multiplication region is uniform. McIntyre's theory predicted that the best noise performance is expected when only one type of carrier undergoes avalanche multiplication, i.e. $\alpha>>\beta$ or $\alpha<<\beta$ and multiplication gain is kept low.

More recently it has been shown that the excess noise decreases with decreasing thickness of the multiplication region *w*. This is the region where there is sufficiently high electric field to create impact ionisation (Tan *et al.*, 200, Ong *et al.*, 1988, Herbert, 1997). This effect is attributed to the increase in the ratio of the dead space to the mean multiplication region width, (*d/w*). Dead space arises from the fact that impact ionisation can only occur when an electron or hole has sufficient energy to impact ionise i.e. E_I. The minimum distance that an electron must travel in order to acquire E_I is the dead space. The dead space reduces the noise by regularising the impact ionisation locations and acts to reduce the probability of higher order multiplication event, i.e. impact ionisation cascades. This is shown to narrow the probability distribution by reducing the randomness of the avalanche multiplication process (Salah *et al.*, 2000). These findings correspond with noise predictions made by Van Vliet, who in 1979 argued that when the number of ionisations per primary carrier is small and ionisation can only occur after a certain path length each event is governed separately by an individual Bernoulli trial (Van Vliet, 1979). Excess noise reduction has been measured in photodiodes with multiplication region widths of the order of 1μm for fields of ~ $10V\mu m^{-1}$ (Tan *et al.*, 2000). Furthermore, it has been shown that an electric field gradient within thin photodiodes extends the reduction in excess noise (Plimmer, 2001). The effect of the gradient is to further reduce the multiplication width, thereby increasing (*d/w*).

In conclusion, the excess noise factor is a function of two physical parameters, both of which are in some way dependent on the electric field. The ratio of the ionisation coefficients *k* is a function of the material, the electric field and the temperature. The relative dead space (*d/w*) is a function of the device thickness, the electric field and the ionisation coefficients. In silicon *k* decreases with decreasing electric field and the dead space is inversely proportional to electric field. The excess noise is also dependent on the level of gain set, which is, in turn, a function of the electric field. A dead space multiplication theory (DSMT) that incorporates all of these factors to predict the excess

noise factor has been developed for thin photodiodes (Hayat *et al.*, 1992) and verified experimentally (Saleh *et al.*, 2000).

2.4.2 Physical properties of the L3 gain register affecting excess noise

In light of the above discussion of the physical parameters affecting the noise factor, it is prudent to examine the physical properties of the L3 gain register. Firstly, consider the parameters k and $\overline{M}$ will be considered. It is expected that impact ionisation is a single-carrier process. This is because the holes that are created are attracted to the surface and drained away along the channel stops (Jerram *et al.*, 2001). This single carrier process is equivalent to $\alpha >> \beta$, which indicates a low noise process. The design of the gain register is such that high gain is achieved using a large number of small gain stages. Each stage has a very low gain ~ $\overline{M} = 1.01$. Physically each gain stage comprises of four electrodes. Multiplication occurs between the $\varnothing_{dc}$ and $\varnothing_2$HV electrodes and therefore the multiplication region is a maximum of 4 μm (the distance between $\varnothing_{dc}$ and $\varnothing_2$HV). Furthermore, the multiplication region will be reduced by potential profile beneath the electrodes. Fringing fields are electric fields that exist under the emptying gate electrode and are caused by the potentials on adjacent gates (Beynon an Lamb, 1980). This effect is illustrated in figure 2.14.

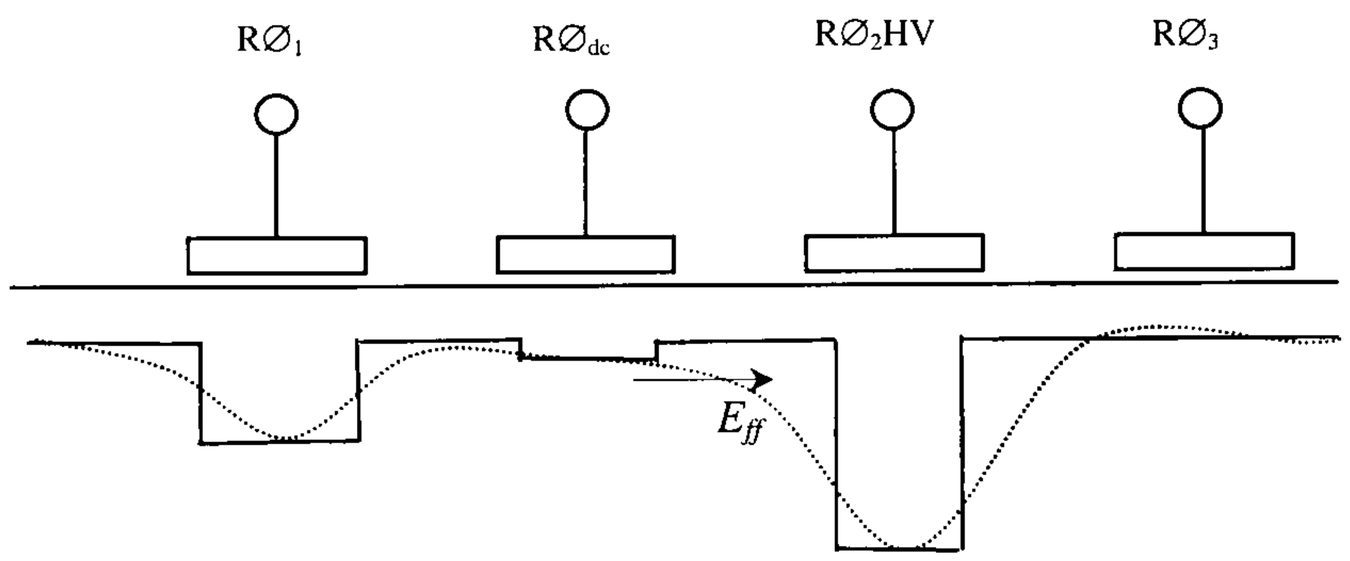

Figure 2.14. *Predicted potential distribution during transfer of charge from RØ1 to RØ2HV. The solid line represents the idealised rectangular potential wells and the dotted line represents the potential wells smoothed out by the fringing field (E_{ff}). Adapted from Beynon and Lamb (1980).*

The fringing field between the electrodes will act to create a varying electric field gradient between the electrodes and the multiplication width will be further reduced.

The relatively low electric field employed will increase the dead space. Accordingly, it is expected that (d/w) will be high in an L3 gain stage, leading to a further reduction in excess noise due to the fact that impact ionisation is confined to specific regions and higher order multiplication events are less likely.

2.4.3 Quantification of the excess noise factor

So far we have considered the physical parameters that affect the excess noise factor. A single gain register element can be expected to have low noise properties due to the predicted low k and high (d/w). Dead space multiplication theory (DSMT) has been successfully used to predict values of excess noise factors for thin photodiodes. However a lack of precise knowledge of the field within the CCD due to fringing fields and the variation of field with depth prevents its application to the L3 gain register. Another consideration is the fact that the L3 gain register is not a single element, but a series of gain stages, and propagation of the excess noise through the gain stage must be taken into account. In order to quantify the excess noise factor for the L3 gain register it is helpful to examine the excess noise factor in devices that are analogous to it. There is one device that may be considered appropriate: the staircase avalanche photodiode (SAPD). The following is a description of the models that have been applied to predict the excess noise factor in the SAPD and a CCD called the Impactron, which incorporates a similar gain register mechanism.

A statistical analysis of the staircase avalanche photodiode excess noise factor has been given by Matsuo *at el.* (1985). These devices are based on alternate thin layers of wide- and narrow-band gap semiconductor materials (Chin *et al.*, 1980). Analogous to the L3CCD gain register, the gain at each location is small and high gains are achieved through multiple gain stages. An expression for the excess noise factor is based upon a cascade of shifted Bernoulli distributions, each representing one gain stage. Each Bernoulli distribution has an outcome of two possible values: 2 or 1 electrons. In terms of the probability that an electron at the start of the SAPD will give rise to a daughter electron, p, the excess noise factor for an m-stage cascade for a single electron entering the device is calculated to be

$$F_m = 1 + \left[\frac{(1-p)}{(1+p)}\right]\left[1-(1+p)^{-m}\right] \tag{2.22}$$

which gives $F_{m\to\infty} = 1$ for $p = 0$ and $F_{m\to\infty} = 2/(1+p)$ for $0 < p < 1$. In the L3 gain register an electron has a small probability of undergoing an impact ionisation event. Thus, using the condition where $m\to\infty$ and $0 < p < 1$, the gain register has a predicted excess noise factor of 2.

Hyneček (2001) has presented values of excess noise factor for a similar CCD named the Impactron, which has been manufactured by Texas Instruments. In this work Hyneček compares measured data to a theoretical analysis of the impact ionisation gain mechanism. Hyneček bases his theory on Burgess's variance theorem: equation 2.24, (Burgess, 1976). For the case where an energetic electron is converted into a number of lower energy electrons, the gain is a random variable with a mean gain $\overline{g}$ and variance σ_g^2. It can be shown that

$$\overline{N}_o = \overline{N}_i\,\overline{g} \tag{2.23}$$

$$\sigma_{N_o}^2 = \overline{N}_i\sigma_g^2 + \overline{g}^2\sigma_{N_i}^2 \tag{2.24}$$

Identical to the treatment of the photo multiplier tube (PMT) described in Barrett and Swindell (1981), the gain stages within the register are considered analogous to the dynodes of a PMT. Burgess's variance theorem is extended for a number of m identical cascaded gain stages giving

$$\sigma_{N_o}^2 = \sigma_{N_i}^2\left[M^2 + \sigma_g^2\left(\frac{M^2-M}{g^2-g}\right)\right] \tag{2.25}$$

where $M = g^m$. The excess noise factor is defined for an input of N_i electrons with a variance $\sigma_{N_i}^2$ and is given by

$$F^2 = \frac{1}{M^2}\frac{\sigma_{N_o}^2}{\sigma_{N_i}^2} \tag{2.26}$$

where F^2 is equal to the excess noise factor. This definition differs from equation 2.21 that is written for the input of a single electron. Here the equation is normalised by the input variance. Using equations 2.25 and 2.26, F^2 can be expressed for an m-stage device as

$$F_m{}^2 = 1 + \sigma_g^2 \left[\frac{\left(1 - \frac{1}{M}\right)}{g(g-1)} \right] \tag{2.27}$$

Equation 2.27 is based upon the assumption that the probability density function of g is the same for all primary incident electrons and for all stages and that the electron multiplication gain for each primary electron is independent of the gain associated with other primary electrons. Hyneček argues that $\sigma_g = (E_P/E_I) = 0.04$, where E_P is the dominant phonon energy, and that by plotting measured values of F^2 against m it is possible to extract a measured value of σ_g. Hyneček has presented a plot of the noise factor as a function of the number of gain stages m and σ_g is calculated to be 0.043. The same analysis has been used successfully to predict values of the excess noise factor for a micro-channel plate (MCP). Moran *et al.* (1997) consider the collision points within a MCP as a series of m cascaded amplifier stages, with the result being equation 2.27.

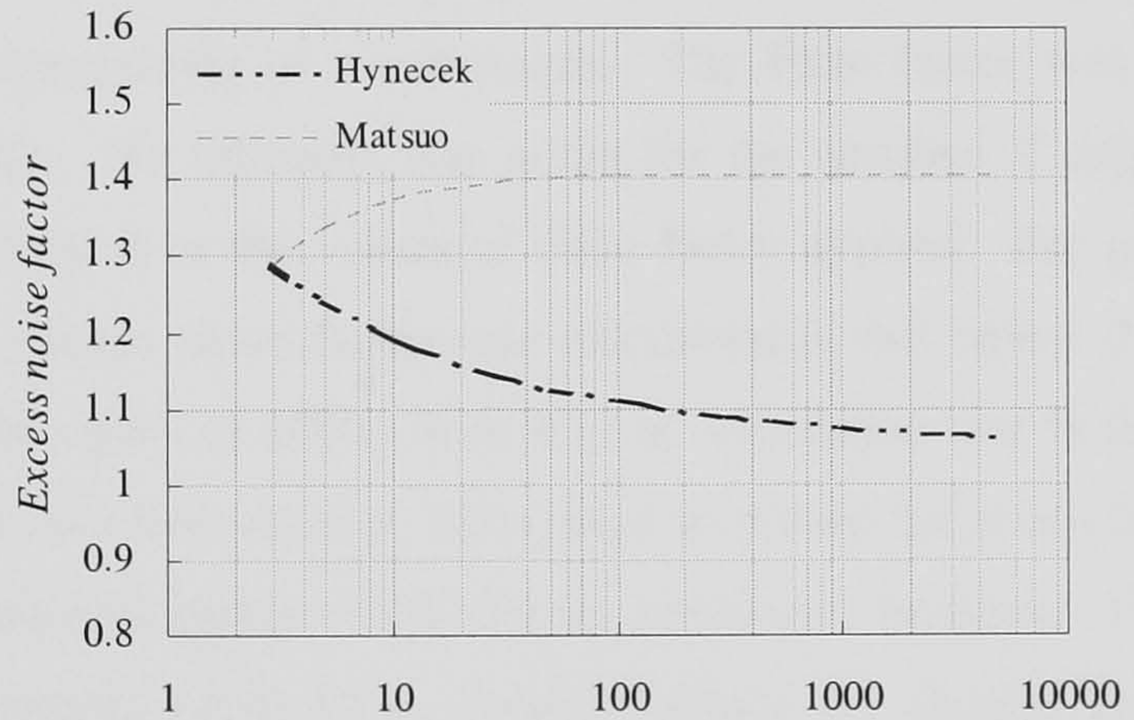

Figure 2.15. *The excess noise factor calculated for the L3 gain register using two approaches (1) √F for Matsuo et al for the SAPD and (2) F for Hyneček for the Impactron.*

It is reasonable to assume that the mean gain of each L3 gain stage is equal because the electrons pass through a large number of gain registers and any temporal variation in applied voltage will be averaged out. Using this assumption the excess noise factor has been calculated for the L3 gain register using the two approaches outlined above and is show in figure 2.15 as a function of multiplication gain M.

The Matsuo analysis shows that the noise factor is an increasing function of gain at low gains (M<100) and reaches an asymptote value of 2 at higher gains. Classically the Bernoulli distribution is used to describe a selection process in which the gain $\overline{g} << 1$ and the probability distribution describes the number of ways x items can be selected from y items (Barrett and Swindell, 1981). The use of the Bernoulli distribution to describe the variance in the SAPD differs in its assumption that each individual electron has an equal probability p of creating a daughter electron at each stage. This 'tracing' of individual electrons results in a doubling of the input variance and a wider distribution in M than in the case of a true selection process. In later work the same group (Hakim *et al.*, 1990) proposed that the Bernoulli distribution model should be adjusted to include a carrier multiplication 'variance-to-mean' or Fano factor (described in Appendix A) which narrows the probability distribution. In the case of small thin devices, i.e. $w \rightarrow 0$, the Fano factor represents the reduction of noise for instantaneous Bernoulli multiplication. Excess noise factors were calculated for double carrier SAPDs as a function of multiplication gain and k. The device was modelled as a series of m planar stages comprising of n sub-stages. The Fano factor was applied to edge regions within a stage. No rationale was given for the number of edge sub-stages the Fano factor was applied to or the values of Fano factor applied. For gains greater than 10 and k<0.001 the excess noise factor was calculated to fall below 2 and approached unity at multiplications gain of 1000. Hakim *et al.* concluded that in devices where the carrier multiplication is constrained to take place at certain locations in the device this restriction reduces the randomness in the impact ionisation locations. Consequently any expression for the excess noise factor should include the multiplication gain, k and factors to incorporate the device structure. The Bernoulli analysis given above only considers the multiplication gain and therefore is insufficient to predict an accurate value of the noise factor.

The Impactron analysis shows gain to be a function of decreasing function of M with the noise factor close to 1.07 at high gain. Again, it is based upon the assumption that the individual electrons independently experience an equal probability distribution at each gain stage. In this result the noise factor is proportional to the variance in the gain σ_g^2, in Hyneček's analysis σ_g is small, leading to a noise factor that approaches unity. The value of σ_g^2 is derived from the physical parameters that influence impact ionisation and its theoretical basis follows that of the Fano factor. That is phonon interactions are a relatively unimportant energy loss mechanism in comparison to impact ionisation and therefore the variance is reduced. Hyneček verified the value of σ_g^2 experimentally, thus, this analysis is more appropriate to the L3 gain register.

CHAPTER 3

Camera Characterisation

This chapter describes the calibration and characterisation of the CCD65 sensor. The purpose of this work is to ascertain the salient features of this novel technology and to highlight any potential benefits the CCD65 may have for the application of the technology to medical imaging. To identify potential applications a full understanding of the CCD gain and noise characteristics must be obtained. These characteristics may then be matched to the requirements of specific radiographic imaging applications, allowing the CCD65 to be compared with other imaging devices.

Descriptions of the L3 camera and the image acquisition system will be given. The imaging system has been calibrated in order to obtain a complete characterisation of the conversion processes leading to the digital output. Sensitivity and signal to noise (*SNR*) performance are strongly influenced by the noise sources within the imaging system, thus the CCD noise floor has been measured and the effect of the multiplication gain on the noise floor has been investigated. The minimum detectable signal will be affected by both the noise due to gain (excess noise factor) and the levels of gain obtainable. The gain has been measured and the magnitude of the excess noise investigated. The gain dependence on electric field ($R\varnothing_2HV$ clock amplitude), temperature and input signal has been measured to determine gain stability.

This characterisation work is some of the first to be undertaken on a L3CCD image sensor. The sensors used were prototype CCD65 devices selected from the first and seventh batches fabricated. Noise measurements performed by the manufacturer have been made soley for comparison with other intensified cameras and therefore are confined to standard TV convention. The noise measurements described here are the first to be undertaken in the digital domain and in such detail. A measurement of the excess noise factor *F*, has not been made by the manufacturer. Instead, a value of $F = \sqrt{2}$ is given in the CCD65 technical note on the use of L3 multiplication gain in the L3

sheet (Marconi Applied Technologies Ltd, 2002(a)). This is derived from the Bernoulli analysis described in section 2.4.3 and has been modelled by Mackay *et al.* (2001).

In addition, the measured performance parameters described above are compared and contrasted against those of other detectors suitable for use in diagnostic radiology and introduced earlier in section 1.4. This comparison is intended to highlight the potential benefits of L3 technology for application to specific imaging techniques.

3.1 Description of the system

3.1.1 Detector design

Each sensor used was provided by E2V Technologies Ltd. It was specifically requested that sensors be adapted by E2V Technologies Ltd to suit the work that would be undertaken. The first sensor used had a fused fibre-optic faceplate bonded by optical adhesive to the front surface of the CCD65. The faceplate, was 5mm thick and had a numerical aperture of 1.0. The faceplate was manufactured using 6μm diameter fibres, giving an image resolution of ~80 line pairs per millimetre. Throughout this thesis this sensor is referred to as CCD65-01. The CCD65-01 is thermoelectrically cooled using a Peltier device, heat sink and fan assembly. The fan was powered from the camera. The Peltier cooler was a 1.4W device powered from a separate variable power supply. This allows adjustment of the voltage to compensate for variations in ambient temperature.

The second sensor (CCD65-02) was designed for single x-ray photon detection. An illustration of this x-ray sensor is shown in figure 3.1. The device was intended for the detection of 15 – 20 keV x-ray photons for diffraction enhanced breast imaging, described later in chapter 5. A quantum detection efficiency of greater than 99% was required, therefore it was decided that the CCD should be used in conjunction with an x-ray phosphor. However, the use of an x-ray phosphor results in a reduction in spatial resolution. It has been calculated that a 160 μm layer of phosphor attenuated 99.7% of incident x-ray photons and provides adequate spatial resolution for diffraction enhance breast imaging. This thickness is the standard thickness for dental CCD manufacture and therefore is readily available. The CCD/phosphor sensitivity Γ, was calculated

using equation 2.5 for the L3CCD and a number of different x-ray phosphors. Europium doped gadolinium oxysulphide (Gd_2O_2S:Eu) x-ray phosphor was found give the highest value of Γ. This is mainly due to its spectral emission, which is well matched to the L3CCDs spectral response, giving a large QE_{eff}. The layer of phosphor was deposited on to the surface of the CCD in order that the best coupling efficiency could be achieved. Further cooling was necessary to achieve adequate sensitivity; it was calculated (as described later) that the CCD thermally generated current should be approximately 1 e^-/pixel/field and therefore cooling to below 0 °C is required. In order to protect the CCD from condensation it was enclosed in a Peltier cooled package.

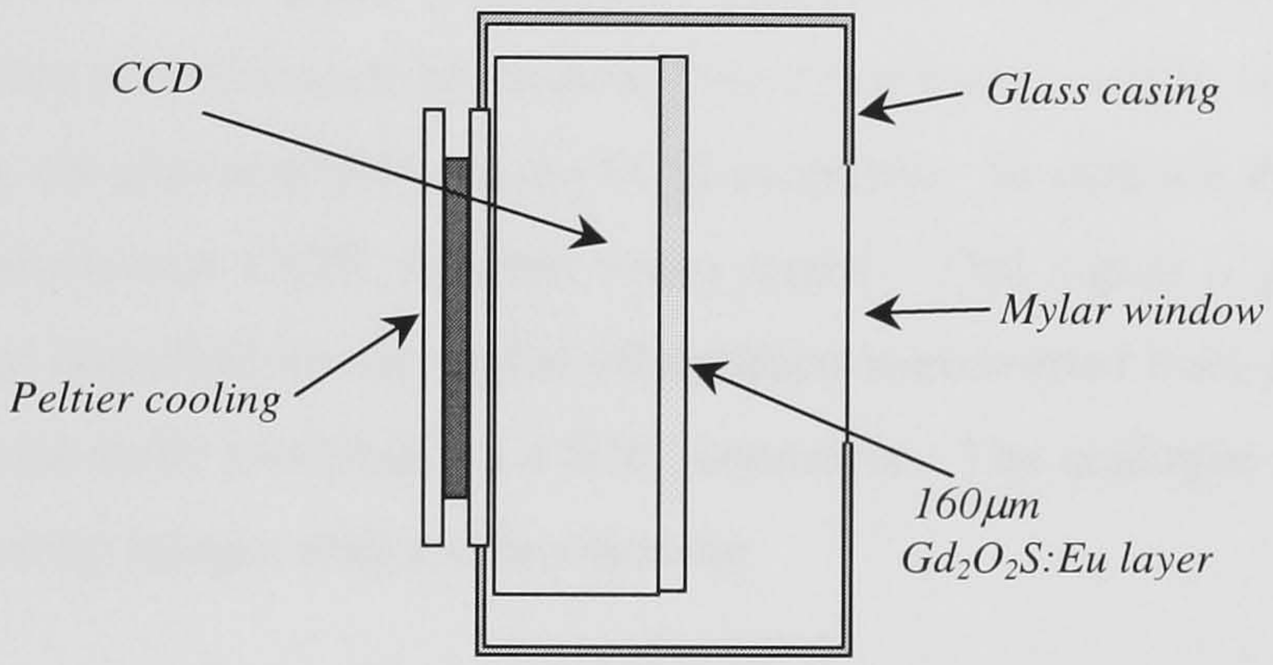

Figure 3.1. *An illustration of the CCD65-02 x-ray sensor design which is intended for single x-ray photon detection in the 15 to 20 keV energy range.*

The Peltier cooled package has a 2.5 mm thick borosilicate glass case (Marconi Applied Technologies Ltd, 2002(b)). In order to maximise the quantum detection efficiency a low attenuation entrance window (50μm Mylar) was used. Care was taken to hermetically seal the package so that it could be back-pumped and filled with a low conductivity inert gas. Due to the fragile nature of the Mylar in comparison to the borosilicate glass normal levels of back-pumping could not be achieved. Consequently molecules of air and water may have remained within the Peltier package and thus, as a precautionary measure, the minimum operating temperature was restricted to –7 °C (the manufacturers recommendation).

3.1.2 The L3CCD camera

The L3CCD camera used in this work was provided by E2V Technologies Ltd. The camera was one of seven prototype cameras designed and built specifically to control

the CCD65 image sensor. The camera was operated using a 3A/13.8V d.c. power supply. Images were acquired continuously at a rate of 25 frames per second. A single frame is formed by two interlaced fields, each of 20ms duration. The information contained in a single image corresponds to a total integration time of 20ms. The output voltage signal from the CCD65 output amplifier undergoes 12-bit digitisation. The analogue to digital conversion was performed by a high speed analogue-to-digital converter (ADC). Correlated double sampling is implemented after signal digitisation. An EEPROM logic chip converts the digital signal into a low voltage differential (LVD) signal, which was available via a 68-pin SCSI connector situated on the rear of the camera chassis. The pixel information comprises a set of 24 signal pulses, 12 complimentary pairs for each bit of data. The drive pulses, which communicate timing information, are also available via the SCSI connector. In addition the camera provides a 50Hz monochrome CCIR standard video signal. This signal is generated from the digital signal described above; signal information is converted back to analogue format by a DAC and made available via a BNC connector. The analogue output is primarily used for viewing images with a video monitor.

The gain and offset level are controlled via two potentiometer controls situated on the rear of the camera chassis. Each potentiometer can be varied between 0V and 5V and the potential difference across it can be measured via output pins also situated on the rear of the camera chassis.

The L3 camera was modified to house the phosphor-coated CCD65-02. In order to accommodate the cooling assembly the header board, upon which the CCD is situated, was changed. A third potentiometer was added to the rear of the camera chassis for the adjustment of the current supplied to the Peltier device. Temperature was monitored via a thermister; the resistance across it is measured from two additional output pins.

3.1.3 Image acquisition

In order to obtain images the digital signal was captured using a digital image acquisition card PCI-1422 (National Instruments). The PCI-1422 is a PC plug-in card that uses a 100-way DIN connector. The LVD signal was transferred via a custom-built

SCSI cable with appropriate connecters attached to each end. The PCI-1422 was controlled using LabWindows CVI (National Instruments) software. The acquisition card uses the timing information sent from the camera to acquire data. Four timing signals were used: *i*) the pixel clock signals the arrival of each pixel, *ii*) the frame enable signal is high at the beginning of each frame, *iii*) the field enable signal is high at the beginning of each field, *iv*) the odd field enable indicates the start of each odd field. The odd field enable was necessary to allow the acquisition card to organise the two fields correctly.

Acquisition and display sequences were programmed using C programming language. Images were acquired and stored in memory buffers allocated using the acquisition programme. Generally, image acquisition was undertaken in two modes:

grab mode: a continuous grab and display of the images where data was collected in a buffer, displayed and then immediately discarded, and

sequence mode: where a specified number of images were acquired to the buffer in computer memory. Once image information is acquired to the buffer it can be displayed and/or saved.

All image data is saved in 16 bit binary image format with no file header. The data acquisition system can also be used to obtain smaller regions of interest within the image or read out signal information from single pixels.

3.1.4 Cooling

The time taken for the system to reach a stable temperature was estimated by making measurements of the sensor temperature as a function of time. The ambient temperature was monitored throughout the experiment and any fluctuations corrected for. The sensor heats up over a period of 60 minutes before reaching thermal equilibrium. At an ambient temperature of 20°C the normal operating temperature of CCD65-01 without cooling is ~38°C. If gain is used, a larger amount of power is dissipated and the normal

operating temperature increases to ~ 43°C. The CCD65-01 is unprotected from the external environment and at temperatures below the dew point water will condense onto the CCD and possibly damage it. Water droplets were observed on the fibre-optic faceplate at approximately +10°C (this temperature is dependant upon the local atmospheric pressure and humidity). Consequently the CCD65-01 was operated at +15°C.

The recommended minimum operational temperature for the CCD65-02 is –7°C. From power on, the time taken for the CCD to stabilise was found to be approximately 20 minutes. The cooling curve for CCD65-02 is shown in figure 3.2.

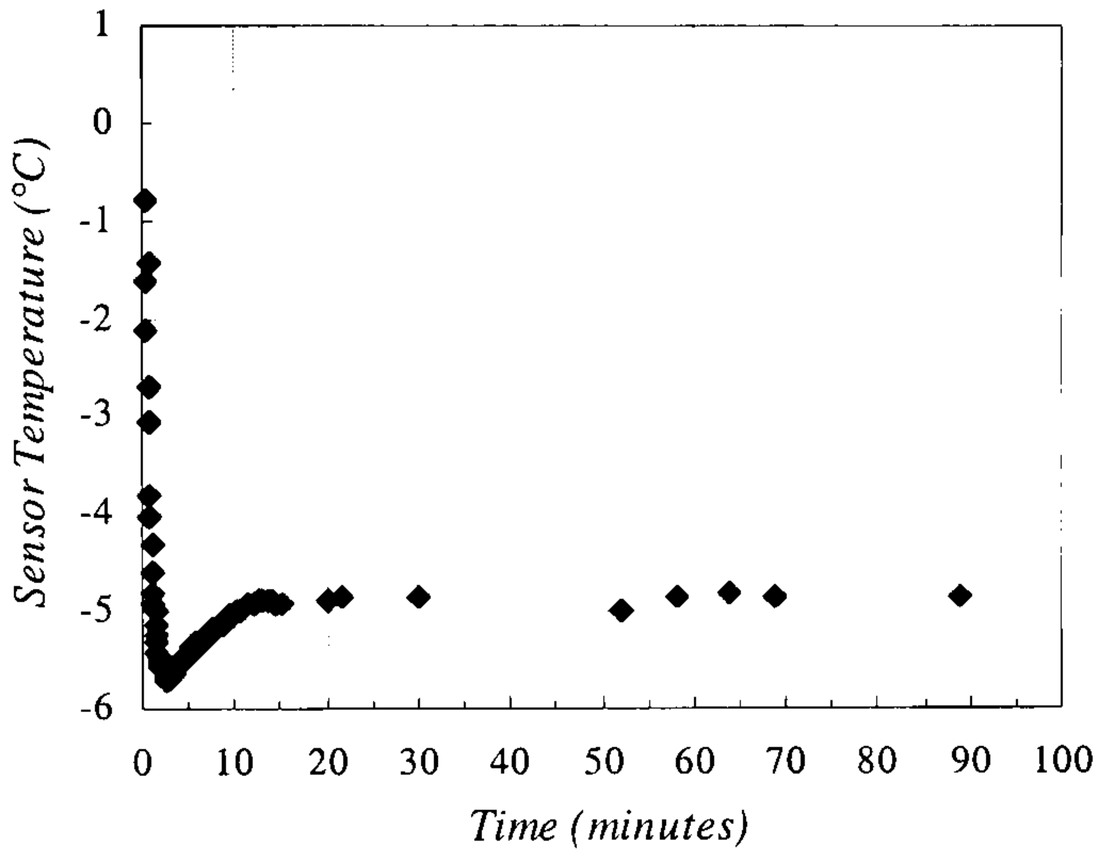

Figure 3.2. *Cooling curve for CCD65-02.*

3.1.5 Full well capacity

The CCD65 differs from conventional charge coupled devices in that there are two stages of device saturation. This is because the gain register has a higher full well capacity than the image and store sections. Under normal operation (unity gain) the device will saturate when the amount of charge generated exceeds the full well capacity of the image section pixels. This condition also applies when the CCD65 is operated in gain mode. However once gain is applied the saturated signal will be amplified in the gain register. The saturation signal will increase until the full well capacity of the gain register is reached. Similarly, with the application of too much gain, a non-saturated

image signal can be amplified above the full well capacity of the gain register resulting in the loss of image information.

3.1.6 Dark current and electrical offset

If there is no incident illumination and the thermal current is zero the digital signal will still not be zero. In this case the value passed out of the camera will be equal to some value set by the electrical offset.

The average digital signal was found for both dark and illuminated fields for various offset voltage settings. Three images were acquired at each voltage setting. The average digital signal was found for each image and the mean value of digital signal for all images was calculated. It was found that as the voltage was decreased there was a linear increase in the signal. The offset signal elevated the saturated fields by the same amount as dark and partially illuminated fields. This indicates that there is no 'white clipping' during digitisation of the signal.

3.1.7 Image correction

A straightforward correction for the variation in dark signal non-uniformity is achieved by subtracting a dark field image. However, care must be taken to use a dark field image that has been acquired at the same level of gain. If the dark field image has been acquired at a different value of the gain, the subtraction process will increase dark signal non-uniformity, rather than correcting for it. For illuminated images, the correction process also requires flat field corrections used to correct for fixed pattern noise. In this thesis illuminated images containing N pixels have been corrected on a pixel-by-pixel basis where the correction for the *ith* pixel is given by

$$S_C(i) = \frac{1}{N}\left[\sum_{i=1}^{N}\left(S_{ff}(i) - S_d(i)\right)\right]\frac{S(i) - S_d(i)}{S_{ff}(i) - S_d(i)} \tag{3.1}$$

where $S_{ff}(i)$ is the corresponding pixel value of the illuminated flat field image, $S(i)$ is the uncorrected raw pixel data and $S_d(i)$ is the pixel data from the dark field image. The illuminated flat field image and the dark image are acquired at the same gain as the raw pixel data. A similar algorithm has been reported by Karellas *et al.* (1993).

3.2 Conversion gain calibration

Digital images acquired using the data acquisition system are comprised of an array of pixels. Each pixel has an associated grey level value or integer digital number (DN). This information is used by the computer to form the image. In a linear system the magnitude of the digital number is proportional to the number of photons incident on the actual CCD pixel area. The CCD65 photon detection process can be described as a series of six gain stages. At each stage the signal is subject to a conversion process with an associated gain. The gain stages involved in the photon detection process using the CCD65 detector system are illustrated in figure 3.3.

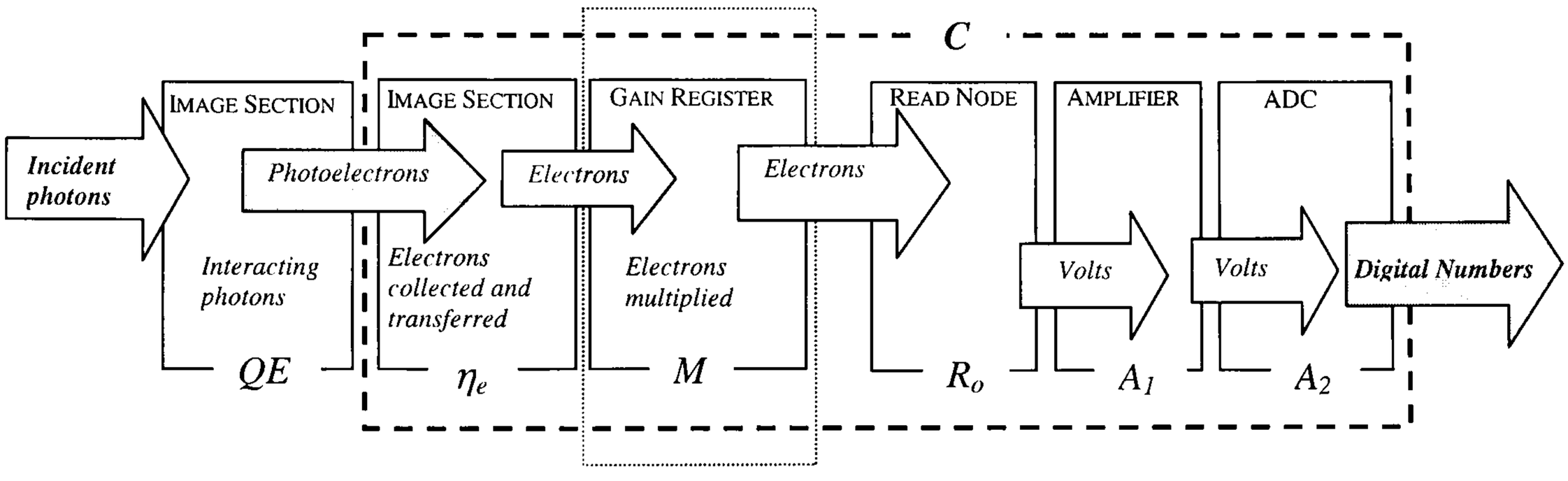

Figure 3.3. *Schematic representation of the gain stages involved in the photon detection process. The conversion factor C, represents the number of photoelectrons per digital number (adapted from Janesick et al. (1987).)*

The average digital output of the CCD65 in DN can be expressed as the product of the successive gains:

$$S(DN) = \Phi QE\eta_e MR_o A_1 A_2 \tag{3.2}$$

where Φ is the mean incident photon fluence per pixel, QE is the CCD quantum efficiency, η_e is the charge collection efficiency and M is the multiplication gain from

impact ionisation. R_o is the responsivity in volts per electron of the output circuitry, given by equation 2.1, A_1 is the amplifier gain and A_2 is the analogue-to-digital converter gain. It is convenient to measure an overall system gain that is independent of the wavelength of the incident photons. Therefore for a system with unity multiplication gain the overall system gain can be represented by:

$$C = \frac{S}{N_i} \tag{3.3}$$

where N_i is the number of photoelectrons generated in the CCD pixel and is equal to ΦQE. System gain is typically defined as the number of digital numbers per signal electron (DNe^{-1}). In this work it will be necessary to determine the input noise, σ_i, to the system so that we can differentiate it from, and thus determine, the system noise. The number of photoelectrons N_i, that are generated in a pixel is Poisson distributed, i.e. $\sigma_i = \sqrt{\overline{N_i}}$. The average digital signal is given by $S = C\overline{N_i}$ and it can be shown that $\sigma_S = C\sqrt{\overline{N_i}}$ and thus, $\sqrt{S} \neq \sigma_i$ (Barrett and Swindell, 1981). Consequently the variance on the input photoelectrons (the input noise) cannot be found from the digital output signal and variance alone. To make a measurement of the input noise a value of C must be obtained.

3.2.1 Determination of *C*

Three techniques are most commonly employed to determine C: radiometric, x-ray methods and mean-variance. In radiometric techniques the input irradiance from a monochromatic and uniform field of light is measured simultaneously with the CCD output. The number of photoelectrons generated per unit irradiance can be calculated using the responsivity of the device and related to the digital output (Holdsworth *et al.*, 1990). A radiometric method has been described by Dávalos (1994). The average digital output is found for a number of incident illumination intensities. The incident illumination intensity is found by positioning a light meter in exactly the same position as the CCD. Average digital output is then plotted as a function of illumination intensity and the slope of the resulting straight line gives a value of digital number per

unit power per unit area ($DNnW^{-1}mm^{-2}$). This value can then be related to the number of the photoelectrons using the number of photoelectrons per unit power per unit area ($e^{-}nW^{-1}mm^{-2}$) and is given by (Beynon and Lamb, 1981):

$$\frac{N_i}{W_\lambda} = \frac{R_\lambda \times A_{pix} \times t_i}{q} \tag{3.4}$$

where N_i is the number of electrons, W_λ is the illumination power, R_λ is the responsivity, q is the charge on an electron, A_{pix} is the pixel area and t_i is the integration time.

The accuracy of this result relies heavily upon the precise measurement of the illumination intensity incident upon the CCD. Inaccuracies in the illumination power measurement can arise from temporal variation in the light source, inaccurate positioning of the light meter with respect to the position of the CCD and the inaccuracy due to the limited precision of the light meter. Furthermore, there are unknown quantities such as the optical attenuation of the fibre optic and the coupling adhesive and the spectral attenuation properties of the Mylar layer and the x-ray phosphor. An additional source of error originates from the value of sensor responsivity that is used in equation 3.4. The responsivity of an individual CCD can vary as much as ± 20% from the nominal value (E2V Technologies Ltd, 2002). The radiometric technique is convenient for the assessment of device linearity, however, considering the potential inaccuracies involved in obtaining an absolute measurement of incident illumination intensity, it is unsuitable to be used for the measurement of *C*.

The second technique, based upon irradiation with sources that emit low energy x-rays, uses the ionisation energy of silicon (3.6eV at room temperature) (Janesick *et al.*, 1987). The average number of digital units per x-ray interaction can be related to the number of electrons generated for an x-ray photon of a known energy. However, the selection of a suitable x-ray source is complicated by the fact that large numbers of x-ray interactions are required to obtain good statistics. In addition, low energy sources (<20keV) are required to minimise errors due to x-rays being absorbed just below the depletion region where charge collection efficiency is poor. Such low energy photons would be highly attenuated by both the fibre optic faceplate and the phosphor layer.

The third technique, the mean-variance technique, uses Burgess's variance theorem to calculate *C*. This involves a statistical analysis of the mean and variance of the output signal. Janesick *et al.* (1987) and Holdsworth *et al.* (1990) have described a technique based upon this statistical theory. The variance in the mean observed signal is given by

$$\sigma_S^2 = \overline{C}^2 \sigma_{N_i}^2 + \overline{N}_i \sigma_C^2 \tag{3.5}$$

where $\overline{C}$ is the mean value of the overall system gain, $\sigma_{N_i}^2$ is the variance on the input signal and σ_C^2 is the variance in *C* (Holdsworth *et al.*, 1990). If $\overline{N}_i$ obeys Poisson statistics then $\overline{N}_i = \sigma_{N_i}^2$ and, from equation 3.3, $\overline{N}_i = \overline{S}/\overline{C}$. Substitution into equation 3.5 gives

$$\sigma_S^2 = \overline{CS}[1 + (\sigma_C / \overline{C})^2] \tag{3.6}$$

If the variance in gain is small with respect to the mean gain, i.e. $(\sigma_C / \overline{C})^2 << 1$, equation 3.6 may be written as $\sigma_S^2 = \overline{CS}$. However, in a real system, system read noise is present and the total variance will be given by

$$\sigma_S^2 = \overline{CS} + \sigma_{sys}^2 \tag{3.7}$$

The overall system gain can then be found by plotting the output signal variance against the mean of the digital output signal. The slope of the curve is *C* and the intersection of the variance ordinate gives the system noise. This technique assumes that the detector is both quantum limited and linear. The mean variance analysis may be preformed with no additional equipment beyond the CCD detector system and a variable light source. There is no requirement for the incident illumination intensity to be known.

The mean-variance technique is clearly the most suitable choice for the determination of *C*. The following is a description of the experimental technique used to assess device linearity and determine *C*.

A 5mW HeNe Laser (λ = 632.8nm, Melles Griot, model no. 05LHR151) and an integrating sphere (Oriel Instruments, model no. 70461) were used as a light source for the calibration of the CCD65. The experimental set up is shown in figure 3.4.

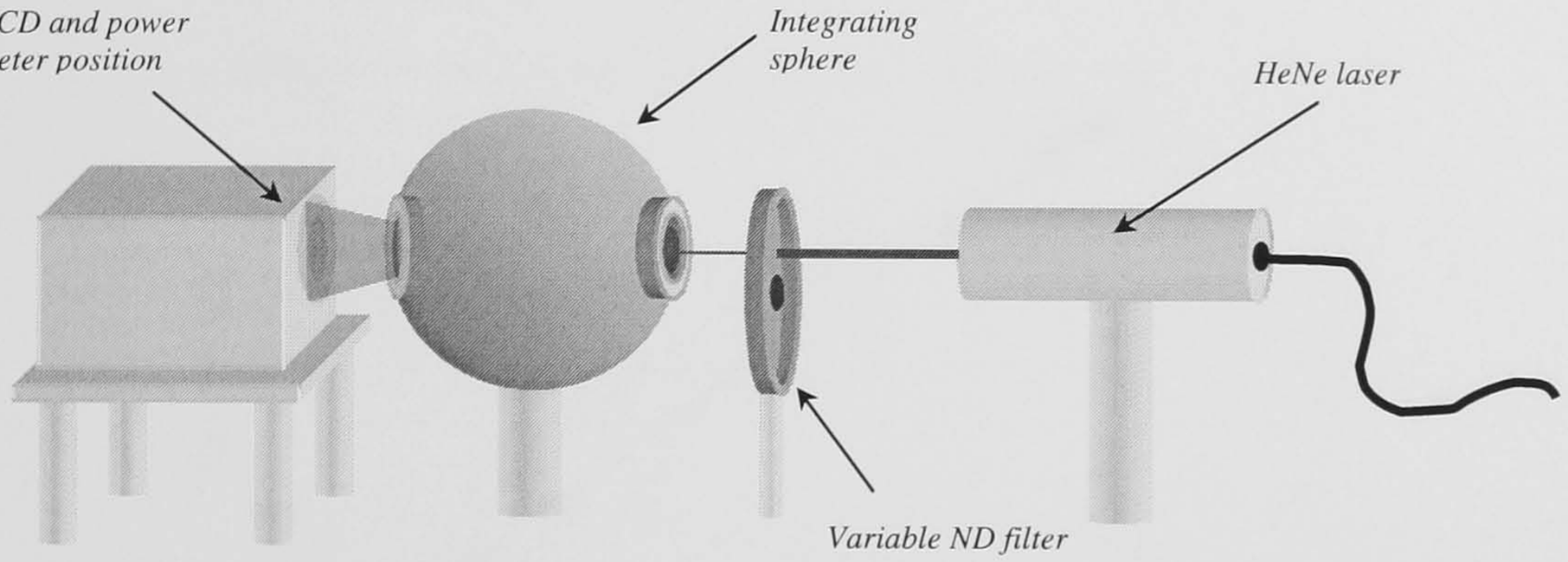

Figure3.4. *Schematic of the experimental set up for the CCD calibration measurements.*

Light emitted by the laser is collected within the sphere, then uniformly reflected and scattered around the spheres interior so that the output is uniform and Lambertian. The variable neutral density filter placed at the entrance of the sphere was used to vary the incident light intensity on the CCD. The flatness of the illumination field across the image was measured by generating a linear plot across the image in both the horizontal and vertical directions. The variation in intensity across the image was found to be less then $\pm$ 3 %.

Images were acquired for a range of illumination powers from no light (dark field) to image saturation. The position of the neutral density filter was carefully recorded for each image acquisition. To assess device linearity the illumination power ($nWmm^{-2}$) was measured using a light meter (Coherent, model no.212) calibrated at 632.8nm. The light meter was placed in the same position as the CCD sensor and the illumination power measured for each neutral density setting. The light meter operates in the range of 10nW to 10W with an overall accuracy of $\pm$ 5%. The stability of the laser illumination intensity was estimated from measurements of light power as a function of time. Over the period of an hour (approximately the time taken to perform the calibration), the light power was found to vary within $\pm$ 5% of an average reading. The measurements were carried out with the multiplication gain set to unity.

For a given irradiance the mean output signal was found from the digital signal (DN) averaged across the entire image. All images were corrected for fixed pattern noise and dark and offset values as described in section 3.17. A plot of illumination power versus digital signal is shown in figure 3.5 to demonstrate CCD65 linearity.

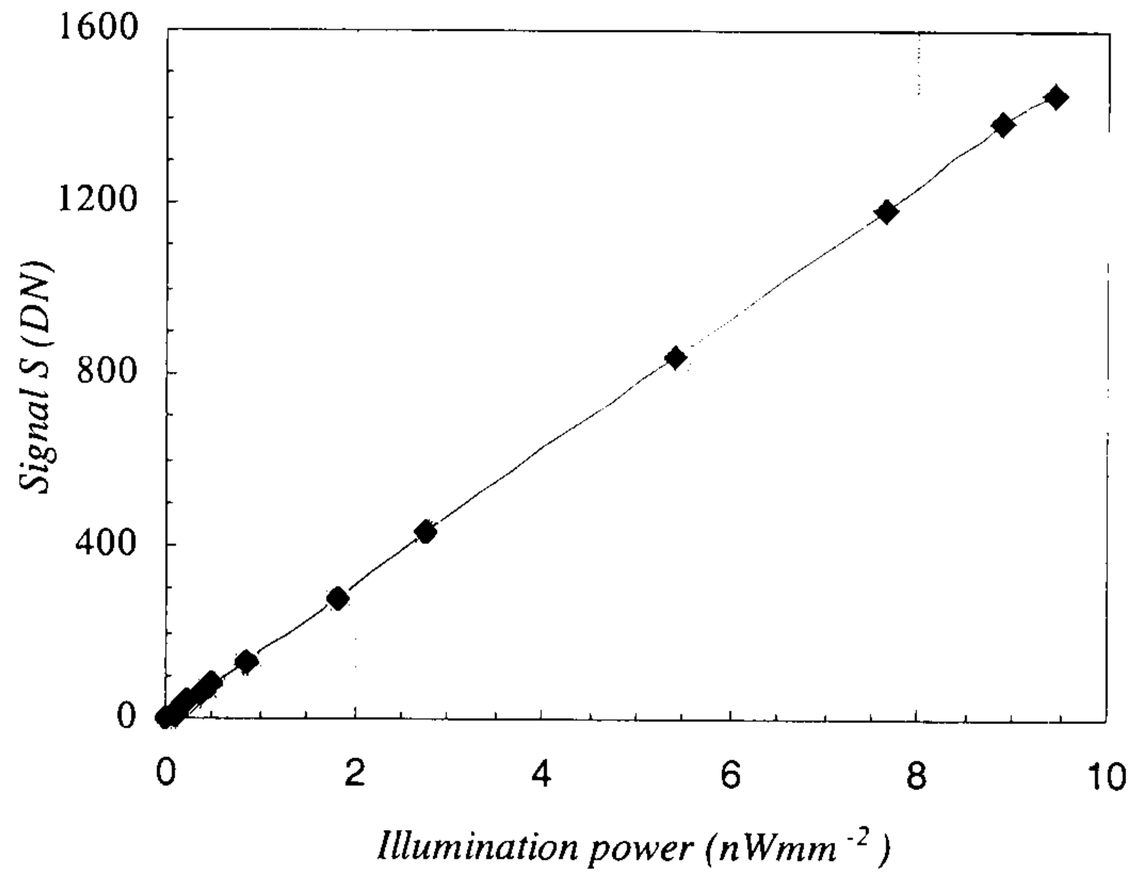

Figure 3.5. *Detector linearity is illustrated in this plot of digital signal versus incident irradiance for CCD65-01. The line has a slope of 155 ± 2.0. The error bars shown indicate the measured fluctuation in illumination intensity.*

The conversion constant *C*, was determined using the mean variance technique described by above. For each level of illumination intensity the mean variance of the corrected image was found using Scion Image Software (Scion Corporation). The measured variance was divided by 2 to correct for the increase in noise resulting from the correction process. Figure 3.6 shows a plot of variance versus signal for CCD65-01. The same measurement was undertaken using the CCD65-02 device, however, it was unsuccessful due to the large levels of system noise in the device. The system noise was measured to be ~ 6.4 DN, almost three times the value of system noise measured in CCD65-01. As a result, measured noise was constant over the full range of input intensities for the CCD65-02. This implies that at unity gain the read noise is the dominant source of noise, even at high signal levels. Consequently, the system is not quantum limited and the calibration could not be made using the mean variance technique. The increased level of system noise is discussed later in section 3.4.2.

The line shown in figure 3.6 is obtained from linear regression analysis of the measured data for the CCD65-01. Using equation 3.7 the regression analysis of the data gives the

total conversion constant $C = 0.0039\ DNe^{-1} \pm 2\%$. As illumination increases a gradual departure from linearity is observed in figure 3.6. This is due to saturation of the image section where there is a decrease in noise as the number of signal electrons approaches the pixel full well capacity.

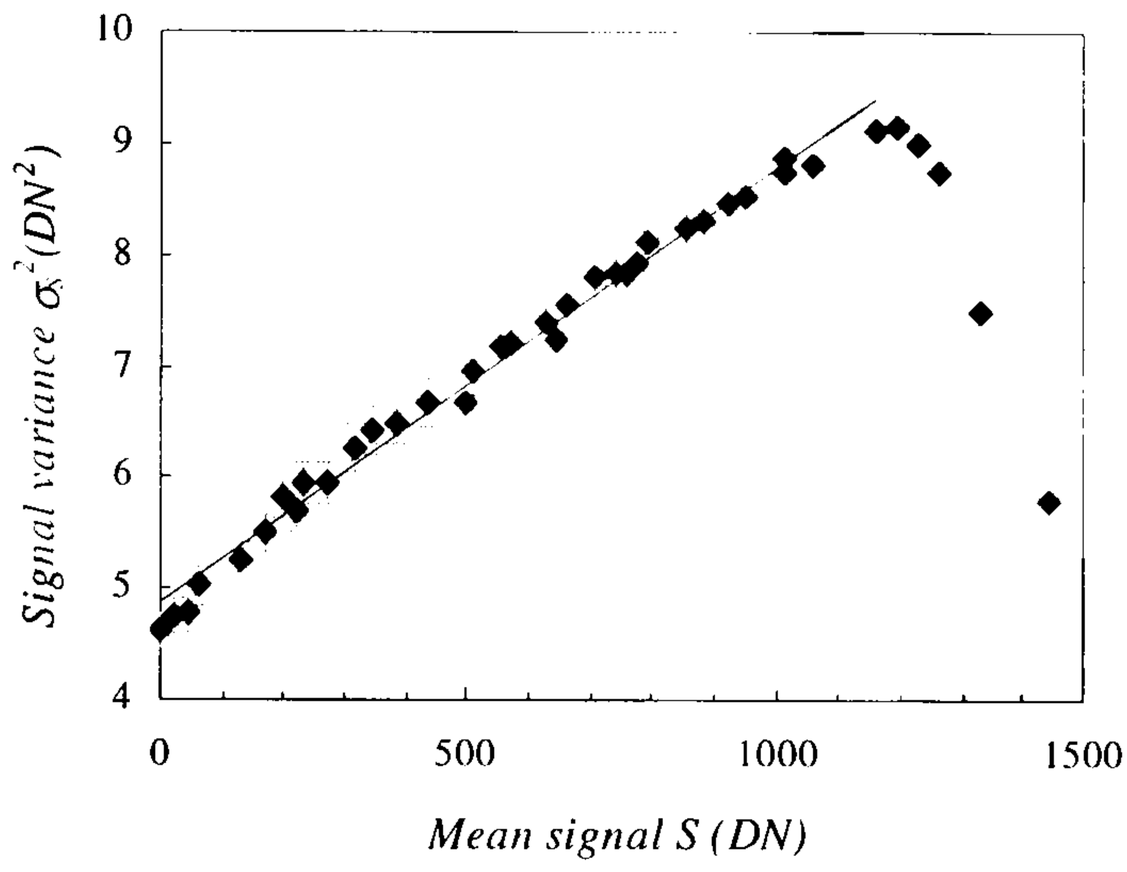

Figure 3.6. *Mean-variance plots obtained CCD65-01. The total conversion constant of the device was determined from the linear regression analysis of the measured data.*

A measure of the precision of the value for C, can be obtained from the saturation signal. The saturation signal, measured in digital numbers, can be converted to electrons using C and compared to the full well capacity of the device measured by the manufacturer. The saturation signal in digital numbers was measured for the CCD65-01 and CCD65-02, both with and without gain. Using a lens, an image of a piece of illuminated graph paper was focused onto the front of the CCD65-01. To measure the saturation signal without gain the illumination level was increased until the lines on the paper were no longer visible. To measure the saturation signal with gain, the gain was increased until the lines on the paper were no longer visible. This is the technique employed by the manufacturer to measure the full well capacity.

The x-ray phosphor prevents an optical image being formed on the CCD65-02, therefore to measure the saturation signal without gain the light from a tungsten lamp was focussed onto the CCD. The aperture of the lens was then adjusted to increase the light intensity until just before the image began to bloom. To measure the saturation signal with gain the lamp was then used to illuminate the whole of the CCD such that

artefacts within the phosphor were visible. The gain was increased until the artefacts became blurred. In each case a digital image was acquired and the saturation signal in digital numbers was found. The full well capacities in electrons of both the image and gain registers of the CCDs were calculated using the conversion factor. To cross check the measured values, they are compared with those supplied by the manufacturer in table 3.1. The saturation values in digital numbers were repeatedly measured and the standard deviation was found to be 4%. Combining this with the error in C, the measured saturation values are precise to within 4.4%. The quoted precision on the manufacturers values is ± 10,000 electrons.

Table 3.1. *Full well capacity data for CCD65-01 and CCD65-02 image and gain register sections. Measured values have been determined using the conversion constant C.*

Device	CCD65-01	CCD65-02
Image/store section (measured)	320,000 ± 20, 000	241,000 ± 15,000
Image/store section (E2V)	302,000	217,000
Gain register (measured)	537,600 ± 32,000	510, 00 ± 30,000
Gain register (E2V)	525,000	520,000

3.2.2 Summary of the calibration results

The CCD65-01 device was found to have a linear response to optical illumination for the range of illumination intensities measured. The conversion factor C has been measured for CCD65-01 and was found, from a linear regression analysis to be C = 0.0039 DNe^{-1} ± 2%. This corresponds to 256 ± 5 photoelectrons per digital number. The conversion factor was measured at unity gain. The number of photoelectrons generated per digital number with gain can be found using:

$$N_i = S / MC \tag{3.8}$$

The value of C has been used to calculate the full well capacity of both devices. Full well capacities measured for the CCD65-01 compare well with those measured by the manufacturer, indicating that the precision of C is 4.4 %. A value of C could not be measured for CCD65-02 because it was found that the system was not quantum limited at unity gain. However, using the value of C obtained for the CCD65-01, the measured

capacities for CCD65-02 image section and gain register compare fairly well with the manufactures values. Table 3.1 shows that the discrepancy between the manufacturers value and the measured value of full well capacity for the image section of the CCD65-02 device is 16%. This is the largest difference between the data sets.

3.3 Gain characterisation

The CCD65 gain mechanism is described in section 2.3.2. The CCD65 gain has been firstly calibrated in terms of the R$\varnothing_2$HV clock amplitude and then measured in order to ascertain what gain levels are achievable. The variation of the gain as a function of temperature has been measured with the aim of evaluating gain stability. The CCD65 will be used to image a variety of input signals, therefore gain linearity has been measured to assess the CCD65 response to varying levels of input signal.

CCD65 gain was determined from measurements of the digital output at unity gain and with gain averaged across the entire image for a constant input. The main requirement for these measurements was a constant input signal. Light emitting diodes (LEDs) provide a convenient and stable source of illumination. A temperature compensation circuit was used to minimise any possible variation in illumination intensity due to fluctuations in temperature. The circuit includes a voltage regulator to keep the LED power supply constant. The output illumination intensity of a multi-LED lamp (peak emission at λ = 630nm, Radio Spares, T1 ¾ Midget groove) was measured as a function of time using a digital light meter calibrated at 633nm. Over a period of 5 hours the illumination intensity remained stable within ± 0.5%. The time for the LED to stabilise was less than 5 minutes. The illumination intensity of the LED could be altered using a variable resistor incorporated in the LED temperature compensation circuit. To obtain a uniform light field across the face of the CCD, the LED was situated behind a diffuse scatterer at a distance of 50 cm from the front of the sensor.

The L3CCD gain is controlled by a potentiometer. Adjusting the voltage across the potentiometer changes the RØHV2 clock amplitude. Voltage across the potentiometer (V_M) can be varied between 0V and 5V. V_M was measured across two output pins

situated on the rear of the camera chassis. The CCD temperature was stabilised, then V_M was increased in increments of ~ 0.2V. A set of dark images was obtained at each voltage setting and the average dark signal as a function of gain found. The measurement was then repeated under constant uniform illumination using the LED light source described above. V_M was measured using a digital voltmeter with an accuracy of 2 decimal places. Measurements were performed to assess the precision with which the gain could be set using the voltmeter reading. V_M was set to 2.5V and 10 readings of the average digital output (averaged over the entire image) were obtained. V_M was set to zero and then back to 2.50V and a further 10 readings were taken. This procedure was repeated 10 times. The average digital output was measured for five values of V_M: 0, 2.50, 3.34, 3.75 and 3.89 volts. The average digital output was found each time the voltage was set and the standard deviation of the ten average signals was calculated. The standard deviation was found to be 0.5%, 0.5%, 0.71%, 1.75% and 2.1% of the signal output for V_M equal to 0, 2.50, 3.34, 3.75 and 3.89 volts respectively. The maximum uncertainty in the measurement of gain M was therefore equal to $\sqrt{2.1^2 + 0.5^2} = 2.16\,\%$.

3.3.1 Gain calibration

The total gain was calibrated for both devices. The CCD65-01 was calibrated at operating temperatures of 15°C and 41°C and the CCD65-02 device was calibrated at -7 °C. The CCD65 total gain M, at voltage setting V_M can be calculated from

$$M_{V_M} = \frac{\overline{S}(V_M) - \overline{S}_d(V_M)}{\overline{S}(0) - \overline{S}_d(0)} \tag{3.9}$$

where $\overline{S}$ is the average digital signal with the camera illuminated and $\overline{S}_d$ is the average digital signal for the dark field. The R$\varnothing_2$HV clock amplitude (volts) is related to the V_M by (E2V Technologies Ltd, 2002)

$$R\varnothing_2HV = 8V_M + 20 \tag{3.10}$$

Figure 3.7 *(a)* shows a plot of the measured total gain determined from equation 3.9 as function of R$\varnothing_2$HV clock amplitude for the CCD65 at –7°C, 15°C and 41°C. From equation 3.10, the clock amplitude of R$\varnothing_2$HV for normal mode operation is 20V. As R$\varnothing_2$HV is increased above 20V, the measured gain remains close to unity until a voltage of 35V, 44V and 46V was reached for the device at –7°C, 15°C and 41°C respectively.

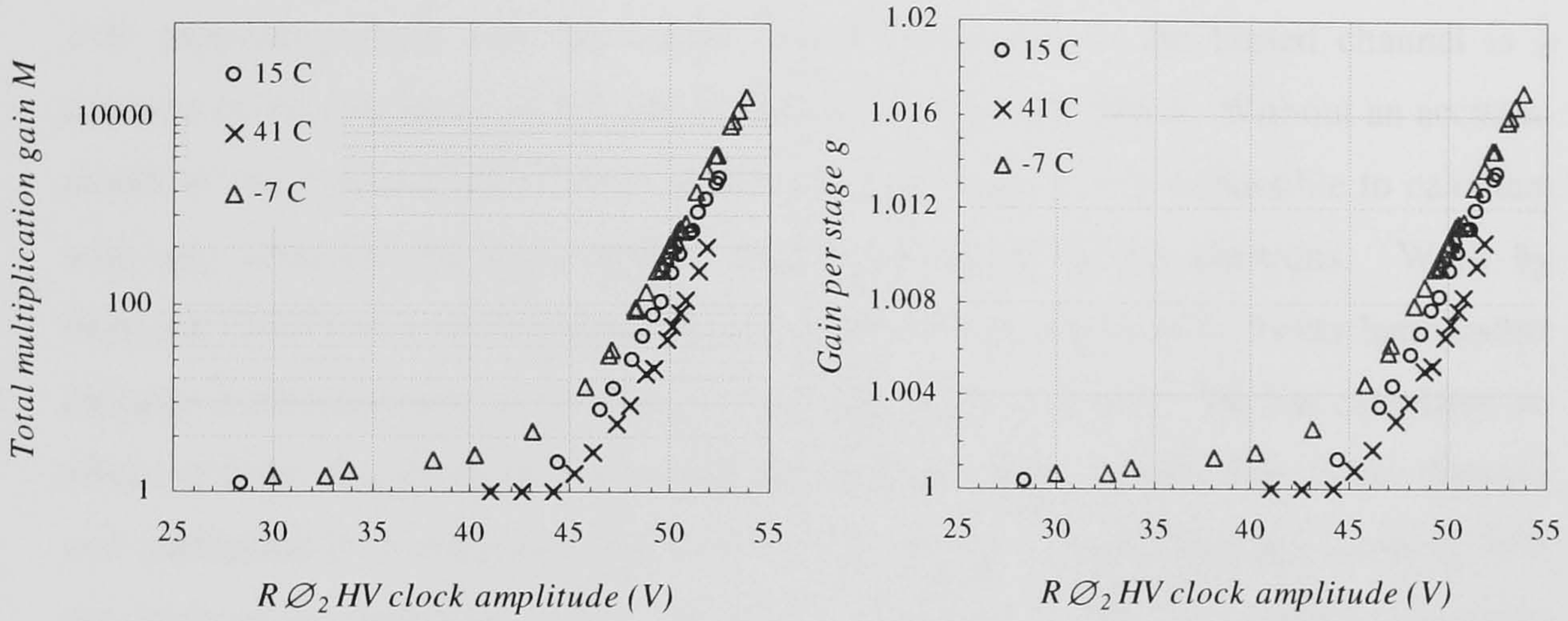

Figure 3.7. *Gain calibration at –7 °C, 15 °C and 41 °C. (a) The total gain as a function of R$\varnothing_2$HV. (b) The gain per stage as a function of R$\varnothing_2$HV. The total gain of the CCD65 gain register is related to the gain per stage g, by $M = g^n$ where n is 591.*

The highest value of gain that can be measured is restricted by the measurement technique and the presence of thermally generated dark current. If the input signal is high then the camera quickly saturates at low values of gain. To measure high gain the input signal has to be small enough such that the device will not saturate. At very high gains the thermally generated dark signal is amplified and makes a significant contribution to the signal, promoting device saturation. The maximum gain measured at –7°C before the camera saturated was approximately 17,000. Assuming that all gain stages are equal, the total gain of the CCD65 gain register can be related to the gain per stage g by $M = g^n$ where n is the number of stages. The number of stages is equal to the number of active horizontal pixels: 591 stages. Figure 3.7*(b)* shows the gain per stage as a function of R$\varnothing_2$HV. The gain per stage increases linearly with R$\varnothing_2$HV above a temperature dependant threshold value.

3.3.1.1 *Theoretical analysis of the gain mechanism*

The gain characteristics can be directly related to the electron ionisation rate, α. The impact ionisation process has been described in detail in section 2.3.3 and can be described by equation 2.20. Calculating the ionisation rate using equation 2.20 is complicated by the fact that the distribution of the electric field in the gain register is unknown. The effect of fringing fields has been discussed earlier in section 2.4.2. These act to make the potential distribution non-uniform. Also, field intensity varies with increasing depth into the silicon and the potential in the buried channel is a function of the properties of the silicon (Beynon and Lamb, 1980). Without an accurate model of the potential distribution within the gain register it is impossible to calculate with any accuracy the total electric field experienced by the electrons. Work by Hynećek (2001) on a similar prototype CCD device manufactured by Texas Instruments includes a measurement of the electric field dependence of gain. He has calculated an effective field, E_{eff}, given by the voltage applied divided by an effective carrier distance and multiplied by a reduction factor to account for the decrease in field intensity with the depth of the depletion region. Hynećek's experiments show the multiplication gain to have a linear dependency on the electric field.

A similar approximation of the electric field in the CCD65 gain register was made in section 2.3.3. The voltage applied is given by the difference between $R\varnothing_{dc}$ and $R\varnothing_2HV$. For the CCD65 at 15°C a threshold voltage of 44 V was measured and the maximum gain was measured at 54V. The distance between the $R\varnothing_{dc}$ and $R\varnothing_2HV$ electrodes, l, is 4 μm. Therefore we can assume an effective electric field variation of approximately 10.5 $V\mu m^{-1}$ to 13 $V\mu m^{-1}$.

A number of workers have measured the electron ionisation rate as a function of electric field for silicon at 300K. (Sze 1981, Maes *et al.*, 1990). However, only the data presented by Maes *et al.* (1990) includes measurements of α in fields of ~10 $V\mu m^{-1}$. Ershov and Ryzhii (1995) have derived values for parameters a and b for the Chynoweth expression (equation 2.20) (Chynoweth 1958) by fitting the model to results derived from Monte Carlo simulations: $a = 7 \times 10^5$ cm^{-1} and $b = 1.2 \times 10^6$ Vcm^{-1} for silicon at 288K (15°C). Using these values Ershov and Ryzhii have compared ionisation rates as a function of electric field with those derived from the data of Van

Overstraeten and De Man (1969) and found excellent agreement. Using a combination of equation 2.20, Ershov and Ryshii's values of parameters a and b and the value of electric field derived above a theoretical prediction of the ionisation rate in the gain register can be made. In order to compare this to the measured data obtained from the CCD65 it is necessary to derive a measured ionisation rate for the CCD65. The gain per stage g, can be defined as 1 plus the average number of electrons created per input electron over the distance which the input electron travels, l. Thus the CCD65 ionisation rate (μm^{-1}) can be calculated using:

$$\alpha_{CCD65} = (g-1)/l \tag{3.11}$$

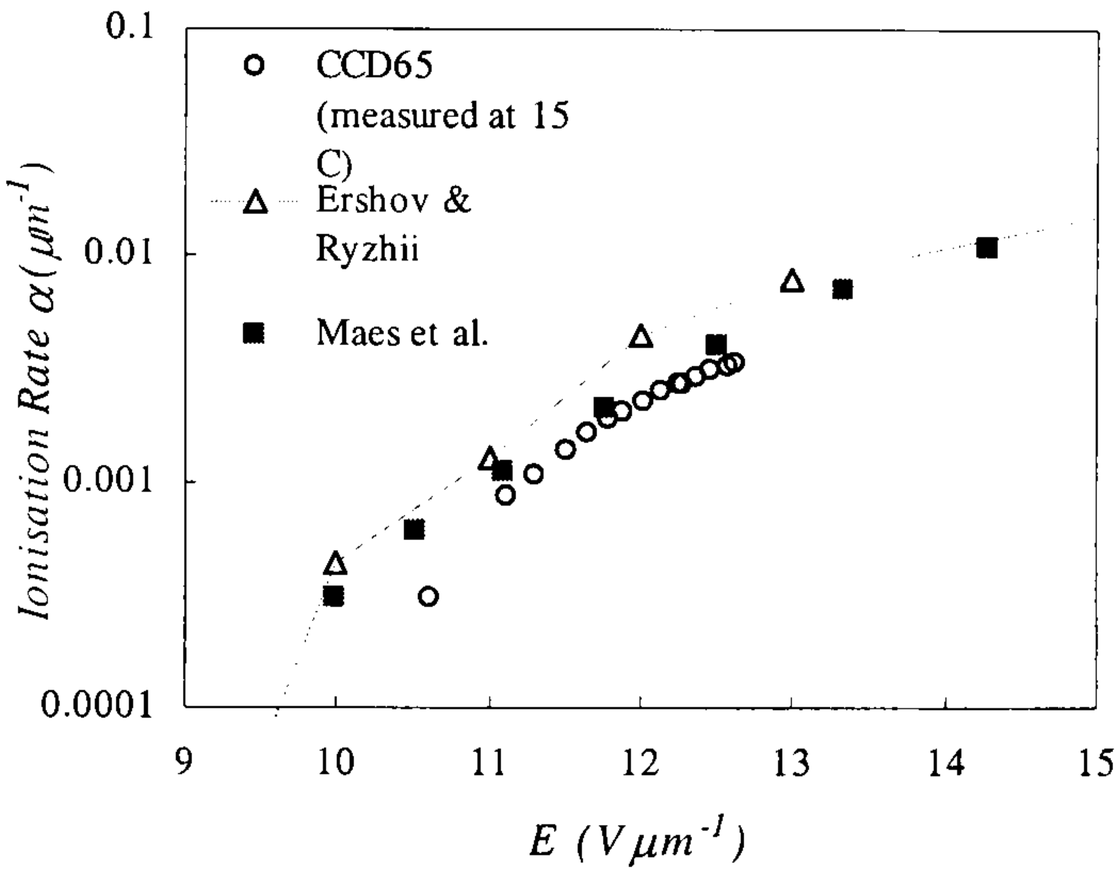

Figure 3.8. *Ionisation rate plotted as a function of inverse electric field. CCD65 ionisation rates are compared to theoretical data (Ershov and Ryzhii, 1995) and experimental data (Maes et al.*, 1990*).*

The CCD65 ionisation rate at 15°C has been plotted as a function of electric field in figure 3.8. It is compared to the theoretical prediction and the experimental data of Maes *et al.* (1990) recorded at 40°C. The variation of ionisation rate with electric field compares well with that measured by Maes *et al.* and the theoretical data calculated for the CCD65 using the analysis of Ershov and Ryzhii (1995). The uncertainty on the calculated values derived from measured data is equal to 2.16% (the error on the measured multiplication gain *M)* and is smaller than the symbol size in figure 3.8. Calculated values of the ionisation rate are up to a factor of 4 lower than those calculated using equation 2.20 (Ershov and Rhyzii data). This indicates that the value of electric field estimated above is too high. Better agreement is observed between the

measured data and the data of Maes *et al.* (1990). This data was recorded at 40°C and the closer agreement is because ionisation rate decreases with temperature, as observed in figure 3.7 and as described in the next section.

3.3.2 Gain as a function of temperature

The temperature dependency of the CCD65 gain can be observed in figure 3.7. As the temperature decreases, the gain increases. To quantify the temperature dependence, gain was measured as a function of temperature. The experiment was conducted with $R\varnothing_2HV = 50V$. Using the above approximation this corresponds to an electric field of $R\varnothing_2HV(V)/l(\mu m) = 50/4 = 12V\mu m^{-1}$.

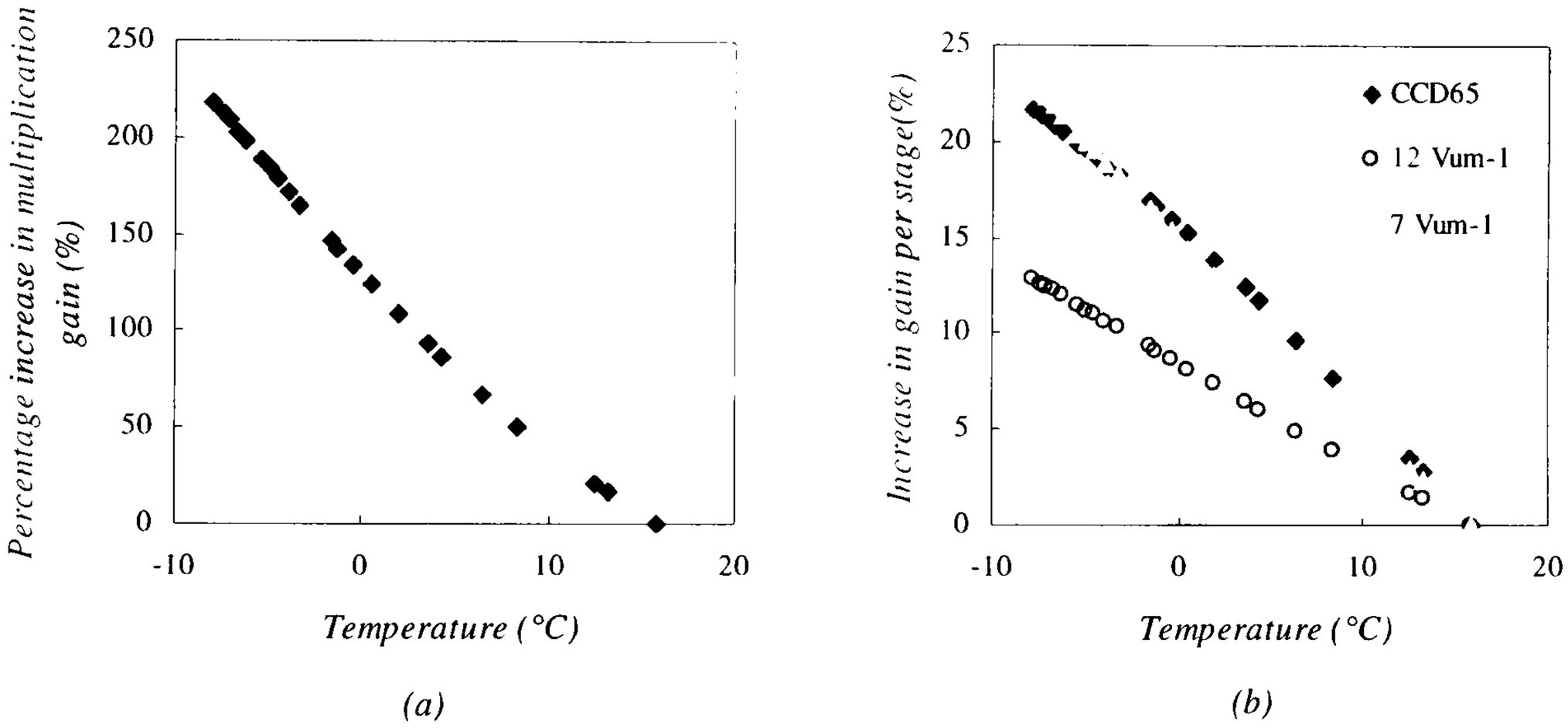

Figure 3.9. *(a) Measured temperature dependence of the total gain. (b) The percentage increase in gain per stage plotted as a function of temperature. Measured values are compared with theoretical values for $12V\mu m^{-1}$ and $7V\mu m^{-1}$.*

The percentage increase in gain is plotted as a function of temperature and is shown in figure 3.9*(a)*. The variation of gain is approximately linear between -8 and +8 °C. This variation with temperature indicates that care must be taken to stabilise camera temperature if the value of gain is to be kept constant. From a linear regression analysis of the data in figure 3.7 between -8 and +8°C, a variation of ± 1° C will result in a 10.6 % change in gain.

3.3.2.1 Theoretical analysis of the temperature dependence of gain

The mechanism of the temperature dependence of impact ionisation was discussed in section 2.3.4. Ershov and Ryzhii (1995) have derived an expression for the temperature dependence of the electron impact ionisation coefficient to be:

$$\alpha(\varepsilon,T) = p(T)\exp(-q(T)/\varepsilon) \tag{3.12}$$

where ε is the average electron energy, T is the temperature in Kelvin. Expressions for the temperature dependant parameters, $p(T)$ and $q(T)$ are derived from Monte Carlo models and are given by:

$$p(T) = p_o + p_1 T \tag{3.13}$$

$$q(T) = q_o \varepsilon_{th}(T) \tag{3.14}$$

where $p_o = 1.166 \times 10^6$ cm^{-1}, $p_1 = 1.227 \times 10^3$ cm^{-1}K^{-1}, $q_o = 4.644$ and $\varepsilon_{th}(T)$ is the threshold energy given by:

$$\varepsilon_{th}(T) = C_1 + C_2 T + C_3 T^2 \tag{3.15}$$

where $C_1 = 1.1785$ eV, $C_2 = -9.025 \times 10^{-5}$ eVK^{-1} and $C_3 = -3.05 \times 10^{-7}$ eVK^{-2}.

Using equations 3.12 to 3.15, the ionisation rate as a function of temperature has been calculated for an electric field of 12Vμm^{-1} and 7Vμm^{-1} where the average electron energy in silicon at 300K is 1eV and 0.25eV respectively (Ershov and Rhyzii, (1995). Theoretical values of the percentage increase in gain as a function of temperature are compared to measured values in figure 3.9*(b)*. Theoretical values for an electric field of 12Vμm^{-1} show less dependence on temperature compared with the measured values. The theoretical values derived for an electric field of 7Vμm^{-1} show good agreement with measured values. This suggests that the approximation of the electric field given in sections 3.3.1.1 and 2.3.3 is too high and agrees with the findings from variation of the ionisation rate with electric field shown in figure 3.8.

The difference in the two sets of theoretical data for the two electric field strengths can be explained by Baraff's theory (Sze, 1981). Baraff's theory states that the phonon interaction cross-section of an electron is inversely proportional to the electron energy. This implies that the lower the electron energy, the more likely it is that the electron will lose it's energy in a phonon interaction. Likewise, as the temperature decreases the mean free path increases, and the phonon interaction cross-section decreases. In high electric fields the electron will have more energy; it will undergo a smaller fraction of phonon interactions and therefore it will be less sensitive to any change in the magnitude of lattice vibrations, i.e. temperature.

3.3.3 Gain linearity

Gain non-linearities can lead to distortion of the radiographic image. For example, if the radiographic projection contains regions of high and low intensity and the non-linearity is such that low input signals are amplified more than high input signal, there will be a loss of image contrast. Thus it is important that gain is independent of the input signal level. CCD65 gain linearity with input signal was measured for medium gains (up to 200). The CCD65 was exposed to four input illumination intensities. This was achieved by placing a filter, comprising four optical densities, between the CCD and a uniform light source. An image was acquired at unity gain to find the input digital signal. A region of interest in the image was defined for each level of illumination and the average digital signal was found. $R\varnothing_2HV$ was increased and the gain in each region of interest was measured. The measurement for each region of interest was made using the same image, thus, any variation in gain with temperature and time will not affect the results, as all regions will be subject to an identical variation. Figure 3.10 shows the measured gain as a function of input signal. The values have been normalised to the measurements obtained for an input signal of 1.4 DN.

Gain is observed to have an input signal dependence that is more pronounced at very low gain. The electric field beneath the electrode is affected by the presence of the charge packet. The cloud of negative charge partially cancels out the positive gate potential. As the charge packet increases, this effect increases, and the magnitude of the

electric field decreases. Consequently, electrons are less likely to undergo impact ionisation. This effect may be more significant at low gain due to the weak electric field, which will be more sensitive to the increase in negative charge present.

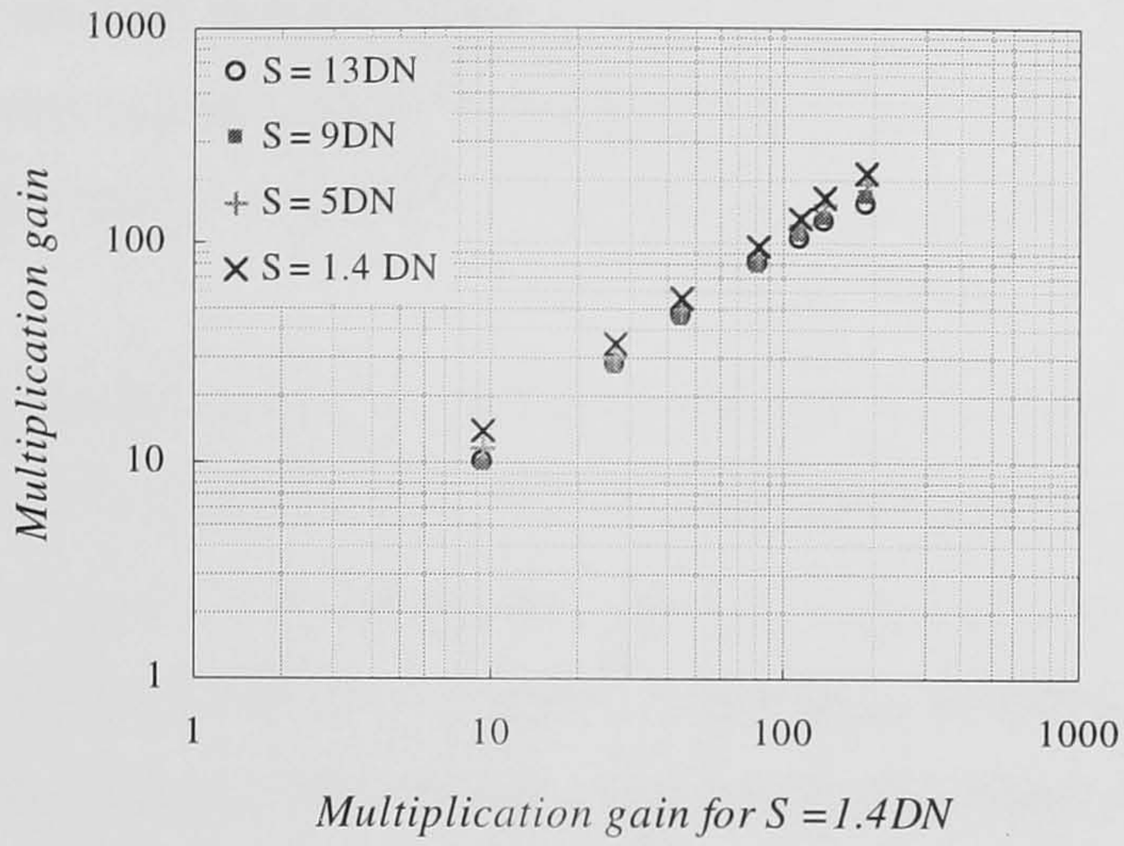

***Figure 3.10**. Measured multiplication gain for different input signals S compared to measured multiplication gain for S = 1.4DN. The gain is observed to be a function of input signal. The gain non-linearity is more pronounced at very low gain.*

As gain increases the signal dependence decreases until it reaches a approximately 2% decrease in gain for a 100% increase in signal. To illustrate the effect this will have in image quality the reduction in contrast can be calculated. If the radiographic projection has two regions of intensity, region A and region B, the contrast between them is given by:

$$Contrast = \frac{M_1 S_A - M_2 S_B}{M_1 S_A + M_2 S_B} \tag{3.16}$$

where S_A and S_B are the average digital signals in regions A and B respectively. If there were no signal dependence on gain, $M_1 = M_2$ and $S_A = 2S_B$, and equation 3.16 would yield a contrast of 33%. If, however, there is a reduction in gain of 2% for region A, $M_1 = 0.98M_2$, and the contrast will be reduced to 31.5%.

3.3.4 Conclusions about the gain mechanism of the CCD65

The gain has been calibrated as a function of $R\varnothing_2HV$ for the two CCD65 devices. The gain dependence on electric field closely follows that predicted from the experimental and theoretical ionisation rate data presented by other workers. Gains of up to 17,000 have been measured and are achieved by using many individual low gain stages. The gain performance of the L3 is compared with that of other devices later in section 3.7.1.

The gain has been measured as a function of temperature for $R\varnothing_2HV = 50V$. This data has been compared to data derived from an expression given by Ershov and Ryzhii (1995). This shows that the temperature variation of gain is also a function of electric field. At higher values of gain there is less temperature sensitivity. These results have shown that a constant temperature should be maintained in order that the signal level is proportional only to the input signal. For low gain (~200 at -7°C) the temperature should be kept stable within ± 0.5°C. This could easily be achieved using a temperature control unit that varies the current supplied to the Peltier cooler according to the sensor temperature. The temperature dependence of gain is common for all devices that employ electron multiplication. Consequently the implementation of temperature control is not uncommon and therefore does not represent any problems for the application of the L3 to diagnostic radiology.

Measurements of gain linearity have revealed that the gain is not independent of input signal. This type of gain non-linearity will reduce image contrast and reduce the useable dynamic range of the device. The reduction in gain is a function of input signal and gain. When imaging low contrast objects it maybe necessary to calibrate the gain response using a step wedge filter that covers the range of signal levels expected in the image. A simple correction may then be applied to the digital image.

3.4 Noise Measurements

The noise within a CCD imaging system has been described in detail in section 2.2. The main sources of noise are FPN, CCD system noise, thermal noise, charge transfer noise and input quantum noise. In an ideal CCD detector system all noise sources,

except the input quantum shot noise, would be eliminated. CCD sensitivity can be defined in terms of the minimum signal that the CCD imaging system is able to detect. Clearly, the minimum detectable signal (*MDS)* is strongly dependant on the noise levels in the CCD. Thus an evaluation of system sensitivity and signal-to-noise performance should include a complete measurement of the noise and its relationship with the gain. This section looks at the magnitude of these noise sources and how they are affected by the multiplication gain.

3.4.1 Fixed pattern noise

At high signal levels the total noise is dominated by fixed pattern noise (FPN). In addition to pixel-to-pixels variations within the CCD, FPN will be introduced by the fibre-optic and the phosphor layer. All fibre-optic faceplates have so-called 'chicken wire' artefacts that are a result of mismatching at multi-fibre boundaries within the faceplate. Variations in phosphor thickness and efficiency will also introduce FPN. Any particle contamination, such as dust trapped between the CCD and the phosphor layer, will introduce image artefacts. At high input signal and no gain the total image variance can be calculated using:

$$\sigma^2_{Total} = \sigma^2_{FPN} + \sigma^2_S + \sigma^2_{sys} \tag{3.17}$$

where σ^2_{FPN} is the FPN, including dark signal non-uniformities, σ^2_S is the input quantum variance and σ^2_{sys} is all the noise that arises from CCD operation. The noise due to the input quanta and that due to the CCD read out noise can be found by subtracting one image from another taken under the same conditions, and finding the standard deviation of the resulting image. *FPN* is then found by subtracting this noise from the total image noise.

Total image noise, CCD read noise and input quantum noise were measured for a range of input illumination levels. Figure 3.11 shows the variation in the measured standard deviation due to *FPN* as a function of the mean output signal.

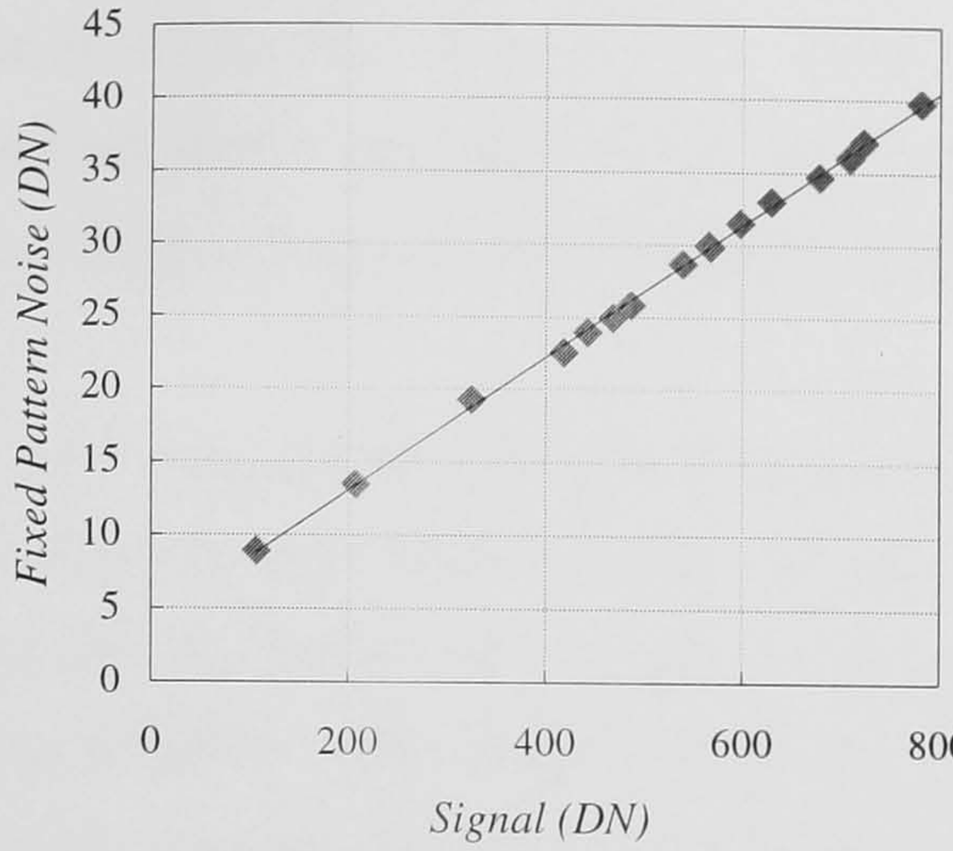

Figure 3.11. *Measured standard deviation due to FPN as a function of the mean output signal.*

The linear increase of *FPN* with signal confirms that the simple algorithm given in section 3.1.7 can effectively eliminate *FPN*.

3.4.2 CCD system noise

At low signal levels the predominant noise source is the CCD system noise. CCD system noise originates from a large number of sources, all of which are discussed in section 2.2.3.

The number of transfers that a charge packet in the central pixel of the image area will undergo in the CCD65 is 3589; 144×2 vertical transfers in the two phase image section, 296×2 vertical transfers in the store section, 296×3 horizontal transfers in the read out register and 591×3 + 16×3 corner transfers in the gain register (see figure 2.8). The charge transfer inefficiency is in the region of 1×10^{-5} (E2V Technologies Ltd, 2002). Charge transfer noise σ_{trans} for the thermal current calculated using equation 2.14 is 0.11 e^- r.m.s at 15 °C and 0.1 e^- r.m.s at –7 °C. A separate contribution for noise due to spurious noise is not included because there is no information on the magnitude of spurious noise in the CCD65 to date. However it is believed to be included in the dark noise measurement given in figure 2.13. The measured value of σ_{therm} is 2 e^- r.m.s. at 15 °C and 0.7 e^- r.m.s. at –7 °C.

In section 3.2.2 we have seen that the maximum output signal is 2100 DN, corresponding to a value of ~11 for N_{bits}. Thus, σ_{dig} = 77 electrons. The predicted reset noise, σ_{reset}, using correlated double sampling is 35 e^- r.m.s and the output amplifier noise, σ_{amp} =100 e^- r.m.s. (Marconi Applied Technologies Ltd, 2002(a)).

Background electronic noise σ_{EMI}, can arise from external electrical sources. The CCD pre-amplifier is very susceptible to external electrical interference. Additional noise may arise from the fan and the Peltier cooler, both of which are situated in close proximity to the CCD pre-amplifier. Measuring the total CCD read out noise with and without the electric fan was measured, an increase of ~ 0.5 DN was observed. For this reason, any measurements of noise were performed without the fan operational.

In section 3.2.1 the mean variance technique was described and the image variance, as a function of the mean output signal, was presented in figure 3.6. The intersection on the variance ordinate gives σ_{sys} = 2.2 DN for the CCD65-01. This corresponds to 566 ± 34 e^- r.m.s equivalent noise. The total CCD system noise calculated from equation 2.17 gives a predicted read noise of 172 e^- r.m.s not including the unknown contribution from external electronic sources. The measured values of σ^2_{sys} are three times higher than those calculated from the nominal values of the individual noise components (see section 3.2.1). The high value of noise is most likely due to background electronic noise and an underestimation of the noise due to the various electronic components within the prototype L3 camera. CCD65-02 read noise is 6.4 DN. This is most likely due to a fault with an electronic component within the L3 camera that arose when the header boards were changed to accommodate the new sensor and Peltier pack. An investigation of the fault is being undertaken by the manufacturers.

3.4.3 CCD system noise as a function of gain

Only the noise sources that are present before the gain register will be amplified. Thus the CCD system noise with gain M is given by:

$$\sigma_{sys} = \sqrt{M^2(\sigma^2_{therm} + \sigma^2_{trans}) + \sigma^2_{reset} + \sigma^2_{dig} + \sigma^2_{amp} + \sigma^2_{EMI}} \qquad (3.18)$$

or simply

$$\sigma_{sys} = \sqrt{M^2\sigma_{pre}^2 + \sigma_{post}^2} \tag{3.19}$$

where σ^2_{pre} is the image variance due to noise sources present before the gain register and σ^2_{post} is the image variance due to noise sources introduced after the gain register. The variation in the standard deviation of a series of dark field images was measured in both CCD65s at various levels of gain. The temperature was kept stable at 19°C ± 0.5°C and –7°C ± 0.1°C for CCD65-01 and CCD65-02 respectively. The CCD system noise is plotted as functions of gain and gain per stage in figure 3.12. The dark noise was observed to remain stable until a gain of approximately 200 was applied to the CCD65-01 and 2000 to the CCD65-02 respectively. From the above discussion of CCD system noise it is seen that at low gain thermal noise and transfer noise contributions are insignificant compared to the other noise sources. As gain increases the thermal noise and transfer noise, which are both amplified by the gain, start to become significant. The noise continues to increase with gain as the thermal noise and transfer noise are amplified. The dotted lines in figures 3.12 *(a)* and *(c)* are calculated from equation 3.18 and use the values of noise quoted in section 3.4.2. The plots represent the theoretical prediction of the gain dependence of system noise. At very high gain the measured data show an exponential dependence on gain which is contradictory to the linear relationship predicted using equation 3.18. This is due to spurious noise in the gain register. Despite the gain register being operated in non-IMO mode the contribution to spurious noise from the gain register has been measured by E2V Technologies Ltd and found to be approximately 30% of the total spurious noise measured (E2V Technologies Ltd, 2002). The non-linear behaviour is explained by the exponential dependence of spurious charge on clock magnitude (Janesick *et al.*, 2002), i.e. $R\varnothing_2HV$. The spurious noise contribution to the total system noise becomes apparent at gains of greater than M ≈1000 and M ≈10,000, for CCD65-01 and CCD65-02, respectively.

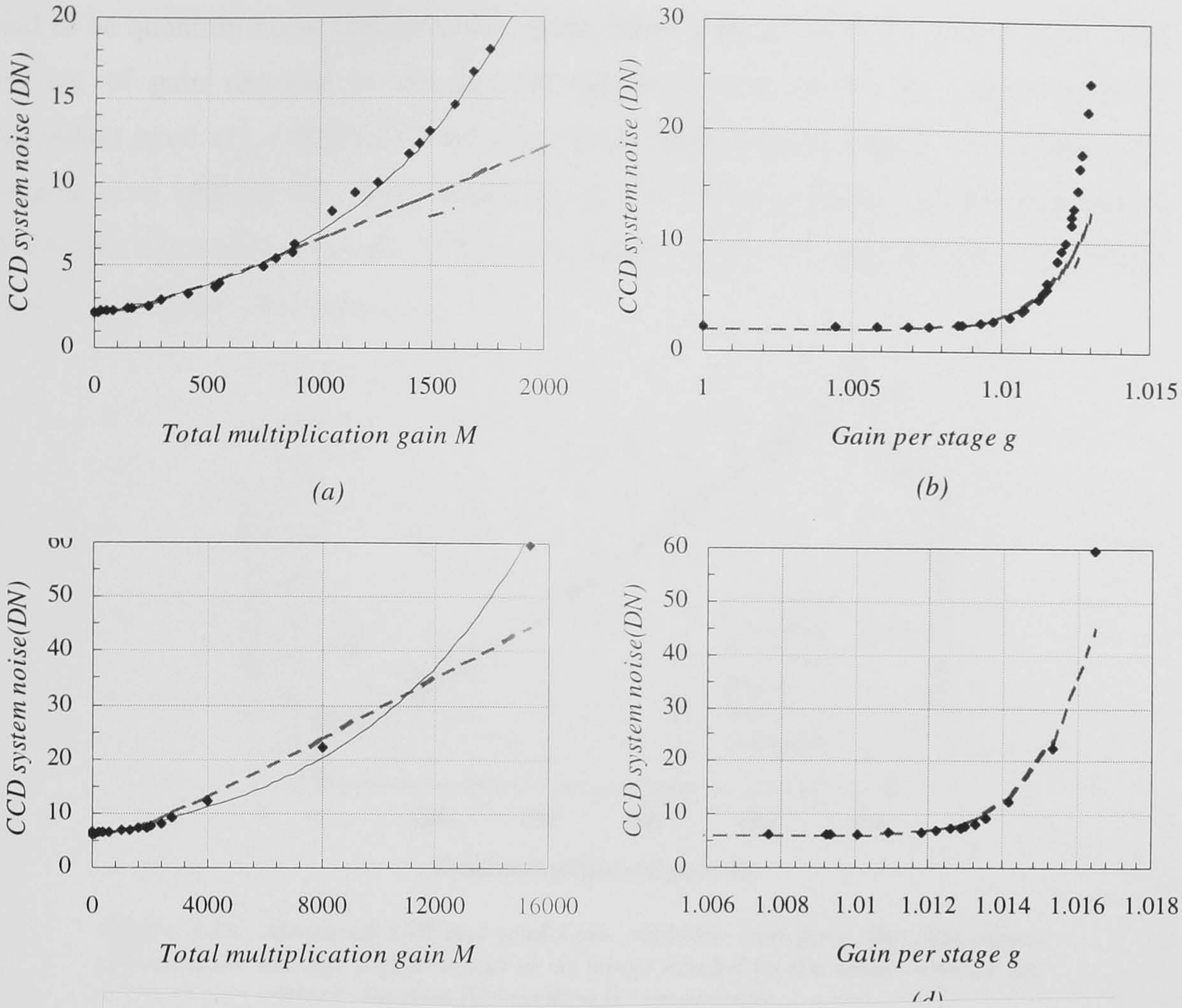

Figure 3.12 *Total CCD system noise as a function of total multiplication gain and gain per stage (a) and (b) for CCD-65-01 and (c) and (d) for CCD65-02*

The high levels of spurious current will limit the *SNR* at high gain and as a result limits the range of useful gain.

3.4.4 Signal to noise ratio as a function of gain

So far we have not considered the noise that is associated with the input quanta. The total output noise is given by (assuming that *FPN* has been removed):

$$\sigma_{Total} = M\sqrt{\sigma_{sys}^2 + \sigma_S^2} \tag{3.20}$$

In an ideal detector system the signal to noise ratio is limited only by the input quantum noise, i.e. $\sigma_{sys}^2 < \sigma_S^2$. It has been observed that quantum limited imaging is not possible with the CCD65-02 without multiplication gain (section 3.2.1). This is a result of the fact that even at high signal levels, $\sigma_{sys}^2 \approx \sigma_S^2$. Most radiographic imaging systems are

said to be quantum noise limited if the signal noise is larger than the system noise. The amount of gain required to amplify the quantum noise above the system noise is dependant upon σ_{sys}^2. If the CCD65 is to find an application in digital radiography, it is necessary to identify the input signal levels for which quantum limited imaging is attainable. Or more practically, if the CCD system noise no longer places a lower limit on the input signal, what does?

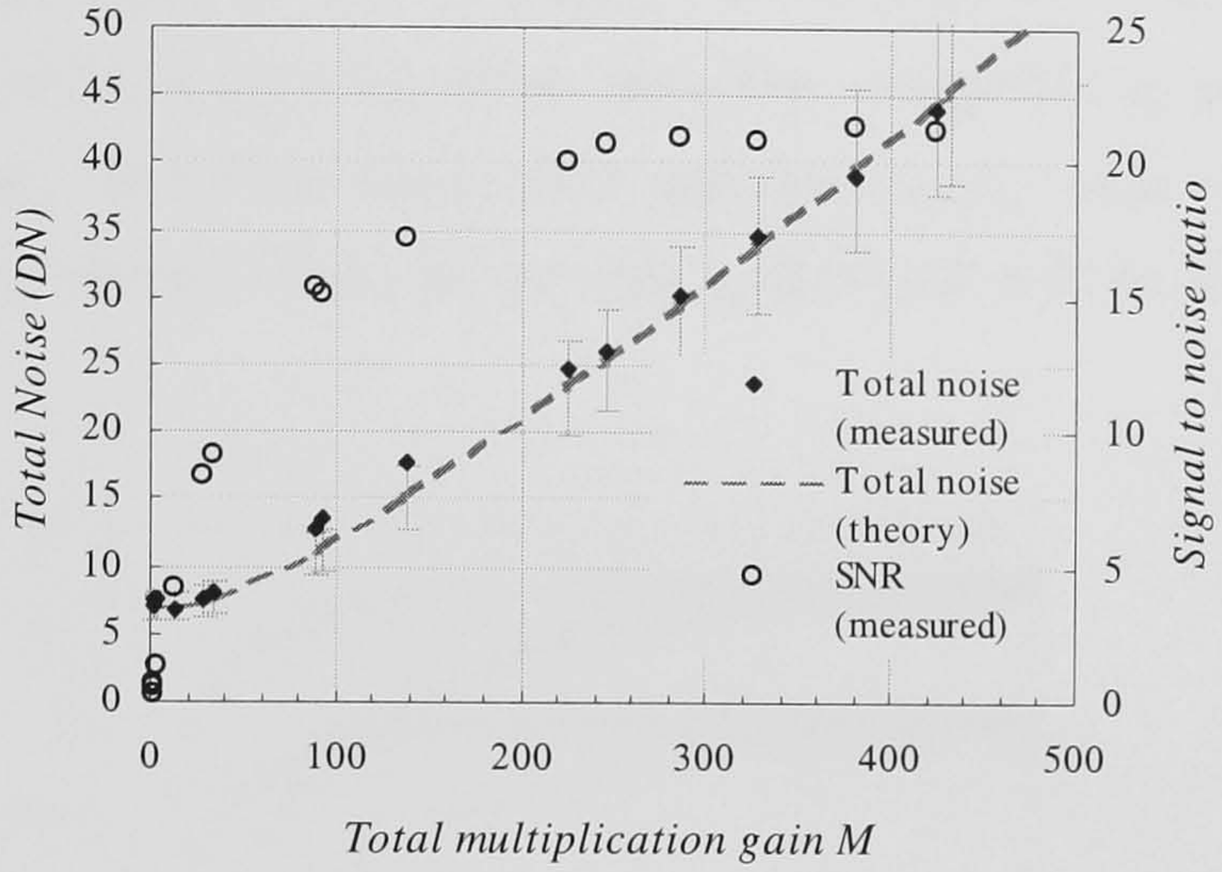

Figure 3.13. *Measured SNR and total noise variation with gain. The data points represent the average digital signal in an image divided by the mean variance for different gain settings. Incident illumination is kept constant.*

The total output noise and the average digital signal were determined as function of gain for an input signal of 2.0 DN ± 0.2 DN for CCD65-02. Figure 3.13 shows the total output noise as a function of gain. Assuming the signal is Poisson distributed, ($S = \sigma_S^2$). A theoretical prediction of total output noise for gains below 2000 (where read noise is the dominant noise source) is given by:

$$\sigma_S^2 = MCS + \sigma_{sys}^2 \tag{3.21}$$

The error bars on the theoretical data represent the error on the measured signal input and the calibration factor *C*. The signal to noise ratio is plotted on the secondary axis. Here the signal to noise ratio (*SNR*) is simply defined as the output signal divided by the total output signal noise. The *SNR* is observed to initially increase with gain as the signal is amplified above the dark noise and then reaches a constant value when the input quanta shot noise is the dominant noise source. Further application of gain

provides no benefit. Thus, at a gain of 250 the imaging system is quantum limited despite the high read noise for an input signal of 512 ± 51.2 electrons.

3.4.5 Calculation of limiting SNR

Clearly, if the input signal is low, more gain will be required to facilitate quantum limited imaging. At lower input signals the noise that is amplified by the gain register, becomes important. The input signal noise and the pre-gain noise sources will be amplified by equal amounts, thus, the pre-gain system *SNR* will be the highest *SNR* attainable.

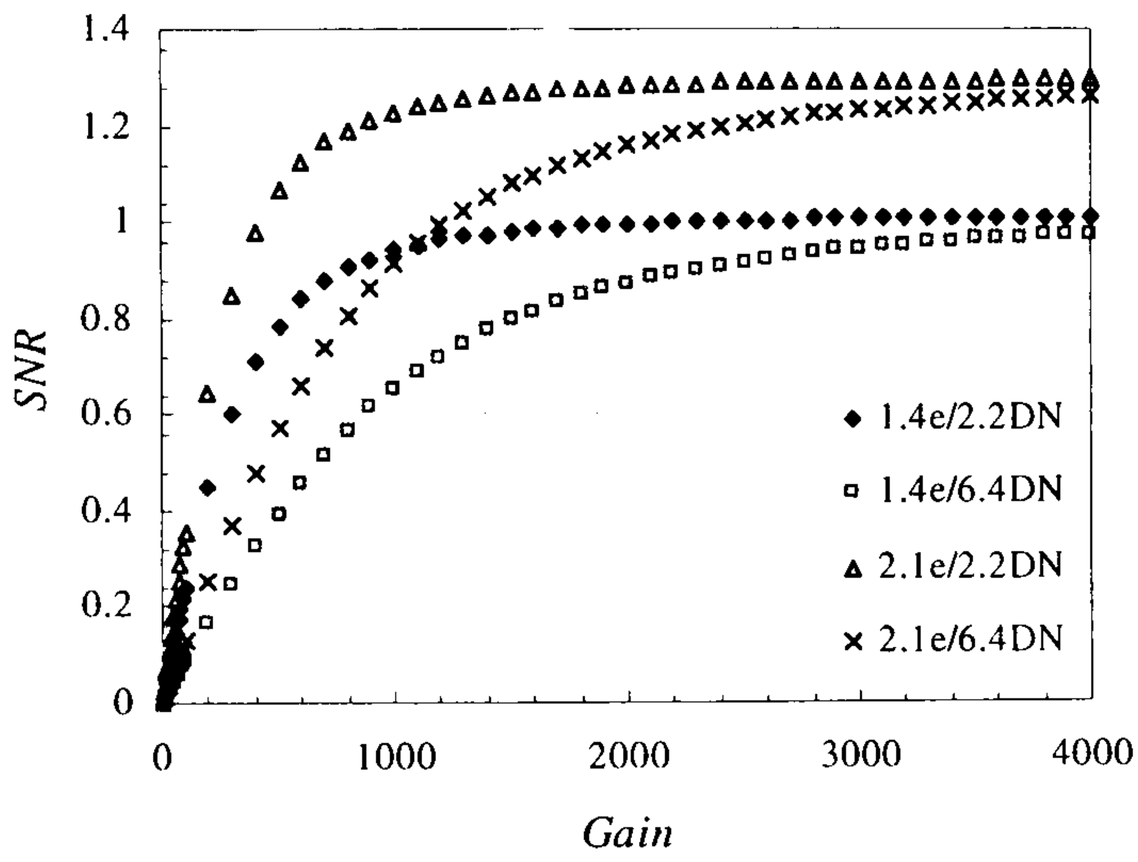

Figure 3.14. *Theoretical plots of SNR versus gain as a function of input signal and system noise. The level of gain required to reach the SNR limit is a function of the read noise.*

Figure 3.14 shows theoretical plots of *SNR* as a function of gain for a CCD65 device at –7 ° C with system noise equal to 2.2 DN and 6.4 DN. The *SNR* is plotted for input signals of 2.1 electrons and 1.4 electrons, which are equal to three and two times the dark noise (see figure 2.13) respectively. The *SNR* is very small (<<1) at low gain where the CCD65 is system noise dominated. As the gain is increased the *SNR* reaches the *SNR* limit, which is given by:

$$SNR_{\lim} = \frac{S_{N_i}}{\sqrt{\sigma_{pre}^2 + \sigma_{N_i}^2}} \tag{3.22}$$

assuming that the excess noise factor is unity. Thus, for the example of the 1.4 electron input $S_{N_i} = 1.4$, $\sigma^2_{therm} = 0.7^2$, $\sigma^2_{trans} = 0.3^2$ and $\sigma^2_{N_i} = 1.18^2$, giving $SNR_{\lim} = 0.99$. The amount of gain required to reach $SNR_{\lim}$ is given by the magnitude of σ^2_{pre} relative to the entire system noise σ^2_{sys}. If we have two noise sources, $V_1 = x$ and $V_2 = 4x$, summed in quadrature then $V_T^2 = \sqrt{\left(x^2 + 16x^2\right)}$. Thus V_2 contributes to 94% of the total noise. Therefore we can say that if $\sigma_{pre} = 4\sigma_{sys}$ then σ_{pre} is the dominant noise. The gain required to amplify σ_{pre} to this level is given by:

$$M_{SNR_{\lim}} = \frac{4\sigma_{sys}}{\sqrt{\sigma^2_{pre} + \sigma^2_{N_i}}} \tag{3.23}$$

3.4.6 Calculation of the minimum detectable signal

It has been shown that the *SNR* is limited by the pre-gain noise (thermal, spurious and transfer) sources within the device as well as the shot noise upon the signal itself. To be able to calculate a *MDS* the problem should be approached from a different direction. Firstly it is necessary to decide what *SNR* is acceptable for signal detection. Classically, Rose defined the smallest acceptable *SNR* as the ratio of the mean signal in a given area divided by the standard deviation of a background region of the same area (Rose, 1948). This definition leads to the widely accepted notion that a *SNR* of between 3 to 5 is acceptable (Cunningham *et al.*, 2001).

In the case of the CCD65-01 the background noise in a non-irradiated pixel comprises 0.11 e^- transfer noise and 2 e^- thermal and spurious (see figure 2.13) noise giving σ_{bac} = 2.003 e^-. The smallest signal detectable in an adjacent pixel $MDS = 3 \times 2 = 6$ e^-. The $SNR_{\lim}$ for this signal is $6/\sqrt{(2.26^2 + 2^2 + 0.19^2)} = 6/3.02 = 1.99$ (where the third term in the bracket is the transfer noise for the dark current plus the signal). The maximum gain required is $M_{SNR} = (4 \times 2.2 \times C)/\ 3.02 = (4 \times 2.2 \times 256)/3.02 = 745$, where C is the conversion factor (see section 3.2).

For the CCD65-02, there is 0.1 e^- transfer noise and 0.7 e^- thermal and spurious noise which gives $\sigma_{bac} = 0.7$ e^-. $MDS = 2.1$ giving $SNR_{\text{lim}} = 2.1/\sqrt{(1.45^2 + 0.7^2 + 0.12^2)} = 1.31$ and $M_{SNR} = (4 \times 6.4 \times 256)/1.6 = 4096$.

Values of M_{SNR} for the CCD65-01 and CCD65-02 show that the gain levels required to detect the *MDS* are below the levels at which spurious charge becomes significant. The values of *MDS* in both devices are small, with the smallest being for the CCD65-02, which has the lowest thermal noise. These values are significant for x-ray work with phosphor screens. The low *MDS* indicates that single x-ray photons can be detected. On average a Gd_2O_2S:Eu phosphor screen emits 1800 light photons (E2V Technologies Ltd, 2002) for a typical diagnostic energy x-ray photon (50keV). Less than half will reach the detector. Providing there is 100% efficient optical coupling and a CCD *QE* of 0.25, 450 photoelectrons will be generated in the CCD per x-ray photon. These photoelectrons will be distributed over a number of CCD pixels; for a 160 μm phosphor layer this could be as much as 42 pixels (Yaffe and Rowlands, 1997); giving an average signal of 10.7 photoelectrons per pixel. This is greater than the MDS and therefore detectable. In comparison, conventional CCDs have ~100 electrons r.m.s. noise at MHz rates and 10 electrons r.m.s noise at kHz rates. Therefore a signal of 10.7 photoelectrons could not be detected by these devices.

3.4.7 CCD dark noise as a function of temperature

CCD system noise measurements were performed at $R\varnothing_2HV$ =53.9V (M = 15000 ± 3.2% at -7°C) between –7°C and 25°C for device CCD65-02. The uncertainty in the gain was found from the standard deviation of 50 repeated measurements. The system noise at zero gain was subtracted from each measurement to give the noise due to thermal, transfer and spurious noise sources only. The dark noise is plotted as a function of temperature in figure 3.15. This shows the dark noise increasing as the temperature decreases. If the thermal noise were the dominant noise source this behaviour would be unexpected as thermal noise decreases with temperature. This behaviour however can be attributed to the temperature dependence of gain and the

presence of spurious noise. The maximum uncertainty on the measured value of noise, was found from the standard deviation of 50 repeated measurements, to be 6.3%.

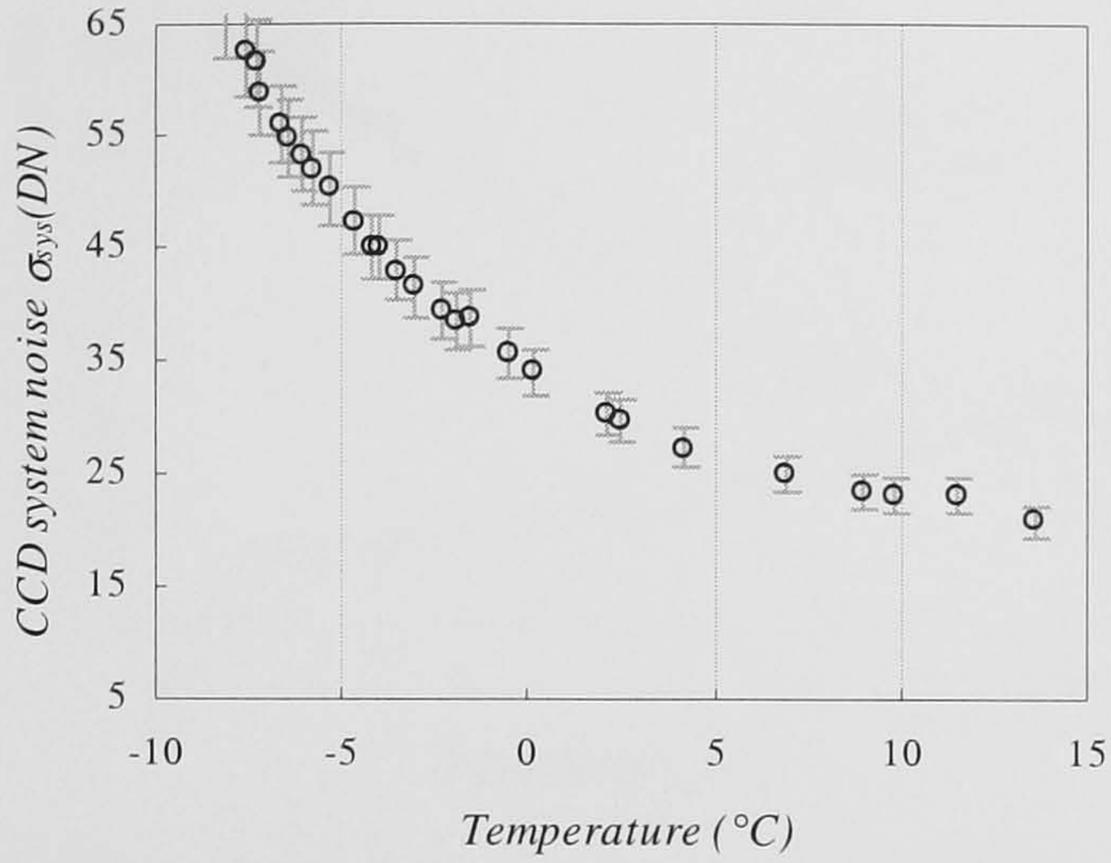

Figure 3.15. *System noise plotted as a function of temperature for CCD65-02 at* R$\varnothing_2$HV=53.9 V. *The error bars represent the largest standard deviation of repeated measurements.*

Figure 3.16 shows the percentage decrease in gain with temperature and the percentage increase in thermal noise and spurious noise with temperature (derived from the measured data given in figure 2.13 and given again in figure 3.17). This illustrates that gain is more sensitive to temperature than thermal and spurious noise.

In addition, the presence of spurious noise will also increase the noise as a function of temperature because not only will it be amplified by the increased gain but also because of the way in which spurious noise is generated (through impact ionisation) it will become a more significant noise source. This therefore explains the increase in system noise as the temperature was lowered.

In order to obtain a value of the CCD thermal and spurious noise it is necessary to derive it from the theoretical prediction of noise and measured data. From equations 3.19 and 3.20 the thermal noise can be found using:

$$\sigma_{therm}^2 + \sigma_{spur}^2 = \left[\frac{\sigma_m^2 - \sigma_{post}^2}{M^2} \right] - \sigma_{trans}^2 \qquad (3.24)$$

where σ_m^2 is the measured image variance corrected for *FPN*.

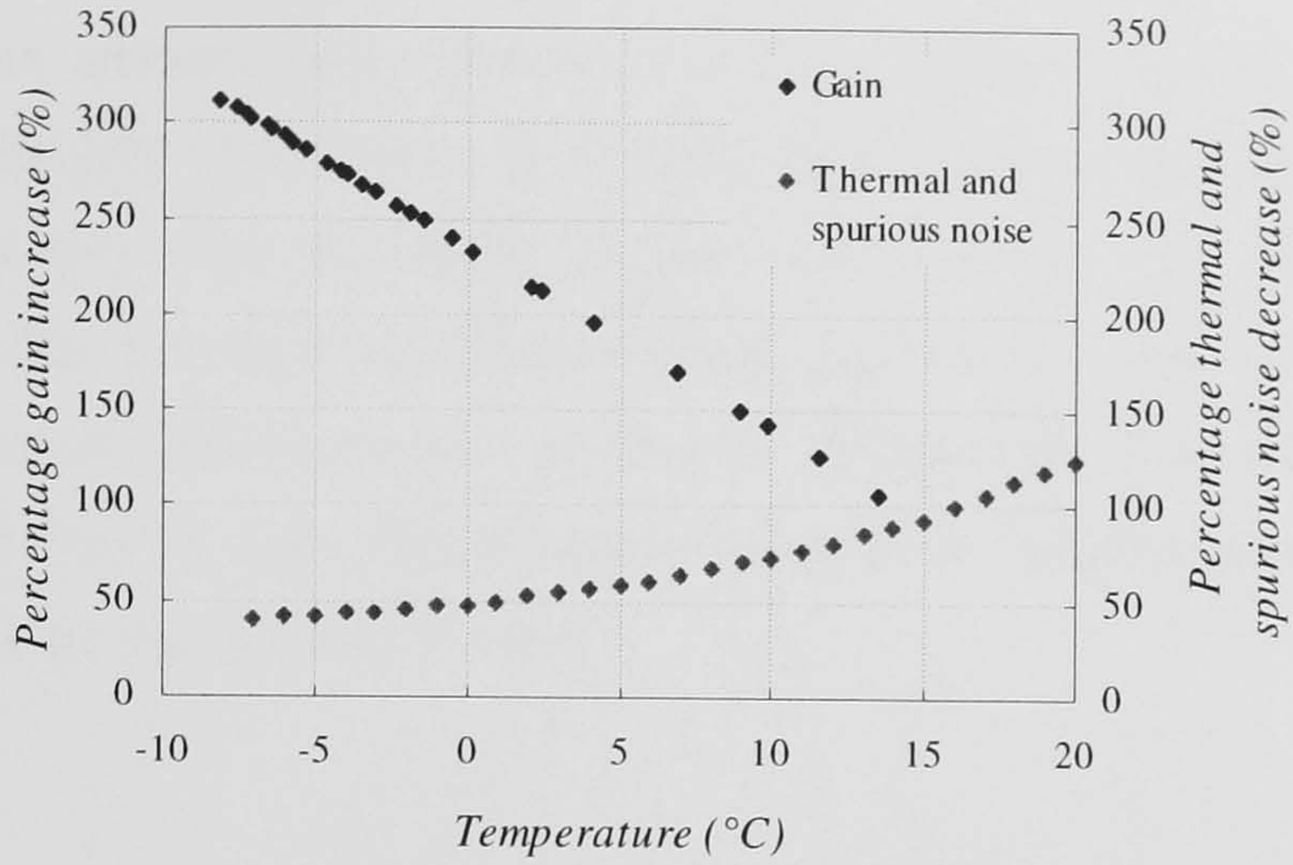

Figure 3.16. *The percentage increase in gain with decreasing temperature and the percentage decrease in thermal noise with decreasing temperature. This illustrates that the gain is more sensitive to changes in temperature.*

The thermal noise is plotted as a function of temperature and compared to the thermal noise measured by E2V Technologies Ltd. at unity gain in figure 3.17.

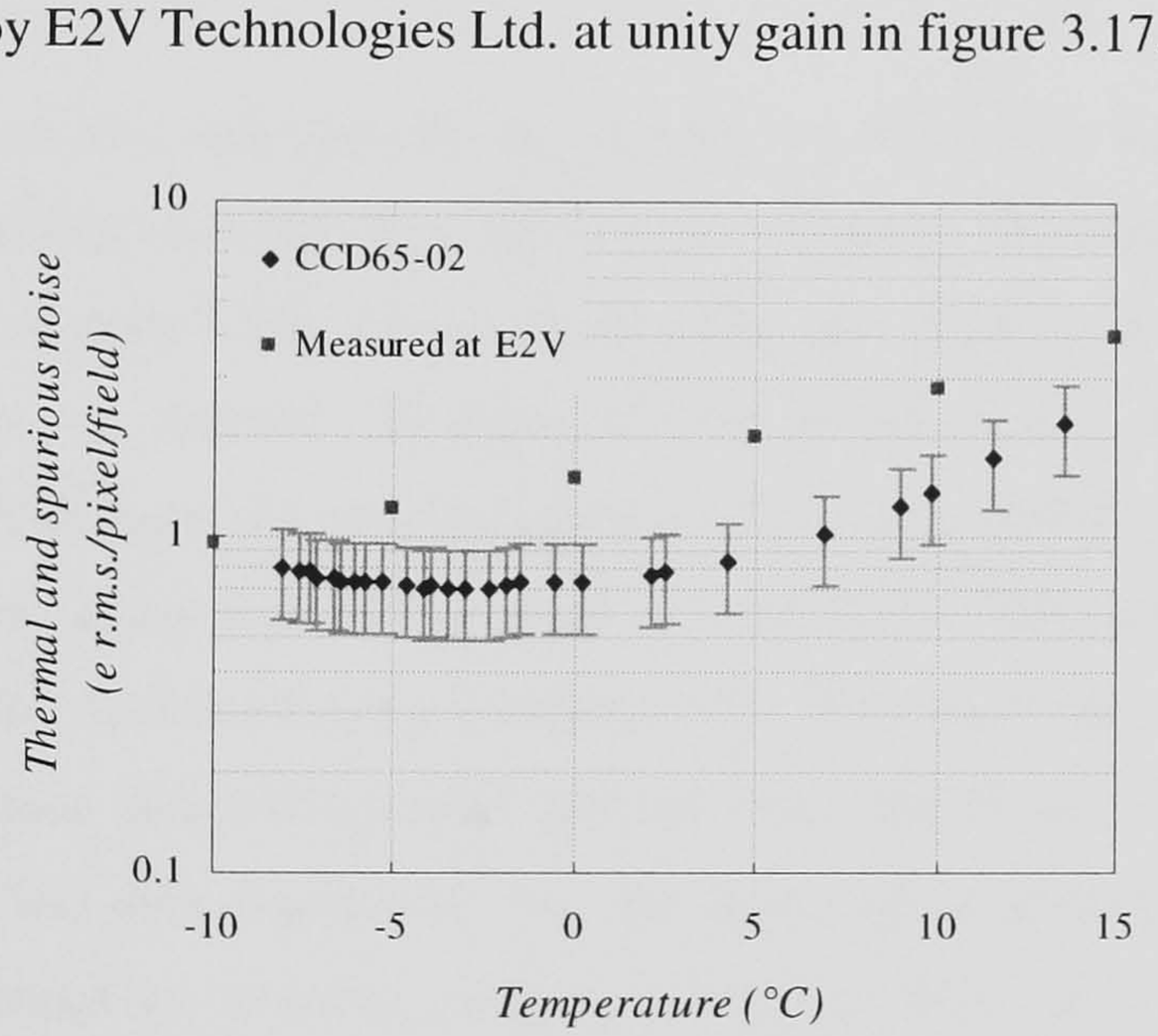

Figure 3.17. *Thermal noise and spurious noise as a function of temperature.*

Figure 3.17 shows a rise in the noise at very low temperatures corresponds to the presence of spurious noise. The uncertainty in the data was estimated from the uncertainty in the measured values of system noise and multiplication gain. The difference in the two data sets can be explained by the variations between devices, as

described in section 2.1.7. Clearly there is little benefit in cooling the device below -5°C (due the onset of spurious noise). A thorough investigation of the relative contributions from spurious and thermal noise as a function of gain is proposed. However, the individual contributions from the thermal and the spurious noise cannot be measured separately using the techniques described. The two noise sources may be separated using different clocking techniques that requires expertise not available at UCL. Also an accurate measurement of the thermal and spurious noise within a specific device without the use of gain requires special circuitry to measure the output signal current (typically a pico-amp meter is used).

3.4.8 Conclusions about CCD65 noise

Large levels of system noise have been recorded for both CCD65 devices. It is expected that this is due to large levels of electronic interference within the L3 camera used to drive the CCD65 sensor.

It has been shown that quantum limited imaging is achievable for low signal levels using multiplication gain, assuming a noise factor of unity. Measurements of the signal to noise ratio have shown that the minimum detectable signal is ultimately limited by the pre-gain noise, i.e. thermal and spurious noise, of the device. For any given input signal level the *SNR* limit is given by equation 3.22. This equation can also be used to find the minimum signal that will produce a given *SNR*. The gain required to reach SNR_{lim} can then be calculated using equation 3.23. This work has shown that CCD65-02 has a minimum detectable signal derived from the Rose criteria equal to 2.1 photoelectrons. The gain required to 'see' the *MDS* can be predicted from the system noise and the thermal and spurious currents. Using this criterion it has been shown that the gain required is less than the threshold gain for the onset of spurious noise and therefore, only the level of thermal noise limits detector performance. Theoretically, further cooling could reduce the thermal noise. However, the optimal operational temperature is –5° C, which is the temperature at which the CCD dark noise is lowest.

3.5 Excess noise factor

All of the noise sources that have been considered so far are found in conventional charge coupled devices. To investigate the gain dependence of the CCD noise floor the major sources of noise within the device have been considered and categorised into post- and pre- gain register noise. It has been found that with sufficient gain, post-gain noise sources become insignificant and the total noise is dominated by the signal noise or the thermal and spurious noise. Yet, it is expected that the gain register itself will introduce an additional source of noise that has been described in section 2.3.6. Accordingly, a full assessment of the *SNR* characteristics of the device would not be complete without a measurement of the excess noise factor.

The excess noise factor for an input with a variance $\sigma_{N_i}^2$ is given by (Hyneček, 2001):

$$F^2 = \frac{1}{M^2}\frac{\sigma_{N_o}^2}{\sigma_{N_i}^2} \tag{3.25}$$

Assuming that the input photoelectron signal N_i is Poisson distributed, i.e. $\sigma_{N_i}^2 = N_i$, the variance can be derived from the input signal. It is necessary to make this assumption (and it is not an unreasonable one) because the quantum shot noise is only measurable at high input signals (see section 3.2) where system noise is not the dominant source of noise. If actual measurements of shot noise were used, due to device saturation F could only be measured at low gain. Thus, the input variance can be found using:

$$\sigma_{N_i}^2 = \overline{S}_i C \tag{3.26}$$

where $\overline{S}_i$ is the average input at unity gain in digital numbers (corrected for dark and electrical offset) and C is the conversion factor for the CCD system measured in section 3.2. Values of $\sigma_{N_o}^2$ can be calculated from:

$$\sigma_{N_o}^2 = \sigma_S^2 - \sigma_{sys}^2 \tag{3.27}$$

where σ_S^2 is the measured variance in the output digital signal S in digital numbers and σ_{sys}^2 is the measured variance in the dark image in digital numbers (this will include all

of the noise sources discussed in section 3.4). From equations 3.25 to 3.27 the excess noise factor squared, measured as a function of gain, is given by

$$F_m^2(M) = \frac{\left(\sigma_S^2(M) - \sigma_d^2(M)\right)C^2}{\overline{S}_i C\left[\frac{\overline{S}(M)}{\overline{S}_i}\right]^2} \tag{3.28}$$

The term in the square bracket is equal to M, which can be calculated from the output signal. Therefore the multiplication gain is independently calculated for each output signal which ensures that gain non-linearity does not affect the calculation.

The excess noise factor has been measured as a function of gain with input signal as an additional parameter for the CCD65-01 device at 15°C. The image variance was found using individual pixels and care was taken not to saturate the image. Signal and variance values were measured by selecting eight individual image pixels across the image and acquiring 10,000 image frames. As each frame was acquired the digital value of the pixels was recorded. Pixel data were acquired for a dark field and a light field without gain and at increasing increments of gain for three values of $\overline{S}_i$. At each increment of gain the average signal was corrected for dark and offset and the signal variance was found. The excess noise factor was then calculated using equation 3.28.

Figure 3.18 *(a), (b)* and *(c)* show the variation of excess noise factor as a function of gain for input digital signal, $\overline{S}_i$ equal to 50 ± 0.2DN, 16.5 ± 0.2DN and 3.4 ± 0.4DN respectively. The excess noise factor was found to tend towards unity as gain was increased in all three case. The variation on the measured input signal was found by collecting 100 images and finding the standard deviation in the average input signal.

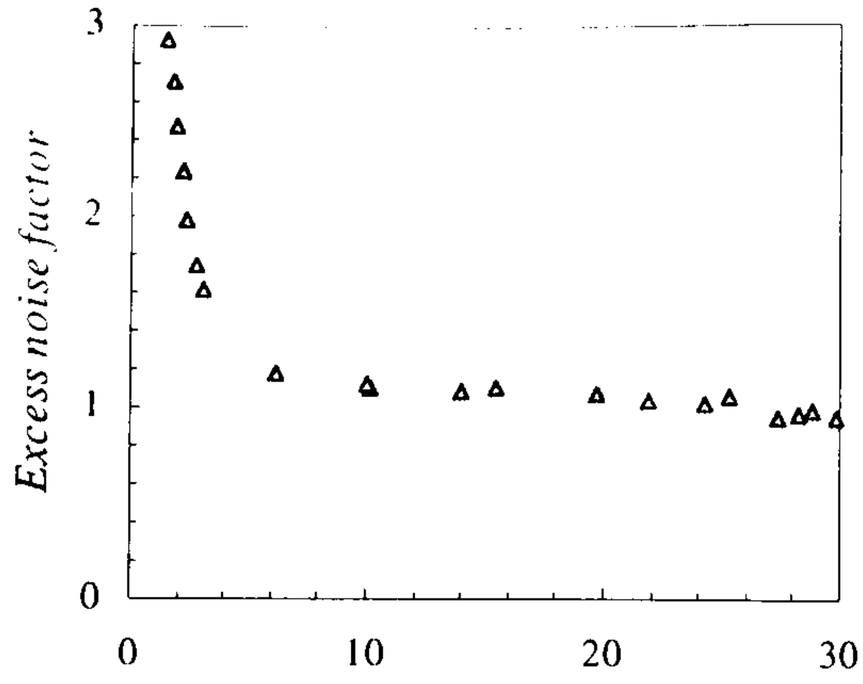

(a)

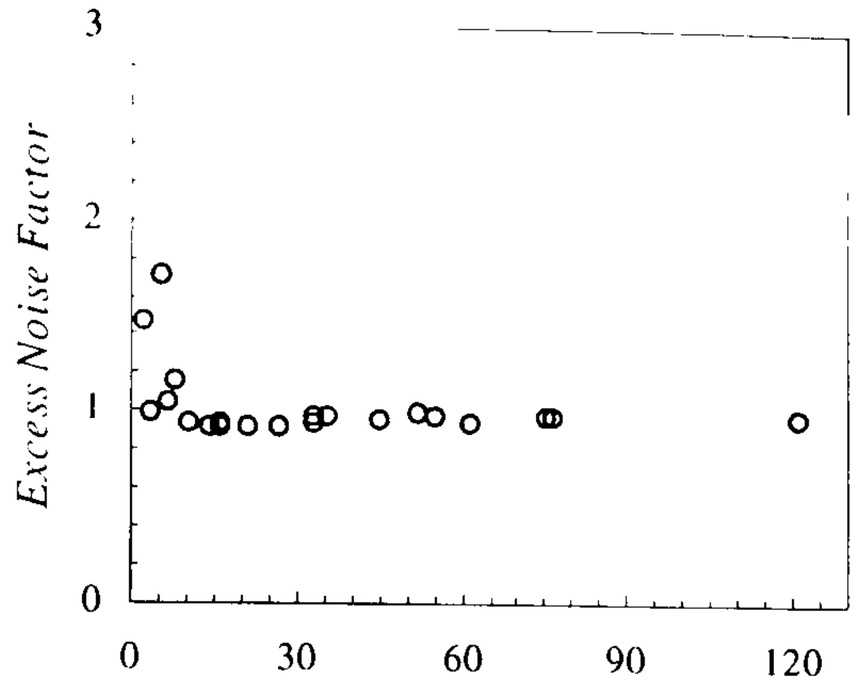

(b)

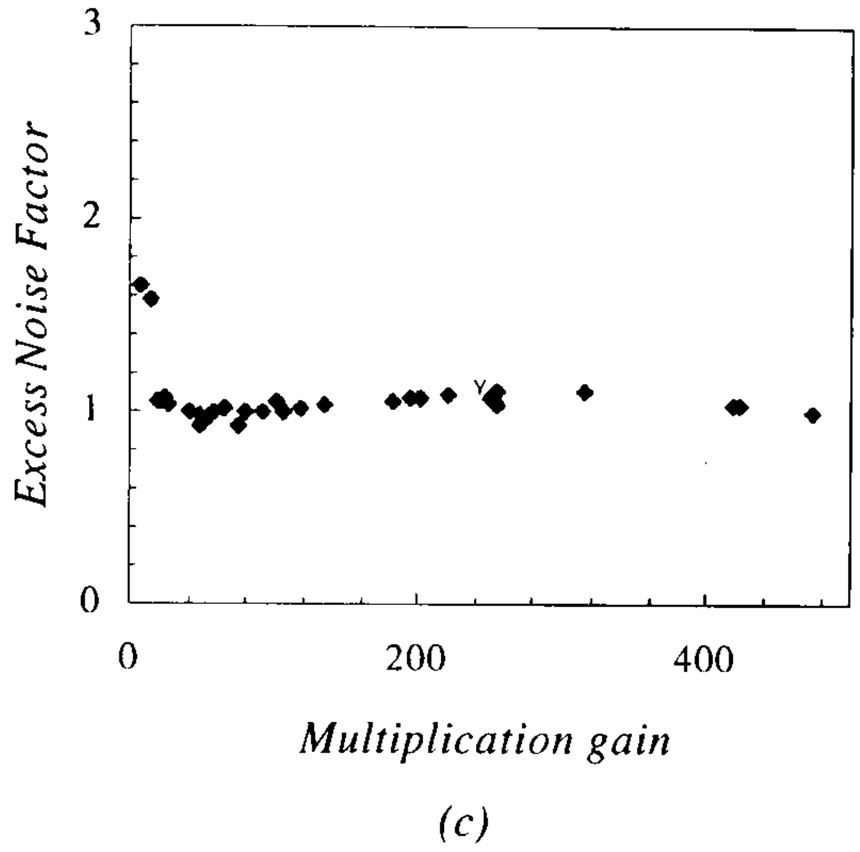

(c)

Figure 3.18. *The excess noise factor plotted as a function of gain, (a) S_i = 50 DN (b) S_i = 16.5 DN and (c) S_i = 3.4 DN. For all values of S_i the excess noise factor is measured to be close to unity and at higher gains (G>10) and is independent of gain.*

From equation 3.28, F is a function of C. The value of C used was estimated to be accurate within ± 6%. $\overline{S}_i$ was accurate to within 12%, 1.2% and 0.4 % for 3.4 DN, 16.5 DN and 50 DN respectively. Combining these errors with the error on the measured image noise and dark noise (~ 5% in each) the maximum error in the F is 14%. Therefore the possible range of values of F is between 1.0 to 1.16. The large noise factors at low gain are a result of the low signal levels, where the noise is dominated by the read noise of the device. This increases the measurement error.

Comparing these values with those predicted using the two statistical analyses described in section 2.3.4, are lower than those values predicted using Hyneček's (2001) analysis. This result can be compared with measurements made on another device analogous to the L3CCD. Noise-free avalanche multiplication has been predicted in silicon solid-state photo-multiplier tubes (SSPMTs) (Kim *et al.*, 1997). The SSPMT has a similar

gain mechanism to the staircase avalanche photodiode and thus the L3CCD register. Gain is achieved through impact ionisation of the shallow impurity levels that lie at energy levels only 54meV below the conduction band. Consequently the electric field required for electron multiplication is lower than that in a conventional avalanche photodiode for the same gain. Similar to the L3 gain register, single carrier multiplication is realised. Furthermore, due to the low electric field in the device the generated electron must be accelerated over a finite period, the distance travelled, the dead space is large in comparison to the multiplication width. This is the dead space effect observed in thin p-i-n diodes discussed earlier in section 2.4.1 (Plimmer *et al.*, 2001). The excess noise factor was measured by Kim *et al.* (1997) using two complementary methods, both techniques yielded a noise factor approaching unity that implies that the variance on the gain σ_g^2 must tend to zero.

The measurement of an excess noise factor of unity implies that there is almost noise free multiplication in the gain register. Accordingly, the use of gain will not reduce the SNR in the radiographic image. This result is important in terms of the application of the L3CCD to radiographic imaging because it means that quantum limited imaging is attainable.

3.6 Dynamic Range

The range of x-ray intensities within a radiographic projection varies according to the mass attenuation coefficients of the structures being imaged. For example a radiograph of the chest requires a detector with a large dynamic range in order that both the highly attenuating bone structure and the less attenuating air cavities are imaged successfully. Hence it is important to consider the dynamic range of the CCD65 imaging system when choosing a suitable imaging application. The dynamic range of a CCD is typically defined as the ratio of the peak signal to the system noise measured at the output. The peak signal levels in an image sensor are determined by the charge handling capabilities of the CCD. The charge handling capabilities are a function of the full well capacity and the charge capacity of any proceeding electronic circuitry, such as the read out node. When considering the potential of the CCD65 for imaging applications, such as

digital radiology, it is more useful to think of the dynamic range in terms of the input signal. The reproduction of x-ray image contrast depends on the minimum and maximum photon fluence that can be imaged by the detector. In terms of the input signal the dynamic range may be defined as the

$$DR = \frac{\text{saturation signal}}{\text{noise equivalent signal}} \tag{3.29}$$

To simplify this discussion it is assumed that one incident photon produces one photoelectron, which is then collected and stored in a CCD potential well. The saturation signal, in terms of the number of photons per pixel per frame, is then equal to the full well capacity of the CCD image pixel, measured in electrons.

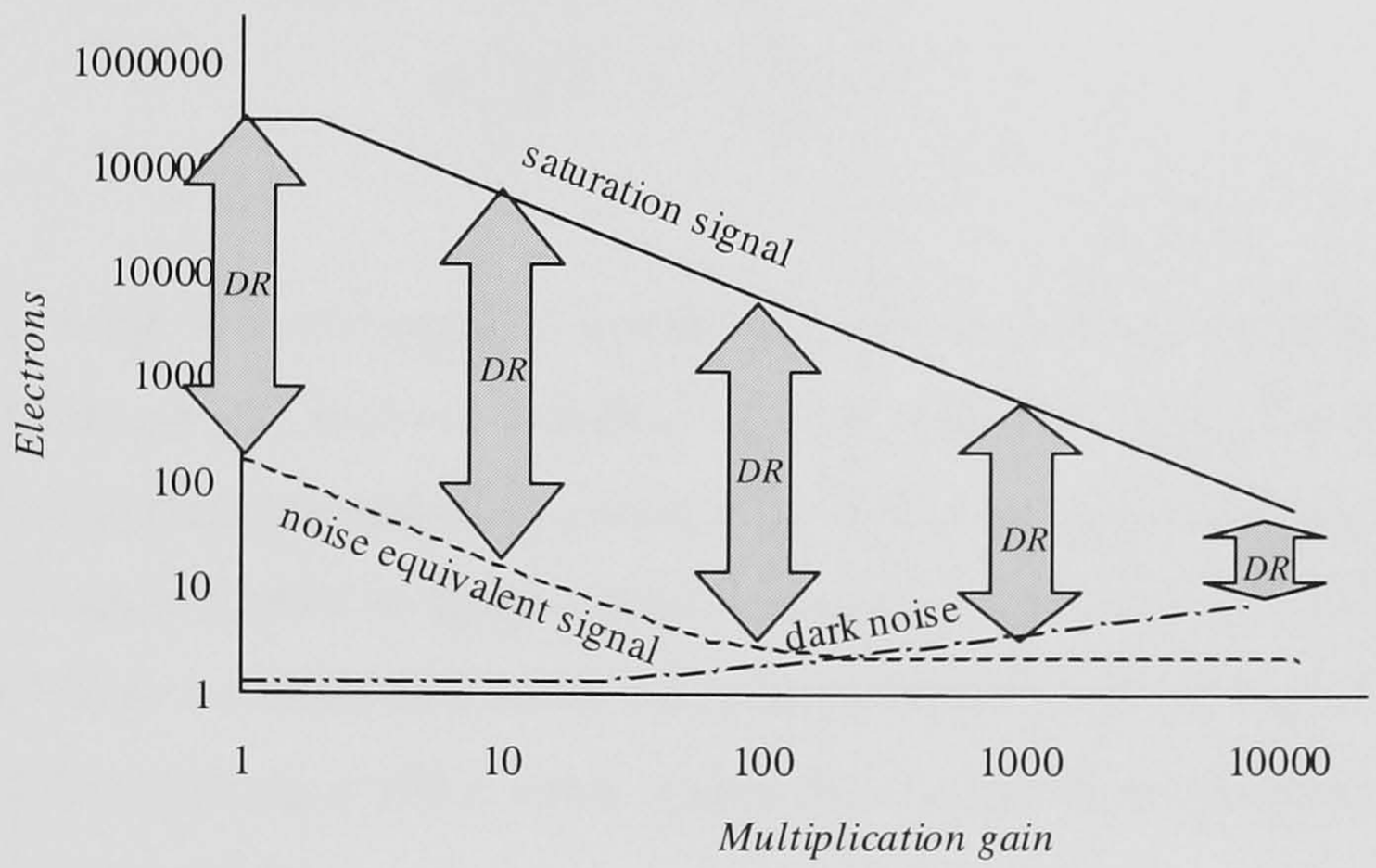

Figure 3.19. *Schematic of the variation of dynamic range with gain. As gain increases the signal required to saturate the device decreases and the dark noise increases. The noise equivalent signal initially decreases as less signal is required to match read noise due to the gain. The noise equivalent signal then reaches a constant value where the system noise is dominated by the thermal noise.*

The noise equivalent signal (*NES*) is the photon fluence that will produce a signal that is equal to the CCD noise. For normal mode operation the dynamic range is simply the image section full well capacity divided by the read noise. $DR = 320{,}000/512 = 625$, for the CCD65-01. In gain mode operation, the maximum signal output is equal to the full well capacity of the gain register.

Therefore we expect an increase in the dynamic range when changing from normal to gain mode. However, once gain is applied, the number of photons required to saturate the gain register is inversely proportional to the gain. When the CCD system read noise is the dominant noise source, the minimum detectable signal is inversely proportional to the gain. Accordingly, a reduction in *NES* is seen with increasing gain. Once sufficient gain is applied, the CCD system noise is equal to the dark noise. Since both input signal and thermal noise are subject to identical gain, the *NES* remains constant. The variation of saturation signal, dark noise and *NES* with gain is illustrated in figure 3.19.

Jerram *et al.* (2001) report that the dynamic range of the CCD65 can be calculated using:

$$DR = \frac{\left(N_{sat} - N_d\right)}{M\sqrt{\left(\sqrt{N_d}\right)^2 + \left(\frac{\sigma_{amp}}{M}\right)^2}} \tag{3.30}$$

where N_{sat} is the full well capacity measured in electrons, N_d is the dark signal in the device and σ_{amp} is the read out amplifier noise in electrons r.m.s.. The dynamic range has been found from the measured values of the full well capacity and CCD dark noise. Dynamic range is plotted in figure 3.20as a function of gain, for both CCD65 devices. The dotted lines are calculated using the manufacturers values of σ_{amp}, N_{sat} and N_d in equation 3.20 where σ_{ro} = 100 e^- r.m.s., values for N_{sat} and N_d are given in table 3.1 and figure 2.13 respectively.

The measured values of dynamic range are significantly lower than those predicted using the values quoted by the manufacturer. This discrepancy is due to the higher levels of read noise in both devices. The dynamic range of the CCD65-02 is greater than the dynamic range of CCD65-01 at higher gain because of the lower levels of thermal and spurious noise in the device.

Figure 3.20 indicates that in order to achieve adequate signal gain a compromise in the available dynamic range must be made. From the above discussion, the dynamic range can be increased by further cooling to reduce thermally generated current or by

extending the full well capacity of the gain register. However, due to spurious current, no reduction in thermal noise is afforded by cooling -5°C (see section 2.2).

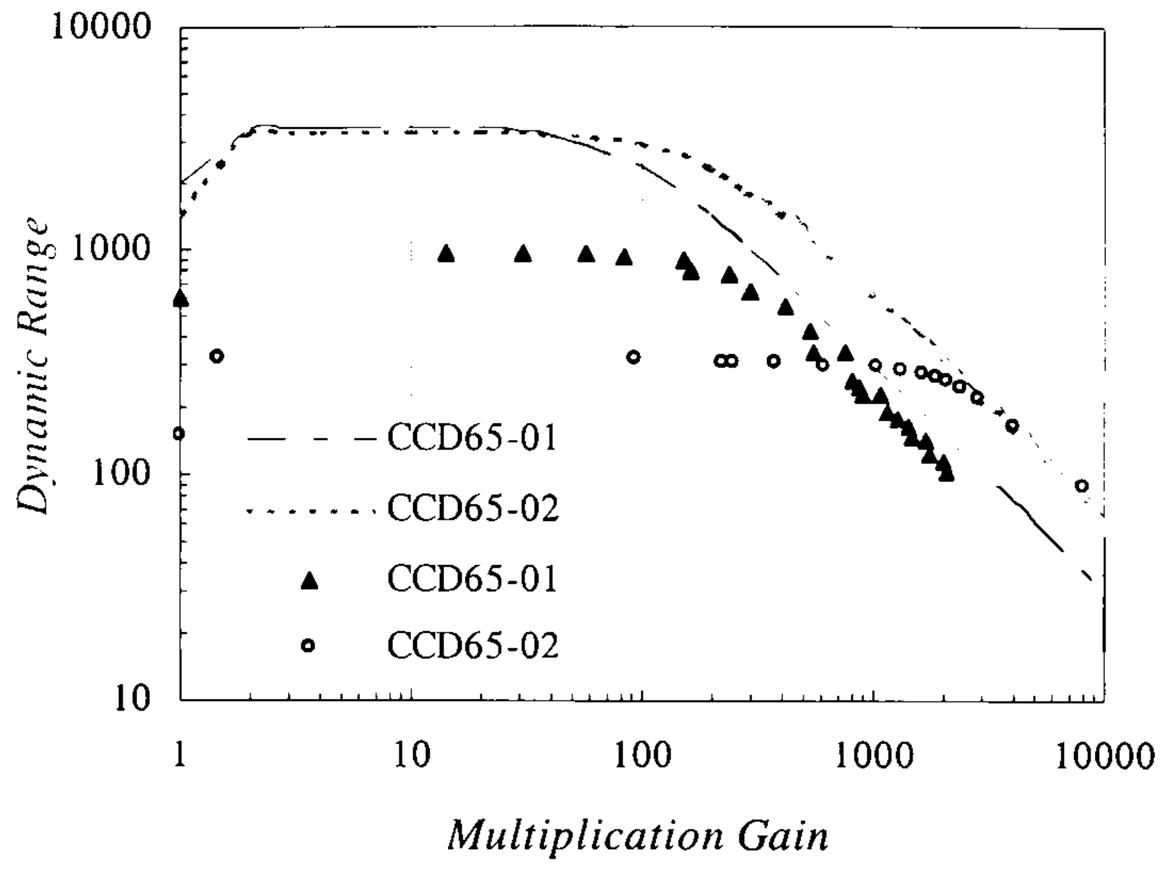

Figure 3.20. *Variation of dynamic range with gain for CCD65-01 operating at 15 ° C and the CCD65-02 operating at -7 ° C. The dotted lines are calculated using manufacturers values of σ_{ro}, N_{sat} and N_{dark} in equation3.31.*

In addition to the loss of dynamic range with increasing gain, there is also a shift in the range of input signals. One method of extending the dynamic range would be to acquire two images, one with, and one without gain. The first acquisition would record the low level input signals and the second would record the high input signals. The two images could then be combined to form an image that extended over the required dynamic range.

Clearly, careful optimisation of the camera is required for imaging applications in which high dynamic range is important. Dynamic range requirements in fluoroscopy, mammography are on the order of 30 (Cowen and Workman, 1992) and 3000 (Maidment *et al.*, 1993) respectively. The use of high gain will severely limit its application to digital radiography. Improvements are being made to the L3CCD to increase dynamic range, however these devices are not yet available (E2V Technologies Ltd, 2002).

3.7 Discussion and conclusions

3.7.1 Characterisation results

This work has investigated the characteristics of the L3CCD camera. The gain and noise performance have been evaluated and compared with theoretical predictions. The level of gain obtainable was measured up to 17,000 for a device that is cooled to –7 °C. The level of gain is compare with that of other photodetectors in table 3.2.

The detectors considered in table 3.2 (and later in table 3.3) include; active matrix flat panel imagers (AMFPIs) (Antonuk et al., 2000, Maolinbay et al., 2000), x-ray image intensifiers (XRIIs) (Cowen, 1992), conventional charge coupled devices (CCDs), electron bombarded charge coupled devices (EBCCDs) (Aebi *et al.*, 1998, Dalinenko *et al.,* 1997, Rossi et al., 2000), intensified charge coupled devices (ICCDs) (Arisaka et al., 2000), avalanche photodiodes (APDs) (Kobayashi *et al.*, 1995, Renker *et al.,* 2002), hybrid avalanche photodiodes (HAPDs) (Arisaka et al., 2000), hybrid photodiodes (HPDs) (Arisaka et al., 2000, Calvi et al., 2002) and position sensitive photo multiplier tubes (PSPMTs) (Arisaka et al., 2000).

Although extremely high gains are achievable, the practical application of gain is limited by the thermal noise in the device. The minimum noise level in the device is obtained at approximately -5°C. Below this the spurious noise, which increases as temperature decreases, becomes significant and there is no benefit obtained in reducing the temperature further.

The gain was found to be a function of temperature. For temperatures between -8 and +8°C, an increase of + 1° C results in a -10.6 % reduction in gain. This behaviour is expected due to the temperature dependence of impact ionisation. Consequently the temperature of the device must be kept stable throughout an imaging sequence to obtain constant gain. Temperature dependence on gain is a common problem in most devices that employ gain. The performance of the L3CCD is compared to other detectors that employ signal amplification in table 3.2.

Thermal, transfer and spurious noise sources are present before the gain register and therefore the noise from these sources is amplified by the same amount as the signal. Consequently the *SNR* before the register is the *SNR* limit.

The measurements of device noise have been used to quantify a minimum detectable signal (*MDS*). Again the *MDS* is limited by the pre-gain register noise in the CCD. For a cooled device (-5°C), the *MDS* = 2.1 electrons. This means that for a CCD with $QE(\lambda) = 0.25$ approximately 8 light photons of wavelength λ collected in one pixel in one integration period (1/50 second) will be detectable. The implication for radiographic imaging is that the L3CCD would be able to detect single diagnostic x-rays even when the conversion process is extremely inefficient. In summary, the optimal settings for the CCD65 device have been identified. The device should be cooled to –5°C and the temperature should be kept stable within ± 0.5°C. Using the Rose criteria (Rose, 1948), the gain required to detect the *MDS* is ~ 4096 (for the CCD65-02). The dynamic range at this value of gain is ~200. To ensure that the *SNR* is not limited by spurious noise contributions only, the L3CCD should not be operated above a gain of 10,000.

Table 3.2. *Comparison of L3CCD performance with other detectors that employ gain.*

	Is the gain linear?	Is the max. < 10^3?	Is the gain temperature independant?	Does the detector employ low voltage?	Is the F=1?
XRII	✔	✔	✔		✔
ICCD		✔			
EBCCD					
L3CCD		✔		✔	✔
HPD	✔				✔
HAPD	✔	✔			
PSPMT	✔	✔			
PD					
AMFPI	✔	✔	✔	✔	✔

The excess noise factor has been measured as a function of gain. The excess noise factor was found to be close to unity (an average noise factor of 1.02 ± 0.15 was measured). The measured values have been compared with a theoretical model proposed for a similar device. Hyneček's analysis (Hyneček 2001) predicts a noise

factor of 1.1 a 591 stage device with $M = 400$ and which decreases as a function of gain. The difference between the measured result and Hynecek's analysis is most likely due to the simplicity of the model. Further work is required to develop a more sophisticated model of the electric field distribution in the L3CCD gain register. An excess noise factor of unity implies that quantum limited imaging can almost be achieved. A comparison of the noise factors of other devices in table 3.2 indicates that a much better noise performance is available using the L3CCD.

The variation of dynamic range with gain also places another practical limitation on the gain that can be used. The measurements have shown that the dynamic range varies as predicted, however, the high noise read out noise has limited the dynamic range in the CCD65-01 and the CCD65-02 devices. If the read out noise was equivalent to the nominal value for the CCD65 (~100 e^- r.m.s.) a dynamic range of 500 is obtainable when $M = 10^3$.

3.7.2 Comparison of L3 performance with other detectors

To ensure that the optimal detector is employed for a specific imaging technique, it is important to compare and contrast the performance of all suitable detectors. The following discussion provides details of the detectors used in medical imaging (and introduced in section 1.4) in order that their performance can be compared with that of the L3CCD. Firstly, L3 technology is compared to other photodetectors that can be used with x-ray phosphors (indirect detectors) and secondly, with direct detectors.

Table 3.3 compares some of the performance parameters of indirect detectors using an x-ray phosphor to convert x-rays into optical quanta. The type of phosphor and its thickness can be optimised for the specific imaging requirements and therefore the x-ray quantum efficiency is assumed to be high in all cases. For each parameter the best performance is highlighted.

Table 3.3. *Comparison ofL3 performance with that of other indirect detectors*

Detector Parameter	QE	Dynamic Range (max)	Gain (max)	Voltage	†Noise (e^- r.m.s.)	Noise factor	Spatial Resolution (**MTF* at 10 $lpmm^{-1}$)	Field (cm^2)	Gain/ Noise
XRII	0.4	10^3	10^4	15k	~500	×	< 0.1	1000	50
CCD	0.25	10^4	1	~10	~100	×	0.8	1	10^{-2}
ICCD	0.2	10^4	10^4	15k	~100	2 - 4	0.3	1	10^2
EBCCD	0.25	10^4	10^3	15k	~100	1.1	0.6	1	10
L3CCD	0.25	10^3	10^4	50	~100	1	0.8	1	10^2
HPD	0.4	10^6	10^3	8k- 20k	~1000	1	×	<1	1
HAPD	0.4	10^6	10^5	8k- 20k	~1000	1.5	×	<1	10^2
PSPMT	0.4	10^7	10^5	1k	~100	1.5	< 0.1	4	10^3
APD	0.8	10^{11}	500	100	~100	2 - 5	×	1	5
AMFPI	0.25	10^4	10^4	~ 50	~2500	×	<0.1	1600	4

† Noise refers to read out electronic noise or leakage current noise, depending upon which is greater for the specific device. The values highlighted are for the detectors with the best performance for a specific performance parameter. * *The MTF at 10lpmm^{-1} is a common measure of the spatial resolution of a detector (Arisaka et al., 2000).*

Comparing the performance of the L3CCD with the other photodetectors in table 3.3 it is seen that the L3CCD gain is comparable with all of the devices except for the PSPMT that has a gain of 10^5.

The L3CCD has superior spatial resolution compared with all other detectors except the conventional CCD. The spatial resolution of the other CCDs is degraded due to electron scattering and spreading in the intensification stages. Comparably, the L3CCD is a low voltage device. Most of the devices employ kilo-voltages to achieve high gains, which may be unsatisfactory for certain clinical imaging applications.

The L3 excess noise factor was found approach unity. Consequently, the L3CCD will have superior *SNR* performance over other electron multiplication devices such as the ICCD, the EBCCD, the PSPMT, the HAPD and the APD, which can never achieve quantum limited imaging due to excess noise. This indicates that the L3CCD should be considered for low x-ray flux applications that could normally undertaken by these detectors.

The last column in table 3.3 is intended to provide a measure of the potential signal to noise ratio. It has been observed that although the L3 has a gain to noise ratio of 10^2 the minimum detectable signal is approximately 2 photoelectrons. Typically it is reported that PSPMTs, HAPDs and APDs can detect single photoelectrons however all of these devices have high excess noise factors which ultimately limits the *SNR* performance. Both XRII and ICCD have high gain to noise ratios but due to inherently noisy scattering and conversion processes that take place in the image intensifiers these devices cannot detect single photoelectrons (Gruner, 2002).

Table 3.4 compares some of the performance parameters of the direct detectors introduced in section 1.4. These detectors include; a cadmium zinc telluride pixel array detector (CZT PAD) (Yin *et al.*, 2002) which is read out using a CCD, a gallium arsenide (GaAs) PAD read out using a photon counting chip (PCC) (Amendolia *et al.* 2001, Ponchut *et al.*, 2002, Renzi *et al.*, 2002, Schwarz *et al.*, 2001), a silicon (Si) PAD read out using a CCD (Mainprize *et al.*, 2002), silicon microstrip detectors (Arfelli *et al.*, 1997, Beauville *et al.*, 1998, Speller *et al.*, 2001,) and AMFPIs (Antonuk *et al.*, 2000, Maolinbay *et al.*, 2000).

Table 3.4. *Comparison of L3 performance with that of direct conversion detectors*

Detector Parameter	†DQE (@ 50keV)	Dynamic Range (max)	Gain	Voltage	Noise (e^- r.m.s.)	Min. pixel size (μm)	Field coverage (cm^2)
AMFPI	>0.9	10^4	10^4	~50	~2500	100	1600
CZT PAD/ CCD	0.6	10^4	1	<150	1000	150	1
GaAs PAD/PCC	NA	10^4	1	340	3600	170	1
Si PAD/CCD	<0.3	10^5	1	170	5000	50	~1
Si microstrip	0.8	×	1	50	~300	100	<1
L3CCD	<0.9*	10^3	10^4	50	100	<20*	1

*† The detective quantum efficiency at 50keV is quoted in order to take into account signal losses specific to the device. *The spatial resolution and QE of the L3CCD will depend upon the phosphor thickness and type of phosphor used. The values highlighted are for the detectors with the best performance for a specific performance parameter. NA = not available.*

The comparison of the L3CCD with these detectors is made on the basis that they are used in direct detection mode as described in the literature. The values of *DQE* and

spatial resolution for the L3CCD are optimal values. It should be noted here that in order to obtain high DQE the phosphor thickness will be such that a decrease in spatial resolution is inevitable (Taibi *et al.*, 1997). With the exception of the AMFPI, a L3CCD used in conjunction with an x-ray phosphor potentially has a better detection efficiency than all other devices in table 3.4. The fact that the L3CCD is a photodetector means that a large area x-ray phosphor may be imaged by using a lens. Use of both the PAD and the silicon microstrip detectors would require numerous detectors and scanning techniques would be needed to cover imaging areas suitable for diagnostic radiology. The same applies to the L3CCD if it is used to view a phosphor screen directly.

The dynamic range of the L3CCD at high gain is poor in comparison with these detectors.

Comparisons with direct and indirect detectors, which are suitable for use in medical imaging have shown that the L3CCD surpasses other detectors in specific performance characteristics and is comparable in others. The competitive performance of the L3CCD indicates that it may afford benefits in those areas in which the L3CCD has superior performance compared to other detectors.

3.7.3 Possible medical applications

Two diagnostic imaging techniques have been identified as possible applications of L3 technology.

3.7.3.1 Fluoroscopy

Fluoroscopy is a real-time low x-ray flux imaging technique. A suitable fluoroscopy detector will have detective quantum efficiency of greater than 50% (Marshall, 2001), a large field of view (<10cm diameter)(Cowen, 1991), low noise and high gain. There is no principle requirement for high dynamic range or high spatial resolution, however, spatial resolutions of greater than 1000 μm are unacceptable (Cowen, 1991).

From tables 3.3 and 3.4 it is clear that the only detectors that have a large field of view are the XRII and AMFPI. The other photodetectors listed in table 3.2 would require the use of de-magnifying optics such as a lens or a fibre-optic taper to couple the x-ray phosphor to the photodetector or an array of many detectors. PSPMTs and large area HPDs and HAPDs have pixel sizes of ~1mm. If a fibre-optic taper of a demagnification factor equal to two was employed, the pixel size at the image plane would be equal to two times the pixel size at the detector. Therefore the use of de-magnifying fibre-optics with these detectors would exceed the spatial resolution requirement. Without demagnification the small size of these detectors would mean that very large numbers of detectors (~ 1000) would be required to cover the field of view, which is costly and impractical. However, the CCD, the EBCCD, the ICCD and the L3CCD have pixel sizes on the order of 20μm which means that relative large demagnification factors can be employed before the spatial resolution is exceeded. Comparison of the L3CCD with the EBCCD and the ICCD show it has superior performance in terms of excess noise factor. The conventional CCD is unsuitable for fluoroscopic imaging due to the fact it has no gain.

Table 3.3 shows that only the direct detection AMFPI has sufficient field of view for fluoroscopic imaging.

In conclusion, the detectors that are most suitable for fluoroscopic imaging are the XRII, the AMFPI and the L3CCD.

Until recently all fluoroscopic imaging has been carried out using x-ray image intensifiers. Digital radiography systems based upon x-ray image intensifiers have several disadvantages. The bulky nature of the intensifier impedes the clinicians' access to the patient. The large number of conversion stages results in a loss of contrast due to x-ray and light scatter within the image intensifier (veiling glare)(Yaffe and Rowlands, 1997). In addition, there is image distortion due to the curved nature of the photocathode and 'S' distortion, which is attributable to the earth's magnetic field. An optically coupled L3CCD based imaging system would not suffer from any of the drawbacks mentioned above. As discussed earlier in section 1.3, use of the L3CCD would mean there are no extra conversion stages that cause scattering and veiling glare.

In addition, the L3CCD like the AMFPI is compact, improving the versatility of an x-ray imaging system in terms of better patient views and mobility.

Active matrix flat-panel imagers (AMFPIs) have found application in real-time x-ray imaging due to their large imaging areas (up to 40cm × 40cm) (Maolinbay *et al.*, 2000). The phosphor layer is read out by a large area photodiode array with active electronic devices (for example thin film transistors). Potential advantages of these systems include compactness and no veiling glare because they are flat. However, extension of this concept to applications involving low exposures i.e. fluoroscopy, has had problems due to the significant reduction in detective quantum efficiency. This is due to relatively large noise levels compared with the gain of the system (Antonuk *et al.*, 2000). Consequently real-time imaging AMFPIs are generally used for electronic portal imaging where signals are relatively higher than fluoroscopy. However, due to improvements in noise performance, systems for applications digital subtraction angiography are beginning to emerge.

In both the direct approach using a-Se or *a*-Si:H and the indirect approach using phosphor screens, the conversion of x-rays to charge are approximately equivalent and thus the level of x-ray signal to noise is comparable (Maolinby, 2000). Accordingly the same comments given above for indirect AMFPIs apply for indirect and direct AMFPIs.

Comparing the performance of the L3CCD with the AMFPI and the XRII shows that the levels of gain to noise are higher, however for the L3CCD to be competitive it must employ de-magnifying optics that will reduce the optical coupling efficiency (Gruner, 2002) and effectively the gain of the system. This will determine the suitability of L3 technology for use in fluoroscopic imaging. An evaluation of an L3-based fluoroscopic system performance has been undertaken and is described in detail in chapter 4.

3.7.3.2 Diffraction enhanced breast imaging

Diffraction enhanced breast imaging (DEBI) has been identified as having the potential to enhance the transmission image, hence raising the sensitivity of x-ray mammography (Kidane *et al.*, 1999). The following discussion considers the requirements of a detector

that could be used in a clinical detector system to collect scatter data during digital mammography.

Due to the small signal levels involved (Kidane, 2001) DEBI requires that a detector with high quantum efficiency be employed to optimise the probability of detecting every coherently scattered x-ray. All of the detectors listed in table 3.3 can be used in conjunction with an x-ray phosphor to obtain high x-ray quantum efficiency. The direct detectors do not meet this requirement.

Typically digital mammography is acquired in slot scan acquisition mode (Yaffe, 2001). Therefore the detector should have a linear geometry in order to detect x-rays scattered from a laminar beam. A linear detector could consist of a row of small detectors. The detectors should be butted together in such a fashion that no gaps are left between the detectors. For this to be achieved the detector should have a rectangular geometry and of practical size such that it can be placed as close to the patient as possible without obstructing the transmission detector. In this arrangement, it may be desirable to use the edge of the detector and therefore it should not suffer from any edge defects, but be uniform over its entire area. The detector should be a position sensitive device in order to obtain images of the scattered radiation. X-ray image intensifiers (XRIIs) have been used to measure linear differential scattering coefficients (Westmore *et al.*, 1996). However due to their bulky nature they are unsuitable for clinical diffraction imaging. The CCD geometry is such that a row of CCDs can easily be abutted together to form a linear array (Mainprize *et al.*, 2000). Mainprize *et al.* have described a mammographic imaging system based upon an array of CCDs. Alternatively, CCDs can be manufactured in a linear format. Devices such as ICCDs, EBCCDs, HAPDs and PSPMTs all employ high voltages (~kVs)(see table 3.3), which may be unsuitable as the scatter detector will be placed in close proximity to the patient. Additionally, the ICCD and PSPMT have noise factors greater than two and the EBCCD has an excess noise factor of ~1.2, which is greater than that of the L3CCD.

Detector noise should be low enough to facilitate the detection of the signal produced by an interacting x-ray photon. DEBI is primarily concerned is with 17.4keV x-ray photons, which have been identified as the most useful part of the mammographic x-ray spectrum. Compared to most radiographic examinations this is low energy radiation.

From the above discussion only HPDs, CCDs and L3CCDs can be considered as suitable for diffraction enhanced breast imaging, however, comparison of the gain to noise ratios for these detectors given in table 3.3 shows that the L3CCD has superior performance.

Additional performance is required for a detector that will image both the transmitted and scattered radiation. Conventional mammography relies upon the detection of micro-calcifications and abnormal breast architecture. The spatial resolution of better than 50μm is required. The detector is a position sensitive device in order to obtain images of the scattered radiation. A dynamic range of 3000 is required for mammography (Maidment *et al.,* 1993). The maximum nominal value for the CCD65 dynamic range is 10^3, however the dynamic range decreases as the gain is increased (see section 3.6). To meet the dynamic range requirement and to employ gain in order to detect the low scatter signal, the following read out protocol is suggested. The image area of the sensor is divided into three horizontal sections. The rows that are used to detect the scattered radiation will be read out with gain. The middle section, used to image the transmitted radiation, could be read out with no gain. The dynamic range required for the scatter radiation is of the order of 10 because the scatter intensity from normal tissue is three times the scatter intensity from diseased tissue.

One requirement, which has not been addressed, is energy resolution. Due to the fact that conventional mammography is performed by using a poly-chromatic x-ray source produced by a Molybdenum-anode target, not all the scattered photons collected at a given scatter angle will have the same value of momentum transfer. For a typical mammographic examination employing 0.3mm of Molybdenum filtration and a tube potential of 30kVp, the spectrum comprises of 42% characteristic radiation and 58% broad spectra bremsstrahlung radiation. This will lead to so-called momentum blurring.

The effect of poly-chromatic radiation on the scatter signature has been investigated by Taibi *et al.* (2000). Using Monte Carlo modelling, the angular distribution of scattered photons was calculated for three qualities of incident radiation. A small difference (~1°) in the peak position was observed for a Mo/Mo 30kVp beam compared to a monochromatic 20keV beam. The profile shape was unaffected. Taibi *et al.* concluded

that for small values of momentum transfer, Mo/Mo spectra can give acceptable scatter distributions. Work by Westmore *et al.* (1996) has shown that a detector without energy resolving capability can be used to measure the differential coherent scatter coefficient. They employed an image intensifier based system and a tungsten x-ray spectrum to detect scatter from different materials including bone, water and Lucite. They conclude that in spite of the poly-energetic spectrum, there are significant detectable differences between materials, allowing the material to be identified. This implies that although, an energy-resolving detector is useful and may improve image quality, it is not essential.

In conclusion, the L3CCD detector characteristics are well matched to the requirements of the imaging task. Comparison of the L3CCD with other detectors (see table 3.3) has shown that the L3CCD is a more suitable device. The feasibility of an L3-based diffraction detector suitable for the acquisition of diffraction images in a clinical environment will be assessed later in chapter 5.

CHAPTER 4

L3 technology application to medical imaging: Fluoroscopic imaging

Taking into account that the L3CCD is an image intensification device, perhaps its most obvious application is a medical imaging technique that traditionally employs image intensifiers. The x-ray image intensifier (XRII) was developed from the image intensifiers used for low light level imaging, and has been used for the past fifty years to produce sequences of x-ray images, forming the basis of fluoroscopic imaging (Gruner *et al.*, 2002).

The primary purpose of this work is to assess the feasibility of the application of L3 technology to fluoroscopic imaging. A review of current fluoroscopic imaging systems and the imaging requirements is given. A simple L3 based fluoroscopic imaging system will be modelled and experimentally evaluated in order to assess the potential performance of the L3CCD.

4.1 Fluoroscopic imaging

Fluoroscopic imaging (or fluoroscopy) uses real-time x-ray imaging to carry out both diagnostic and interventional techniques. Technically it can be categorised into two main imaging modalities: digital subtraction angiography (DSA) and digital spot-fluorographic imaging (DSI) (Cowen, 1991).

DSA is utilised as the human vascular structure cannot be imaged directly using x-rays. This is because the attenuation due to blood is indistinguishable from that of the surrounding tissue. By introducing a iodine based contrast medium either intra-arterially or intra-venously the vascular structure is rendered radio-opaque and therefore can be imaged. To improve image contrast, which is reduced by overlying anatomical structures, image subtraction is used. In DSA, a 'mask' image is taken prior to the

introduction of the contrast medium and subtracted from all images taken after the contrast media has been introduced. Images are subtracted using image-processing algorithms.

DSI is a grey-scale (non-subtractive) imaging technique. It is used in a wide range of diagnostic examinations, such as those of the gastro-intestinal tract, using contrast media such as barium swallows, meals and enemas. It is also useful in other iodine-based studies such as intravenous pyelograms, venograms and myelography (Cowen, 1991). More recently, DSI has been employed to guide interventional procedures such as the placement of stents and catheters and renal interventions.

4.1.1 Fluoroscopic imaging systems

4.1.1.1 X-ray image intensifiers

The XRII is a vacuum tube device which uses an input phosphor, normally CsI(Tl), is coupled to a photo-cathode. Together they form an x-ray-to-electron converter. Incident x-rays are stopped in the phosphor and converted to light. Optical photons incident on the photo-cathode are then absorbed and produce electrons via the photo-electric effect. Electrons that are generated in the photo-cathode, are accelerated across a vacuum by a high potential field (typically ~25 kV) and at the same time they are focussed electro-statically onto an output phosphor. A CCD or video camera is coupled to the output phosphor via a lens or a tapered fibre optic. For a comprehensive description of the operation of the XRII the reader is referred to Yaffe and Rowlands (1997). Despite the disadvantages of the XRII, discussed earlier in section 3.7.1.1, the XRII remains the imaging system of choice for fluoroscopy. This is most likely a result of its ability to perform x-ray quantum limited imaging over a wide range of input exposure levels. The XRII can achieve quantum-limited imaging due to three specific features inherent in its design. Firstly, the photo-cathode is evaporated directly onto the phosphor. This intimate coupling provides a very efficient x-ray-to-electron converter. Secondly, the electrostatic collection of electrons is very efficient and electrostatic focussing is the most efficient way of reducing the image. Consequently, large demagnification factors can be achieved with minimal losses (Gruner *et al.*, 2002).

Thirdly, the acceleration of the electrons within the tube provides high gain, which compensates for any losses in the following optical coupling and imaging system.

4.1.1.2 Active matrix flat panel imagers

Active matrix array technology has made possible the concept of flat panel imaging systems for radiography. In the conventional approach a thin-film circuit built on glass contains the necessary switching components (thin-film transistors or TFTs) to read out an image formed in either of two ways. The first (direct method) employs a photoconductive layer of amorphous selenium (*a*-Se) to detect x-rays. The second, (indirect method) uses an active matrix to read out a phosphor layer. Principle advantages of using active matrix flat panel imagers (AMFPIs) include fast readout, compactness and no spatial distortion. However, extension of this concept to DSI, has had problems due to the significant reduction in detective quantum efficiency at low exposure levels. This is due to relatively large noise levels compared with the gain of the system (Antonuk *et al.*, 2000). The main noise sources arising from TFTs are thermal noise and pre-amplifier noise. A large number of scientific evaluations of the physical characteristics of AMFPIs for application to fluoroscopy have been carried out (Schiebel *et al.*, 1994, Siewerdsen *et al.*, 2000). More recently the subjective quality of an AMFPI which using CsI(Tl) scintillating layer has been evaluated and compared to a conventional image XRII/TV imaging system (Davies *et al.*, 2001). Contrast detail detectability was measured in both systems using a test tool,. This work concluded that at low levels of entrance exposure the AMFPI had inferior performance due to additive read out noise.

4.1.2 Imaging requirements

When assessing the feasibility of a new imaging system its performance should be evaluated in terms of the imaging requirements of the task it is required to undertake. Despite its limitations and the advances in flat panel technology, the XRII remains the gold standard in fluoroscopic imaging. The following is a list of some of the more important measures of detector performance, which are routinely met by XRII systems.

4.1.2.1 Input dose rate

Fluoroscopic imaging procedures typically range from tens of seconds of exposure to minutes and possibly, in extreme cases, hours. Accordingly the dose rate to the patient has to be very low in order that the risk of radiation-induced disease is justifiable. Quality control procedures performed by hospital physicists measure the typical input dose rate at the entrance of the image intensifier under automatic dose control. Typically, acceptable input dose rates are between 0.1 μGys^{-1} and 1 μGys^{-1}. However, in a recent dose survey of clinical fluoroscopic imagers, Marshall *et al.* (2001) have reported that for cardio-angiography (DSA), which employs rapid acquisition rates (typically 12.5 or 25 images s^{-1}), the input dose is on the order of ~ 1 to 4 μGy per image. For standard DSI (10 images s^{-1}) the mean dose per image is ~ 0.6 to 1.5 μGy per image. These values imply that dose rates can be as high as 15 μGys^{-1} for DSI and in some instances reach 100 μGys^{-1} for cardio-angiography.

4.1.2.2 Dynamic range

A practical definition of the effective dynamic range is 'the range of x-ray intensities arriving at the receptor over which diagnostically useful information can be derived'. In the clinical context this reflects the range of tissue attenuation over which image details can be reproduced. The dynamic range of a digital fluoroscopy system depends upon the x-ray exposure per image frame, the maximum signal capability of the TV-read out system and the electronic noise arsing at the TV preamplifier. Typical values of dynamic range are 30 for DSA and 10 for DSI (Cowen, 1991).

4.1.2.3 Detective quantum efficiency

The detective quantum efficiency (*DQE*) is defined in section 1.6. An ideal detector would have a *DQE* of 100%. Manufacturers of XRII typically quote the DQE for 59.5keV photons, this being in the energy range of greatest efficiency (Thirwall, 1999). In product guides Siemens a quote value of 65% and Hammamatsu quote 60%. These measurements are for zero spatial frequency. Measured values of the spatital frequency dependant DQE have shown that the *DQE*s of clinical systems are in the region of 5 to 50 % (Marshall, 2001).

4.1.2.4 Spatial resolution

The theoretical limiting resolution of the system is given by the Nyquist frequency, f_N, which is calculated according to:

$$f_N = \frac{1}{2.\Delta x} \tag{4.1}$$

where Δx is the pixel dimension at the plane of the phosphor screen. The limiting resolution will depend upon the demagnification factor (the ratio between the object size and the image size) and the TV/CCD pixel dimensions. For DSA and DSI imagers, limiting resolutions typically range between 0.5 to 1.5 mm^{-1} and 1.0 to 2.0 mm^{-1}, respectively.

4.1.2.5 Field of view

To provide the necessary anatomical coverage, in large-field x-ray image intensifiers of diameters 10 cm up to 40cm are normally used (Cowen, 1991).

4.1.3 L3 fluoroscopic imaging

It is proposed that an L3CCD optically coupled to a phosphor screen could be used instead of a conventional XRII imaging system. The following is a theoretical investigation into the feasibility of such a system. A model of an L3 based fluoroscopic imaging system is derived and used to assess the L3 performance. A quantum accounting diagram (QAD) analysis described by Cunningham *et al.* (1994) has been employed in order to represent the signal and noise transfer in the model and to calculate the detective quantum efficiency (*DQE*). The results of this analysis have been used in conjunction with the L3CCD noise measurements in order to assess the resulting signal-to-noise (*SNR*) performance. The variation of *SNR* performance for three field sizes is investigated, both theoretically and experimentally, and compared to the XRII system. Improvements to the basic proposed system are suggested and the potential improvement in *DQE* has been calculated.

4.2 Modelling the L3 fluoroscopic imaging system

4.2.1 Linear systems analysis

When evaluating new ideas, system designers often use linear systems analysis. In this analysis an imaging system is represented as a series of cascaded processes or gain stages; the quanta 'leaving' one stage form an effective input to the next stage and primary input quanta are converted to secondary quanta in one or more stages before contributing to the final image. Each stage has an associated gain where g_i is the gain of the *ith* stage. The average number of quanta, and therefore the signal corresponding to one image pixel, can be determined at each stage. This provides information about the propagation of signal through the system and reveals information about the noise transfer characteristics, which are strongly dependant upon the number of quanta passing through each stage. Linear systems analysis can be represented in graphical form (Cunningham and Shaw, 1999) where the average number of quanta at each stage is shown on a vertical axis as a function of the stage number on a horizontal axis. This is a so-called quantum accounting diagram or QAD. The QAD is used to identify both the stages at which signal losses occur and the stage that limits the SNR. The limiting stage is the stage with the fewest quanta N_{min}, which results in it having has the largest statistical uncertainty. This stage is called a quantum sink. The quantum sink places a fundamental limit on the image SNR. It can be no greater than the square root of N_{min}. On this basis, if the mean number of secondary quanta per interacting x-ray quanta is greater than unity at every stage, the statistical fluctuation in the number of quanta is the dominant source of noise.

In this work, linear systems analysis approach has been used to assess the signal and noise transfer in a simple fluoroscopic imaging system based on the L3CCD. A QAD is used to identify the quantum sink and to find a predicted value for the zero-frequency DQE. This approach has two limitations. Firstly, the QAD does not include the effects of additive electronic noise sources arising from the detector. In the case of the L3CCD, electronic noise sources are rendered negligible by internal gain. However some consideration should be given to the thermal and spurious noise, which can limit the *SNR* when the number of signal photoelectrons becomes comparable to the dark current (see section 3.3). Therefore the QAD will be adjusted to include these additive

noise sources. The second limitation is that the analysis assumes that all secondary quanta correspond to the same location in the image as the primary quanta. This neglects that fact that scattering or spreading processes can occur leading to further degradation of the *SNR*. Thus this analysis contains no examination of the signal and noise properties at the system at any spatial frequency. Accordingly it is referred to as a zero-frequency analysis. Cunningham *et al.* (1994) have described a spatial frequency dependant QAD which includes spreading mechanisms at each stage. This model requires a detailed knowledge of the signal and noise transfer characteristics of the individual system components. This approach is beyond the scope an initial system evaluation.

4.2.1.1 Zero-frequency noise propagation

The imaging system will be modelled as a series of cascaded gain stages. Each stage is characterised by an average number of quanta $\overline{N}_i$, a gain g_i, and a gain variance $\sigma_{g_i}^2$. Using Burgess's variance theorem for two cascaded gain stages i -1 and i

$$\overline{N}_i = g_i \overline{N}_{i-1} \tag{4.2}$$

$$\sigma_{N_i}^2 = \overline{g}_i^2 \sigma_{i-1}^2 + \sigma_{g_i}^2 \overline{N}_{i-1} \tag{4.3}$$

The value of $\sigma_{g_i}^2$ is dependant upon the physical processes involved in gain stage i. For deterministic gain there is no variance in the gain and $\sigma_{g_i}^2 = 0$. Where gain is Poisson distributed $\sigma_{g_i}^2 = g_i$. If the gain represents an interaction probability or a coupling efficiency it is a binary selection process and obeys Bernoulli statistics (see Appendix A) giving $\sigma_{g_i}^2 = g_i(1-g_i)$. If the variance in $\overline{N}_i$ is not Poisson distributed, i.e. $\sigma_{N_b}^2 \neq \overline{N}_i$, then it is convenient to introduce a Poisson excess $\in_{N_i}$. The Poisson excess is given by:

$$\in_{N_i} = \frac{\sigma_{N_i}^2}{\overline{N}_i} - 1 \tag{4.4}$$

Similarly a Poisson excess is introduced for the gain, $\in_{g_i}$. Equation 4.4 can be combined with equation 4.3 to give:

$$\in_{N_i} = \frac{g_i^2 \sigma_{i-1}^2 - \sigma_{g_i}^2 \overline{N}_{i-1}}{\overline{N}_i} - 1 = g_i(1+\in_{N_{i-1}}) + \in_{g_i} \tag{4.5}$$

For the three situations given above $\in_{N_i} = 0$ and $\in_{g_i} = 0$. If N_i or g_i are Poisson distributed, $\in_{g_i} = -1$. If the gain is deterministic and if g_i represents a binary selection process $\in_{g_i} = -g_i$ (Cunningham and Shaw, 1999).

4.2.1.2 Zero-frequency DQE

The *DQE(0)*, which includes additive noise for an *m*-stage linear system, has been derived by Cunningham *et al.* (1994) and is given by:

$$DQE_m(0) = \left[1 + \sum_{i=1}^{m} \left(\frac{1 + \in_{g_i} + (\sigma_{a_i}^2 / \overline{N}_i)}{P_i} \right)\right] \tag{4.6}$$

where $P_i = \prod_{j=1}^{i} g_j$ and $(\sigma_{a_i}^2 / \overline{N}_i)$ is the ratio of the additive noise variance to the mean signal at the *ith* stage.

4.2.2 Coupling efficiency

The coupling efficiency of the system is an additional way in which to measure the system efficiency. It is defined as the number of electrons per interacting x-ray quantum. It is generally accepted that the coupling efficiency must be greater than unity in order to achieve quantum limited imaging. However, Maidement and Yaffe (1994) have assessed the dependence of the spatially dependant *DQE* on coupling efficiency, and have shown that a coupling efficiency of 10 e^-x-ray^{-1} is required to ensure a detector system is x-ray quantum noise-limited.

4.2.3 System description

The linear systems analysis described above was used to model an L3 based fluoroscopic system that could be built in order to predict its performance. The modelled system was subsequently assembled and used to test the model predictions. This section describes the L3 fluoroscopic system. Although the L3CCD is sensitive to x-rays, its small size and low x-ray quantum efficiency at fluoroscopic x-ray energies (20 – 90keV) make it unsuitable for direct detection. An alternative is to absorb the x-rays in a larger area and higher x-ray quantum efficiency phosphor screen, similar to the XRII. The largest screen available ($15 \times 15 cm^2$) was a $80 mg cm^{-2}$ Gd_2O_2S:Eu phosphor screen. The screen was deposited by E2V Technologies Ltd on a thin layer (~100μm) of transparent polyurethane held taught in an embroidery hoop. The light that is emitted from the phosphor screen is coupled to the L3CCD via a lens. The lens is a 25mm compound lens with an *f*-number ($F_\#$) equal to 1.2 (Cosmicar Pentax C-mount Model No. H612A). The $F_\#$ is the ratio of the focal length of the lens (f) to the limiting aperture diameter (D). A mirror is placed at a 45° angle to the phosphor screen and is situated between the screen and the lens. The purpose of the mirror is to move the CCD away from the direct x-ray beam. The L3CCD is the CCD65-01 device and therefore the model includes the fibre-optic faceplate (FOFP) attached to its front surface.

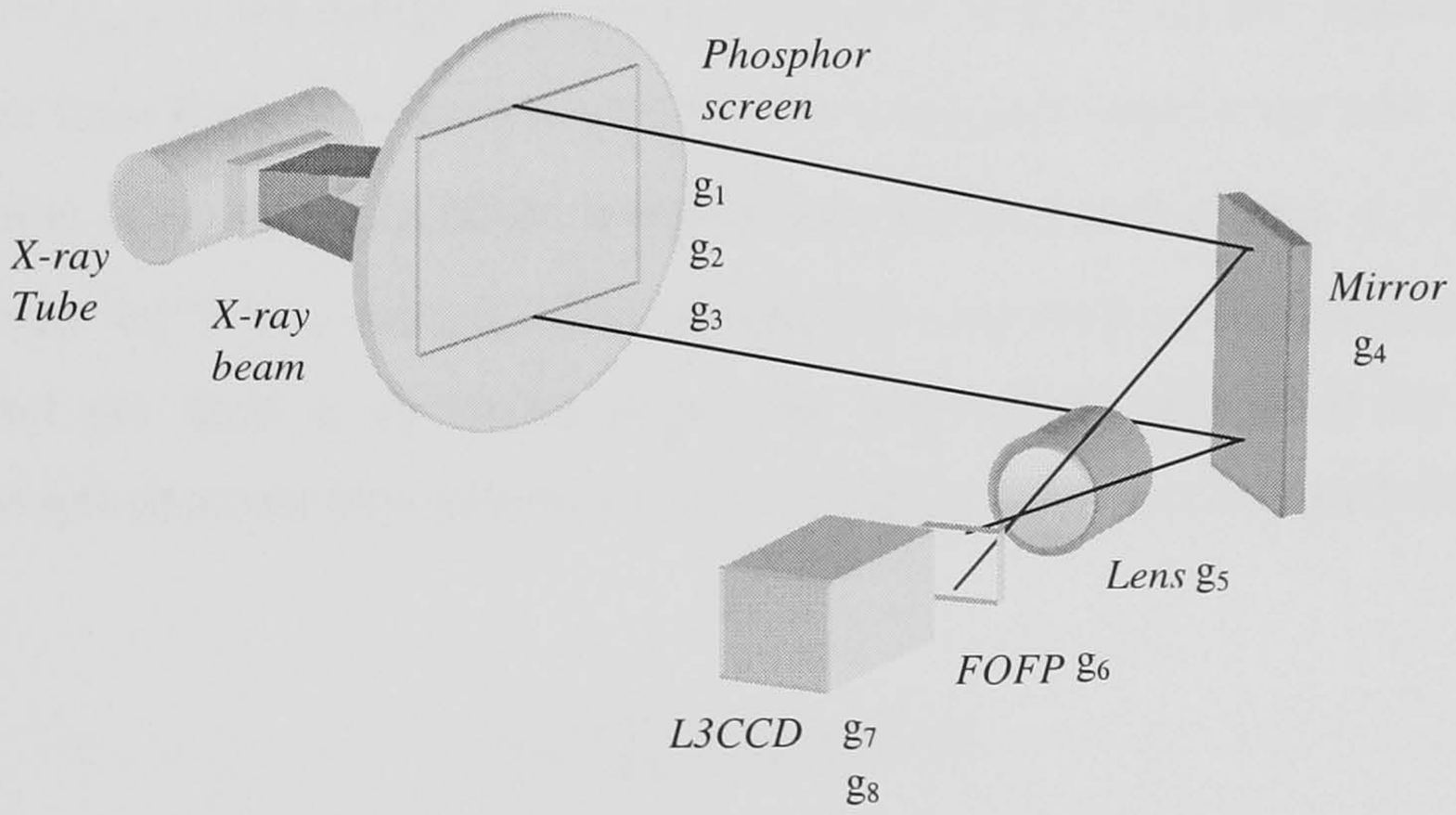

Figure 4.1. *Schematic of the L3 based fluoroscopic system. Each phyiscal component of the sytem has one or more gain processes associated with it.*

Fig 4.1 shows a schematic diagram of the experimental L3CCD fluoroscopy system. Also shown are the gain stages associated with each physical component. The system

demagnification factor m is dependant on the desired field size, given by dividing the object size by the image size. For this system $m = 10$.

4.2.4 Stages and quantities used in the model

For the purpose of the QAD analysis the system has been divided into 8 stages. The following is a description of each gain stage and an explanation of how $\overline{N}_i$, g_i, and $\in_{g_i}$ are calculated.

Incident x-ray quanta

A spectrum of Poisson distributed x-ray quanta is considered as the input to the model. For a given x-ray spectrum the mean fluence per unit dose in x-rays.mm^{-2}Gy^{-1} is calculated using:

$$\frac{\overline{q}_0}{D} = \int_0^\infty \frac{k_1 k_2 q(E)}{E(\mu_{en}(E)/\rho_{air})} dE \qquad (4.7)$$

where k_1 is a constant (5.45×10^8eVg^{-1}mR^{-1}) determined by the definition of the Roentgen, $q(E)$ is the incident x-ray spectrum, k_2 is a constant that converts exposure in mR into dose in air in Gy (0.0083Jkg^{-1}R^{-1}) (Johns and Cunningham, 1983) and $(\mu_{en}(E)/\rho_{air})$ is the energy absorption coefficient (cm^{2}g^{-1}) for air. Spectral data was obtained from Birch and Marshall (1979). For a tungsten target x-ray tube with 2.5mm aluminium of filtration, an 80kV tube potential and 1mA tube current $\overline{q}_0 / Dt$ = 20063 x-rays mm^{-2}Gy^{-1}s^{-1}at a distance of 75cm from the x-ray focal spot. The incident quanta per pixel per field at the input plane (the front of the phosphor) for a medium fluoroscopic dose rate (see section 4.1.2.1) of 0.5μGys^{-1} can be calculated using:

$$\overline{q}_x = \frac{\overline{q}_0}{Dt} \times A_{pix} \times m^2 \times t_i \qquad (4.8)$$

where t_i is the L3CCD integration period (0.02s) and A_{pix} is the L3CCD pixel area (6×10^{-4}mm^2).

Stage 1: Interaction of x-ray quanta in phosphor

This stage represents the interaction of incident x-ray quanta in the phosphor where g_1 is the mean fraction of x-rays that interact in such a way as to produce light. For an x-ray spectrum incident upon a phosphor with a mass attenuation coefficient $\mu(E)/\rho$ and a surface density s (gcm^{-2}), the gain is given by:

$$\overline{g}_1 = \frac{\int_{E_{min}}^{E_{max}} q_x(E)(1-e^{-(\mu(E)/\rho)s})dE}{\int_{E_{min}}^{E_{max}} q_x(E)dE} \tag{4.9}$$

The gain, g_1, is essentially the quantum efficiency of the x-ray phosphor and is the upper limit of the DQE. This interaction process obeys binomial statistics and therefore $\in_{g_i} = -g_1$.

Stage 2: Generation of optical quanta

For an incident x-ray spectrum the average number of optical quanta per interacting x-ray is given by:

$$\overline{g}_2 = \frac{\int_{E_{min}}^{E_{max}} q_1(E) g_{op}(E)dE}{\int_{E_{min}}^{E_{max}} q_1(E)dE} \tag{4.10}$$

where q_1 is the interacting x-ray spectrum and g_{op} is the average number of optical quanta generated per interacting x-ray of energy E. For a Gd_2O_2S:Eu phosphor screen g_{op} is 36.4 optical quanta per keV of x-ray energy absorbed (E2V Technologies Ltd, 2002). For thin screens $\in_{g_i}$ is related to the Swank factor I and is defined in Appendix A. No value for the Swank factor is available for the phosphor screen, thus here it is assumed that I is unity and therefore $\in_{g_2} = 0$.

Stage 3: Emission of optical quanta

Due to the attenuation of the optical quanta in the phosphor and the isotropic nature of its emission, only a fraction, g_3, will escape through the exit surface of the phosphor (the surface closest to the mirror) and be reflected by the mirror. Using the approximations given in the literature g_3 has been estimated to be 0.45 (Holdsworth *et al.*, 1990, Drake *et al.*, 2001). Since this process involves the attenuation of the optical quanta it is assumed to follow binary statistics and $\in_{g_3} = -g_3$.

Stage 4: Reflection of optical quanta by the mirror

Optical quanta incident on the surface of a front-silvered mirror are either absorbed or reflected. The proportion that are reflected, g_4, is given by the reflectivity of the mirror. The reflectivity of the mirror is quoted to be 0.9 by the manufacturer. Due to the fact that photons are either reflected or absorbed, the gain can be considered as a binary selection process.

Stage 5: Collection of optical quanta by the lens

The fifth stage involves the collection efficiency of the lens. The collection efficiency of a lens illuminated by a Lambertian source is given by (Yaffe and Rowlands, 1997):

$$g_5 = \frac{\tau_L}{4F_{\#}^2 (m+1)^2} \tag{4.11}$$

where τ_L is the transmission efficiency, $F_{\#}$ is the *f*-number of the lens, m is the demagnification factor and τ_L is typically 0.8 – 0.9 and in this set up is assumed to be 0.9 (Bissonnette *et al.*, 1997). $F_{\#}$ is 1.2. This is a binary selection process.

Stage 6: Transmission of optical quanta by the FOFP

The fraction of optical quanta transmitted by the fibre optic face-plate from air is given by:

$$\overline{g}_6 = NA^2 T_F (1 - L_R) F_c \tag{4.12}$$

where T_F is the transmisson of the fibre core, which is usually 0.8, F_c is the fill factor of the fibre core, which is 0.9, and L_R is the loss at the surface due to Fresnel reflection,

which can be assumed negligible (Hejazi and Trauernicht, 1997). The numerical aperture (NA) is equal to 1 for a standard FOFP (Gruner *et al.*, 2002). Again, this is a binary selection process.

Stage 7: Interaction of optical quanta with the L3CCD

The seventh stage, g_7, is given by the number of electrons generated in the CCD per optical quantum. This is the probability that one incident optical photon will generate one electron in the CCD and is a function of the wavelength dependant quantum efficiency $QE(\lambda)$ of the CCD. The overall effective quantum efficiency for the x-ray phosphor is found using equation 2.4. The value of g_7 has been calculated from the spectral output of the Gd_2O_2S:Eu phosphor screen (Phosphor Technologies Ltd, Essex, U.K., 2002) and the spectral response of the L3CCD. The interaction of optical quanta with the CCD is a binary process.

Stage 8: L3CCD gain

The final stage gain, g_8, is the L3CCD gain. From chapter 3 we have seen that the gain must be large enough to amplify the signal above the system of the CCD65-01. Therefore the gain required will be a function of the signal entering the L3CCD (N_7).

Additive Noise

The L3CCD will introduce an additive noise source before the L3 gain stage, the noise arising from the presence of thermal and spurious currents. Therefore an additive noise term will be introduced to stage 7 where $\sigma_{a_7}^2 = \sigma_t^2$, which is calculated in section 3.3 and is given to be $(2.003)^2$ electrons at room temperature. The system noise is introduced at stage 8. The measured noise of CCD65-01 is 563 e^- r.m.s, thus $\sigma_{a_8}^2 =$ $(563)^2 = 316969$ electrons.

4.2.5 Results of the model

A linear systems analysis has been used to describe a L3 based prototype fluoroscopic system. The gain and Poisson excess are summarised in table 4.1 for each gain stage.

Table 4.1. *Description of the gain and Poisson excess values for each stage of the L3 imaging system.*

Stage, i	Gain/efficiency g_i	$\in_{g_i}$	Description
q_x	12, 27, 75	0	No. of incident x-ray quanta for 0.5 μGys^{-1} (for 10cm, 15cm and 25 cm input field sizes respectively)
1	0.8	-0.8	Interaction of x-ray quanta in phosphor
2	1310	0	Generation of optical quanta
3	0.45	-0.45	Emission of optical quanta
4	0.9	-0.9	Reflection of optical quanta by mirror
5	9.5×10^{-4},4.5×10^{-4}, 1.7×10^{-4}	$-g_5$	Collection of optical quanta by lens (for 10cm, 15cm and 25 cm input field sizes respectively)
6	0.72	-0.72	Transmission of optical quanta by FOFP
7	0.295	-0.295	Interaction of optical quanta with the L3CCD
8	>5000	0	L3CCD gain

4.2.5.1 Quantum accounting diagram

Zero-frequency QADs are given in figure 4.2 for three input field sizes, 10 cm, 15 cm, and 25 cm. The zero-frequncy QAD shows that the stage which involves the greatest loss is stage 5 which is the collection of optical quanta via the lens. The QAD shows that the loss is greatest for the largest field size. This is due to the fact that g_5 is a decreasing function of the demagnification factor. The QAD shows that after stage 5 is reached the average number of secondary quanta per interacting x-ray falls below unity. Consequently the SNR will be degraded and the imaging system will not be x-ray quantum noise limited. The quantum sink occurs at stage 7, where the limiting *SNR* can be calculated by multiplying N_7 by the number of input quanta q_x. For the 15cm input field the limiting $SNR_7 = \sqrt{q_x \times P_7} = \sqrt{35 \times 0.04} = 1.04$, compared to $\sqrt{27} = 5.2$ if the system were quantum noise limited.

Furthermore, if we consider the thermal noise in the CCD. The signal at stage 7, $\overline{N}_7 =$ 1.4 electrons per CCD pixel, is less than the thermal noise in the device (2 e^- r.m.s) and therefore a further degradation of *SNR* occurs.

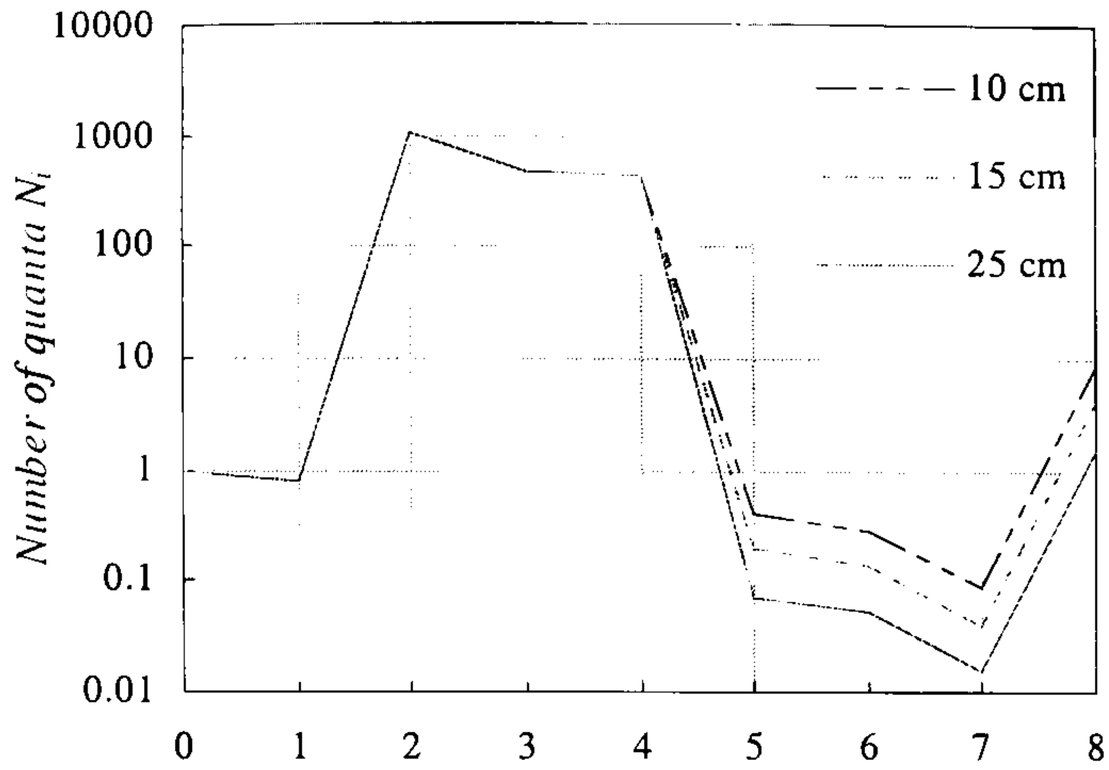

Figure 4.2. *QADs for the three square input field sizes for the L3 fluoroscopic system with M =100. This shows the number of quanta per incident x-ray in each stage. The stage with the greatest loss is stage 5. This is due to the poor collection efficiency of the lens. The quantum sink occurrs at stage 7 and is greatest for the largest field size because of the need for greater demagnification.*

4.2.5.2 Coupling efficiency

The coupling efficncy is given by the QAD and is equal to the number of quanta at stage 7. The predicted coupling efficiencies are 0.085 e^-x-ray^{-1}, 0.041 e^-x-ray^{-1} and 0.015 e^-x-ray^{-1} for field sizes of 10cm, 15cm and 25cm respectively.

4.2.5.3 Zero-Frequency DQE

Table 4.2 contains the calculated values of the zero-frequncy *DQE*. The *DQE*(*0*) has been calculated using equation 4.6 for four cases.

System one: To assess the efficiency of the system preceeding the CCD, the *DQE*(*0*) has been calculated for stages 1 to 7 only, without the addition of additive noise.

System two: The *DQE*(*0*) is calculated for a system that has a conventional CCD at stage 8 with a typical read out noise of 100 e^- r.m.s at MHz read out rates. In this case the *DQE* has been calculated for stages 1 to 7 and additive electronic system noise has been introduced at stage 7. This value of *DQE* is a function of the input x-ray quanta q_x, i.e. the larger the signal propagating through the system the smaller the effect that additive noise will have on the *DQE*. The factor $(\sigma_{a_7}^2 / \overline{N}_7)$ has been calculated using $\sigma_{a_7}^2 = (100)^2$ and $\overline{N}_7 = P_7 q_x$ where q_x is calculated for for an input dose rate of 0.5 μGys^{-1}.

Sytem three: The third system employs the L3CCD gain at stage 8. In this case the additive noise is the dark noise value for the CCD65-01 at room temperature and is added to stage 7. The *DQE* was calculated for the L3CCD gain required to amplify the signal ($\overline{N}_7$) above the system noise in order that SNR_{lim} is reached (see section 3.4.2) and M = 5000. $M_{SNR_{\text{lim}}}$ is calculated using equation 3.23. The value of system noise used was the CCD65-01 system noise, which is equal to 563 e^- r.m.s. This value is also used to calculate the additive electronic system noise.

System four: Is a system that incorporates a L3CCD at unity gain with additive dark noise, but no system noise.

Table 4.2. *Zero-frequency DQE values for the modelled fluoroscopic imaging system: (1) the DQE of the phosphor and optical system, (2) a conventional CCD based system with typical readout noise, (3) a L3CCD based system with thermal noise and measured system noise for two different gains and, (4) a L3CCD with additive thermal noise, but no gain or system noise.*

System	Additive Noise (electrons)	L3CCD gain	*DQE*(*0*) (%) 10 cm	*DQE*(*0*) (%) 15 cm	*DQE*(*0*) (%) 25 cm
1	×	×	8.3	3.9	1.5
2	$\sigma^2_{a_7} = 10000$	×	8.8×10^{-4}	4.4×10^{-5}	1.76×10^{-5}
3	$\sigma^2_{a_7} = 4.1$ $\sigma^2_{a_8} = 316969$	11264, 992, 628	0.031	0.013	0.003
3	$\sigma^2_{a_7} = 4.1$ $\sigma^2_{a_8} = 316969$	5000	0.13	0.07	0.03
4	$\sigma^2_{a_7} = 4.1$	×	1.4	0.67	0.26

The *DQE*(*0*) for system 1 is the maximum possible *DQE* of the imaging system described above, i.e. as if it were used in conjunction with a noiseless detector. Including the additive noise of a conventional CCD (system 2) results in a value of *DQE*(*0*) which is a factor of 10^5 lower than achieved in clinical fluoroscopic imaging units (50%). The results for system 3 which includes the L3CCD gain show that for $M_{SNR_{\text{lim}}}$, the *DQE*(*0*) remains unacceptably low. Increasing the gain increases the *DQE*(*0*). This is due to the fact that as gain is increased the system noise is rendered

increasingly neglible. As gain is increased the *DQE* will tend towards case 4, where the only additive noise is thermal noise.

4.2.5.4 Spatial resolution

Three input field sizes have been considered in the L3 fluoroscopic system. The limiting spatial resolution is calculated using equation 4.1 where Δx is the pixel size at the plane of the input phosphor. The limiting spatial resolutions were found to be 2.0 mm^{-1}, 1.6 mm^{-1} and 1.0 mm^{-1} for the 10cm, 15 cm and 25 cm field size, respectively and are satisfactory for fluoroscopic imaging.

4.2.5.5 Dynamic range

From the results given in table 4.2 it is shown that the maximum *DQE*(*0*) achievable with the CCD65-01 is 1.4%, 0.67% and 0.3% for 10cm, 15 cm and 25 cm field sizes respectively. Comparing systems 3 and 4, it is evident that a gain in excess of 5000 is required. The dynamic range of the CCD65-01 device is ~ 40 at M = 5000; gains that are greater than this will result in dynamic ranges that are only just acceptable to DSA and DSI. The dynamic range could be improved by using a cooled L3 device.

4.2.5.6 Conclusions about the model results

The QAD analysis has shown that a quantum sink occurs at stage 7 and that the greatest signal loss is due to the poor collection efficiency of the lens. Further losses are also attributed to the mirror and the FOFP, both of these can be removed from the system which would result in a small increase in *DQE*(*0*). The *DQE* analysis has shown that with adequate L3CCD gain, at clinical dose rates the upper limit of the *DQE*(*0*) for the 25 cm field is 0.3%, which is very low in comparison to existing clinical systems. This system would require a 20-fold increase in patient dose in order to achieve the same image quality. Accordingly, such a system would be unacceptable for clinical use. Clearly, the optical coupling needs to be improved if the L3CDD is to compete with the XRII.

An alternative method of coupling the optical quanta to the CCD is to use a fiber optic taper. In de-magnifying geometries, fused fiber optics are generally more efficient than

lenses. The collection efficiency of a fiber optic taper is given by: (Yaffe and Rowlands, 1997)

$$F_c T_F \frac{NA^2}{m^2} \tag{4.13}$$

A taper with 10 times demagnification (m = 10) has a collection efficiency of 0.7%. If such a taper was to couple the L3CCD to a $10 \times 10 cm^2$ phosphor screen then the system would have an upper $DQE(0)$ limit of 47% (not including additive noise sources) which would be comparable to an XRII system. From equation 4.13, we can see that similar to the lens, the collection efficiency of the taper is inversely proportional to the m^2. Consequently, a more efficient system would be realized if smaller demagnification factors were employed and the area was covered by tiling a series of L3CCDs. Equally, the smaller demagnification factors could be used if a larger L3CCD was manufactured. Tapers with demagnification factors greater than 5 are rare and extremely expensive, thus a L3CCD fluoroscopic imaging system would have to employ several sensors to achieve large image areas.

An example of a feasible L3 system would employ 4×4 tiled CCD65 devices using a 5:1 taper on each covering a 5×5 cm^2 area of phosphor. The efficiency of the fiber optic is 2.9 %. Using equation 4.6 for a L3CCD that is cooled to –7 °C has a nominal read out noise performance of 100 e^- r.m.s., and is operated at a gain of 10,000, the $DQE(0)$ is equal to 67% at 0.5 μGys^{-1}. Such system would have a limiting resolution of 10 $lpmm^{-1}$, a field coverage of 20 cm and a dynamic range of ~ 100. All of these criteria out perform the XRII. The L3CCD system would have a coupling efficiency of 2.7 e^-x-ray^{-1}, which may result in the loss of DQE at higher spatial frequencies (Maidment and Yaffe, 1994). However, the XRII system also displays DQE losses at higher spatial frequencies due to x-ray and light scattering within the image intensifier tube (Marshall, 2001).

It is worth mentioning that if this system were to incorporate a conventional CCD the number of secondary quanta generated in the CCD would be $2.7 \times 3.9 = 10$ electrons per pixel per field for 0.5 μGys^{-1}. The conventional CCD system noise is approximately

100 e^- r.m.s. which lead to an unacceptable *SNR* of ~ 0.1. Thus such a system is only possible with a CCD that incorporates an intensification stage. The benefits of a phosphor/taper/L3CCD system with an equal *DQE* to the XRII system would be its smaller size, lower spatial distortion, non-susceptibility to electro-magnetic interference and linear response characteristics (Tate *et al.*, 1997).

4.3 L3 fluoroscopic system measurements

The zero-frequency QAD analysis has shown that in order to produce an efficient L3 based fluoroscopic system, the modelled system would require considerable improvements in the optical coupling. A taper/L3CCD system has been proposed on the basis of the results of the model. Using the QAD analysis an approximate quantification of the required increase in the *DQE*(*0*) of the prototype system has been made. It was felt that this work had reached an appropriate conclusion in terms of identifying the suitability of an L3CCD based system for fluoroscopy. The costly construction of such a system was deemed outside the scope of this thesis, so it was decided to qualify the result and validate the model by measuring the zero-frequency *DQE* and the coupling efficiency of the laboratory imaging system described in section 4.2. Additionally, a measurement of the spatial frequency dependant *DQE* (*DQE*(*f*)) of the whole system will be obtained. The measurement of DQE(*f*) will provide information about the signal and noise transfer characteristics of the system and will help to predict whether or not the value of *DQE* is underestimated.

4.3.1 System linearity, zero-frequency DQE and coupling efficiency

To assess the system linearity and to calculate the coupling efficiency the output *SNR* was measured as a function of input dose. The x-ray source used was a MEM (Model: EXEL) tungsten target source. A tube potential of 80kVp with 2.5mm of aluminium filtration was employed. The optics in the imaging system were arranged such that an input field of size $10 \times 9 cm^2$ could be imaged i.e. the demagnification of the system was arranged to be $m = 10$. Dose rate measurements were preformed using a dosimeter

(Keithly model no. 35050A) and ion chamber (Keithly model no. 96035A) positioned at the same distance from the x-ray tube focal spot (FSD) as the phosphor screen. The dose rate was varied by altering both the tube current and the FSD. The dose rate ranged from $25\mu Gys^{-1}$ to $1.45 \times 10^4 \mu Gys^{-1}$. The minimum dose rate that could be determined was limited due to the insufficient sensitivity of the ion chamber. The L3CCD multiplication gain was decreased as the dose rate was increased in order to avoid saturation of the camera. For each measurement the gain was adjusted so that the signal level was at half full well capacity. Measurements of the SNR were obtained from uniformly exposed x-ray images. The flatness of the field was assessed using the technique described in section 3.2 and found to be uniform to within ± 3%. At each dose rate a total of 50 images were acquired. All images were corrected for fixed pattern noise and dark level using the algorithm described in section 3.1.7. The mean signal and standard deviation was found in each image. The result was averaged over the 50 images giving a standard deviation 6%. Figure 4.3 shows the variation of SNR_o^2 as a function of input dose rate where SNR_o^2 is the output signal to noise ratios squared.

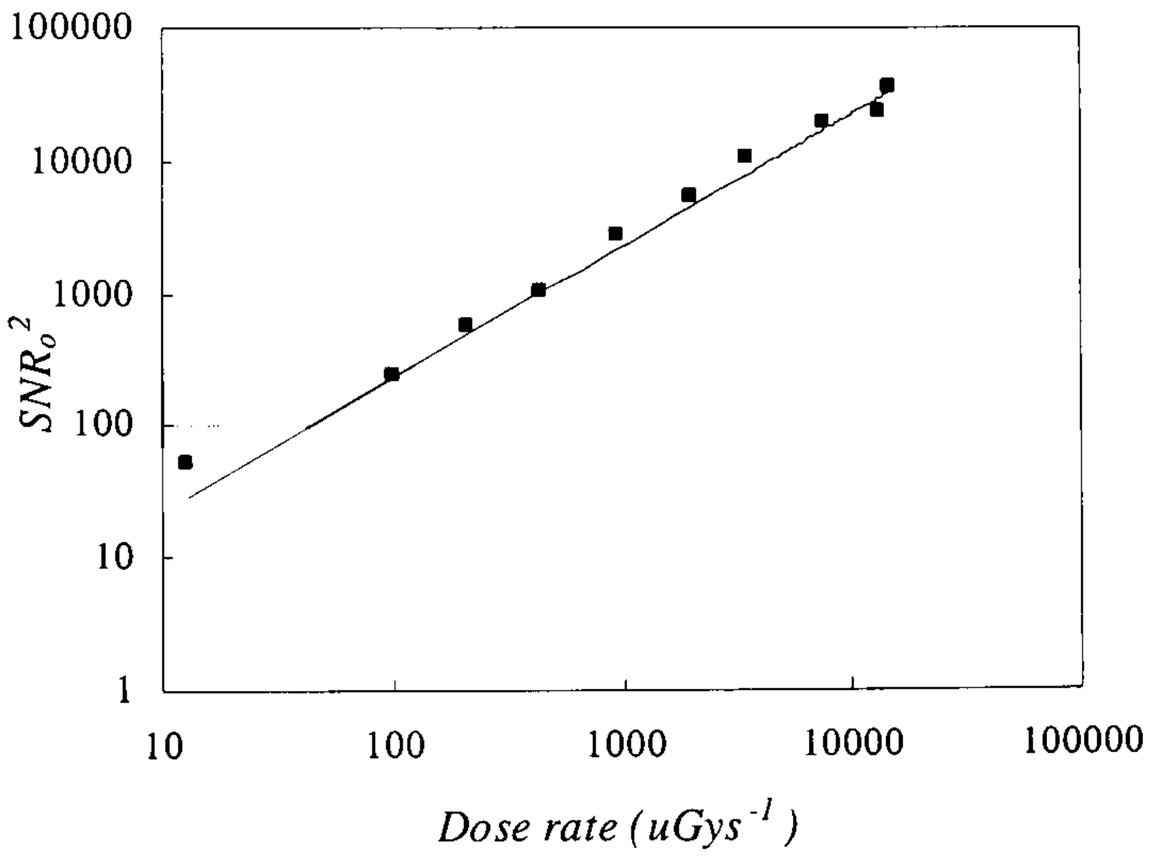

Figure 4.3. *Measured variation of SNR with incident dose rate. The line shows a linear regression fit.*

The line of best fit is linear and a linear regression analysis gives a 99.8% goodness of fit. This shows that the system has a linear dose response over the range of dose rates and multiplication gains measured.

DQE which includes the effects of additive noise, is a function of the input signal and the L3CCD gain. For each measurement of *SNR* a different level of gain was used in

order to keep the signal level within the dynamic range of the device. Validation of the *DQE* analysis requires the comparison of measured and predicted values, thus the *DQE*(*0*) for each measurement point was calculated using the correct levels of x-ray input flux and multiplication gain. The measured *DQE*(*0*) is found by evaluating equation 1.1. SNR_i^2 is equal to the number of x-ray quanta per image pixel at the plane of the phosphor, q_x, which was calculated using spectral data from Birch and Marshall (1979). The catalogue data gives a value of 20063 x-ray $mm^{-2}\mu Gys^{-1}$. The number of quanta per pixel per frame was calculated using equation 4.8 to be 24 at a dose rate of $1\mu Gys^{-1}$. The measured *DQE*(*0*) is found by dividing SNR_o^2 by $M^2 SNR_i^2$. Measured values of DQE are compared to the predicted values in figure 4.4.

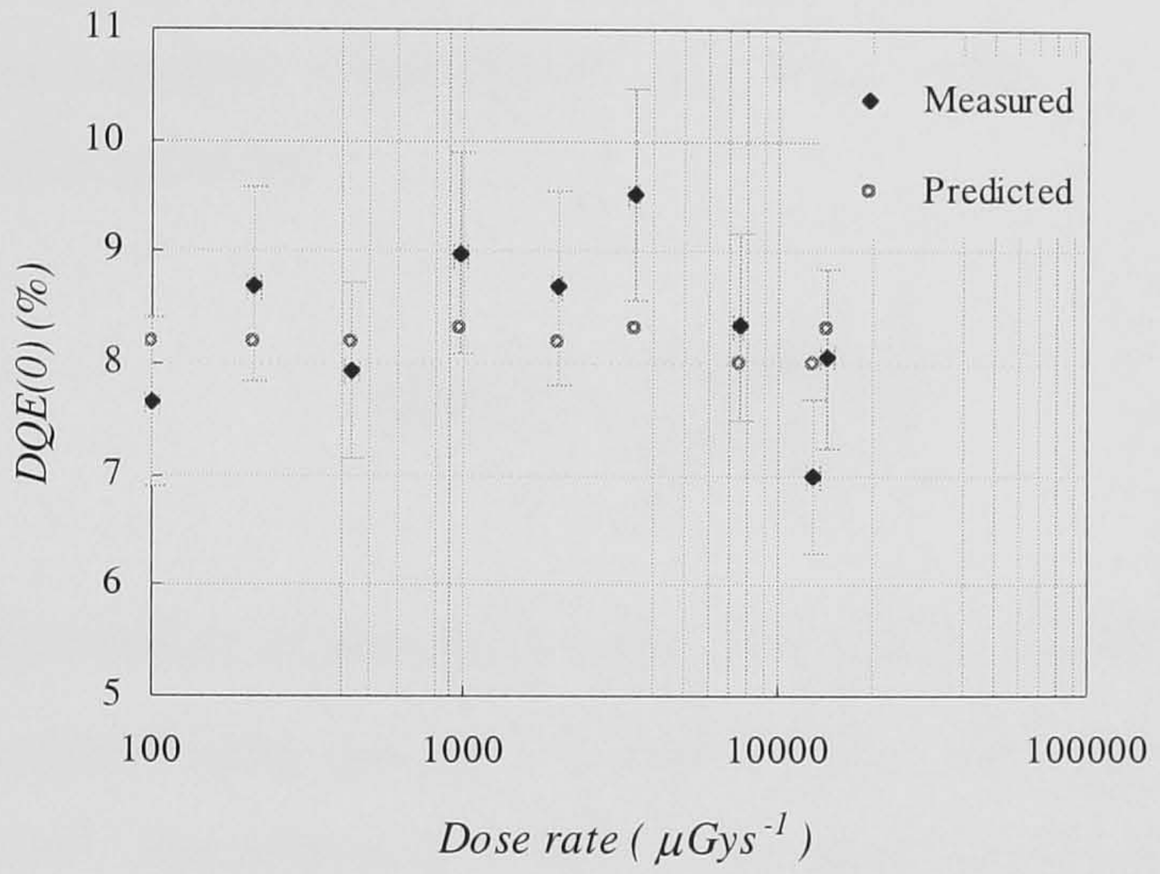

Figure 4.4. *Comparison of predicted and measured DQE(0). Predicted values have been calculated using* $\sigma_{a_8}^2$ *= the variance of the CCD65-01 read noise*

Predicted and measured values of *DQE*(*0*) agree reasonably well and show that the model can predict the *DQE*(*0*) within ± 20%. The measured values of *DQE*(*0*) are all approaching the maximum value of 8.3%, which was predicted from the QAD analysis. This is expected because the high levels of input dose rate mean that high signal levels are propagated through the system and both dark and read out noise are negligible in comparison.

The coupling efficiency was calculated from q_x per unit dose rate and the mean signal in electrons per unit dose rate. Similar to SNR_o^2, the latter was found by finding the mean

signal in DN, dividing by the multiplication gain, calculating the slope of a linear fit and multiplying it by the conversion factor *C*. The measured coupling efficiency was found to be 0.062, which agrees well with the predicted value in section given in section 4.2.5.2.

4.3.2 Frequency dependant detective quantum efficiency

The spatial frequency dependant detective quantum efficiency, *DQE(f)*, describes the transfer of signal to noise ratio from the input to the output of the detector. The signal modulation is described by the system modulation transfer function *MTF(f)*, whilst the noise transfer is characterised by the noise Weiner spectrum, *NPS(f)*. It can be shown that for a linear system (Cunningham and Shaw, 1999) the measured frequency dependant *DQE* is given by:

$$DQE(f) = \frac{d^2 MTF^2(f)}{\bar{q}_0 NPS_{DN}(f)} \tag{4.13}$$

where $\bar{q}_0$ is the number of photons per unit area incident on the detector (mm^{-2}) and d is the average signal value per pixel in digital units. $NPS_{DN}(f)$ is the output *NPS* in units of DN^2mm^2. The following describes the measurements that were performed to obtain the *MTF(f)* and *NPS(f)* and the evaluation of *DQE(f)*.

4.3.2.1 Modulation transfer function

When an object is imaged by a radiographic system the spatial distribution of the object is degraded by the resolution properties of the imaging system, and various noise sources are superimposed on the image. The analysis in section 4.2 has shown that high gains may be required to overcome the high system noise. To investigate the transfer of signal through the system and the effect of the use of high gain to compensate for low input signal, the resolution of the imaging system was measured for four levels of coupling efficiency.

The *MTF* can be calculated from the Line Spread Function (*LSF*) using the fact that there exists a simple relationship between them. The *MTF* of the system is given by the one-dimensional Fourier transform of the *LSF*. The *LSF* can be obtained by differentiating the response of the imaging system to a sharp edge, the Edge Spread Function (*ESF*). The pre-sampling *MTF* was measured based upon the extended edge technique (Cunningham and Fenster, 1987). This method eliminates the problems that can be caused by under-sampling of the *LSF* (Judy, 1976). The *ESF* was provided by positioning a 0.5mm hardened steel plate with a straight edge in contact with the x-ray tube side of the phosphor screen, between the screen and the x-ray source. The edge was placed at an angle of approximately 3° with respect to the columns of the CCD, thereby forming an image with one *ESF* in a number of columns. Images were then corrected for FPN. The displaced *ESF*s were aligned and averaged to obtain a single composite over-sampled profile. The composite *ESF* was obtained by using 20 individual *ESF*s. This over-sampled ESF was then numerically differentiated to obtain the *LSF*. The Fourier transform of the normalised *LSF* was found to obtain the *MTF*. *MTF*s were measured for four different optical coupling efficiencies. This was achieved by placing ND filters between the lens and the mirror. The ND filters were chosen to reduce the coupling efficiency rather than changing the $F_{\#}$ of the lens which could change the inherent resolution of the phosphor screen (Maidment and Yaffe, 1994). In order to compensate for the loss of incident light, the gain was adjusted so that the average number of DN/per pixel in the digitised image remained constant throughout the experiment at half the full well capacity.

ND filters of optical densities (ODs) 0.6, 1.6 and 2.6 were inserted between the mirror and the lens. The values for the ND filters are quoted to be within ± 10%. The values of gain used to compensate for the lower exposure levels were 4, 45 and 500 respectively. *MTF*s have been corrected for the demagnification of the imaging system and are therefore quoted for the image at the plane of the phosphor.

The results of *MTF* measurement show that the data are indistinguishable within experimental error. The *MTF* falls to 10% at ~ 0.4 mm^{-1}. Cowen and Workman (1992) assessed a clinical digital spot fluoroscopy system. The *MTF* was found to be 10 % at ~ 1.25 mm^{-1} for a 15 cm field size. However, the comparison of the four optical coupling efficiencies has shown that the gain has not affected the resolution properties of the

system. Therefore, the use of multiplication gain to overcome system electronic noise in a de-magnified system will not impair the imaging performance.

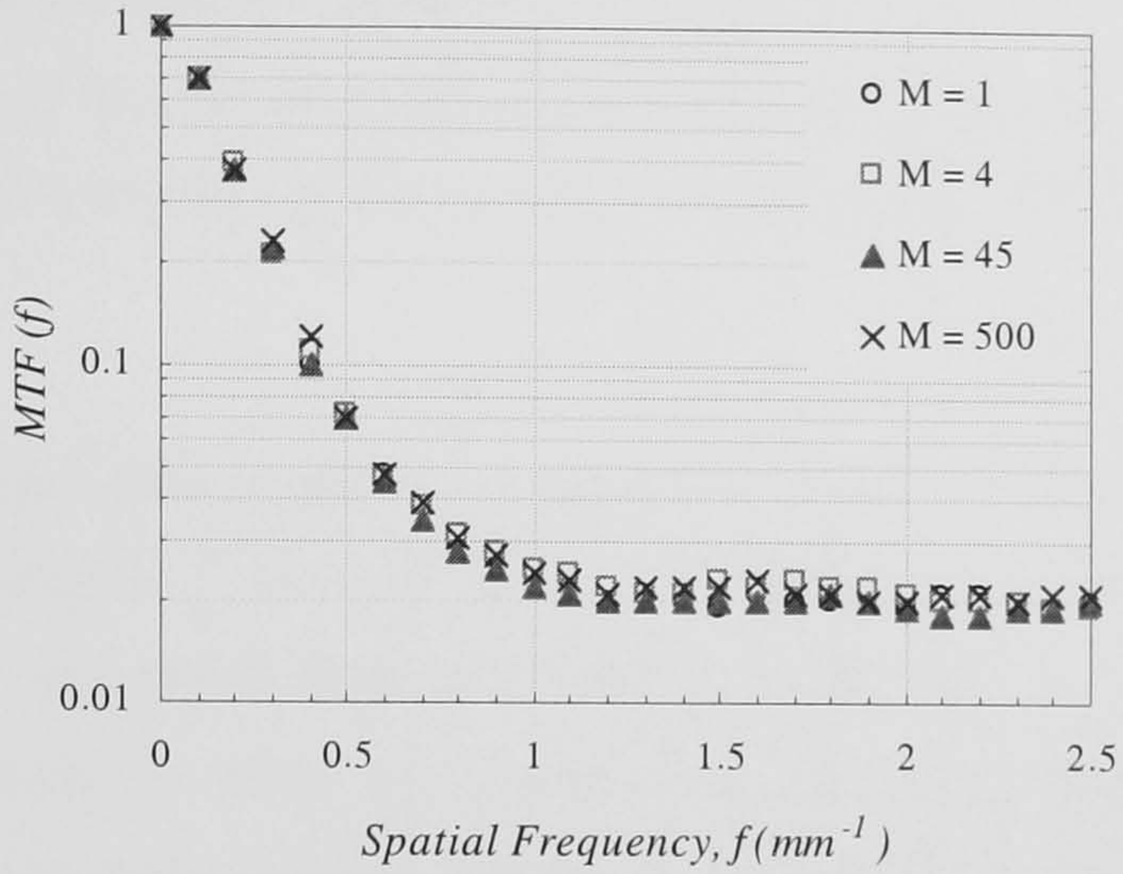

Figure 4.5. *The MTF of the imaging system with different levels of gain used to compensate fall in coupling efficiency affected by the use of ND filters.*

4.3.2.2 Noise power spectra

The variance in the digital signal has previously been used to describe the magnitude of the noise. The Noise Power Spectra provides information about the spatial and temporal characteristics of the image noise (Dainty and Shaw, 1974).

Measurements of the Noise Power Spectrum (*NPS*) were made using the direct Fourier transform method (Vedantham *et al.*, 2000, Wagner, 1977). Image data used to calculate the NPS was acquired with the phosphor screen uniformly irradiated with x-rays at a dose rate of $100\mu Gys^{-1}$. All images were corrected FPN and dark images were subtracted. The data was summed in one direction to synthesize the effect of a scanning slit with a width of 1 pixel ($30\mu m$) and a length of 100 pixels (2mm). The slit was scanned across the image to produce a 2-D data sample; this was performed for 20 images. Each sample was 256 elements long, allowing the calculation of spectral estimates for spatial frequencies between $0.2mm^{-1}$ and $48.6mm^{-1}$.

In order to reduce random error in the spectral estimates a large number of data samples were obtained by subtracting the data samples from each other. Using a computer

program this created 190 data samples giving an uncertainty of ~7%. The program comprised of a short routine that subtracted images 2 to 20 from image 1, then images 3 to 20 from image 2 and so on. The subtraction process increases the image variance by a factor of two and therefore all measurements of noise power were corrected by dividing by 2. Noise power spectra were obtained from the direct Fourier transform of the data samples. In each case data was normalized to the average digital signal per pixel in each image.

Noise power spectra data are shown in figure 4.6. Data has been binned into 0.4mm^{-1} intervals and averaged. Typically, for x-ray imaging systems of this kind, the noise power is high at low spatial frequencies and gradually falls of with increasing spatial frequency; this trend is a result of x-ray quantum mottle (Maidment and Yaffe, 1994). However, the noise power spectra shown here demonstrate a flat response with spatial frequency.

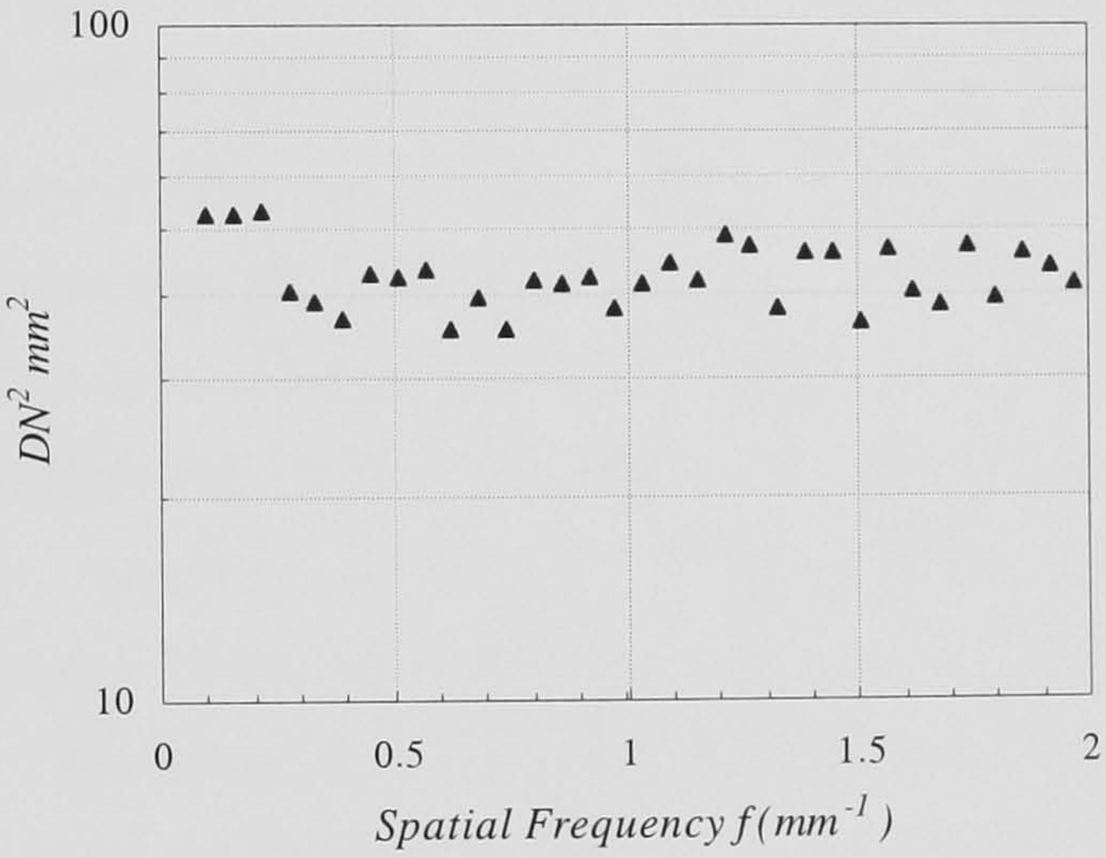

Figure 4.6. *Noise power spectra for the L3 fluoroscopic imaging system. Data has been binned into 0.4 mm^{-1} intervals and averaged.*

Maidment and Yaffe (1994) have shown that poor coupling efficiencies have been shown to effect the auto correlation function (*ACF*) of the spatial distribution of the electrons recorded by the CCD. This is a result of the reduced number of photons incident on the CCD. As a result of poor correlation and the shape of the *ACF* changes. The *NPS* increases at higher spatial frequencies, resulting in a flattening of the *NPS*.

4.3.2.3 Frequency dependant DQE

The *DQE(f)* was calculated using equation 4.14 and is shown in figure 4.7.

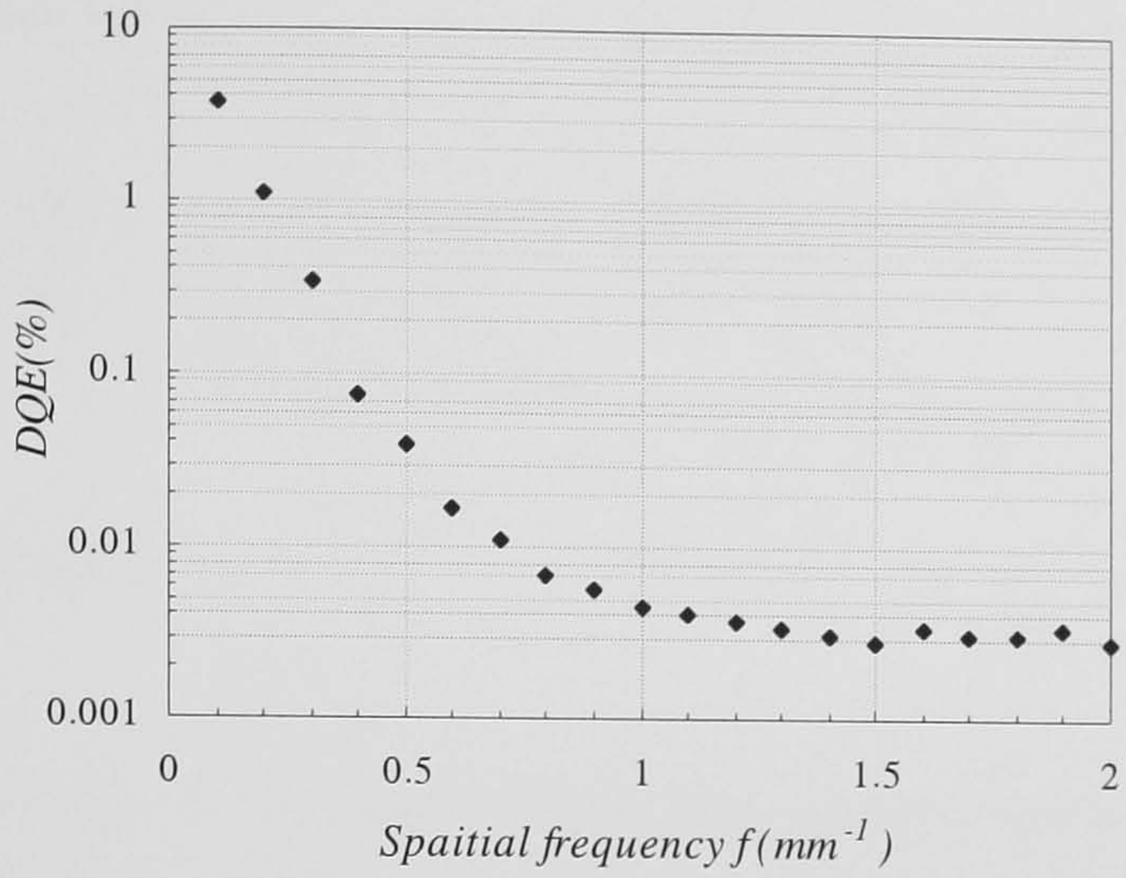

Figure 4.7. *The DQE as a function of spatial resolution for the L3 fluoroscopic imaging system.*

The *DQE(f)* shows a rapid fall off with increasing spatial frequency. Marshall (1994) has measured *DQE(f)* for three clinical digital fluoroscopy systems. He has presented results that show factors of 7, 3.5 and 1 reduction in *DQE* between spatial frequency values 0.1 and 1mm^{-1} for these three systems. Similarly, measurements made by Cowen and Workman (1992), on a digital spot fluoroscopy system predict a factor of 4 reduction in *DQE* between spatial frequency values 0.1 and 1 mm^{-1}. Figure 4.6 shows a reduction which is 3 orders of magnitude between the same spatial frequency values. The poor *DQE* performance of the L3 system is a result of the high *NPS* at higher spatial frequencies. Typically, and it is shown in the papers of Marshall (1994), and Cowen and Workman (1992), the noise power decreases as a function of increasing spatial frequency. The reduction in *NPS*, the denominator in equation 4.13, increases the *DQE*. However, as discussed in section 4.3.2.2, the *NPS* is high at higher spatial frequencies due to the poor coupling efficiency.

Drake *et al.*, (2000) have developed a fluoroscopic imaging system for use in radiotherapy patient set up. Using a conventional CCD in an almost identical set up to the modelled and experimental system described above they have measured an *MTF* value of 10% at 0.5 mm^{-1} and a *DQE(0)* of 10%. A fluoroscopic patient set up system (portal imaging system) places less demand on spatial resolution because it is only intended to quantify and correct patient set up errors and is not for use in diagnostic work. Equally, *DQE* requirements are less demanding because the imaging is part of the overall radiotherapy treatment and therefore higher doses are justifiable. As part of

the analysis given in section 2.2 it was shown that a further degradation in *SNR* occurs due to electronic additive noise. Clearly, an L3 based system could meet the requirements of portal imaging systems without the expense of realising optimal coupling efficiencies.

4.4 Conclusions

To assess the feasibility of a L3 based fluoroscopic imaging system, a prototype system has been evaluated theoretically. In order to predict the zero-frequency *DQE*, the system has been modelled using linear systems analysis. A quantum accounting diagram has shown that despite the L3 multiplication gain, inefficient optical coupling will result in a large quantum sink and thus, poor *DQE*. The use of a lens has been shown to be particularity problematic even at low demagnification factors, i.e. low input field sizes. The inefficiency of the lens leads to poor coupling efficiency, which was calculated to be 0.085 e^-x-ray^{-1}. Work by Cunningham *et al.* (1994) has shown that the coupling efficiency should be >1 e^-x-ray^{-1} for quantum noise limited imaging at zero-frequency.

For the smallest field size evaluated, 10 cm, the maximum *DQE(0)* was calculated to be 8.3 % at 0.5 μGys^{-1}, however, when consideration is given to the thermal noise in the L3 the *DQE* falls to 1.3%. This value of *DQE* is ~50 times lower than acceptable in clinical practice. As a result of the findings the model has been used to suggest an alternative arrangement of an L3 based fluoroscopic system. This alternative system would employ a fibre-optic taper to couple the light from the phosphor to the L3CCD. Calculations have shown that if using a fibre optic a coupling efficiency of 2.7 e^-x-ray^{-1} could be achieved for a taper with $m = 5$. Consideration of the additive electronic noise sources has shown that a conventional CCD would be unsuitable for such a system and it would only be feasible using an L3CCD. Measurements of the zero-frequency *DQE* have been made in order to validate the model and its predictions. Comparison of the measured *DQE(0)* and the predicted values have shown that the model can predict the *DQE(0)* within ± 20%. Measurements have shown that as a result of the poor coupling efficiency, the system has a reduced *DQE(f)* at high spatial frequencies, thus,

confirming that any system, based upon the L3 must have sufficient optical coupling efficiency.

In conclusion, it has been shown that a small field L3/taper fluoroscopic system is feasible. Such a system would have improved spatial resolution and a competitive *DQE*. Coupled with the fact that the CCD system would be less bulky, would not suffer from spatial distortion nor susceptibility to magnetic fields and does not require high voltages, an L3-based fluoroscopy system is worth investing in. Comparison with a portal imaging system shows that the proposed L3/taper system has a $DQE(0)$ of seven times greater than the system designed by Drake *et al.* (2000), indicating that the L3 system could result in either a seven-fold dose saving or greater image quality, which would improve patient positioning and therefore radiotherapy treatment accuracy.

CHAPTER 5

L3 technology application to medical imaging: Diffraction enhanced breast imaging

Mammography has 90% sensitivity, i.e. about 10% of carcinomas are not detected during the mammographic examination. In x-ray mammography, distinction between tissue types is dependent upon differences in linear attenuation coefficient. The difference between the linear attenuation coefficient of fibro-glandular tissue and that of carcinoma is extremely small. At 17.4keV, which is the most effective energy in current transmission x-ray mammography, the difference is 5%. This results in low contrast in the image. The contrast is further reduced by the abundance of scattered radiation reaching the image plane. For a typical non-collimated mammography system the ratio of the primary radiation to the scattered radiation can be as low as 50%. As a result, carcinomas with a diameter of less than ~1cm are detectable only through indirect signs, such as micro-calcifications or distortion of the normal breast architecture, which are associated with the presence of carcinoma.

Using an energy dispersive x-ray diffraction technique, Kidane *et al.* (1999) have demonstrated that there is a detectable difference in the shape of the scattering energy distribution from healthy and diseased breast tissue. Furthermore, this difference results in an image contrast between the tissues that was found to be higher than conventional transmission image contrast. This indicates that scattered radiation can be used to improve the conventional mammogram. Work by Chapman *et al.*, (1997), Lewis *et al.* (2000) and Fernandez *et al.* (2002) have published results that show that there are detectable difference between diseased and normal breast tissues using x-ray diffraction, hence confirming the results of Kidane *et al.*, (1999). Using a high angular resolution diffractometry technique and a synchrotron radiation source, Lewis *et al.* (2000) have also shown differences in the peak signal momentum transfer values of benign and cancerous breast tissues.

DEBI employs coherently scattered radiation. The ratio of intensities between coherently scattered and transmitted photons is about 10^{-3} for a typical breast examination. Ideally the radiation dose to the patient would not be increased to collect the scatter image. The small signal levels involved require that a detector with high sensitivity be employed so that all the scattered radiation is detected. If a clinical system is to be realised a suitable detector must be identified.

This chapter describes the work that has been undertaken to assess the suitability of L3 technology to the application of DEBI. Diffraction images acquired using an L3 detector, designed for use in DEBI, are presented here. This work is intended to be a continuation of work previously undertaken at the Department of Medical Physics, UCL by Kidane (2001) in order to advance the technique towards clinical application.

5.1 Diffraction enhanced breast imaging

5.1.1 Physics of diffraction mammography

There are two types of scatter during diagnostic x-ray examinations. Small-angle x-ray scatter (<10°) is predominantly coherent (so-called Rayleigh scatter). The magnitude of the Rayleigh scatter is governed by an appropriate form factor. At larger scattering angles, incoherent photon scattering (or Compton scatter) is dominant and forms a structureless background. Taibi *et al.* (2000) have shown, through the use of a Monte Carlo simulation, that the ratio of coherent scatter to incoherent scatter is as high as 200:1 at a scatter angle of 9°. Diffraction enhanced breast imaging is based upon the signal that is obtained from Rayleigh scatter. Typically, Raleigh scatter is described using the differential coherent scattering cross section, which is written as the product of the Thompson (free electron) cross section multiplied by a form factor (Johns and Cunningham, 1987):

$$\frac{d\sigma_{coh}}{d\Omega} = \frac{r_0^2}{2}(1+\cos\theta)\left[F^2(x,Z)\right] \qquad (5.1)$$

where $d\Omega$ is the solid angle subtended by the detector, r_0 is the classical electron radius, $F^2(x,Z)$ is the atomic form factor and x is the momentum transferred to the photon causing it to be deflected through an angle θ and is given by:

$$x = \frac{1}{\lambda}\sin\left(\frac{\theta}{2}\right) = \frac{E}{hc}\sin\left(\frac{\theta}{2}\right) \tag{5.2}$$

where λ and E are the wavelength and energy of the incident x-ray photon.

In condensed states of matter the atomic form factor should be modified to take into account interference effects in the coherent scattering from neighbouring atoms. The differential coherent scatter cross section can then be expressed as:

$$\frac{d\sigma_{coh}}{d\Omega} = \frac{r_0^2}{2}(1+\cos\theta)\left[F_m{}^2(x,Z)\right] \tag{5.3}$$

where $F_m{}^2(x,Z)$ is the molecular form factor. For a thorough explanation of the differential coherent scatter cross section, the reader is referred to Johns and Yaffe (1996).

5.1.2 Description of DEBI work undertaken at UCL

The following is a brief summary of some the work that has been carried out by Kidane *et al.* (1999). This work was initiated to measure the level of contrast between the intensities of scattered radiation from diseased and normal breast issues, and to assess the feasibility of using this information in a clinical environment. A detailed account of this work is given by Kidane (2001).

5.1.2.1 Distinction between diseased and normal tissue

The differential coherent scattering coefficients from samples of pure carcinoma, pure fibro-glandular tissue and normal breast tissue (50:50 fat/fibrous mixture) were measured and compared. Scatter signatures were measured using an energy dispersive x-ray diffraction technique in which the scatter of a poly-energetic x-ray source is measured at a fixed scattering angle. The results are shown in figure 5.1. It can be seen

that the scatter signature from carcinoma shows a significant difference from the scatter signature of normal breast tissue. From this work two regions of momentum transfer (~1.1nm^{-1} and ~1.6nm^{-1}) were identified as providing the highest contrast between diseased and normal breast tissue. The scatter contrast is given by

$$c = \frac{[\chi_h - \chi_d]}{[\chi_h + \chi_d]} \tag{5.4}$$

where χ_h and χ_d are the linear differential scattering coefficients for healthy tissue and carcinoma respectively given in figure 5.1. At 1.1nm^{-1} the scatter contrast of normal tissue to carcinoma was found to be 51%. This is significantly larger than the equivalent contrast of only 5% generated by the linear attenuation coefficient.

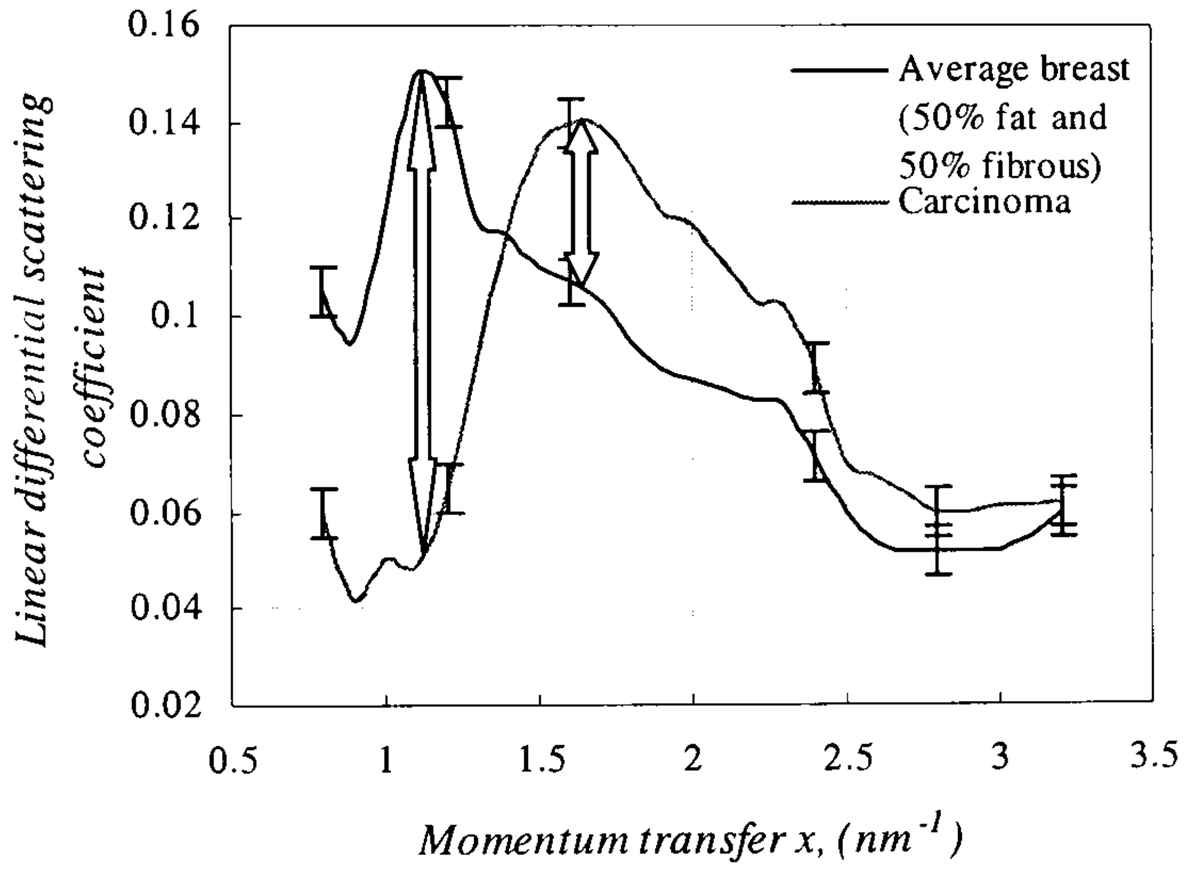

Figure 5.1. *Comparison of the scatter signatures for the 'pure' carcinoma sample with that of normal breast tissue (50:50 fat/fibrous mixture). Momentum transfer values that provide the higher contrast between diseased and normal breast tissues are shown.*

5.1.2.2. Breast imaging

In order to assess the feasibility of using diffraction techniques to improve the contrast of conventional radiography a 'spectral selective momentum transfer imaging system (SSMTI)' was designed for the purpose of acquiring scatter images. Figure 5.1 shows the greatest difference between breast tissue types at a momentum transfer value of 1.1nm^{-1}. This corresponds to a scatter angle of 9° at the predominant mammographic x-ray energy of 17.4keV. A pencil beam of radiation was used to image a human tissue

phantom that was constructed of cancerous tissue inclusions (of 9mm, 4mm, 3.5mm and 2mm thickness) in a bulk of healthy tissue. Transmitted radiation was detected using a small CsI(Tl) crystal coupled to a PMT via a fibre optic. Amorphous materials produce circularly symmetric scatter signatures around the primary direction. Scattered radiation was collimated using an annular collimator at 9°. This ensures that all photons scattered at 9° are collected from the entire circumference of the pencil beam. Scattered photons were detected using a 5cm diameter NaI(Tl) detector with an energy resolution of 1.4keV at 17.4keV. All cancerous tissues were better resolved in the scatter image, whilst the general visibility was poor in the transmission image. On average contrast between normal and diseased tissue was measured to be 50% higher in the scatter image than in the transmission image (Kidane 2001).

The measurements described above have confirmed that the contrast information from the scattered radiation is greater than that of the transmitted. It also confirms the feasibility of the diffraction technique and illustrates that there is a potential for scatter imaging to be used for screening in conjunction with conventional transmission mammography to improve the contrast of the images.

The system described above was designed only to assess the feasibility of the technique; it has restricted performance and is impractical for clinical work. The system employs a pencil beam of radiation. The patient remains stationary during the examination, thus the beam and the detector must be scanned. The breast examination is performed with the breast under compression, this reduces non-uniformities in attenuation and helps to visualise overlying structures within the breast. Breast compression is restricted to 1 second in order to minimise patient discomfort. Consequently, a scanning pencil beam system would have to employ rapid 2-dimensional movement to scan the whole breast. Achieving this is costly and as a result scanning pencil beam systems are not typically found in routine diagnostic use (Yaffe, 2001). It is intended that diffraction imaging will be used as a complimentary technique to conventional breast imaging. The above system does not easily facilitate the simultaneous acquisition of the transmission and scattered images.

5.1.3 Proposed clinical DEBI system

The viability of diffraction imaging relies heavily upon its practical implementation in the clinical environment. A suitable DEBI system would be based upon a linear scanning array. Linear scanning arrays are already widely employed in digital mammography systems (Yaffe 2001). A proposed clinical system is shown in figure 5.2. A slot collimator is used to form a line of radiation. A linear detector array is used to scan across the breast following the movement of the radiation beam. Ideally one detector would be employed to acquire both the transmitted and the scattered radiation simultaneously. This is achieved using a tri-directional collimator, which is shown in figure 5.2.

The collimator is designed to collect radiation at the required scattering angle either side of the linear beam of radiation. The transmitted radiation would be allowed to pass through the middle of the collimator. Perceivably this design could easily be incorporated into existing linear array mammography systems with no requirement to increase the examination times. Using the same detector for the detection of transmitted and scattered radiation also helps to minimise the cost of implementing such a system.

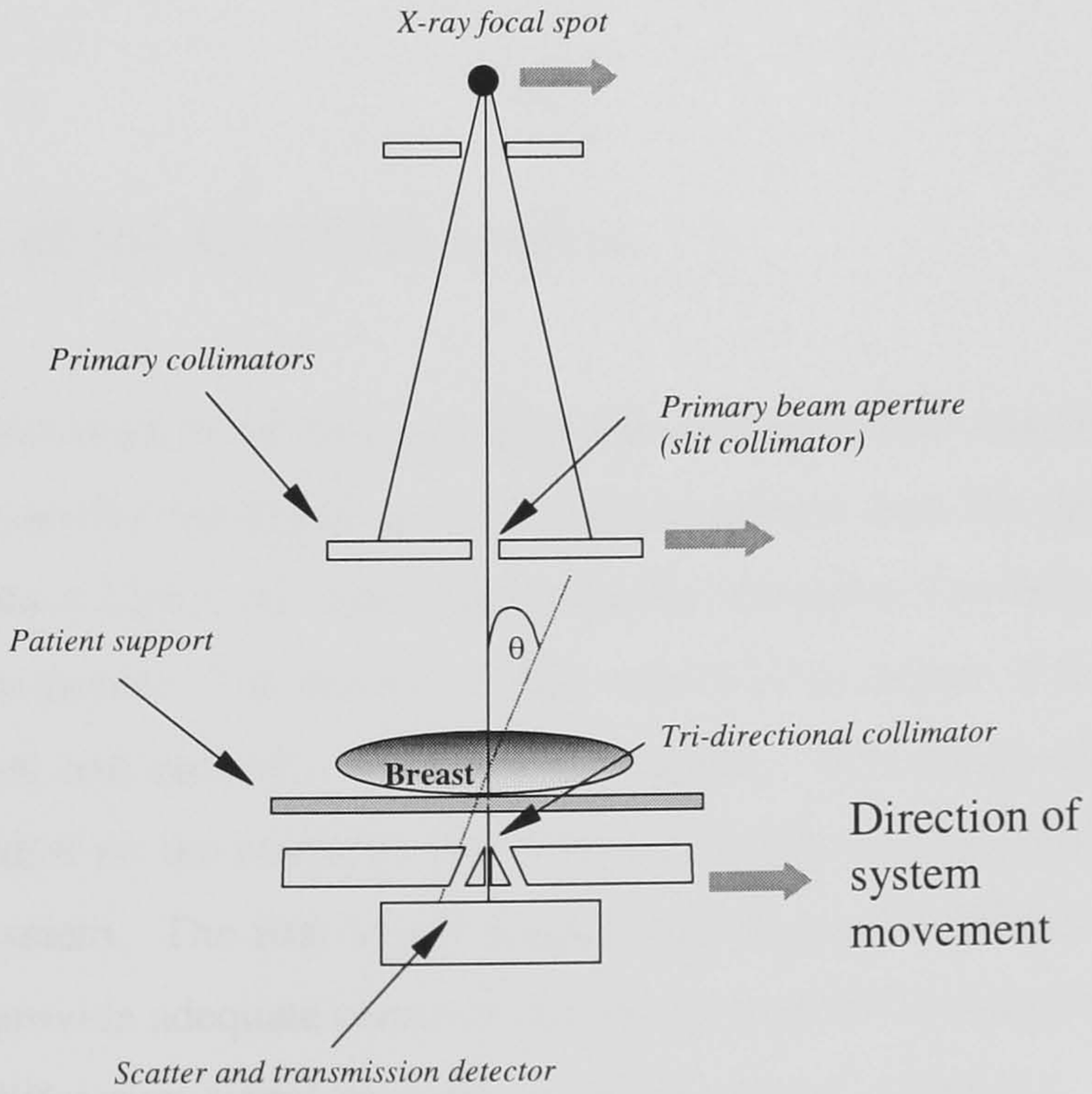

Figure 5.2. *The proposed DEBI system.*

5.1.4 Aims and objectives of this work

DEBI will increase the sensitivity of the mammographic examination. The intention is to bring this technique to the clinical environment and therefore a suitable imaging system must be employed. Discussion of the requirements of a potential detector for a clinical DEBI imaging system in section 3.7.3.2 has shown that the L3CCD has potential as a suitable detector. It was the aim of this work that the viability of an L3-based DEBI system be experimentally verified. This has involved designing a suitable L3 detector, designing and building an experimental imaging system and collecting diffraction data. A synchrotron x-ray source offers the best conditions to conduct an experiment to this aim. The synchrotron facility offers high photon fluxes providing short experimental times. It is a tuneable mono-energetic source, which can facilitate an investigation into different momentum transfer space without the need to employ smaller angles. Additionally, it offers an accurate collimation and alignment system and there is little beam divergence in the vertical direction (1.7×10^{-5}°), assisting accurate definition of the scatter volume. Therefore, in order to verify the feasibility of an L3 based DEBI system, the L3 detector has been taken to the synchrotron source at ELETTRA, Trieste, Italy to collect diffraction data from human breast tissue.

5.2 Design of the L3 DEBI system

The important parameters in the design consideration of the DEBI imaging system were the momentum transfer resolution of the imaging system and the design of an L3 detector. Using the CCD65, the momentum transfer resolution was defined exclusively by the collimation system. The purpose of this section is the design of firstly, a suitable collimation system and secondly, the detection system. The design of a suitable L3 detector is dependent on the available scatter signal, which is in turn is dependent upon the collimation system. The first step towards establishing the viability of a L3 based system that will provide adequate contrast between normal and diseased breast tissues is to calculate the diffraction signal available from an optimal collimator. To initiate the design process a model of a diffraction imaging system will be developed.

5.2.1 Components of the diffraction imaging system

The following is a description of the components of the diffraction imaging system that will be modelled. The imaging system comprises of four main components: the x-ray source, the scatterer which for the purpose the model development will be considered to be a block of tissue, the collimation system and the detector.

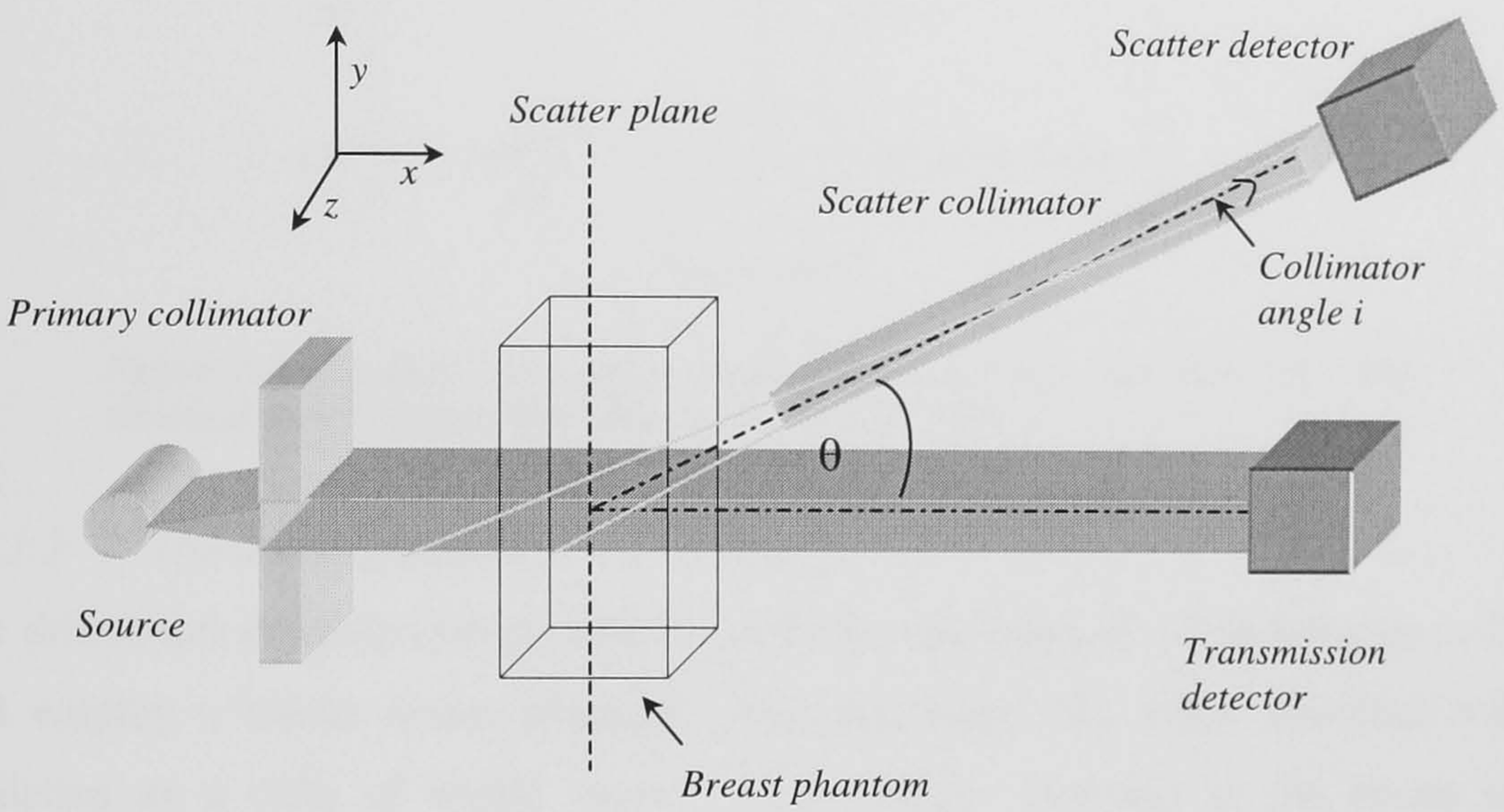

Figure 5.3. *A schematic of a diffraction set-up. The collimated beam passes through the breast, some x-rays are scattered and collected within the scatter collimator.*

Figure 5.3 shows a schematic diagram of the experimental set up for diffraction imaging. The x-ray beam is collimated into a thin line beam by the primary collimator. The majority of x-rays pass through the phantom; the transmission detector detects them. Some x-rays that enter the breast undergo coherent scatter and are collected by the scatter collimator. The x-rays that are scattered into the solid angle subtended by the exit aperture of the collimator are incident upon the detector.

5.2.1.1 The x-ray source

To assess the clinical viability of the proposed imaging system typical mammographic spectra were employed as the x-ray source. Figure 5.4 shows a typical mammography spectrum. The incident x-ray flux is 4.7×10^5x-rays.mAs^{-1}.mm^{-2}, which is the x-ray flux at a distance of 50cm from the x-ray focal spot for a 30kVp exposure and 0.3mmMo filtration (Birch and Marshall, 1979).

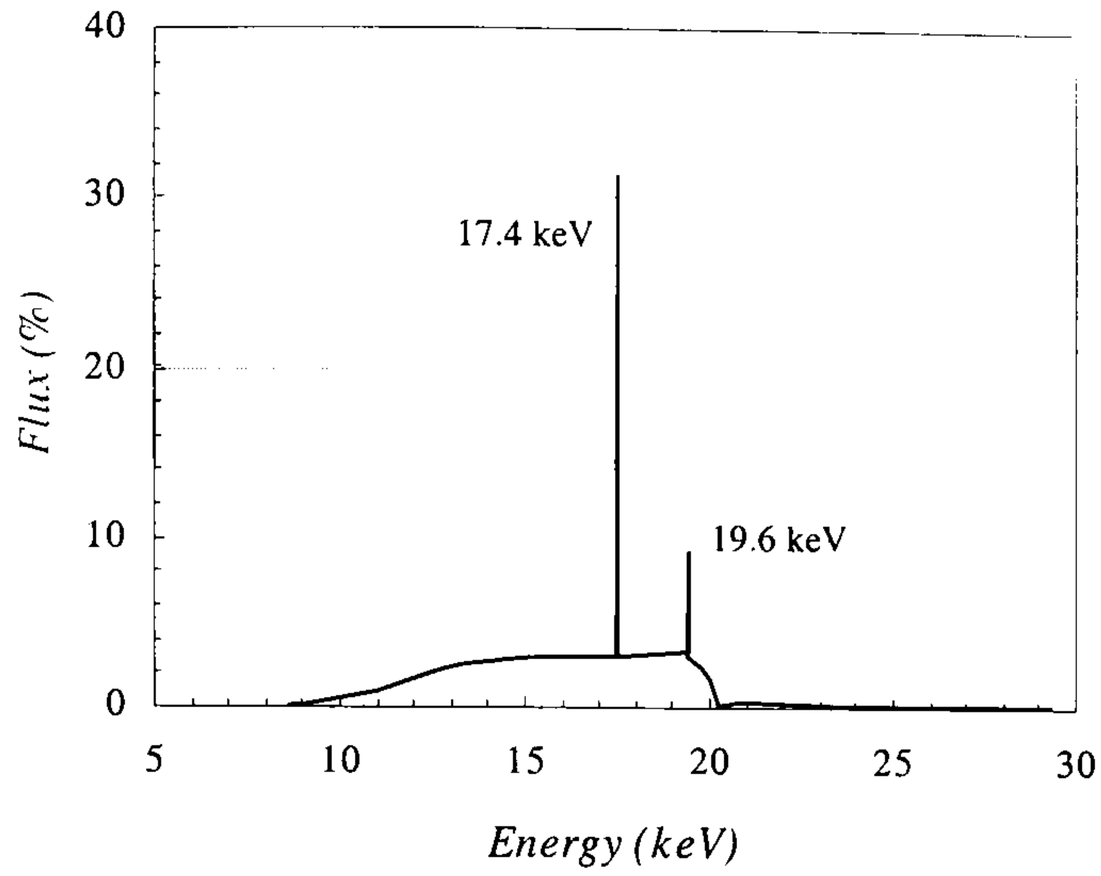

Figure 5.4. *Incident x-ray spectra from Mo anode/filter x-ray tubes at 30kVp. Obtained from tabulated data (Birch and Marshall, 1979).*

5.2.1.2 The breast phantom

The diffraction imaging system used to verify the suitability of L3 technology to DEBI will employ a breast tissue phantom. For simplicity, the breast phantom will be modelled as a cube of breast tissue. The average thickness of the breast under compression in the U.K. is ~3.0 cm. This was the thickness was chosen for the breast tissue phantom (in the direction of the x-ray beam) (Kidane, 2001). The molecular form factor for breast tissue is a function of Z, the atomic number and x the momentum transfer. The momentum transfer was calculated from equation 5.2 and the molecular form factor for normal breast tissue was found from tabulated values (Peplow, 1998).

5.2.1.3 The collimation system

The collimator geometry defines the measurement or scatter volume within the phantom. The dimensions of the scatter volume define the spatial resolution in the x-, y- and z- direction. Ideally, the scatter volume will be small enough so that only the inclusion of interest, i.e. tumour, is contained within the measurement volume. This will provide the maximum contrast between normal and diseased tissue. However, in the case of small tumours this may be difficult to achieve because if the scatter volume is decreased the diffraction signal will decrease. This will lead to a reduction in the SNR. A reduction in *SNR* will result in an increased uncertainty in the measurement

and thus, the sensitivity of the technique. Consequently, a compromise between signal and spatial resolution must be reached.

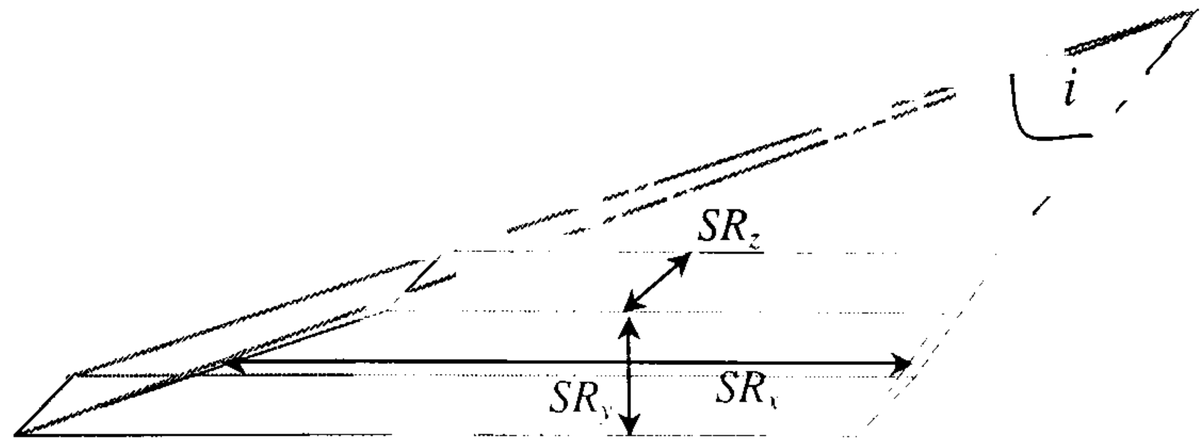

Figure 5.5. *The scatter volume defined in terms of the spatial resolution in the x-, y- and z- directions.*

The scatter volume is the volume of the breast tissue from which scattered x-rays can be collected by the scatter collimator. It is rhomboidal in shape and may be defined in terms of the spatial resolutions in the *x*-, *y*- and *z*- directions. The scatter volume is shown in figure 5.5.

It can be shown that the spatial resolution in the *x*-direction at the centre of the beam width is given by:

$$SR_x = (D + L/2)\sin\theta\left[\frac{1}{\tan(\theta - i)} - \frac{1}{\tan(\theta + i)}\right] \tag{5.5}$$

where D is the distance between the centre of the phantom (the scatter plane of interest) and the entrance of the collimator hole and is given by:

$$D = \frac{(W/2 + S)}{\tan^{-1}\theta} + \frac{T/2}{\cos\theta} \tag{5.6}$$

and L is the collimator length, W is the collimator width, B is the beam width, i is the angle at the centre of the collimator, T is the phantom thickness and θ is the scatter angle.

The angular acceptance is determined by the width W, and the length L, of the collimator and is equal to $2i$ where i is given by:

$$i = \tan^{-1}\left[\frac{W}{L}\right] \tag{5.7}$$

The spatial resolution in the y-direction is given by the beam width B. The beam is assumed to be non-divergent and the spatial resolution in the z-direction is given by

$$SR_z = 2\times(D + L/2)\tan i \tag{5.8}$$

Equations 5.5 and 5.8 indicate that in order to keep spatial resolution high in the x- and z- directions the distance between the scatter plane and the entrance aperture of the collimator, D, must be kept a short as possible.

5.2.1.4 Scatter detector

It is the intention that the scatter detector will be a L3 based x-ray detector, the specifications of which will be based upon the calculations of the diffraction signal and the requirements outlined earlier in section 3.7.1.2.

5.2.2 Collimation system design

The diffraction imaging technique can be described in terms of 2 main processes. The first is the scatter process, in which x-ray photons are coherently scattered within the solid angle subtended by the exit aperture of the collimator and collected within the collimator. The number of scattered x-ray quanta which are incident upon the detector, N_S, gives the x-ray diffraction signal. An optimal collimation system will produce the required spatial and angular resolution and collect the largest possible diffraction signal. The second process is the detection process, in which the N_s x-ray quanta interact with the L3 detector leading to the generation of N_i signal electrons in the CCD65. The detection process will be considered further in the detector design. The scatter can be described using a linear systems model in which the process is represented as a series of gains. The scatter model is illustrated in figure 5.6.

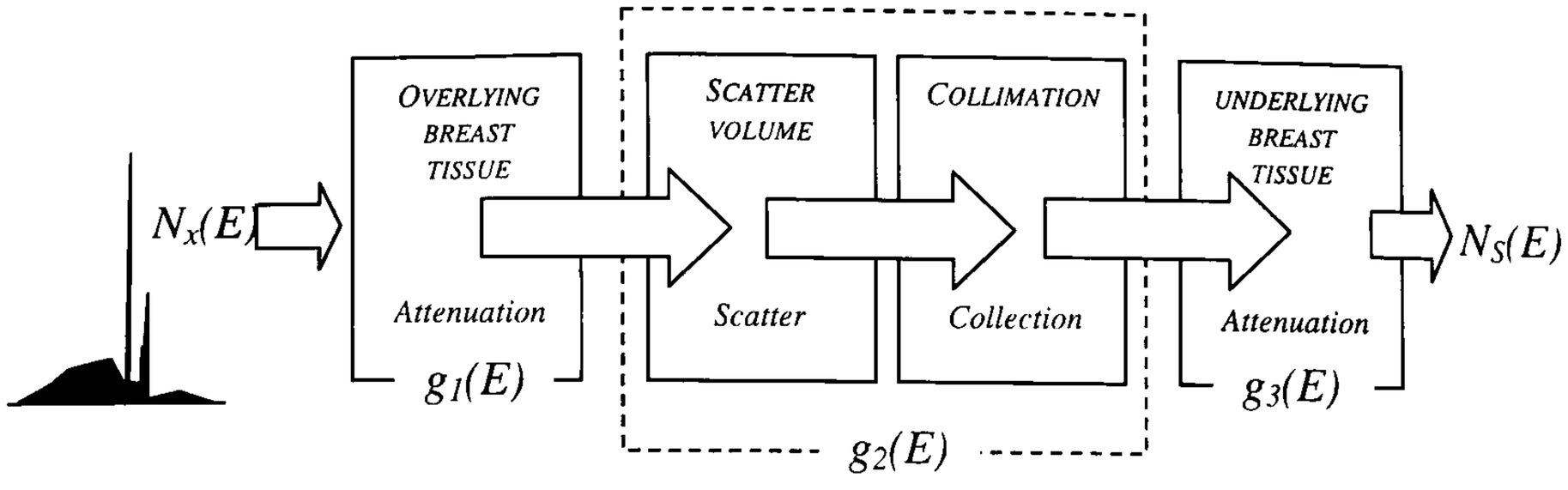

***Figure 5.6**. Schematic representation of the gain stages involved in the photon scatter process.*

The diffraction signal N_s can related to the number of x-ray photons incident upon $1mm^2$ of breast tissue, N_x by:

$$N_s(E)=.g_1.g_2.g_3.N_x(E). \tag{5.9}$$

where $N_x(E)$ is the incident x-ray spectrum. The proportion of x-rays reaching the scatter volume is g_1. If we consider the scattering volume to be at the centre of the breast, the average distance travelled by the x-ray photons before scatter in this volume is $T/2$. Gain g_1 is found using:

$$\overline{g}_1 = \frac{\int_{E_{min}}^{E_{max}} N_x(E)(1-e^{-(\mu(E)T/2)})dE}{\int_{E_{min}}^{E_{max}} N_x(E)dE} \tag{5.10}$$

where $\mu(E)$ is the linear attenuation coefficient of the breast phantom and T is the thickness of breast tissue. Gain g_2 is the probability that a photon will be coherently scattered through an angle θ into $d\Omega$, the solid angle subtended by the detector. It is equal to the differential coherent scattering coefficient, given by equation 5.1 multiplied by the density of electrons in the scatter volume and the solid angle subtended by the detector, $d\Omega$. It can be shown that $d\Omega$ is given by:

$$d\Omega = \frac{W^2}{(L+D)^2} \tag{5.11}$$

Once the scattered photons have been deflected through an angle θ, they will be attenuated further. The attenuation was calculated using the thickness of the breast tissue lying between the point of scatter and the point where they exit the phantom. $\overline{g}_3$ is given by:

$$\overline{g}_3 = \frac{\int_{E_{min}}^{E_{max}} N_1(E)(1-e^{-\mu(E)\cos\theta T/2})dE}{\int_{E_{min}}^{E_{max}} N_1(E)dE} \qquad (5.12)$$

where $N_1(E)$ is the pre-attenuated and scattered spectra after stages 1 and 2.

5.2.2.1 Collimator design parameters

From equations 5.9 and 5.11, it is evident that *Ns* is a function of $d\Omega$ (*D,L,W*) which is determined by the collimation system. In addition (to the diffraction signal) the collimation system needs to define other parameters. The value of momentum transfer that provides the greatest contrast between diseased and normal breast tissue is 1.1nm^{-1}. For a typical exposure, (described in section 5.2.1.1) the 17.4keV spectral line corresponds to 32.4% of the incident x-ray quanta. Using equation 5.2 the corresponding scatter angle is 8.99°. Due to the finite width of the collimator, x-rays from other angles will be accepted. The angular acceptance is equal to 2*i*, where *i* is given by equation 5.7. Assuming all of the scattered photons have an energy of 17.4 keV, an angular acceptance of 2° corresponds to an momentum transfer spread of 0.24nm^{-1}. The range of momentum transfer values that will be recorded is shown in figure 5.7. As a result the momentum is blurred and the contrast will be degraded. From equation 5.4 the contrast is equal to (B-C)/(B+C), where B and C are the areas beneath the curves for average breast tissue and carcinoma respectively that are bounded by 0.98nm^{-1} and 1.22nm^{-1}, shown in figure 5.7.

For a mono-energetic beam of 17.4keV photons the contrast was be calculated using :

$$c_{total}(x) = \frac{\int_{x=0.98}^{x=1.22} c(x).x.dx}{\int_{x=0.98}^{x=1.22} x.dx} \tag{5.13}$$

where $c(x)$ is the contrast between normal tissue and carcinoma at the momentum transfer value x.

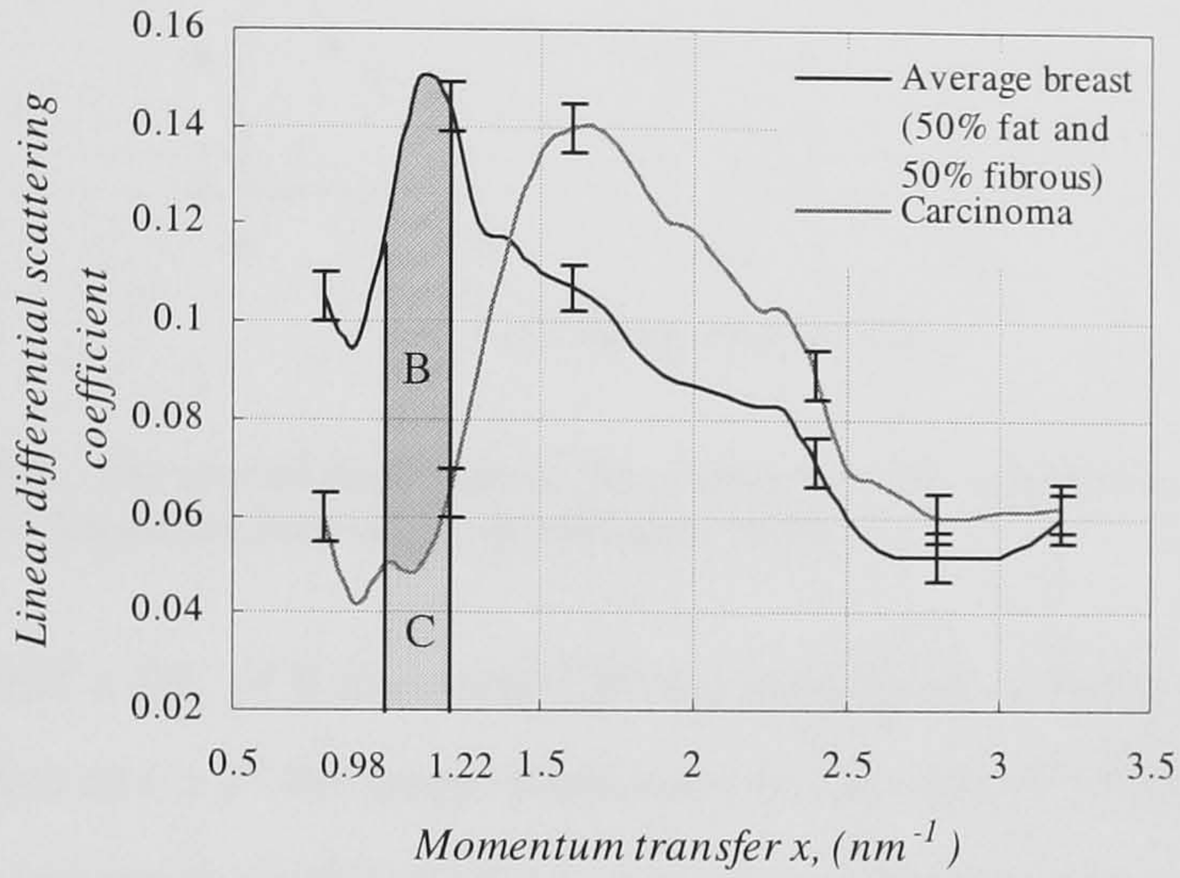

Figure 5.7. *Range of momentum transfer values recorded as a result of the finite angular acceptance of the collimator*

From figure 5.1 the transfer value that gives the maximum contrast of 51% is at 1.1nm^{-1}. Equation 5.13 gives a value of 44 %, which is a 9% reduction from the maximum contrast 51%.

Conventional mammography is sensitive to carcinoma greater than 10 mm in size. Due to the acute scatter angle the scattering volume is elongated in the x- direction. To discover the combination of collimator dimensions, which provide a value of SR_x on the same order as conventional mammography, SR_x has been calculated using equation 5.1 for a scatter angle of 9 ° for different collimator dimensions.

Figure 5.8 shows SR_x as a function of collimator length for various collimator widths. From figure 5.8 it is observed the collimator lengths should be kept shorter than 100mm as they have little effect upon SR_x if greater in length. A SR_x of less then 3mm is attainable when W = 0.25mm, however to obtain this the collimator would require a

length of greater than 50mm, which would be difficult to machine and is therefore unavailable.

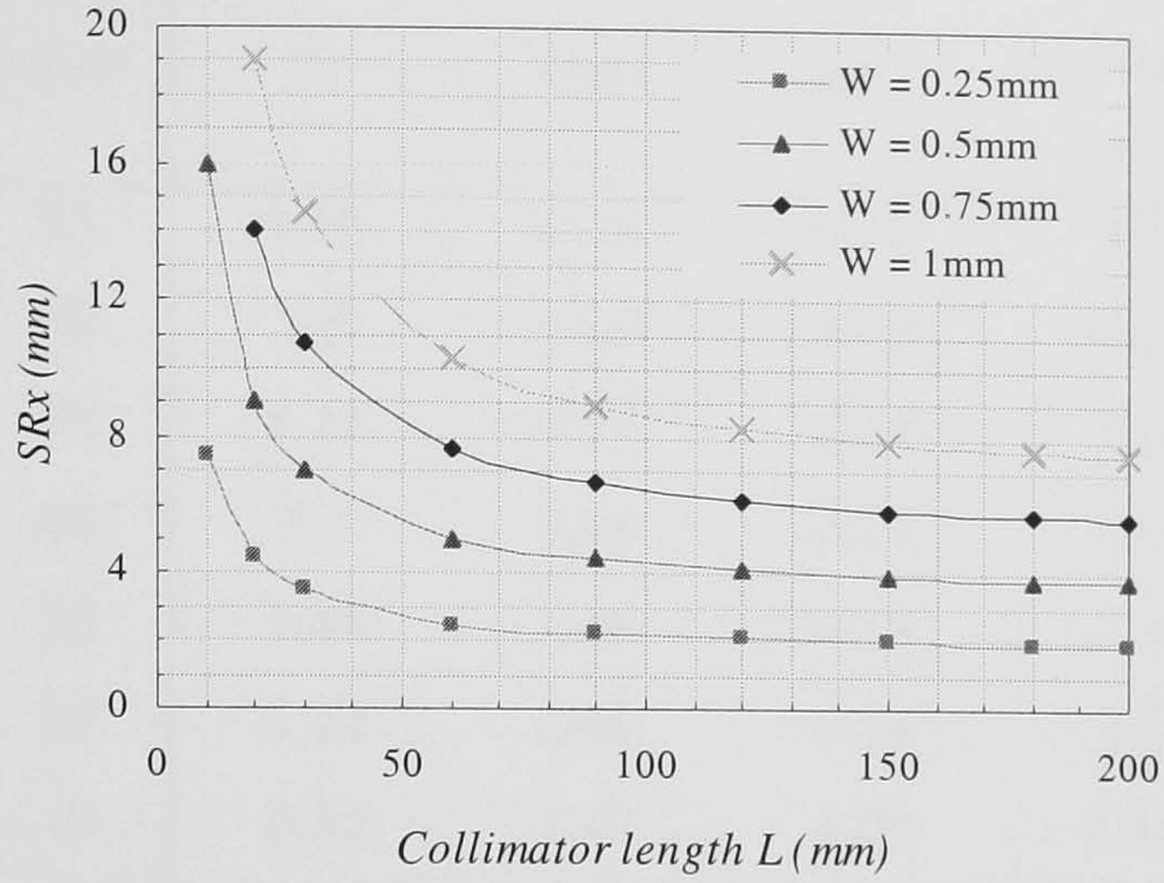

Figure 5.8. *The spatial resolution in the x-direction (SR_x) plotted as a function of collimator length for fixed values of collimator width.*

It was decided that a SR_x of 8 mm would be the maximum acceptable spatial resolution due to the fact that at $i = 1°$ the larget dimension of the scatter volume in the x-direction ≈ 1mm. This corresponds to the smallest size of calcification that can be imaged using transmission mammography (see figure 5.5). Thus, the collimator dimensions used as inputs to the model were chosen to provide a SR_x of between 3mm and 8mm and an angular acceptance of 2°.

5.2.2.2 Model results

The number of photons scattered from normal breast tissue reaching the detector N_S has been calculated using equation 5.9 for a variety of different combinations of collimator widths and height. Table 5.1 shows the results from the scatter model. Only those combinations which produce an angular acceptance of less than 2° are included. The results given are for an input beam of $1mm^2$, it is assumed that the beam has width 1mm and is constant throughout the breast phantom, i.e. there is no beam divergence. The value of N_S, the number of quanta incident upon the scatter detector per mm^2 is given for a 30kVp and 40mAs x-ray exposure. If the entire breast were irradiated at once with this exposure and scattered radiation was collected from across the whole beam, N_s is the number of x-ray quanta scattered through each collimator hole.

Table 5.1. *Output parameters from the diffraction model for various values of SR_x. SR_y is equal to the beam thickness, 1mm. The number of photons incident upon the scatter detector is given for a Mo/Mo 30kVp 40mAs exposure for healthy breast tissue*

SR_x (mm)	W (mm)	L (mm)	$2i$ (°)	SR_z (mm)	Δx (nm^{-1})	Scatter volume (mm^3)	N_S (x-rays/mm^2)
8	0.75	55	1.56	1.23	0.19	9.8	40
7	0.5	30	1.9	1.09	0.19	7.6	40
7	0.75	75	1.14	1.10	0.14	7.7	30
6	0.5	40	1.7	0.94	0.22	5.6	31
5	0.25	20	1.44	0.69	0.18	3.5	26
4	0.25	25	1.14	0.60	0.14	2.4	21
3	0.25	40	0.35	0.47	0.09	1.41	14

The L = 30 mm and W = 0.5 mm collimator was chosen for the diffraction set up. This is because larger collimator lengths are hard to manufacture and this collimator provides the largest diffraction signal with a relatively small length.

5.2.2.3 Collimator description

The collimator dimensions were chosen to provide an acceptable compromise between signal and spatial resolution. A detailed illustration of the collimator designed for use at ELETTRA is given in figure 5.9. It is made from two separate pieces of brass, one of which has ten linear sections, 0.5 mm wide and 0.5 mm deep removed from its upper surface. The second piece of brass is placed on to the first to form long thin collimator holes. Screws tightly hold the two pieces of brass together. The height and the width of the collimator holes defined the angular resolution and the scatter volume.

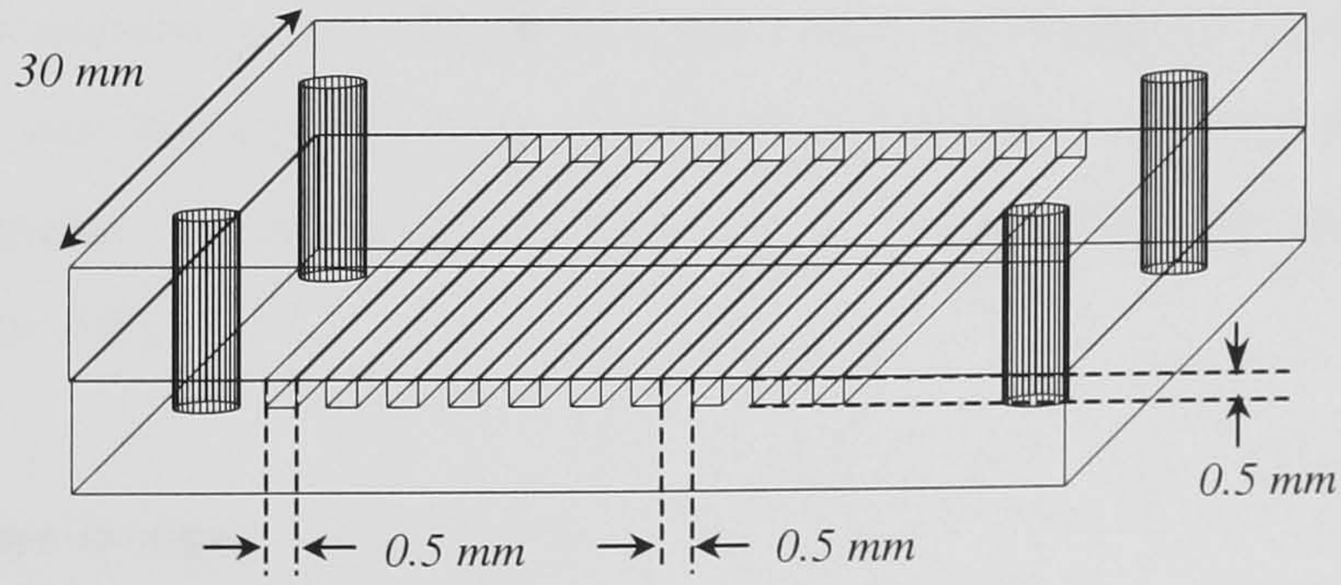

Figure 5.9. *A schematic of the design of the scatter collimator to be used in the L3 DEBI system at ELETTRA.*

5.2.2.4 *Momentum resolution of the L3 DEBI system and predicted contrast*

The ability of the L3 DEBI system to distinguish between normal and diseased breast tissue will depend upon the momentum resolution of the experimental set-up. The momentum is a function of energy and scatter angle.

Mono-energetic radiation: The finite dimension of the collimator results in a range of scattering angles distributed around the nominal angle, arriving at the detector. The angular acceptance is equal to $2i$, where $i = 0.95°$, given by equation 5.7. This gives an error in the momentum of ± 0.24 nm^{-1}, giving a momentum spread due to the detector system of 22 %. The contrast between normal and diseased breast tissues for this system is approximated using equation 5.13 and is 44%.

Poly-energetic radiation: Due to the fact that clinical mammography x-ray sources are poly-energetic there will be a momentum spread due to the spread in energies present. The resulting signal contrast between diseased and normal tissue for a poly-energetic source was calculated using the model described above and using the following:

$$c_{total}(E) = \frac{\int_{E_{min}}^{E_{max}} N_S(E).c(E).dE}{\int_{E_{min}}^{E_{max}} N_S(E).dE} \qquad (5.14)$$

where $c(E)$ is the contrast as a function of energy for a fixed scatter angle and angular acceptance and is given by equation 5.4. This equation ignores any contributions from multiple or incoherent scatter which are expected to be negligible (Taibi *et al.*, 2000). For a typical mammographic x-ray exposure (described in section 5.2.1.1) and the collimation system described above, the contrast between diseased and normal tissue was found to be 38%.

5.2.3 Detector design

The following is a decription of the calculations that lead to the design of the CCD65-02 detector described in section 3.1.1.

From the above calculation of the diffraction signal, N_S is on the order of tens of x-ray quanta for a typical mammograpghy exposure. Such small signal requires that the quantum efficincy of the detctor should approach 100%. The CCD65 is based upon a standard front-illuminated CCD design. The sensor has an active thickness of 20μm, consisting mainly of silicon. The percentage of the scattered photons, which are absorbed in the CCD, was calculated using:

$$\eta = \frac{\int_{E_{\min}}^{E_{\max}} N_S(E)(1-e^{-\mu(E)w})dE}{\int_{E_{\min}}^{E_{\max}} N_S(E)dE} \tag{5.15}$$

where $\mu(E)$ is the energy dependant linear attenuation coefficient for silicon and w is the active thickness of silicon. The x-ray quantum efficiency was found to be 0.3%, which is poor. Accordingly, the CCD65 will be used in conjunction with an x-ray phosphor in order to increase the quantum efficiency

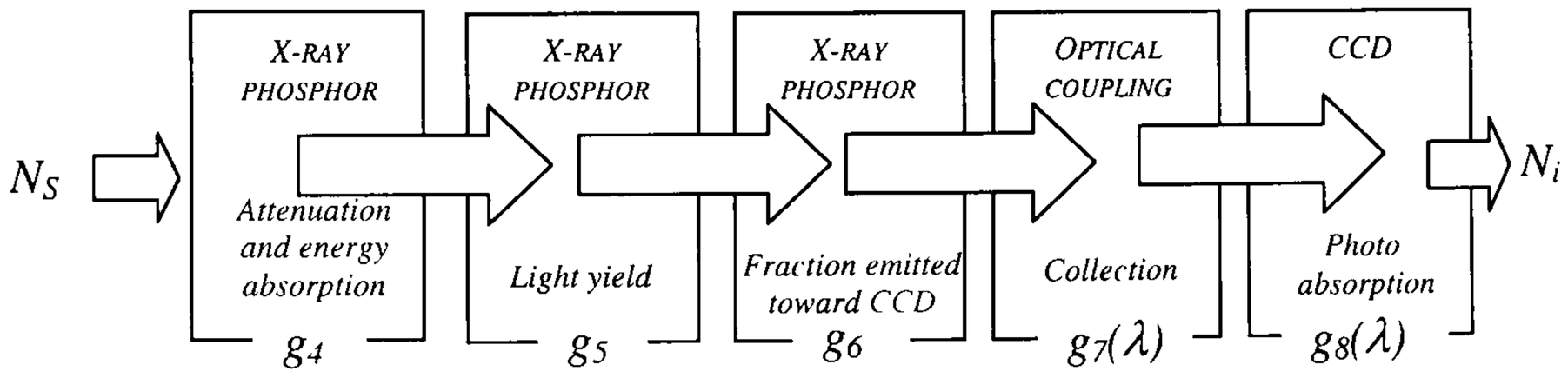

Figure 5.10. *Schematic representation of the CCD65 detection process for a 17.4keV x-ray photon.*

The detector has been designed using the same analysis described for the collimation system. In order to calculate the number of signal electrons generated in the L3 detector the model is extended to include the x-ray detection process, in which the N_s x-rays interact with the L3 detector leading to the generation of signal electrons, N_i in the CCD65. The detection process for a 17.4keV x-ray photon using an x-ray phosphor and the CCD65 is shown in figure 5.10.

5.2.3.1 Model results

Stages g_4, g_5 and g_6 are equivalent to stages g_1 g_2 and g_3 in section 4.2.4. For a 160μm layer of Gd_2O_2S:Eu and 17.4keV x-ray quanta, $g_4 \times g_5 \times g_6 = 285$ light photons per x-ray photon (calculated using equations 4.9 and 4.10). Assuming a coupling efficiency of 100%, $g_7(\lambda) = 1$. The effective quantum efficiency $g_8(\lambda)$, is calculated to be 0.295 using equation 2.4. The product of these factors gives 84 photoelectrons generated per x-ray photon. The distribution of light from a scintillation event, and hence the area of the CCD over which it is spread, will depend upon the depth of interaction. The maximum spread in the light emission is predicted to be approximately equal to the thickness of the phosphor. Using a 160μm phosphor layer, the light will spread over an area of approximately 42 pixels squared (Yaffe and Rowlands, 1997). If the light distribution were to be evenly spread over this area the signal would be ~ 2 electrons/pixel, which is just lower than the *MDS* calculated in section 3.4.6.

The CCD65 sensitivity is ultimately limited by the thermally generated current, spurious current and transfer noise (see section 3.4). For a CCD65 device at room temperature there is $2e^-$ r.m.s of pre-gain noise. In order to improve the *SNR* it was decided that a Peltier pack should be added to reduce the thermal noise. From the data given in figure 3.17 it is seen that cooling the CCD to –5°C will reduce the pre-gain noise to $0.72e^-$ r.m.s. This will give a SNR_{lim} of $2/\sqrt{(0.72^2 + 1.41^2)} = 2/1.6 = 1.25$.

The low number of photons available means that a loss even just one or two will result in a significant reduction in the SNR. Therefore a Mylar window in the Peltier packaging was designed in order to minimise the attenuation of the scatter signal.

The detector design was based upon the above calculations. The above assumes individual 17.4keV x-ray photon can be seen providing there is 100% coupling efficiency between the phosphor and the CCD. In practise, it is hard to achieve a coupling efficiency of 100%. To ensure maximum coupling efficiency it was decided that the x-ray phosphor be deposited directly upon the surface of the CCD65.

5.2.3.2 *Detector Performance*

In order to verify that the detector can visualise single x-ray photons the following experiment was carried out. The experimental set up was designed so that a small number of x-ray photons are scattered toward the L3 detector. A mammographic x-ray source with a Molybdenum target and 300 μm of Molybdenum filtration was employed. An x-ray scatterer comprising of a Perspex block was situated approximately 20 cm from the x-ray tube focal spot. The L3 detector was positioned at a distance of 20cm behind the x-ray scatterer at an angle of approximately 9°. The x-ray tube was operated in continuous mode at a tube current of 0.1mA. The L3 gain was set to $M_{SNR_{\lim}} = 4096 \pm 86$, which was calculated using equation 3.24. Scattered photons were observed using a TV monitor connected to the analogue output of the CCD65-02. Digital images of the scattered photon interactions were acquired. X-ray photon interactions in the phosphor (indirect interactions) were observed as circular 'blobs' of light spread over a large number of pixels.

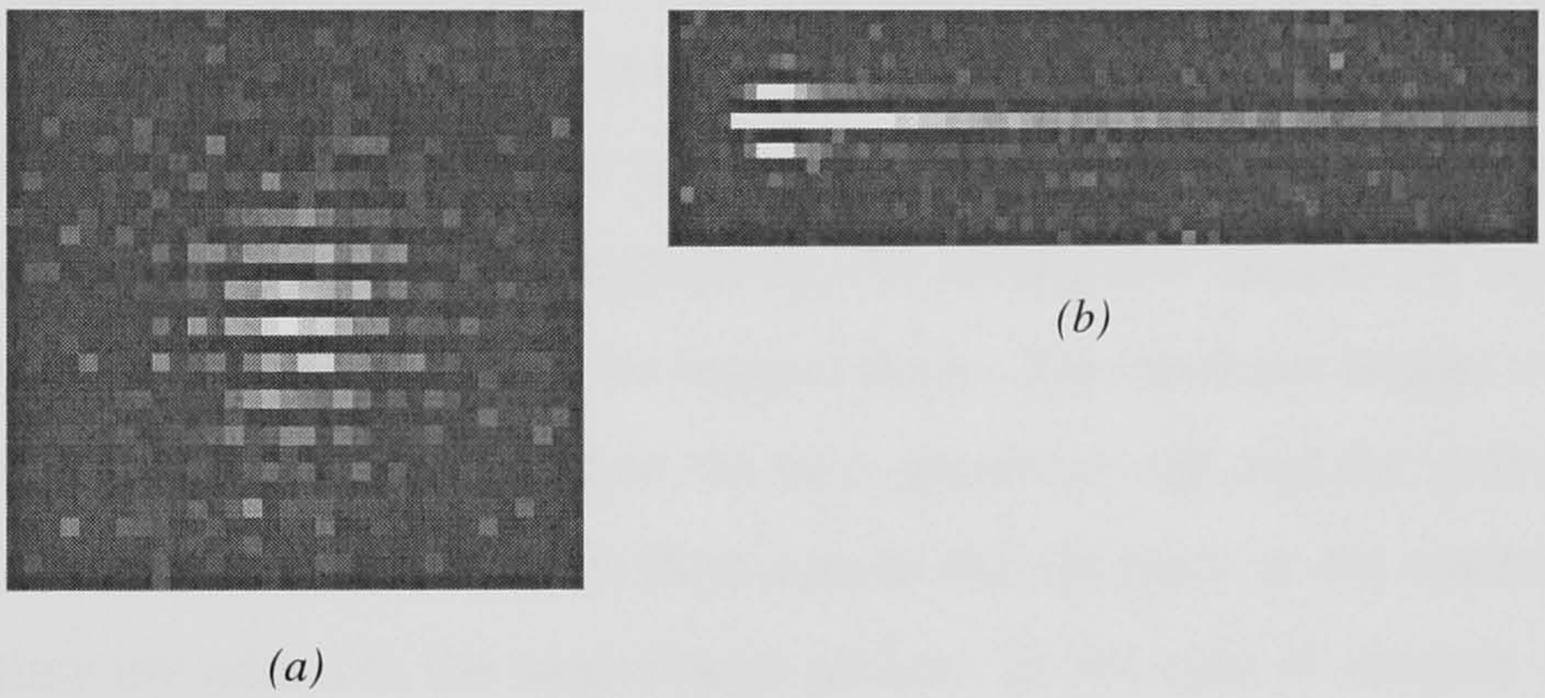

(a) *(b)*

Figure 5.11. *Images of (a) indirect and (b) direct x-ray photon interactions acquired with the CCD65-02 with gain M =4096±86. The striped effect is due to image interlacing*

The image in figure 5.11*(a)* shows that individual x-ray photons of mammographic energies can easily be visualised using the L3 detector as predicted by the model and therefore is suitable for use in diffraction mammography.

The interaction size and total signal in DN was found for a sample of 500 interactions. The average size of indirect interactions was found to be 121 pixels with a standard deviation of 42. The large standard deviation is a result of the fact that the interaction size is a function of energy and the depth of the interaction in the phosphor. X-ray

interactions in the silicon (direct interactions) were also evident; these appeared brighter and were contained within 3 to 5 rows. Direct interactions were generally smeared along the pixel row always in the direction of the CCD read out. Examples of the direct x-ray interaction images are shown in figure 5.13*(b)*.

The total signal in the direct interactions was found to be approximately twice that of the indirect interactions. Observation of the scatter x-ray image shows that this charge smearing only occurs for the directly interacting x-ray quanta and thus is a phenomenon that only occurs when input signal are high. A 17.4keV photon interacting in the silicon produces 4793 secondary electrons. The saturation signal is equivalent to the full well capacity of the gain register divided by the gain. This is equal to 530,000/4369 = 121 electrons, which is significantly lower than the input signal from one directly interacting x-ray photon. The loss of charge could be explained by the charge smearing and/or inefficient charge collection, as now described.

The smearing of charge in the direct interactions is explained by the fact that as the gate potential becomes increasingly positive, negative charge stored beneath the electrode is attracted toward the surface. There is a larger density of trapping states at the surface. Some electrons will make the transition from the conduction band to the surface states, which are lower in energy and will be trapped there. The electrons remain trapped until the stored electrons are transferred to the next potential well and the gate potential is returned to zero. The surface states then release the electrons to the conduction band, and then they are added to the next charge packet. In the case of the gain register the gate voltages are unusually high and if we combine this with the large signal from the direct interaction we get poor transfer efficiency.

5.3 Materials and methods

The feasibility of a clinical L3–based DEBI system has been verified using an appropriate model of a DEBI system. A L3 detector has been designed and built based upon the diffraction signal available, which was calculated using the diffraction model. Laboratory experiments have shown that the L3 detector is able to detect individual 17.4keV x-ray photons and is therefore suitable to collect diffraction data. A L3 DEBI

system was constructed and taken to the Synchrotron Radiation for Medical Physics (SYRMEP) beam line, ELETTRA, at Trieste, Italy for evaluation. The materials and methods used to collect diffractions data from human breast tissue are now described.

5.3.1 Description of the experimental set-up

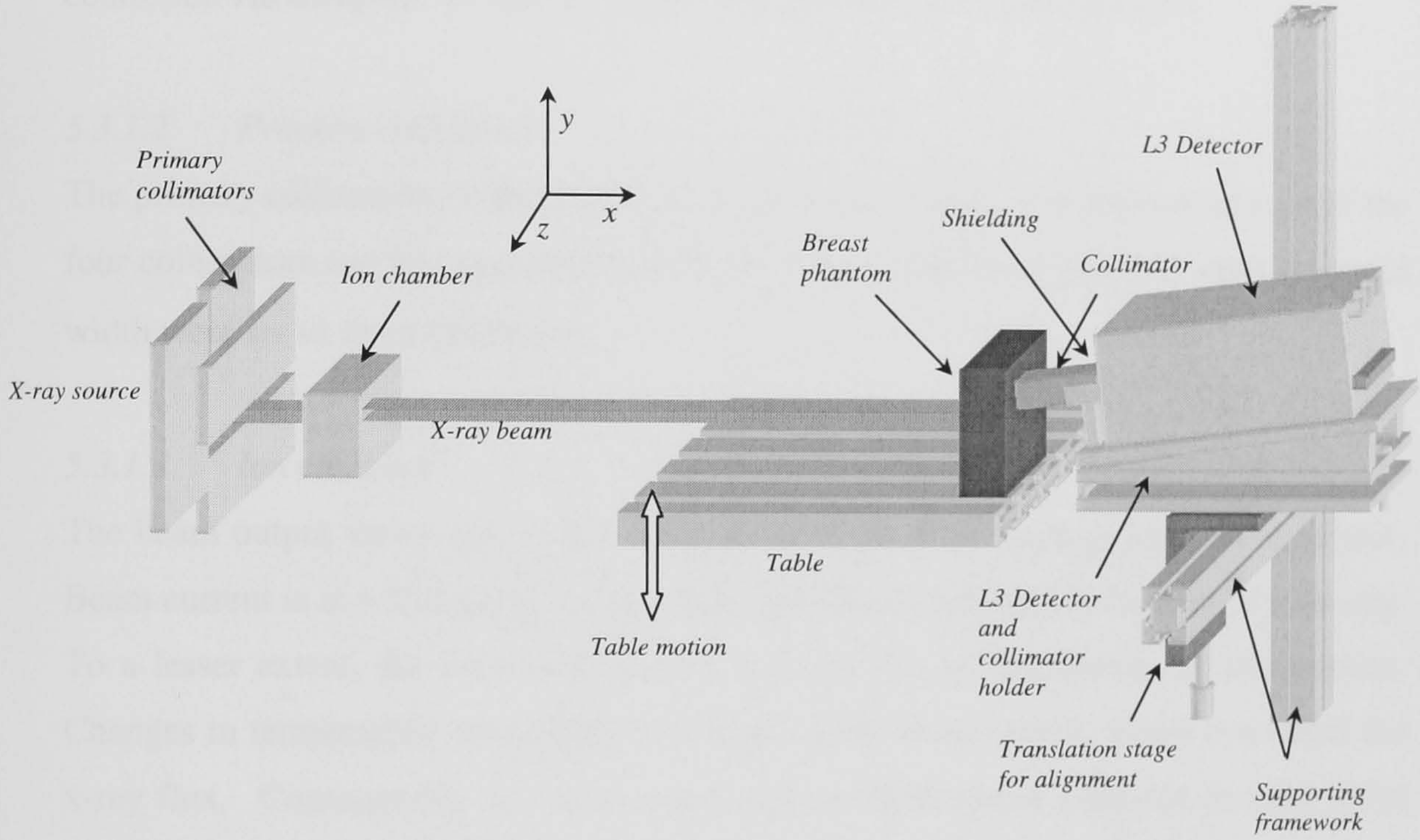

Figure 5.12. *A schematic of the experimental L3 DEBI set up at the SYRMEP beam line.*

Figure 5.12 is a schematic of the equipment set up in the experimental room at the beam line. The L3 detector and the collimator are described earlier in sections 5.1.1 and 5.2.2.3 respectively. The following is a description of the main components of the diffraction experiment. Figure 5.13 is a photograph showing the phantom, the L3 detector, the collimator and the detector and collimator holder.

5.3.1.1 X-ray source: The SYRMEP beam line

The SYRMEP beam line is one of 20 operational beam lines at the ELETTRA synchrotron laboratory in Trieste, Italy. It is designed specifically for research in medical diagnostic radiology. The beam line is organised into two distinct areas, an experimental room and a control room. In the experimental room, SYRMEP provided a monochromatic x-ray beam. The energy range of the beam was 8keV to 35keV with an

energy resolution, $\Delta E/E$ is 2×10^{-3}. The radiation beam was laminar-shaped to facilitate acquisition of large area images. It had a maximum area of $120 \times 4mm^2$ at a distance of 20m from the x-ray source. The maximum photon flux at 23m at an x-ray photon energy of 20keV was 2×10^8 photons/s/mm^2 and 2×10^7 photons/s/mm^2 for a 2.4GeV and a 2.0GeV electron beam energy respectively. The beam divergence was 1.7×10^{-5}°. The monochromator and the primary collimators, which define the beam size, are controlled via computer terminals; these were situated in the control room.

5.3.1.2 Primary collimators

The primary collimators collimate the beam in the *y*-*z* plane. The position of each of the four collimators can be controlled to within ± 1 μm. The beam height (*y*-direction) and width were set to 1mm by 10mm.

5.3.1.3 Ion chamber

The beam output varies due to the exponential decay of the storage ring beam current. Beam current is at a maximum immediately after beam injection at the start of each day. To a lesser extent, the beam output can also vary due to fluctuations in temperature. Changes in temperature cause small variations in the beam optics, which can affect the x-ray flux. Consequently an ion chamber and an electrometer (situated in the control room) were used to monitor the beam output so that the appropriate corrections could be made to the diffraction data.

5.3.1.4 L3 Detector and collimator holder

The detector holder shown in figures 5.12 and 5.13, was designed to hold the collimator against the L3 detector. Both collimator and L3 detector were fixed with respect to an aluminium positioning plate. The angle of the plate could be adjusted using a screw mechanism situated on the rear of the holder. The positioning plate is at 9° when the two base plates are parallel. The collimator wais held in place with thumbscrews. If required, these may be undone in order to exchange the collimator for an alternative. The holes in the side of the holder are necessary to reduce the weight of the apparatus.

5.3.1.5 *Supporting equipment*

The breast phantom, the translation table and the L3 detector are shown in figure 5.13. To minimise the size of the scatter volume the breast phantom was positioned so that it is just in contact with the scatter collimator (see section 5.2.2.1).

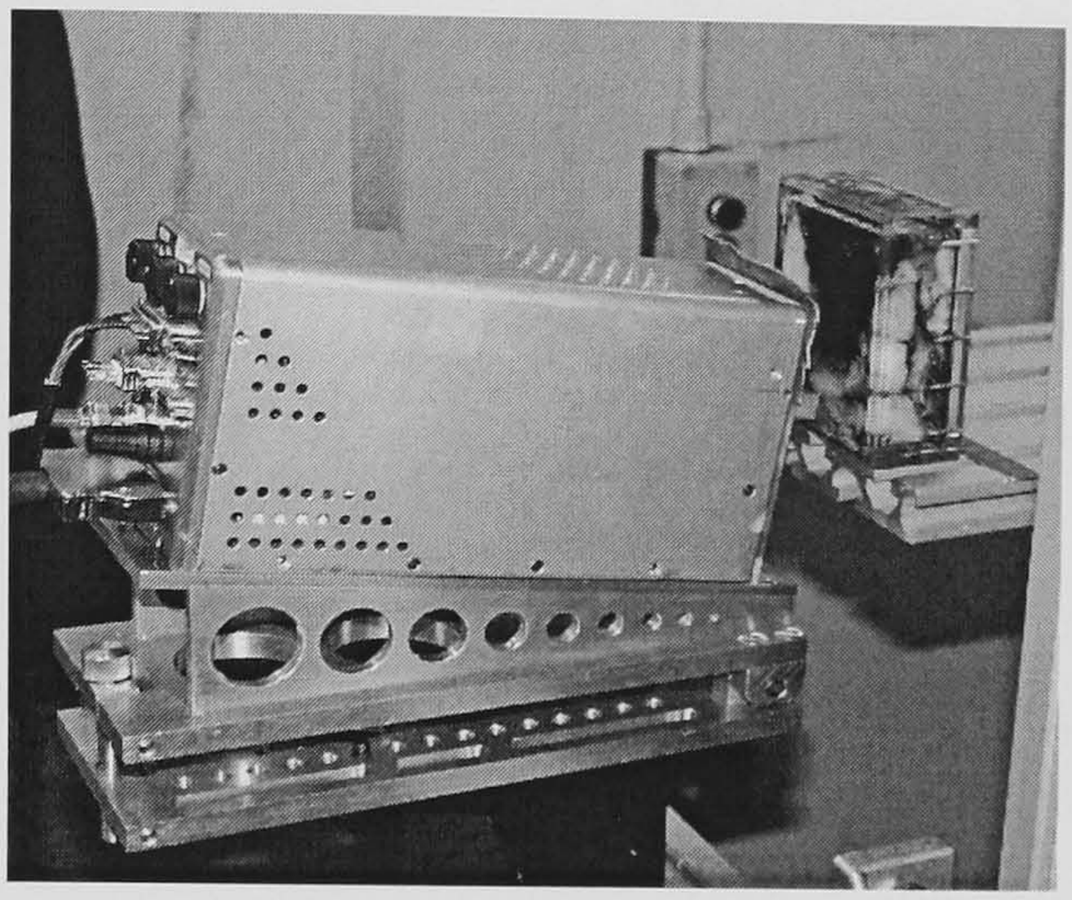

Figure 5.13. *Photograph of the L3 detector, the collimator and the breast phantom. The detector and the collimator are held in place by the holder secured to aluminium framing.*

5.3.1.6 *Primary beam shielding and multiple scatter*

In all x-ray experiments there will be a small amount of x-rays that are scattered from the primary beam by surrounding equipment. A lead mask was positioned around the collimator to reduce the probability of these scattered x-rays penetrating the camera housing and being detected. Incoherent may enter the scatter collimator, however, this is expected to be negligible (Kidane *et al.*, 1999, Taibi *et al.*, 2000).

5.3.1.7 *The breast tissue phantom*

The phantom used cancerous human tissue inclusions in a block of healthy breast tissue. Figures 5.14 *(a)* and *(b)* show a schematic and a radiograph of the phantom. This sample was prepared by consultant histo-pathologist Prof. Andrew Hanby of St. James Hospital, Pathology Department, Leeds, U.K.

Both the cancerous and healthy tissue were obtained from a patient undergoing mastectomy operations. The tissue was cut to fill a Perspex sample holder with a $60 \times 80 \times 30$ mm^3 cavity. The overall thickness of the phantom, including the Perspex wall,

was 33mm. The attenuation of 1mm of Perspex is equivalent to the attenuation of 1.2 mm of normal breast tissue (Kidane, 2001). The overall attenuation of the phantom was equal to 33.6 mm of normal breast tissue. Regions of cancerous tissue were identified from the radiograph by Prof. Andrew Hanby.

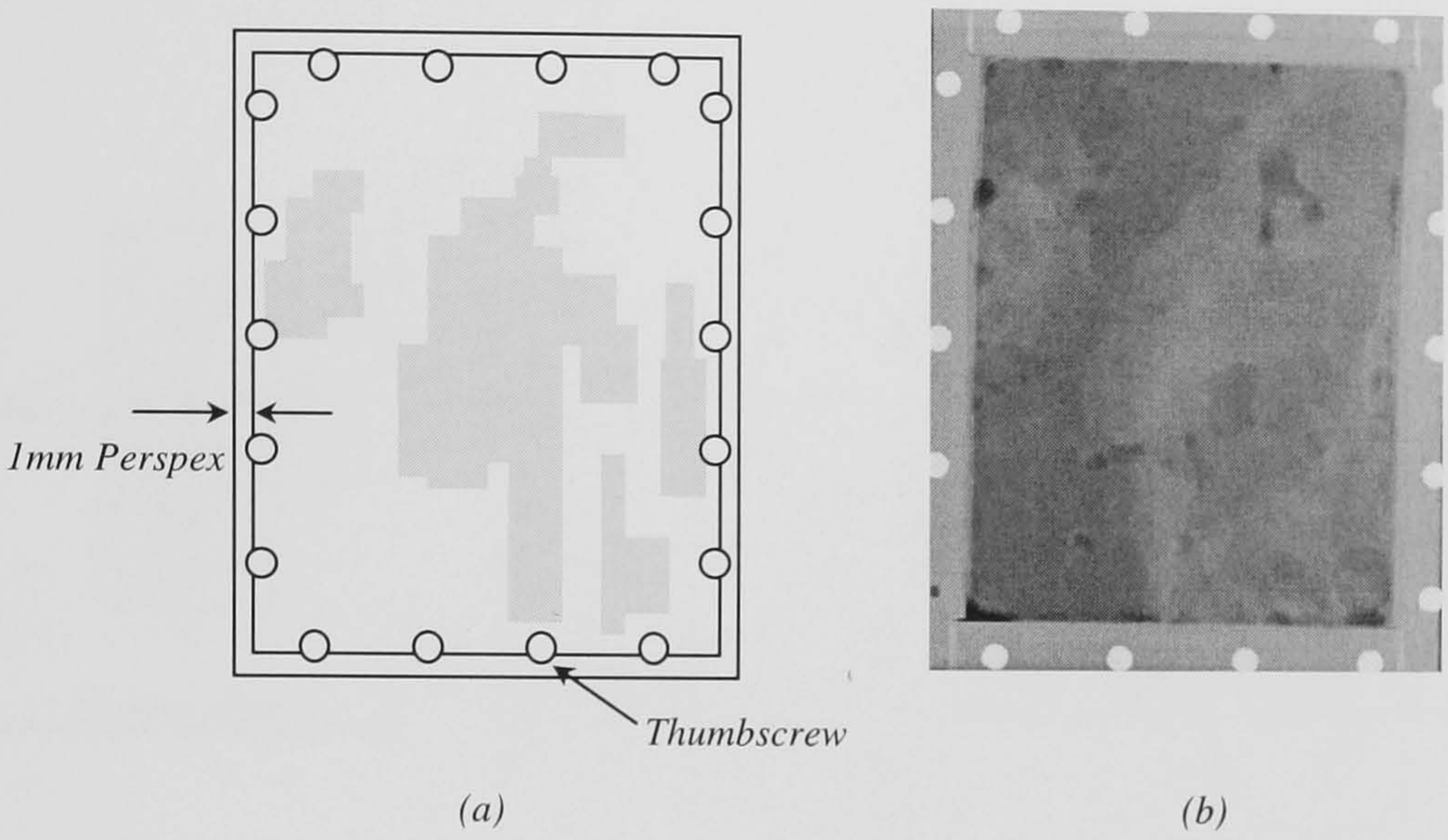

Figure 5.14. *The human breast tissue phantom, (a) schematic representation of the Perspex holder and the position of the cancerous inclusions identified by the pathologist (indicated by the grey areas) and (b) digital radiographic image of the phantom.*

5.3.2 Data acquisition

The following is a description of the methods used to collect 2-dimensional images of the breast tissue phantom using the experimental set-up described above. Vertical raster scanning of the phantom was carried out using the translation table (on which the breast phantom was mounted) to construct a 2D scatter image.

5.3.2.1 System alignment

The position of the scatter plane is defined by the height of the collimator with respect to the x-ray beam, y. The effect of increasing or decreasing y is shown in figure 5.15(a) If y is too large, the scatter plane will be in front of the phantom. If it is too small the scatter plane will be behind the phantom and the collimator will intersect the primary beam. To ensure maximum contrast, it is important that the scatter volume is contained entirely within the breast tissue, i.e. there is no scatter from either Perspex or air contributing to the diffraction signal.

The system was aligned so that the scatter plane was positioned in the middle of the phantom. This was achieved using a thin piece (3mm) of Perspex. The Perpsex was placed at a distance of 17.5mm from front of the collimator in a vertical position. This distance is half the width of the phantom.

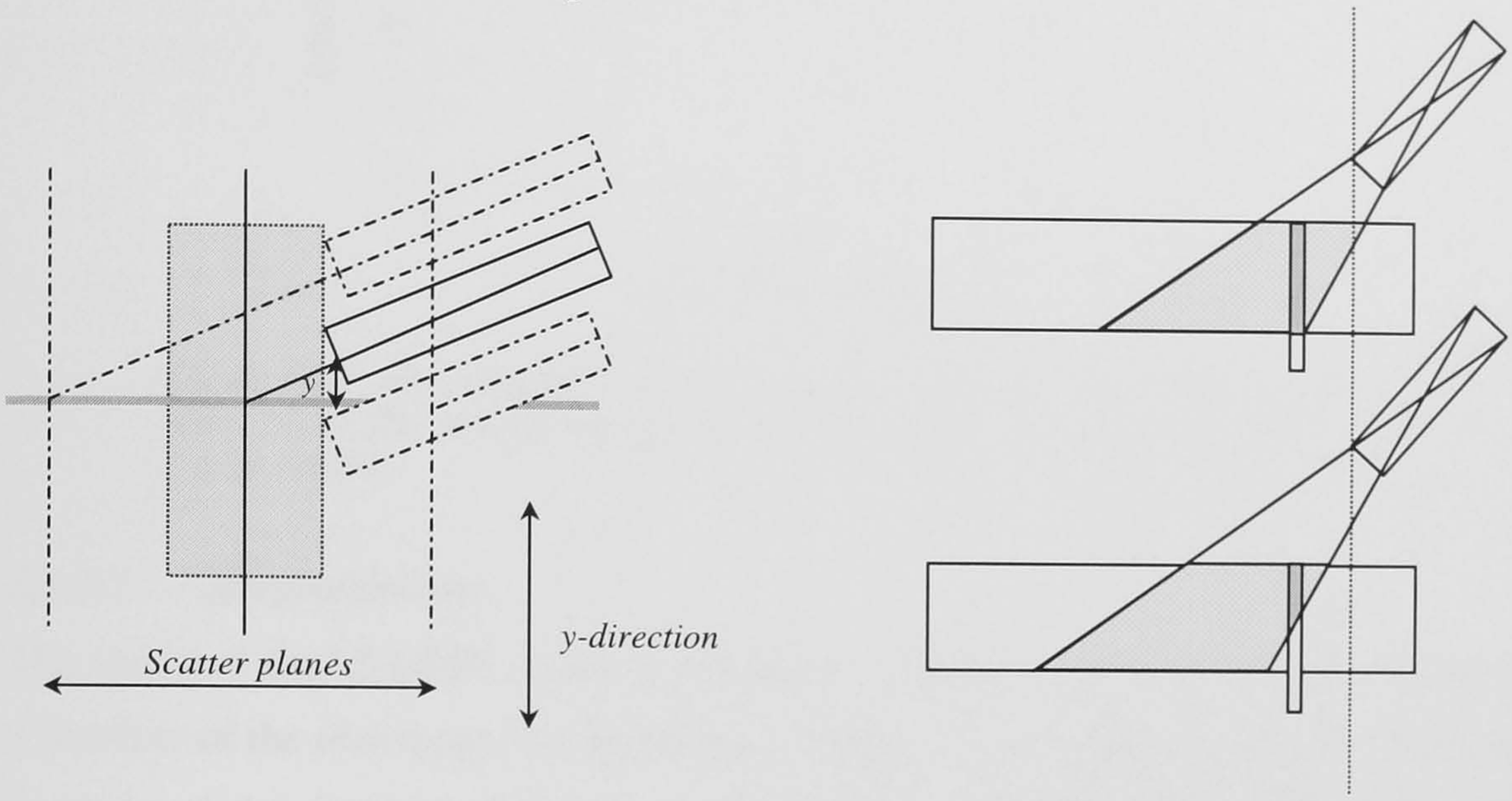

Figure 5.15. *System alignment. (a) Diagram to illustrate how the height of the collimator above the beam effects the position of the scatter volume. (b) Illustration to show how the proportion of Perspex contained in the scatter volume varies with collimator height.*

The proportion of the Perspex that fills the scatter volume is a function of the distance *y*. This is illustrated in figure 5.15*(b)*. Accordingly the magnitude of the scatter signal recorded by the L3 detector will also depend on *y*. The height of the collimator with respect to the beam was adjusted using the translation stage, which allows vertical movement of the detector holder. The scatter signal was measured as a function of *y*. Figure 5.16 shows a plot of the relative intensity of the scatter signal against collimator height. Using this information the collimator could be positioned so that the scatter volume was entirely within the tissue.

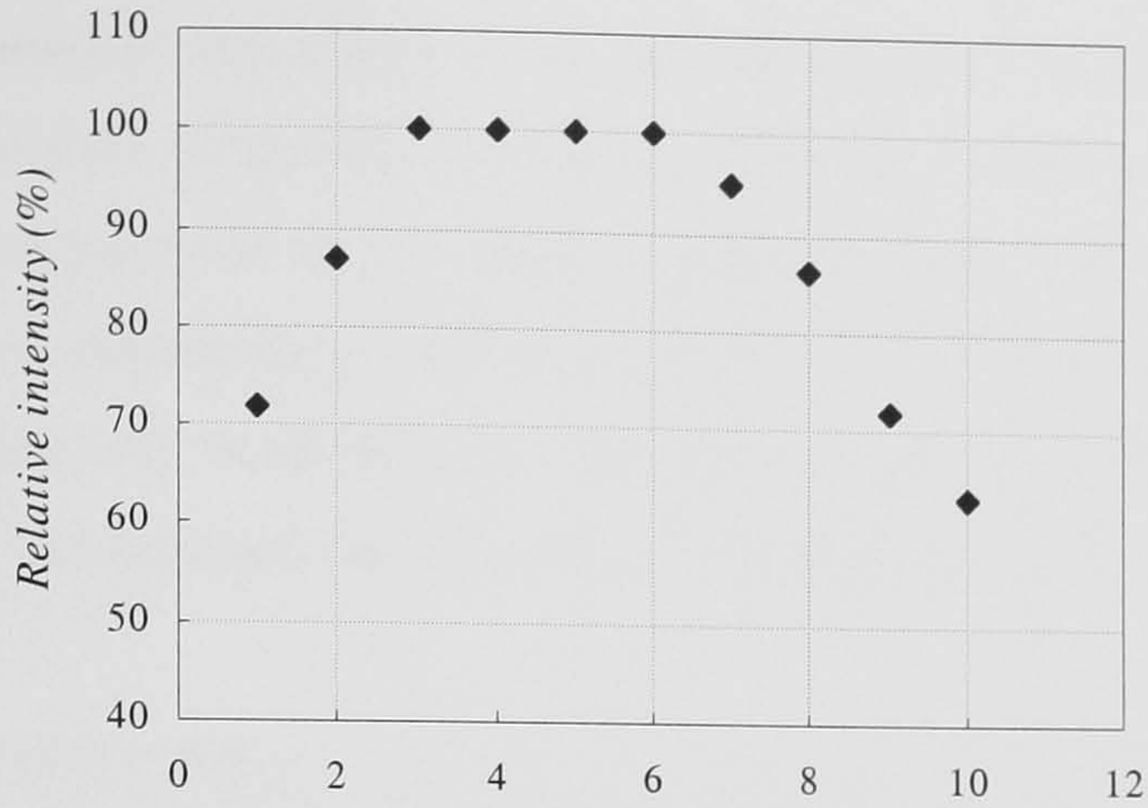

Figure 5.16. *The variation in scatter intensity with variation of collimator height above beam. The intensity is proportional to the amount of Perspex contained in the scatter volume.*

5.3.2.2 Integration time

The ability of the L3 DEBI system to distinguish between normal and diseased tissue is a function of the uncertainty on the diffraction signal. The uncertainty can be measured in terms of the standard deviation on the signals. Assuming the contribution to the momentum spread due to the spread in beam energy is negligible the predicted contrast, $c_{total}(x)$, is 44% using equation 5.13. Using equation 5.4 it is found that the intensity of signal from diseased tissue, N_d, is equal to $0.39N_h$, where N_h is the intensity of signal from normal tissue, N_h. This figure neglects any differences in attenuation that may also be present, which will act to reduce the signal further alter the contrast. For the two signals to be resolved with a 99.7% certainty the difference between them D, should be equal to $5\sqrt{N_d} + 5\sqrt{N_h}$ (Knoll, 1979). To determine the signal level, which provides adequate signal resolution, the scatter signal from a region of normal tissue was obtained in terms of photoelectrons/pixel/frame. The region of normal tissue used had been previously identified by the consultant histo-patholgist in Leeds using an transmission image of the phantom. The integration period was calculated so that $D = (1 - 0.39)N_h$. Due to the variations in beam output, the integration period was adjusted throughout the experiment to maintain this signal level.

5.3.2.3 Description of program used for data collection

A computer program was written to control the data collection. It was designed such that the total integration period in seconds could be input before acquisition. As each

image was acquired it was added to the previous image. This resulted in a summed image which was then divided by the number of images acquired. The programme then summed the pixel values in each of the 11 regions of interest across the image. The 11 regions of interest correspond to the 10 collimator holes and an additional dark region, where no radiation was incident for normalisation purposes. Each collimator hole was 45 × 30 pixels. The summed intensity values were then recorded.

5.3.2.4 Data corrections

In order to correct for variations in dark signal non-uniformity and offset, dark images were obtained at the beginning and end of each vertical scan of the phantom. Dark image data was normalised to the dark eleventh hole (no radiation) data in each image to correct for any small variation in temperature and offset, and subtracted from the image data.

To correct for FPN due to either non-uniformity in the beam intensity or spatial variation in the response of the L3 detector, an x-ray flat field image was acquired. Using a 3 cm thick piece of Perspex as a scatterer, a scatter image was collected for 10 minutes. To correct for non-uniformity in the data the flat field image was dark corrected and all subsequent scatter images were corrected using the algorithm given by equation 3.1.

The level of background radiation from any scatter of the primary beam was measured. Images were acquired with the tissue phantom in place, the x-ray beam on, and lead shielding positioned over the collimator holes. When a dark subtraction was made, the signal due to background radiation was found to be negligible.

The probability of direct interactions in the silicon of the L3 is extremely low, ~ 0.01 %. In addition, in section 5.2.3.6 it was seen that the signal from a direct interaction is approximately twice that of an indirect interaction. Consequently it is assumed that the contribution to the signal from direct interactions will not be significant.

A gain non-uniformity correction has not been applied. Diffraction information will be integrated over a number of frames. In each frame it is expected that only a few x-rays

will be incident upon the detector. The generated charge will vary according to the interaction depth within the silicon and will vary throughout the pixels, which record the interaction. Thus any gain non-uniformity correction would be difficult to quantify.

5.4 Diffraction Imaging

5.4.1 In vitro diffraction imaging using the L3 detector

Diffraction image data for the breast phantom was recorded using the L3 DEBI detector system described above. A 2.0GeV electron beam energy was available for diffraction imaging. Diffraction data was collected from only three fifths of the phantom due to the long integration periods required to achieve a good signal to noise ratio.

Transmission image data was used to measure the contrast due to attenuation. A transmission image of the phantom was acquired at 17.4 keV using a Fuji imaging plate. The imaging plate is a photo-stimulable phosphor plate which is used in a manner similar to x-ray film. The image was recorded by scanning the plate and phantom through the x-ray beam. The image underwent 16-bit digitisation using a Fuji scanner with 100 μm spatial resolution.

All recorded diffraction data were reconstructed as 2D images. For comparison, transmission image pixels have been binned so that one pixel represents an area of 1×1 mm^2. This enables a direct comparison of contrast due to transmission and the contrast due to scatter to be made. The transmission image has been cropped to show the same regions of the phantom that were scanned using the L3 DEBI system. Figure 5.17(a) and 5.17(b)) show the scatter and transmission images of the cancerous tissue inclusions in the healthy breast tissue. Cancerous inclusions are shown as regions of high intensity. Large cancerous inclusions are easily resolved in the both the diffraction image and the transmission.

The contrast between carcinoma and normal breast tissue obtained using the two techniques was investigated. A background or offset level for the transmission image

can be obtained from the average grey level in a region of the image upon which no direct radiation was incident.

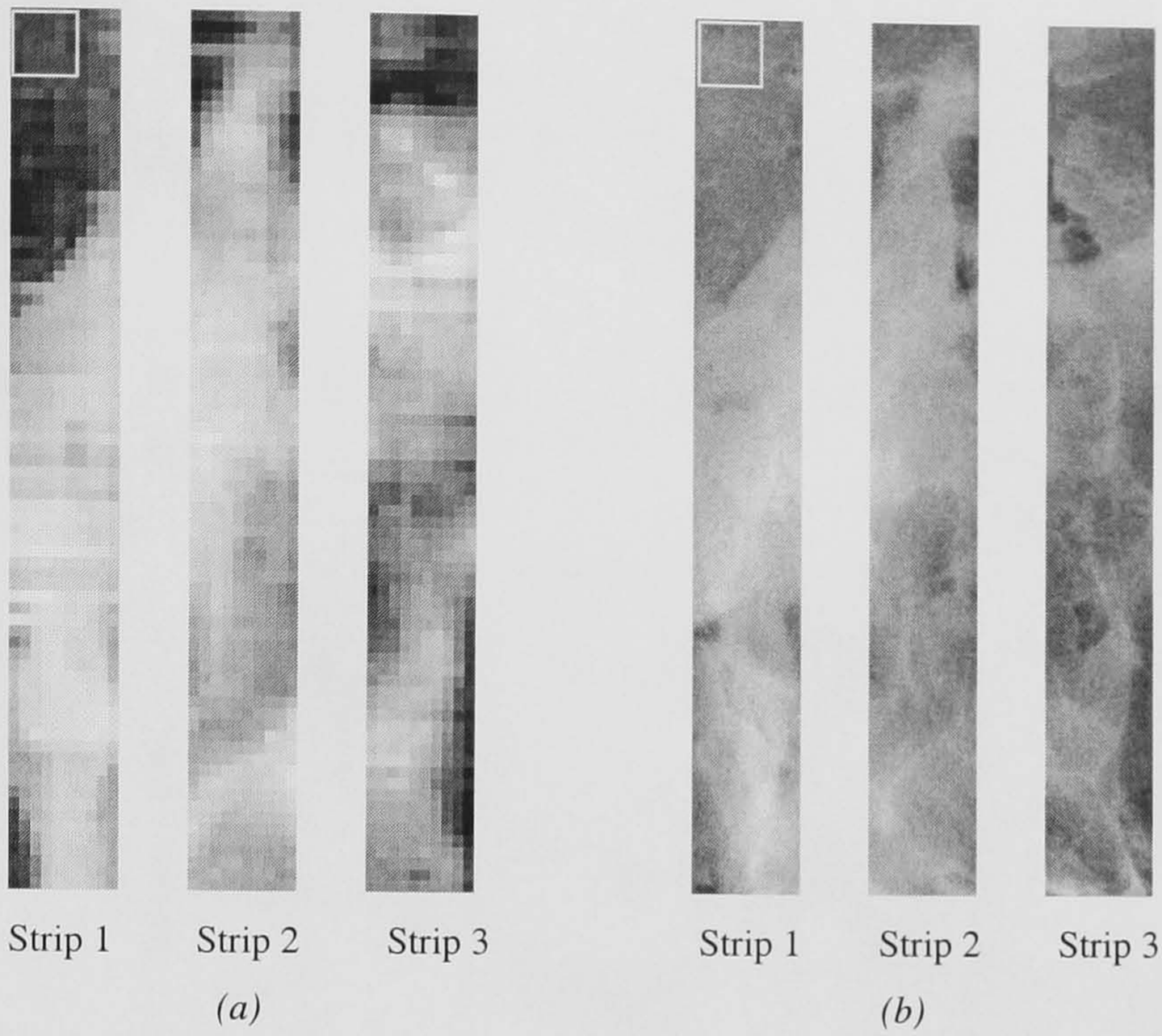

Figure 5.17. *Images of the cancerous tissue inclusions in the breast tissue phantom (a) diffraction and (b) transmission. The highlighted area shows a region of normal breast tissue, which was used to normalise the images for comparison.*

This background level was found from the area that was shielded by the steel thumbscrews that form part of the phantom. The signal in this region was subtracted from the entire image in order to gain a true measure of contrast. The imaging plate has a linear radiation response and, providing the phantom was imaged within the dynamic range of the detector, the difference in attenuation between diseased and normal tissue will be unaffected by the photon flux. Vertical profiles were plotted for each column of pixels. Profiles were obtained for corresponding columns in the transmission and the diffraction images and used to identify the maximum and minimum signal values, corresponding to the normal and diseased tissues types identified. The contrast between diseased and normal breast tissue was then found for each profile using equation 5.4. Nominal values suggest that the imaging plate has a spatially uniform response within ± 5%. Figures 5.18*(a), (b)* and *(c)* show profiles through strips 1, 2 and 3, respectively.

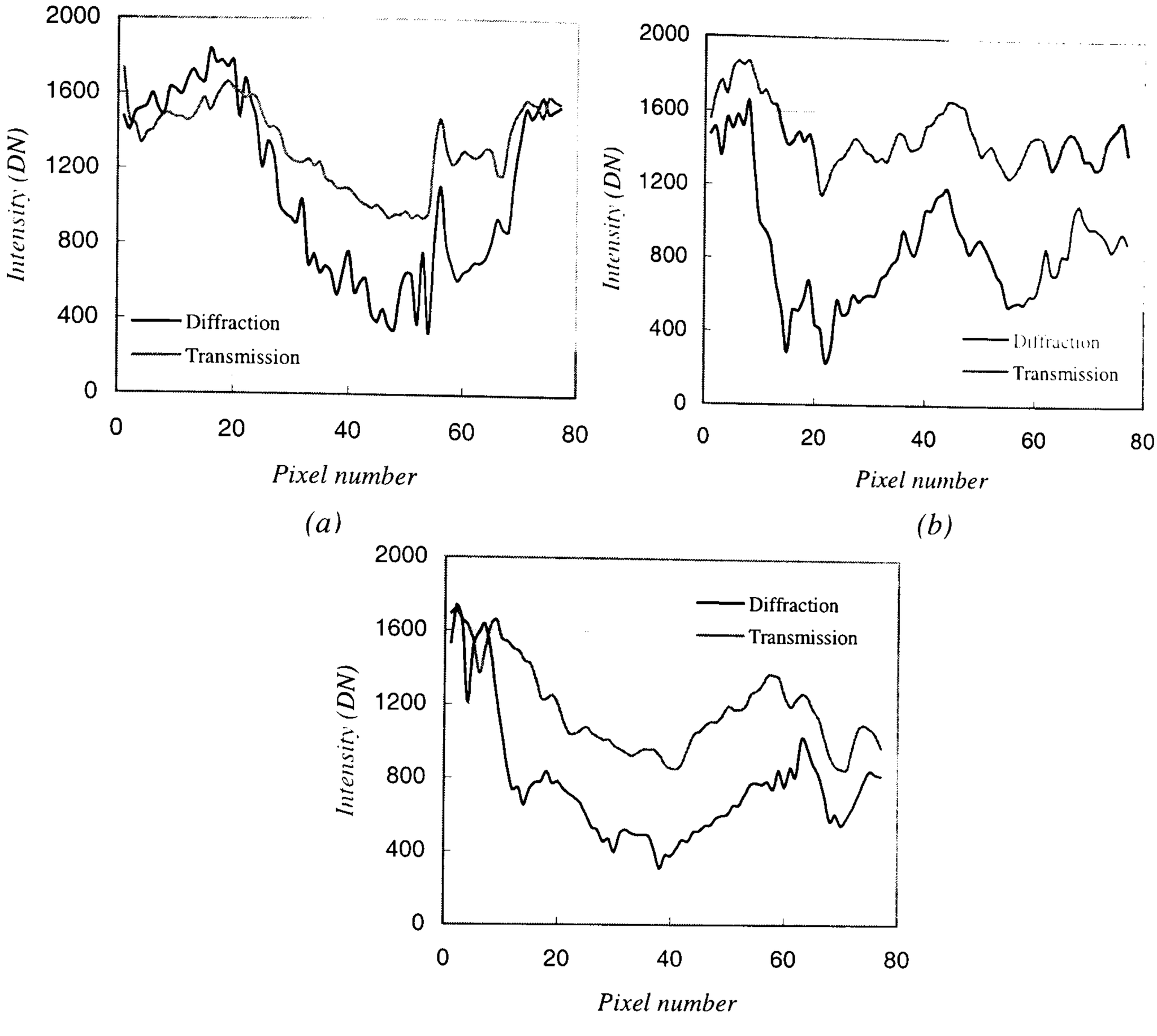

Figure 5.18. *Profiles through scatter and transmission images (a) strip1, (b) strip2 and (c) strip3. The y-ordinate values equal the total digital signal per image pixel.*

Transmission data was multiplied by a normalisation factor in order that the profiles could be plotted on the same axis. The normalisation factor *nf* was calculated using

$$nf = \frac{S_D(DN)}{S_T(DN)} \tag{5.16}$$

where S_D and S_T are the average digital signal values within a region of interest for the diffraction and transmission images respectively. The region of interest is shown in figure 5.17. This region is the most homogeneous region of normal breast tissue. The peaks in the scatter profiles are more prominent than those in the transmission data.

The gradients of the profiles between maximum and minimum values are higher in the scatter images, indicating that better tumour edge detection is feasible.

The average values of contrast for each set of profiles (one vertical image strip) have been calculated using the maximum and minimum intensity values and are given in table 5.2.

Table 5.2. *The average measured contrast between diseased and normal tissue for each image strip.*

	Diffraction (%)	Transmission (%)
Strip 1	54 ± 3.8	33 ± 1.0
Strip 2	51 ± 4.6	25 ± 0.8
Strip 3	61 ± 4.9	34 ± 1.0

An improvement in contrast of 60 – 100% is observed in the scatter images when compared to the transmission images. This is a greater improvement than measured previously by Kidane *et al.* (1999). The cancerous inclusions contained in the breast tissue phantom are sufficiently large so that a higher proportion of the scatter volume contained cancerous tissue. Subtracting the transmission contrast from the scatter gives an extra contrast due to scatter of 21%, 26% and 27 % for strip 1, 2 and 3, respectively. These values are slightly lower than the predicted value of scatter contrast of 44%. This is most likely due to that fact that the scatter volume will not always contain 100% tumour or 100% normal tissue. The experimental error in the measured contrast is due to the uncertainty on the signal, the uncertainty in the dark signal and the uncertainty in the ion chamber reading used to correct the images for reduction in beam intensity. Thus, the error is calculated by finding the standard deviation on the maximum and minimum signal, the standard deviation of the dark signal and the maximum percentage error on the ion chamber reading. The percentage errors are then added in quadrature. The value quoted is the maximum error for each strip.

5.4.2 Investigation of additional contrast information

The L3 DEBI system was used to investigate alternative regions of momentum transfer space. The maximum contrast between diseased and normal tissue is 51% at a momentum transfer value of 1.1nm^{-1}. A second region of high contrast is available at

1.6nm^{-1} where the contrast is reversed. Using equation 5.4 gives a contrast of 13%. At a scatter angle of 9°, 1.6nm^{-1} corresponds to a photon energy of 26.9keV. Another area of interest is at 1.4nm^{-1} (22.1keV at $\theta = 9°$) where the two curves cross, indicating there is no difference in the differential coherent scattering coefficient and thus zero contrast (shown in figure 5.19). Obtaining diffraction images at each of the 3 momentum transfer values enables the level of image contrast to be related to the differential scattering coefficient data.

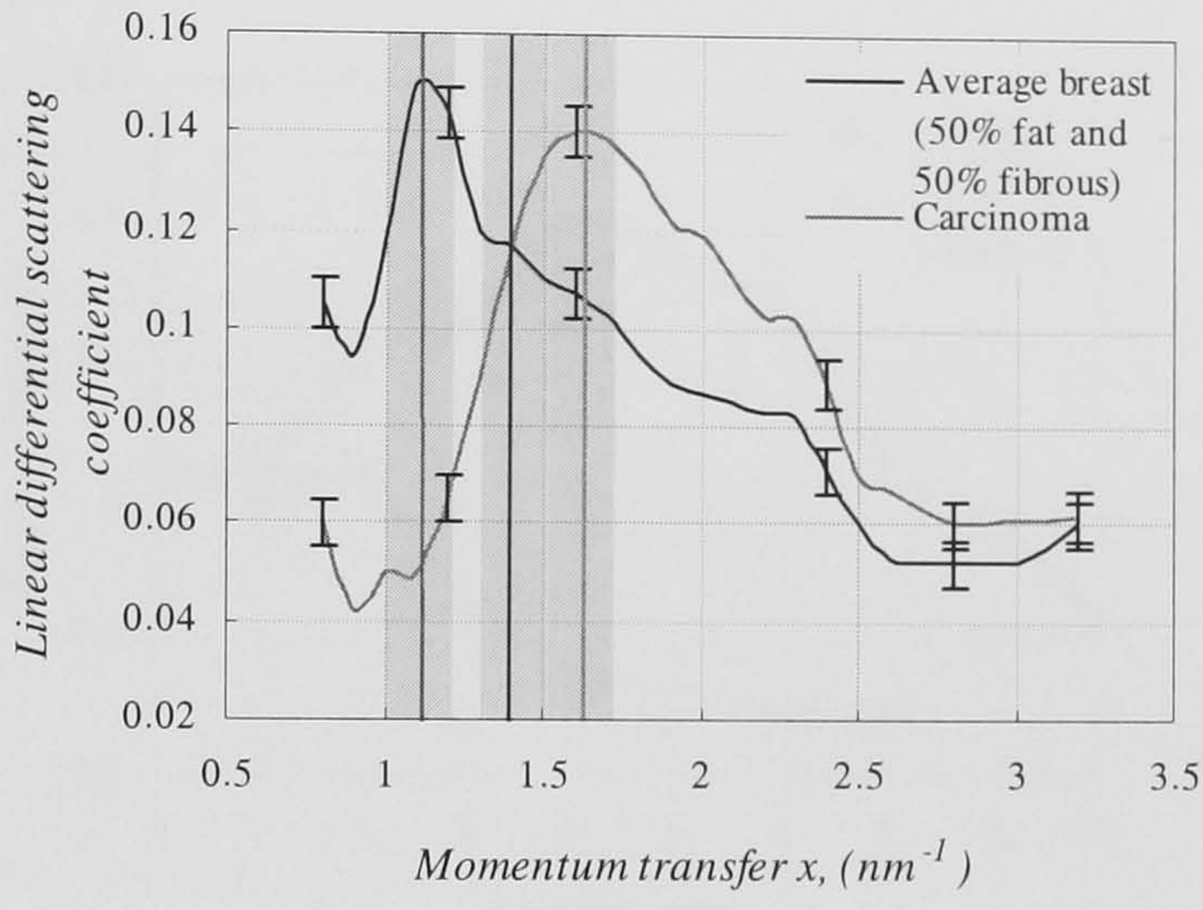

Figure 5.19. *Momentum transfer values of interest; 1.1nm^{-1} provides the maximum contrast (51%), at 1.6nm^{-1} the contrast is reversed (-13%) and at 1.4nm^{-1}, $\chi_h = \chi_d$ and the contrast is zero. The bands of colour show the momentum blurring of the DEBI system.*

Momentum blurring (illustrated in figure 5.19) will act to reduce the contrast in all three regions. Thus, using equations 5.2 and 5.13, the predicted contrast is calculated to be 44%, 0.7% and -12.8 % for momentum transfer values of 1.1nm^{-1}, 1.4nm^{-1} and 1.6nm^{-1} respectively. Diffraction and transmission data were recorded for a 10×10mm^2 region of breast tissue using 22.1keV and 26.9keV x-radiation. The region of tissue was chosen from the diffraction images obtained using 17.4keV x-radiation. From the diffraction image it was evident that this region contained both cancerous and normal tissue. To investigate how the contrast changed with momentum transfer the diffraction data was corrected for attenuation. The transmission data was normalised so that the average pixel value in the transmission and diffraction images were equal. The transmission image was then subtracted from the diffraction image. Figure 5.20 *(a), (b)* and *(c)* show the resulting diffraction images for 17.4keV, 22.1keV and 26.9keV respectively.

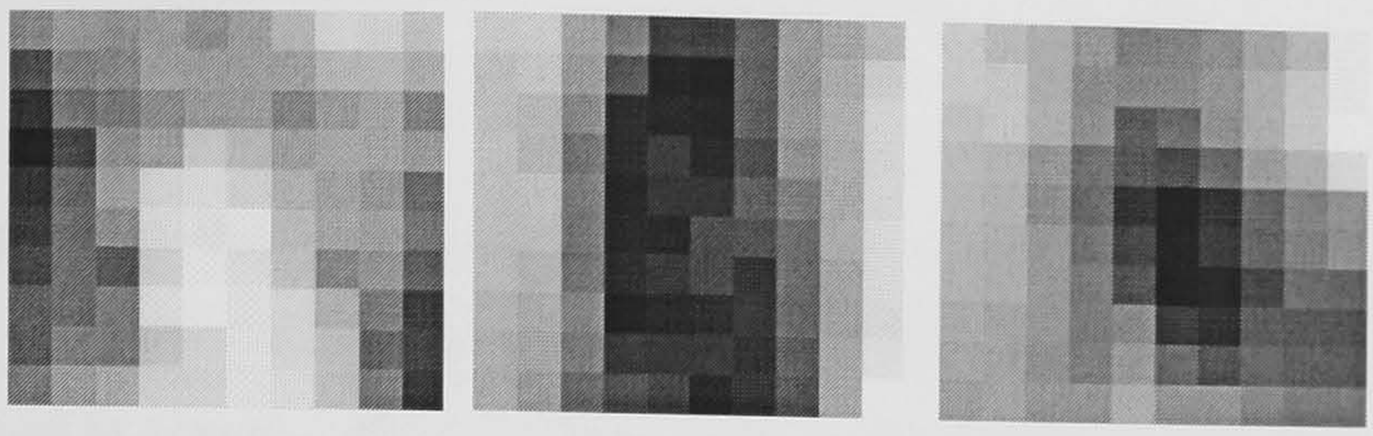

(a) (b) (c)

Figure 5.20. *Diffraction images recorded at 3 different momentum transfer values and corrected for attenuation (a) 1.1nm^{-1}, (b) 1.4nm^{-1} and (c) 1.6nm^{-1}.*

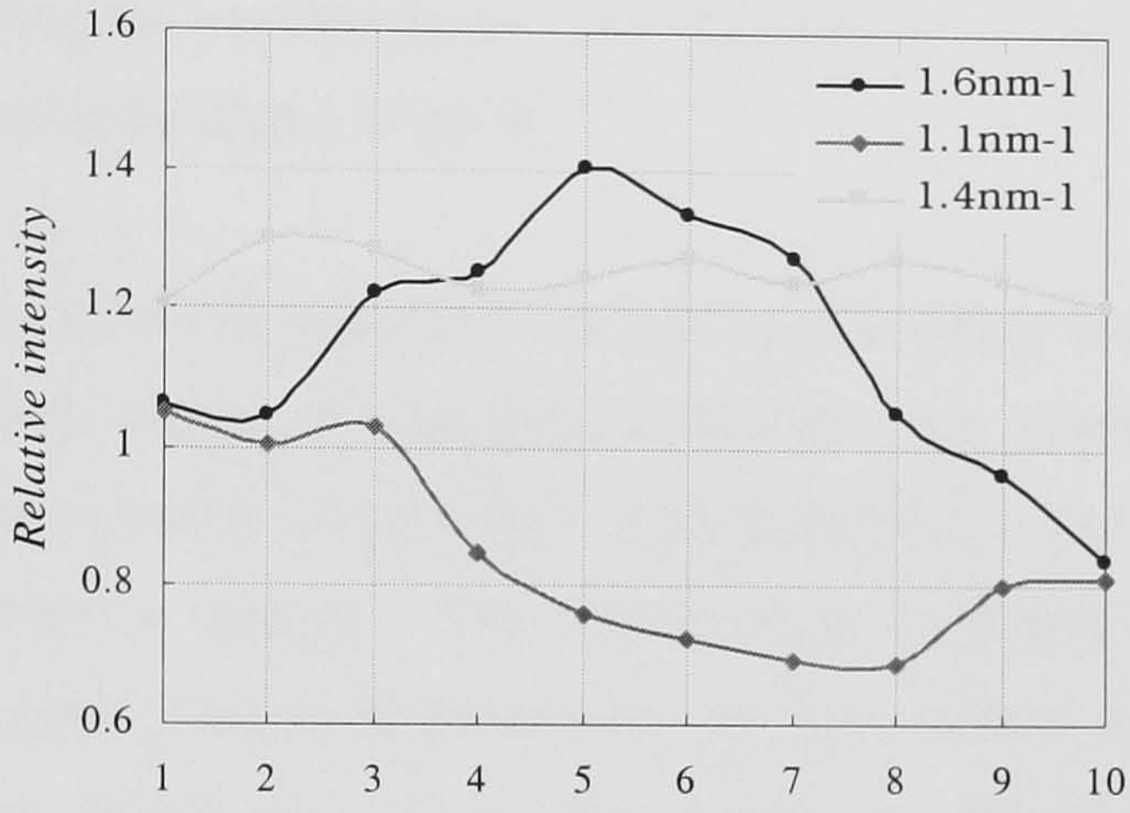

Figure5.21*. Profiles through the centre column of pixels for diffraction image recorded using at 1.1nm^{-1} 1.4nm^{-1} and 1.6 nm^{-1}.*

The profile through the image taken at a momentum transfer value of 1.4nm^{-1} is almost flat corresponding to almost zero contrast, which is predicted by the linear differential scattering coefficients. The contrast is reversed at 1.6nm^{-1} as expected. Calculating the measured contrast (scatter only) using the maximum and minimum intensity values in the profiles shown in figure 5.23 gives a measured scatter contrast of 20% ± 1.4% and – 22 % ± 3.3% for 1.1nm^{-1} and 1.6nm^{-1} respectively. The value of contrast at 1.6nm^{-1} is almost twice that predicted using the linear differential scattering coefficients measured by Kidane (2001). This result indicates that further contrast information can be obtained at a larger angle. However, further work is required to confirm this, further measurements of the linear differential scattering coefficients will be performed using a synchrotron radiation source.

5.5 Conclusions

The main purpose of this work was to validate the use of the L3CCD in diffraction imaging. An L3 detector has been designed to detect individual x-ray photons and successfully used to obtain diffraction data in a clinical environment. The paramters of the L3 that make it suitable for this work are high quantum efficiency (>99%), high *SNR* performance, position sensitivity, small size and low voltage requirements. The most salient feature of the L3 detector is that single x-ray photons are clearly visible at mammographic energies. Consequently the L3 detector is suitable to be used in a clinical setting to measure scatter contrast.

The feasibility of an L3 DEBI system has been demonstrated by using the L3 detector to record the diffraction images of cancerous inclusions in a matrix of normal human breast tissue. Transmission images were also measured in order to compare their contrast with diffraction images. The results have confirmed that a 60 – 100% improvement in image contrast between diseased and normal tissues is achievable. Measurements have shown that despite large levels of momentum transfer blurring, (22%) diseased and normal tissue could be resolved.

The reversal of image contrast at $1.6nm^{-1}$ has been confirmed using the breast tissue phantom. The increase in measured contrast at the momentum transfer value of $1.6nm^{-1}$ indicates that further contrast information is obtainable at larger scatter angles. The corresponding scatter angle at 17.4keV is 13.1°. A larger scatter angle could improve the resolution in the *x*-direction. Additionally, it is a more convenient angle to collect the scattered radiation from, as the entrance to the collimator will be further from the primary beam. The fact that the contrast is reversed can be used to provide more scatter information. If scatter data is collected at both $1.1nm^{-1}$ and $1.6nm^{-1}$ the difference between the intensities could possibly be used to make a positive identification of diseased tissue with increased certainty.

The gradients of the profiles between maximum and minimum values are higher in the scatter images, indicating better tumour edge detection is feasible and therefore better localisation of the tumours is possible.

An L3 DEBI system has been modelled and it has been shown that a clinical system is feasible and that the signals between normal and diseased breast tissue are 99.7% resolvable with theoretical contrast of 30%.

This work has confirmed that the L3 is useful for diffraction imaging. A clinical system would incorporate a 2-D collimator array, which will take advantage of the 2-D nature of the CCD. This will improve the spatial resolution in the x-direction due to the scatter volumes overlapping at the plane of the phantom. A 2-D collimator will provide 3-D information about the position of the tumour within the breast. This will assist in locating tumours during surgery.

CHAPTER 6

Conclusions and further work

An evaluation of the performance of a novel low light level CCD technology that could be suitable for the development of new digital radiographic systems has been presented in this thesis. The evaluation process has included a full characterisation study of two L3 charge coupled devices in order to identify their salient performance parameters and optimal operational settings. The measured performance has been compared to that of other detectors in order to identify potential imaging applications, conclusions have been made to this end. The practical application of L3 technology to two x-ray imaging applications has been assessed using linear systems analysis, experimental measurements and consideration of the effect of various detector parameters upon the imaging performance of digital radiographic systems.

6.1 Evaluation of L3 technology

The evaluation of the performance parameters of the L3CCD sensors showed that the signal to noise characteristics and the minimum detectable signal of the device are limited by thermal and spurious noise properties of the device. Measurements of system noise have shown that high levels of read noise can be rendered insignificant using multiplication gain. As signal is amplified above the system read out noise, the *SNR* increases until it equals the pre-gain *SNR*. However, the amplification of dark and spurious currents restricts the maximum *SNR* attainable. To increase the *SNR* performance thermal and spurious currents need to be reduced. Thermal current can be reduced by cooling, however, the presence of spurious current, which is inversely proportional to temperature, counteracts the benefits of cooling. The optimal operational temperature was found to be -5°C. Measurements of excess noise factor

have shown that there is no additional contribution to noise and hence no further degradation of *SNR* arises from the multiplication gain mechanism.

The sensitivity in terms of the minimum detectable signal is an important parameter to consider in the design of an L3CCD based detector system. When used in conjunction with an x-ray phosphor, the optical coupling efficiency between the CCD and the phosphor will determine the proportion of light incident upon the CCD. The minimum detectable signal can be used to ascertain acceptable levels of optical coupling efficiency. The minimum detectable signal was measured to be approximately of two photoelectrons per pixel per frame.

In addition to limiting the noise performance of the device spurious current also limits the maximum useable gain. However, this is a secondary concern as it has been shown that the gain necessary to 'see' the minimum detectable signal is below the threshold for which spurious becomes significant. Clearly, to achieve optimal performance, further work is required to identify methods of reducing spurious noise. However, the minimum detectable signal is relatively low in comparison with most detectors. The L3CCD surpasses conventional CCDs in sensitivity by two orders of magnitude. This leads to the conclusion that the L3CCD should be considered before the CCD in all applications where low signal detection is required.

Measurements of dynamic range as a function of multiplication gain have shown that the L3CCD has poor dynamic range performance at high gain. High dynamic range ($\sim 10^3$) is required for the majority of radiographic techniques. Consequently the application of the L3 technology in its current state will be limited to low dynamic range imaging techniques such as diffraction imaging, fluoroscopy and electronic portal imaging. Extension of the dynamic range is under investigation by the manufacturer.

With the exception of dynamic range, the performance of the L3CCDs is comparable with that of other photodetectors used in medical imaging and exceeds that of other charge coupled devices. This indicates that the L3 should be considered in the design and optimisation of new and existing x-ray imaging modalities.

6.2 L3 technology application to medical imaging

The application of L3 technology to two specific diagnostic imaging techniques was investigated. These techniques were chosen after consideration of the measured performance characteristics of the L3CCD and the comparison of L3 technology with other detectors.

Fluoroscopy employs low flux x-ray detection to facilitate real-time x-ray imaging. Typically, its dynamic range requirements are low (Cowen, 1992). Linear systems analysis has been used to predict the performance of an L3 based fluoroscopic imaging system that employs a lens to couple the L3CCD to an x-ray phosphor. In order to meet the field of view requirements the image is de-magnified leading to inefficient optical coupling. Calculations have shown that despite the fact that the L3CCD has a low minimum detectable signal the phosphor/lens/L3CCD system cannot compete with the performance of the x-ray image intensifier (XRII). Experimental validation of the model has confirmed this conclusion. Further calculations have been made for another proposed system employing an array of phosphor/taper/L3CCD detectors. Comparison of the predicted performance of this system with systems in clinical use show that such a detector system would be a completive alternative to XRIIs.

Given the numerous potential benefits of the exclusion of the image intensifier from the imaging chain, i.e. less bulk, no image distortion and no 'veiling glare' (Tate *et al.*, 1997), a phosphor/taper/L3CCD is attractive. Indeed, these advantages have lead to the introduction of flat panel imagers despite their inferior *DQE* performance. Further work is required to evaluate the advantages of an L3 based system. The proposed system comprises 4×4 tiled L3CCDs using a 5:1 taper on each covering a 5 $\times$ 5cm^2 area of phosphor. A prototype system consisting of one phosphor/taper/L3CCD device would be built and its performance extrapolated for a large area imaging system.

Diffraction enhanced breast imaging (DEBI) has been identified as having the potential to enhance the transmission image, hence raising the sensitivity of x-ray mammography. Linear systems analysis has been used to predict the requirements of

an L3-based DEBI system that can be used to collect scatter data in a clinical environment. Calculations of the diffraction signal has shown that the number of scattered quanta during the mammographic examination is low. This will ultimately limit the *SNR* performance of the technique. In order that the detection system does not degrade *SNR* further, it is important that the diffraction detector can detect almost every x-ray photon. To this end, an L3 detector has been built and evaluated. Individual x-ray photons of 17.4keV have been imaged successfully. It is calculated that 99.7% of the x-ray photons are stopped in the detector.

To demonstrate the use of the L3 detector for DEBI it has been used to acquire diffraction images of human breast tissue with cancerous inclusions. Measurements of scatter contrast confirm improvements in scatter contrast compared to transmission contrast. Measurements of contrast at different regions of momentum transfer also show that further improvements in the positive identification of diseased tissue can be made.

The successful demonstration of the L3CCDs ability to collect diagnostic information has shown that the L3CCD is suitable for DEBI. Moreover, the L3CCD has potential for use in other areas that employ diffraction imaging such as diffraction CT (Batchelar and Cunningham 2002).

Further work is required to evaluate the *SNR* attainable with a clinical based DEBI system. Measurements should also be made to determine the optimal collimation requirements to produce the highest tissue discrimination. Further work is required to confirm the increased levels of image contrast measured at 1.6nm^{-1}. This work will be undertaken using the L3CCD and will fully quantify the benefits of the DEBI technique.

APPENDIX A

Definition of terms used in this thesis

Poisson noise

Radiographic images are inherently noisy because of the quantum nature of radiation. The fluctuation of x-ray intensity follows Poisson statistics so that the variance $\sigma_{N_i}^2$ about the mean number of x-ray quanta N_i falling on a given area of a detector is equal to N_i.

The Bernoulli distribution

The Bernoulli distribution arises in a binary selection process in which there are two possible outcomes. If there are exactly N_i optical photons incident on a detector, each photon is either detected or it is not; this is a binary selection process. If the probability of detection is p, then the probability that a photon will not be detected is $q = 1 - p$. The probability of detecting N_o from the total number of incident photons is given by

$$\Pr(N_o / N_i) = \frac{N_i!}{(N_i - N_o)!N_o!} p^{N_o} q^{N_i - N_o} \tag{A.1}$$

$\Pr(N_o/N_i)$ is the Bernoulli distribution. The Bernoulli distribution is applicable where N_i is fixed. However N_i may not fixed. In the case of most physical problems, N_i is itself a random variable. In the case of N_i governed by Poisson statistics it can be shown that $\Pr(N_o)$ is Poisson and that the mean and the variance is (Barrett and Swindell, 1981)

$$\overline{N}_o = pN_i \tag{A.2}$$

$$\sigma_{N_o}^2 = pN_i \tag{A.3}$$

The Swank factor and the Fano factor

When considering the number of optical photons generated in a x-ray phosphor by a single x-ray it cannot be assumed that the number is a Poisson random variable. The optical photons are not produced independently. They result from a cascade process, in which the energy of the x-ray, ε_x, is transferred to n optical photons of energy ε_λ. If there was no dissipative mechanism, all energy would be transferred to $n = \varepsilon_x/\varepsilon_\lambda$ optical photons. The number n would then have zero variance and the condition $\sigma_N^2 = \overline{N}$, characteristic of a Poisson process, is violated. It is only by introducing another energy dissipative mechanism, such as phonon generation that a non-zero variance can be obtained. Swank was the first to demonstrate that the output variance was equal to

$$\sigma_{N_o}^2 = IpN_i \tag{A.4}$$

where I is the Swank factor, which has a maximum value of unity.

An analogous situation occurs in semiconductors, where secondary electrons are created in a cascade process. In semiconductor detectors

$$\sigma_{No}^2 = FpN_i \tag{A.5}$$

where F is the Fano factor. Numerically, F may be as low as 0.005 for silicon detectors so that the variance is one twentieth of what it would be for Poisson statistics (Barrett and Swindell, 1981).

REFERENCES

Aebi V. W., Costello K. A., Edgecumbe J. P., Boyle J. J., Robbins W. L., Bell R., Burt D., Harris A., Palmer I., and Pool, P., 'Gallium Arsenide electron bombarded CCD technology,' Presented at the SPIE International Symposium on Optical Science, Engineering and Instrumentation, Conference 3434A, San Diego, (1998).

Amendolia S. R., Bisogni M. G., Bottigli U., Ciocci M. A., Delogu P., Dipasquale G., Fanticci M. E., Maestro P., Marzulli V., Mikulec, B., Pernigotti E., Rossso V., Stefanini A., and Stumbo S., 'Test of a GaAs-based pixel device for digital mammography,' Nuclear Instruments and Methods in Physics Research A, Vol. **460** (1), pp. 50 – 54, (2001).

Antonuk L. E., Jee K. W., El-Mohri Y., Maolinbay M., Nassif S., Rong X., Zhao Q., Siewerdsen J. H., Street R. A., and Shah K.S., 'Strategies to improve the signal and noise performance of active matrix, flat panel imagers for diagnostic applications,' Medical Physics, Vol. **27** (2), pp. 289 – 306, (2000).

Arfelli F., Barbiellini G., Bonvicini V., Bravin A, Cantatore G., Castelli E., Cristaudo P., Di Michiel M., Longo R., Olivo A., Pani S., Pontoni D., Poropat P., Prest M., Rashevsky A., Tomasini F., Tromba G., and Vacchi A., 'SYRMEP: an innovative detection system for soft x-rays,' Nuclear Instruments and Methods in Physics Research A, Vol. **392** (1-3), pp. 188 – 191, (1997).

Arisaka K., 'New trends in vacuum-based photon detectors,' Nuclear Instruments and Method in Physics Research A, Vol. **442**, (1) pp. 699 – 709, (2000).

Barrett H. H. and Swindell W., Radiological Imaging, The Theory of Image Formation, Detection, and Processing, Vol. **1**, p. 97, Academic Press, New York, U.S.A., (1981).

Batchelar D. and Cunningham I. A., 'Material specific analysis using coherent scatter imaging,' Medical Physics, Vol. **29**, (8), pp. 1651 – 1660, (2002)

Beuville E., Cahn R., Cederstrom B., Danielsson M., Hall A., Hasegawa B., Luo L., Lundqvist M., Nygren D., Oltman E., and Walton J., 'High resolution imaging using a silicon strip detector,' IEEE Transactions on Nuclear Science, Vol. **45** (6), pp. 3059 – 3063, (1998).

Beynon J. D. E. and Lamb R. R., 'Charge-coupled devices and their applications,' McGraw-Hill Book Company (U.K.) Limited, London, U.K., (1980).

Birch R., Marshall M. and Ardan G.M., 'Catalogue of spectral data for diagnostic X-rays', Hospital Physics Association, Scientific Report Series **30**, (1979).

Bissonnette J., Cunningham I. A., Jaffray D. A., Fenster A., and Munro P., 'A quantum accounting and detective quantum efficiency analysis for video based portal imaging,' Medical Physics, Vol. **24** (6), pp. 815 – 826, (1997).

Boyle W. S. and Smith G. E., 'Charge coupled semiconductor devices,' Bell Systems Technological Journal, Vol. **49**, pp. 587 – 593, (1970).

Burgess A. E., in Van der Zeil A., 'Noise in measurements' John Wiley and Sons, New York, U.S. (1976)

Burt D. and Bell R., of E2V Technologies Ltd, Personal communication, (2001).

Calvi M., Cattadori C., Matteuzzi T., and Tabarelli de Fratis T., 'Characterisation of large area proximity focussed photodiodes,' Nuclear Instruments and Methods in Physics Research A, Vol. **369** (1), pp. 157 – 163, (2002).

Capasso F. 'Semiconductors and Semi metals,' edited by Willardson R. K. and Beer A. C., Academic, New York, 1885), Vol. 22 Part D, pp. 1-172.

Chapman D., Thomlinson W., Johnston R. E., Washburn D., Pisano E., Gmir W., Zhong Z., Menk R., Arfelli F., and Sayers D., 'Diffraction enhanced imaging,' Physics in Medicine and Biology, Vol. **42**, pp. 2015 – 2025, (1997).

Chin R., Holonyak N., Stillman G. E., Tang J. Y., and Hess K., 'Impact ionisation in multilayed heterojunction structures,' Electronic letters, Vol. **40**, pp.38-40, (1980).

Chynoweth A. G., 'Ionisation rates for electrons and holes in silicon,' Physical Review, Vol**. 109**, pp. 1537 – 1540, (1958).

Corrigan N. M., Chavez A. E., Wisner E. R., and Boone J. M., 'A multiple detector array helical x-ray microtomography system for specimen imaging', Medical Physics, Vol. **26** (8), pp. 1708-1713 (1999).

Cowen A. R., 'Digital x-ray imaging; Review Article,' Measurement in Science and Technology, Vol. **2**, pp.691 – 707, (1991).

Cowen A. R. and Workman A., 'A physical image quality evaluation of a digital spot fluorography system,' Physics in Medicine and Biology, Vol. **37**, (2), pp. 325 – 342, (1992).

Cowen A. R. Parkin G. J. S., and Hawkridge P., 'Direct digital mammography image acquisition,' European Radiology, Vol. **7**, pp. 931 – 934, (1997).

Cunningham I. A. and Fenster A., 'A method for modulation transfer function determination from edge profiles with correction for finite element differentiation,' Medical Physics, Vol. **14** (4), pp. 533 - 537 (1987).

Cunningham I. A., Westmore M. S., and Fenster A., 'A spatial frequency dependant quantum accounting diagram and detective quantum efficiency model of signal and

noise propagation in cascaded imaging systems,' Medical Physics, Vol. **21** (3), pp. 417 – 427, (1994).

Cunningham I. A. and Shaw R., 'Signal-to-noise optimisation of medical imaging systems,' Journal of the Optical Society of America A., Vol. **16** (3), pp. 621 – 632, (1999).

Cunningham I. A., Moschandreou T., and Subotic V., ' The detective quantum efficiency of fluoroscopic systems: The case for a spatial-temporal approach (or does the ideal observer have infinite patience?),' Proceedings of SPIE Vol. **4320,** (2001).

Crowell C. R. and Sze S. M., 'Temperature dependence of avalanche multiplication in semiconductors,' Applied Physocs Letters, Vol. **9** (6), pp. 242 – 244, (1966).

Dainty J. C. and Shaw R., *Image Science*, Academic Press: New York, U.S.A. (1974).

Dalinenko I., Kossov V., Kozlov V., Lazovsky L., Maluarov A., Vishnevsky G., Vydrevitch M., Zhuk A., and Golovkin S., 'Design and fabrication technology of thinned backside excited CCD imagers and the family of electron-bombarded CCD image tubes,' Nuclear Instruments and Methods in Physics Research A, Vol. **387** (1-2), pp. 294 – 296, (1997).

Daválos A., 'An investigation of the imaging performance of new digital detectors,' PhD thesis, submitted to the University of London, (1994).

Davies A. G., Cowen A. R., and Kengyelics S. M., 'Threshold contrast detail detectability measurement of the fluoroscopic image quality of a dynamic solid-state digital x-ray image detector,' Medical Physics, Vol. **8** (1), pp. 71 – 15 (2001).

Drake D. G., Jaffray D. A. and Wong J. W., 'Characterization of a fluoroscopic imaging system for kV and MV radiography', Medical Physics, Vol. **27** (5), pp. 898 – 905, (2000).

E2V Technologies Ltd, Personal communication, (2002).

Ershov M. and Ryzhii V., ' Temperature dependence on the electron impact ionisation coefficient in silicon,' Semiconductor Science and Technology, Vol. **10**, pp. 138 – 142, (1995).

Frenandez M., Kerioloinen J., Serimaa R., Torkkeli M., Karjalainen-Lindsberg M. L., Tenhuman M., Thomlinson W., Urban V., and Suortti P., 'Small angle x-ray scattering studies of human breast tissue samples,' Physics in Medicine and Biology, Vol. **47**, pp. 577 – 592, (2002).

Gajar S. A. and Burke B. E., 'Charge amplification by impact ionisation in charge coupled devices,' IEEE Transactions on Electron Devices, Vol. **35** (12), pp. 2435 – 2436, IIIB-7, (1988).

Grove A. S., *The Physics and Technology of Semiconductor devices,* John Wiley and Sons, New York, U.S. (1967).

Gruner S. M., Tate M. W., and Eikenberry E. F., Charge-coupled device area x-ray detectors, Review of Scientific Instruments, Vol. **73** (8), pp. 2815 – 2842, (2002).

Hakim N. Z., Saleh B. E. A. and Teich M. C., 'Generalised excess noise factor for avalanche photodiodes of arbitrary structure,' IEEE Transactions on Electron Devices, Vol. **37** (3) pp. 599-610, (1990).

Hayat M. M., Saleh B. A. E., and Teich M. C., ' Effect of dead space on gain an noise in Si and GaAs avalanche photodiodes,' IEEE Journal of Quantum Electronics, Vol. **28**, pp. 1360 – 1365, (1992).

Hess K., 'Advanced theory of semiconductors,' Prentice-Hall, London , U.K. (1988).

Hejazi S. and Trauernicht D. P., 'System considerations for digital chest radiography and digital mammography', Medical Physics, Vol. **24** (2), pp. 287 – 297, (1997).

Herbert D. C., 'Avalanche noise in sub-micrometre pin diodes,' Electronic Letters, Vol. **33** (14), pp. 1257 – 1258, (1997).

Holdsworth D. W., Gerson R. K., and Fenster A., 'A time-delay integration charge-coupled device camera for solt scanned digital radiography,' Medical Physics, Vol. **17** (5), pp. 876 – 885, (1990).

Howes M. J. and Morgan D. V., 'Charge-coupled devices and systems,' p. 66, John Wiley and Sons, Chichetser, U.K., (1979).

Hynecek J. 'CCM – A new low noise charge carrier multiplier suitable for charge detection of small pixel CCD image sensors,' IEEE Transactions on Electron Devices, Vol. **39** (8), 1972 - 1975, (1992).

Hynecek J., 'Impactron – A new solid state image intensifier,' IEEE Transactions on Electron Devices, Vol. **32** (10), pp. 2238 - 2241, (2001).

Janesick J. R., Elliott T., Collins S., Blouke M. M., and J. Freeman J., 'Scientific charge-coupled devices,' Optical Engineering, Vol. **26**, pp. 693 – 714, (1987).

Janesick J. R., 'Pixel Vision Tutorial – Spurious Charge,' http://www.pvinc.com/janesicks-spurious-letter.htm, Downloaded 24/09/2002.

Jerram P., Peter P., Bell R., Burt D. J., Bowring S., Spencer S., Hazelwood M., Moody I., Catlett N., Heyes P. S., 'The LLLCCD: Low light imaging without the need for an intensifier,' Proceedings of SPIE, Vol. **4036,** pp. 178 – 186**,** (2001).

Johns P. C. and Yaffe M. J., 'Coherent scatter in diagnostic radiology,' Medical Physics, Vol. **10** (1), pp. 40-50 (1996).

Johns H. E. and Cunningham J. R., *The Physics of Radiology,* 4th edition, Charles C. Thomas: Illinois, U.S.A. (1983).

Jones R. C., 'A new classification system for radiation detectors,' Journal of the Optical Society of America, Vol. **39**, pp. 327 – 343, (1949).

Judy P. F., 'The line spread function and modulation transfer function of a computed tomography scanner,' Medical Physics, Vol. **3** (2), pp. 233 - 236 (1976).

Karellas A., Lui H., Reinhardt C., Harris L. J., and Brill A. B., 'Imaging of radionuclide emissions with a low noise charge-coupled device', IEEE Transactions on Nuclear Science, Vol. **40** (4), pp.979–982, (1993).

Kidane, G, Speller R, Royle G. and Hanby A., 'Scatter signatures for normal and neoplastic breast tissues', Physics in Medicine and Biology, Vol. **44**, pp. 1797 – 1802, (1999).

Kidane G., 'Breast tissue charcterisation using low angle x-ray scattering,' PhD thesis submitted to the University of London (2001).

Kim, J., Yamamoto Y. and Hogue H.H. 'Noise-free avalanche multiplication in Si solid state photo-multipliers', Appl. Phys. Lett. **70** (21) 2852-2854, (1997).

Knoll G. F., 'Radiation Detection and Measurement,' John Wiley and Sons, New York, U.S.A., (1979).

Kobayashi S., Yamaoka K., Amami M., and Kobayashi M., ' Evalaution of the avalanche photodiode (APD) as scintillation sensor,' Nuclear Instruments and Methods in Physics Research A, Vol. **364** (2-3), pp. 95 – 102, (1995).

Lewis R. A., Rogers K. D., Hall C. J., Towns-Andres E, Slawson S., Evans A., Pinder S. E., Ellis I. O., Boggis C. R. M., Hutton A. P., and Dance D. R., 'Breast cancer diagnosis using scattered x-rays,' Journal of Synchrotron Radiation, Vol. **7**, pp. 348 – 352, (2000).

Lui H., Karellas A., Harris L. J., and D'Orsi, C. J., 'Optical fibre tapers and their impact on the performance of a fibreoptically coupled CCD x-ray imaging system,' Proceedings of SPIE, Vol. **1894**, pp. 136-147, (1993).

Mackay C. D., Tubbs N., Bell R., Burt D., Jerram P., and Moody I., 'Sub-electron read noise at MHz pixel rates,' Proceedings of SPIE, Vol. **4306**, pp. 289 – 298, (2001).

Maes W., De Meyer K., and Van Overstraten R., 'Impact ionisation in silicon: A review and update,' Solid-State Electronics, Vol. **33** (6), pp. 705 – 718, (1990).

Maidment A. D., Fahrig R., and Yaffe M. J., 'Dynamic range requirements in digital mammography,' Medical Physics, Vol. **20** (6), pp. 1621 – 1633, (1993).

Maidment A. D. A. and Yaffe M. J., Analysis of the spatial-frequency-dependent DQE of optically coupled digital mammography detectors, Medical Physics, Vol. **21** (6), pp. 721 – 729, (1994).

Mainprize J. G., Ford N. l., Yin S., Tumer T., and Yaffe M. J., 'A slot scanned photodiode-arrray/ccd hybrid detector for digital mammography', Medical Physics, Vol. **29** (2), pp. 214-225 (2002).

Maolinbay M., El-Mohri, Y., Antonuk L. E., Jee K.-W., Nassif S., Rong, X. and Zhao Q., 'Additive noise properties of active matrix flat panel imagers,' Medical Physics, Vol. **27** (8), pp. 1841 – 1854, (2000).

Marconi Applied Technologies Ltd, 'Data sheet: CCD65 series ceramic pack, low light-CCD sensor' http://e2vtechnologies.com /datasheets/l3vision_ccds/llcer.pdf , (2002(a)).

Marconi Applied Technologies Ltd, 'Low-light technical note 2: The use of multiplication gain in L3 vision CCD sensors,' http://e2vtechnologies.com /datasheets/l3vision_ccds/lltn2.pdf , (2002(b)).

Marshall N. W., 'The practical application of signal detection theory to image quality assessment in x-ray image intensifier-TV fluoroscopy,' Physics in Medicine and Biology, Vol. **46**, pp. 1631–1649, (2001).

Marshall N. W., Kotre C. J., Robson K. J. and Lecomber A. R., 'Receptor dose in digital fluorography: a comparison between theory and practice,' Physics in Medicine and Biology, Vol. **46**, pp. 1283 – 1296 (2001).

Matsuo K., Teich M. C., and Saleh B. A. E., 'Noise properties and time response of the staircase avalanche photodiode,' IEEE Transactions on Electron Devices, Vol. **32** (12), pp. 2615-2623, (1985).

McIntrye R. J., 'Multiplication noise in uniform avalanche photodiodes,' IEEE Transactions on Electron Devices, Vol. **13** pp. 164-168, (1966).

McIntrye R. J., 'A new look at impact ionisation- Part I: A theory of gain, noise, breakdown probability, and frequency response', IEEE Transactions on Electron Devices, Vol. **46** (8) pp. 1623-1631, (1990).

Moran S. E., Ulich B. L., Elkins W. P., Strittmatter R. L., and DeWeert M. J., 'Intensified CCD (ICCD) dynamic range and noise performance,' Ultrahigh and high-speed photography and image-based motion measurement, SPIE, Vol. **3173**, pp. 430 – 457, (1997).

Ong D. S., Li K. F., Rees G. J., Dunn G. M., David J. P. R., and Robson P. N., ' A Monte Carlo investigation of multiplication noise in thin p^+-i-n^+ GaAs avalanche photodiodes,' IEEE Transactions on Electron Devices, Vol. **45** (8), pp. 1804 – 1810, (1998).

Peplow D. E., and Verghese K., 'Measured molecular coherent scattering form factors of animal tissue, plastics and human breast tissue,' Physics in Medicine and Biology,' Vol. **43,** pp. 2431 – 2452, (1998).

Phosphor Technology Ltd, Nazeing, Essex, U.K., $Gd_2O_2S_2$:Eu data sheet.

Plimmer S. A., David J. P. R., Jacob B., and Rees G. J., ' Impact ionisation as functions of two-dimensional space and time,' Journal of applied physics, Vol. 89 (5), pp. 2742 – 2751, (2001).

Ponchut C., Visschers J. L., Fornaini A., Graafsma H., Mairino M., and Mettivier G., Calvert D., 'Evaluation of a photon-counting hybrid pixel detector array with a synchrotron X-ray source,' Nuclear Instruments and Methods in Physics Research A, Vol. **484** (1-3), pp. 396 – 406, (2002).

Renzi M. J., Tate M. W., Ercan A., Gruner S. M., Fontes E., Powell C. F., Macphees A. G., Narayanan S., Wang J., Yue Y., and Cuenca R., 'Pixel array detectors for time resolved radiography,' Review of Scientific Instruments, Vol. **73** (3), pp. 1621 – 1624, (2002).

Rose A, 'Sensitivity performance of the human eye in an absolute scale,' Journal of the Optical Society of America, Vol. **38**, pp. 196 – 208, (1948).

Rossi M., Casili F., Golovkin S. V. and Govorun V. N., 'Digital radiography using an EBCCD-based imaging device,' Applied Radiation and Isotopes, Vol. **53**, pp. 699 – 709, (2000).

Saleh M. A., Hayat M. M., Saleh B. E. A., and Teich M. C., ' Dead-space-based theory correctly predicts excess noise factor for thin GaAs and AlGaAs avalanche photodiodes,' IEEE Transactions on Electron Devices, Vol. **47** (3), pp. 625 – 633, (2000).

Schiebel U. W., Conrads N., Jung N., Weibrecht M., Wieczorek H., Zaengel T. T., Powell M. J., French I. D., Glasse C., 'Fluoroscopic imaging with amorphous silicon thin film arrays,' Proceedings of SPIE, Vol. **2163**, pp.128 – 140 (1994).

Schwarz C., Campbell M., Goeppert R., Ludwig J., Mikulec B., Runge K., Smith K. M., and Snoeys W. 'Measurements with Si and GaAs pixel detectors bonded to photon counting read out chips,' Nuclear Instruments and Methods in Physics Research A, Vol. **466** (1-3), pp. 87 – 94, (2001).

Siewerdsen J. H., Antonuk L. E., ElMohri Y., Yorkston J., Huang W., Boudry J. M., Cunningham I. A., 'Empirical and theoretical investigation of the noise performance of indirect detection, active matrix flat-panel imagers (AMFPIs) for diagnostic radiology,' Medical Physics Vol. **24** (1), pp. 71 – 89, (2000).

Speller R. D., Royle G. J., Triantis F. A., Manthos N., Van der Stelt P. F., and di Valentin M., 'Digital X-ray imaging using silicon microstrip detectors: a design study,' Nuclear Instruments and Methods in Physics Research A, Vol. **457** (3), pp. 653 – 664, (2001).

Renker D., 'Properties of avalanche photodiodes for applications in high energy physics, astrophysics and medical imaging,' Nuclear Instruments and Methods in Physics Research A, Vol. **486** (1-2), pp. 164 – 169, (2002).

Sze S. M., 'Physics of semiconductor devices,' Wiley, New York, U.S.A., (1981).

Taibi A., Del Guerra A. Gambaccini M., Marziani M., and Tuffaelli A., 'Evaluation of a digital x-ray detector based on a phosphor-coated CCD for mammography,' Nuclear (1997).

Taibi A., Royle G. J., and Speller R. D., 'A Monte Carlo simulation study to investigate the potential of diffraction enhanced breast imaging' IEEE Transactions on Electron Devices, Vol. **47** (4), pp. 1581 - 1586, (2000).

Tan C. H., Clark J.C., David J. P. R., Rees G. J., Plimmer S. A., Tozer R. C., Herbert D. C., Robbins D. J., Leong W. Y. and Newey J. 'Avalanche noise in thin Si p^+-i-n^+ diodes,' Applied Physics Letters, Vol. **76** (26), pp. 3926-3928, (2000).

Tate M., Gruner S. M., and Eikenberry E. F., 'Coupling format variations in x-ray detectors based upon charge coupled devices,' Review of Scientific Instruments, Vol. **68** (1), pp. 47 – 54, (1997).

Thirwall J. T., 'The detective quantum efficiency of medical x-ray intensifiers,' Review of Scientific Instruments, Vol. **69** (11), pp. 3953 – 3957, (1998).

Van Overstraeten R. and De Man H., 'Measurement of the ionization rates in diffused silicon p-n junctions,' Solid State Electronics, Vol. **13**, pp. 538, (1969).

Van Vliet K. M. and Rucker L. M., 'Theory of carrier multiplication and noise in avalanche devices –Part I: one carrier processes,' IEEE Transactions on Electron Devices, Vol. **26,** pp. 746-751, (1979).

Vedantham S., Karellas A., Suryanarayanan S., Levis I., Sayag M., Kleehammer R., Heidsieck R., D'Orsi C. J., 'Mammographic Imaging with a small format CCD-based digital cassette: Physical characteristics of a clinical system,' Medical Physics Vol. **27** (8), pp. 1832 –1840 (2000).

Wagner R. F., 'Fast Fourier digital quantum mottle analysis with application to rare earth intensifying screens', Medical Physics, Vol. **4**, pp. 157 - 162 (1977).

Westmore M. S., Fenster A., and Cunningham I. A., 'Angular-dependant coherent scatter measured with a diagnostic x-ray image intensifier-based imaging system,' Medical Physics, Vol. **23** (5), pp. 723-733 (1996).

Yaffe M. J. and Rowlands J. A., 'X-ray detectors for digital radiography', Physics in Medicine and Biology, Vol. **42**, pp. 1-39 (1997).

Yaffe M. J., 'Digital mammography – detector considerations and new applications,' Nuclear Instruments and Methods in Physics Research A, Vol. **471** (1-2), pp. 6 – 11, (2001).

Yin S., Tümer T. O., Maeding D., Mainprize J., Mawdsley G., Yaffe M. J., Gordon E. E., and Hamilton W. J., 'Direct conversion CdZnTe and CdTe detectors for digital mammography,' IEEE Transactions on Nuclear Science, Vol. **49** (1), pp. 176 – 181, (2002).